Dissertation
submitted to the
Combined Faculties of the Natural Sciences and Mathematics
of the Ruperto-Carola University of Heidelberg, Germany
for the degree of
Doctor of Natural Sciences

Put forward by
Andrea Demetrio
born in: Genova (Italy)

Oral examination: 10th July, 2018

Feasibility of a gravity measurement on antimatter using a Talbot-Lau interferometer

Referees: Prof. Dr. Markus K. Oberthaler
Prof. Dr. Markus Arndt

Abstract

The past two decades have witnessed an increasing focus on cold antimatter physics, with the development of the Antiproton Decelerator at CERN as a supply of low-energy antiprotons. Among the open questions concerning antimatter, the result of a gravity measurement on anti-atoms as a direct test of the weak equivalence principle has attracted the interest of several collaborations (AE$\bar{g}$IS, GBAR, ALPHA). This work describes the use of a Talbot-Lau interferometer as a tool to perform a gravity measurement on antihydrogen. This device, composed of two or three material gratings, has been successfully used to reveal the wave behavior of different particle species and, in its classical limit, to perform inertial measurements on neutral and charged particles in the past. In order to study its suitability as a gravimeter for antimatter, systematic effects which can prejudice the outcome of the measurement are analyzed in detail. These include misalignments of the interferometer and influences of external field gradients. Simple mathematical formulas which quantify their prominence are produced and tested via numerical simulations. State-of-the-art production rates of cold antihydrogen are used to calculate the time required to retrieve the sign of the gravitational acceleration of antimatter using this setup. The result is an estimation of the feasibility of this measurement in the framework of the AE$\bar{g}$IS experiment.

Zusammenfassung

Mit der Entwicklung des Antiproton Decelerator am CERN, der niederenergetische Antiprotonen erzeugt, hat sich in den letzten zwei Jahrzehnten die Physik kalter Antimaterie zu einem aktiven Forschungsgebiet herausgebildet. Zu den ungelösten Problemen der Antimaterie, gehört auch die Frage nach dem schwachen Äquivalenzprinzip. Mehrere Kollaborationen (ALPHA, GBAR, AE$\bar{g}$IS) haben sich daher eine Gravitationsmessung an neutralen Antiatomen als Hauptziel genommen. Die vorliegende Arbeit beschreibt die Anwendung eines Talbot-Lau Interferometers, um eine solche Gravitationsmessung an Antiwasserstoff durchzuführen. Dieses Gerät, bestehend aus zwei oder drei Gittern, wurde bereits erfolgreich verwendet, um sowohl die Wellennatur von verschiedensten Teilchen zu zeigen, als auch, in seiner klassischen Variante, Trägheitmessungen an neutralen und geladenen Teilchen zu realisieren. Systematische Effekte, die eine Gravitationsmessung verhindern könnten, wie die Ausrichtung des Interferometers oder der Einfluss von Feldgradienten, werden hier dargelegt. Diese Störeinflüsse werden in analytischer Form beschrieben und durch numerische Simulationen bestätigt. Um eine Abschätzung der benötigten Messzeit einer zukünftigen Gravitationsmessung zu geben, wird als Ausgangspunkt die aktuell beste Produktionsrate von kaltem Antiwasserstoff genommen. Das Resultat stellt eine Bewertung der Machbarkeit einer solchen Messung im Rahmen des AE$\bar{g}$IS-Experiments dar.

Contents

Chapter 1

Introduction

Antimatter has been the subject of increasing research interest in the last two decades. Since the commissioning of the Antiproton Decelerator at CERN [Mau97; HW13] and the production of the first cold antihydrogen atoms by the ATHENA collaboration in 2002 [Amo+02], the precision with which the properties of antimatter have been known has increased exponentially, now rivaling the measurements on matter. In 2015, the BASE experiment performed a comparison between the charge-to-mass ratios of protons and antiprotons with a precision of 69 parts per trillion [Ulm+15], while in 2017 the very same collaboration managed to measure the magnetic moment of the antiproton on a part-per-billion level [Smo+17; Nag+17]. The ALPHA collaboration managed to put a limit on the charge of antihydrogen in 2016 [Ahm+16], and later to improve the trapping efficiency of antihydrogen [Ahm+17a], with important results such as the measurement of its 1S-2S transition [Ahm+17b; Ahm+18] and its hyperfine structure [Ahm+17c]. In recent years, the interest in performing a gravity measurement on antimatter has become a central point in this expanding field. On the one hand, there are several theoretical arguments against the possibility that gravity acts in a different way on antimatter, such as the Gedankenexperiment by Morrison [Mor58]. On the other hand, there are also theories which incorporate significant differences between gravity and antigravity [Cha93]. A precise experimental verification of how the gravitational interaction works on antihydrogen would therefore be a precious contribution to the ongoing research. Several proposals to measure the gravitational acceleration on antimatter have been submitted by different scientific collaborations in the last decade: the AE$\bar{g}$IS collaboration [Dro+07], the GBAR collaboration [Cha+11] and the ALPHA collaboration, with the introduction of the ALPHA-g setup [Han16].

Antihydrogen has been, as of today, the only neutral antimatter species produced and trapped in significant numbers at cold temperatures [Ahm+17a], making it the only suitable candidate for a pure anti-

matter gravity measurement. Positronium (Ps), which is a bound state between an electron and a positron, is a mixture between matter and antimatter and has a lifetime of some hundreds of nanoseconds [THK06; Agh+17], which is practically too short for this kind of inertial measurements.

A first preliminary direct measurement, performed by the ALPHA collaboration in 2013 [Amo+13], put weak bounds on the magnitude and direction of the (anti)gravitational acceleration $\bar{g}$, concluding that $-65g < \bar{g} < 110g$, with g being the gravitational acceleration constant on matter. The measurement used the imbalance on annihilations on the top and the bottom of a horizontal trap as a way to estimate the magnitude of gravity. While this measurement has mostly been a byproduct of the antihydrogen production runs, the ALPHA collaboration plans to improve this result by using a vertical antihydrogen trap built exactly for this purpose [Han16].

The AEḡIS collaboration, instead, proposed the use of a device known as moiré deflectometer as a tool to measure gravity on antimatter. This device, described in the work of Oberthaler et al. [Obe+96], is composed by two or three material gratings and a particle detector and it constitutes the classical limit of a Talbot-Lau interferometer [Tal36; Lau48]. This kind of interferometer has seen extended use in the field of matter wave interferometry, with electrons [BGB13], atoms [CL94], and even heavy molecules like C_{60} [Bre+02]. Given its achievable sensitivity, it makes an interesting case of an atom optic tool which could be applied to antimatter measurements. A proof-of-principle was achieved in 2014, when a two-gratings device was used to reveal a fringe pattern for antiprotons [Agh+14], while still operating in the classical regime. Followup tests with a moiré deflectometer have been performed on the secondary antiproton beamline GRACE [Pac+16] between 2015 and 2017 [Bil15]. Since modifying the distance between the gratings or their periodicity can make the classical description not suitable for the system, the most generic and correct way to approach the design of such a measurement tool is to study the device in the wave regime and, in case it is justified by the geometrical parameters, restrict the scope of the analysis to ballistic trajectories.

The goal of this work is to present a feasibility study on a gravity measurement on antihydrogen, using a Talbot-Lau interferometer. The basic premise of the measurement combines interferometric techniques developed in the last two decades with the proposal of the AEḡIS experiment [Dro+07], of which our research group is part of. The original idea of using a device composed by two or three material gratings in the classical regime is expanded to include the wave behavior of the particles and build a unitary framework for producing consistent evaluations. In the end, we produce an estimation for the time needed to perform such

a measurement for a precision sufficient to determine the direction of the gravitational interaction.

1.1 Thesis outline

This thesis is focused on the use of a Talbot-Lau interferometer as a tool to measure gravity on antimatter. The chapters are organized as follows:

In the remaining part of this section, we further discuss the physical motivations, introducing the weak equivalence principle (WEP) and the current indirect boundaries on antimatter gravity. We also introduce the Antiproton Decelerator at CERN and the AE$\bar{g}$IS experiment, in the context of which the measurement will be ideally carried out.

In Chapter 2, we introduce the Talbot-Lau interferometer and we obtain analytic formulas to calculate the signal of such a device as a function of its geometrical parameters.

In Chapter 3, we consider the effects of an imperfect alignment of the interferometer and we deduce formulas for identifying the parameters that are most critical while designing the device.

In Chapter 4, we study the effect of external forces acting on the particles traveling through the interferometer and how they can affect the quality of the signal.

Finally, in Chapter 5, we use the results and evaluations from the previous chapters to obtain a time estimation for a gravity measurement on antimatter, given the current status of the AE$\bar{g}$IS experiment and the state-of-the-art numbers for antihydrogen production in different experimental regimes.

1.2 The weak equivalence principle

One of the reasons why it is important to perform a precise gravity measurement on antihydrogen, is to verify the weak equivalence principle on antimatter. The weak equivalence principle (WEP) states that the gravitational mass m_g of an object is equal to its inertial mass m_I. This means that the acceleration of a body experiencing free-fall is independent on its internal structure. This principle is a fundamental component of the Einstein equivalence principle, together with the local Lorentz invariance and the local position invariance. These two additional principles can be summarized as follows [Wil14]:

- the outcome of any local non-gravitational experiment is independent of the velocity of the freely-falling reference frame in which it is performed (local Lorentz invariance);

Figure 1.1: Part of the CERN Anitproton Decelerator facility as of December, 2017. The control rooms of the ASACUSA experiment [ABB97; Wid99] and the ALPHA experiment [HB05] can be seen in the background.

- the outcome of any local non-gravitational experiment is independent of where and when in the universe it is performed (local position invariance).

We hereby provide an example on how the WEP can be experimentally tested, in a similar fashion to the original formulation by Eötvös [Eöt90]. Consider two large bodies with different internal structures (e.g. two spheres made up of two different materials) with different inertial masses m_1 and m_2 respectively. By applying Newton's Second Law we get

$$\begin{cases} m_1 \mathbf{a}_1 = m_{g1} \mathbf{g} \\ m_2 \mathbf{a}_1 = m_{g2} \mathbf{g}, \end{cases} \tag{1.1}$$

where $\mathbf{g}$ is the gravitational acceleration, $\mathbf{a}_1$ and m_{g1} are the acceleration and the gravitational mass associated to the first body, while $\mathbf{a}_2$ and m_{g2} are the acceleration and the gravitational mass associated to the second body respectively. If we negate the weak equivalence principle, implying that the inertial mass m_I and the gravitational mass m_g are distinct physical quantities, then interactions due to internal forces should produce a difference between m_I and m_g, such that

$$m_g = m_I + \sum_A \eta_A \frac{E^A}{c^2}, \tag{1.2}$$

where A marks a generic interaction, η_A is an adimensional parameter which quantifies the WEP violation for said interaction, and E^A is the

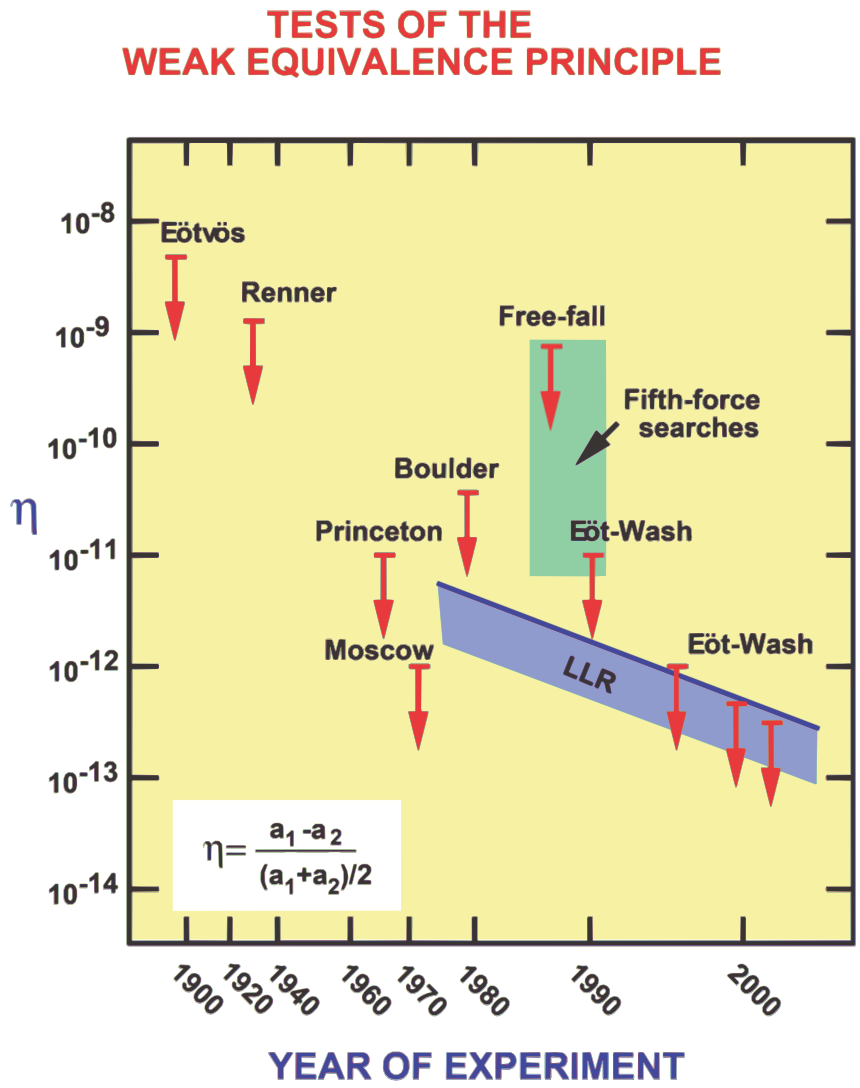

Figure 1.2: The Eötvös ratio is a measure on how much the weak equivalence principle (WEP) is satisfied. The formal expression of the Eötvös ratio η is shown in Eq. (1.3). This quantity has been measured with increasing precision in the last two decades, going down to a relative precision of 1×10^{-13}. This infographic depicts the evolution on WEP validation measurements from 1990 to the early 2000s. The free-fall and Eöt-Wash experiments (torsion balance experiments, see [Wag+12]) were originally performed to search for a fifth force (green region). The blue band shows the bounds for η considering gravitating bodies from lunar laser ranging (LLR), which indirectly sets limit on the WEP [Tal+88]. The figure is a vectorized reproduction of Fig. 1 from [Wil14] by Clifford M. Will, released under a creative commons CC-BY-NC license.

potential energy associated with A. If the WEP holds, $\eta_A = 0 \,\forall\, A$. By using both Eq. (1.1) and (1.2), we can define the Eötvös ratio η as [Wil14]:

$$\eta \stackrel{!}{=} 2\frac{|a_2 - a_1|}{|a_2 + a_1|} = \sum_A \eta_A \left(\frac{E_1^A}{m_1 c^2} - \frac{E_2^A}{m_2 c^2} \right). \tag{1.3}$$

The evaluation of this general parameter η as a result of an experiment can be thus used to place limits on the WEP violation as well. Concerning matter-matter interactions, several experiments have been performed with increasing precision. A diagram showing the evolution of this trend during the years is shown in Fig. 1.2. As of 2014, the Eötvös ratio has been measured to be smaller than 10^{-12} [Sch+08], while there are no measurements on antimatter with a comparable precision.

1.3 Gravity measurement on light atoms

Measuring gravitational effects on light atoms (or antiatoms) is in itself a daunting task: the average fall Δy due to gravitational acceleration $\mathbf{g} = -g\hat{\mathbf{y}}$ for a particle with velocity v on a distance L is

$$\Delta y = \frac{1}{2} g \frac{L^2}{v^2}. \tag{1.4}$$

If we consider a thermal source of particles at a temperature T, v can be estimated as $\sqrt{k_\mathrm{B} T/m}$, with the Boltzmann constant $k_\mathrm{B} = 1.38 \times 10^{-23}\,\mathrm{J\,K^{-1}}$. For light atoms, we can assume the mass m to be of the same order of magnitude as the mass of hydrogen $\simeq m_\mathrm{H} = 1.67 \times 10^{-27}\,\mathrm{kg}$. This makes the fall Δy per meter of path approximately given by

$$\Delta y = 1\,\mathrm{mm\,K\,m^{-2}}. \tag{1.5}$$

At room temperature ($T \simeq 300\,\mathrm{K}$), the fall of a hydrogen atom is therefore of the order of $1.5\,\mathrm{\mu m\,m^{-1}}$. In case we consider a divergent beam, we see that it becomes challenging to measure a fall of this order of magnitude by means of locating the center of mass of the detected particles [Dro+07] - the major issue being the extremely low statistics achievable nowadays in terms of produced anti-atoms. The idea of using a Talbot-Lau interferometer represents an attempt at solving this issue, as the gravitational fall is translated into a phase shift relative to the periodicity of the gratings d, which can be as small as 100 nm on a surface of the order of square millimeters [Sav+95]. Therefore, as long as the fall due to gravity is of the same order of magnitude as the grating periodicity, this tool constitutes a good alternative to perform this kind of measurement. The Talbot-Lau interferometer and its application as an inertial sensor are discussed in detail in Chapter 2.

1.4 Indirect boundaries on antimatter gravity

Despite the lack of conclusive experimental evidence, it is important to notice that there have been already indirect measurements which can place boundaries on a hypothetical asymmetry between matter and antimatter for what concerns the gravitational interaction. In this section, we review two of those arguments: the effect on the lifetime of neutral kaons and antikaons and the cyclotron frequency of trapped protons and antiprotons. Both arguments conclude that it is not expected that matter and antimatter behave differently under the influence of a gravitational potential. However, a model-independent direct measurement would still be crucial in order to verify this claim.

1.4.1 Neutral kaons decay as a WEP test

An asymmetry between hadronic matter and antimatter would mean that there is a difference in their prime constituents, quarks and antiquarks. It should be therefore possible to measure those effects on other particle species which are composed by these constituents, such as mesons. The CPLEAR collaboration reported in 1999 the results of a test of the weak equivalence principle using the decay of neutral kaons K^0 and antikaons $\bar{\mathrm{K}}^0$ in charged pions π^+ π^- [Apo+99]. The neutral kaons mix via the weak interaction, giving birth to two variations known as $\mathrm{K_S}$ and $\mathrm{K_L}$, where S stands for the short-lived state (lifetime $\tau \simeq 89\,\mathrm{ps}$) and L for the long-lived one ($\tau \simeq 51\,\mathrm{ns}$). The mixing matrix for neutral kaons is written as

$$M = \begin{pmatrix} m_{\mathrm{K}^0} & \delta m/2 \\ \delta m/2 & m_{\mathrm{K}^0}, \end{pmatrix} \tag{1.6}$$

with $\delta m = m_{\mathrm{K_L}} - m_{\mathrm{K_S}}$ and $m_{\mathrm{K}^0} = m_{\bar{\mathrm{K}}^0}$ is the inertial mass of the neutral (anti)kaon, which can be considered the same under the assumption that the CPT symmetry holds [Apo+99]. However, the neutral kaons are not eigenstates of the CP symmetry, therefore, they have to be written as linear combinations of the two eigenstates of CP, $|\mathrm{K}_1\rangle = 1/\sqrt{2}(|\mathrm{K}^0\rangle + |\bar{\mathrm{K}}^0\rangle)$ and $|\mathrm{K}_2\rangle = 1/\sqrt{2}(|\mathrm{K}^0\rangle - |\bar{\mathrm{K}}^0\rangle)$. The long-lived and short-lived states can be therefore expressed as

$$|\mathrm{K_L}\rangle = \frac{1}{\sqrt{1+|\epsilon|^2}}(|\mathrm{K}_1\rangle + \epsilon\,|\mathrm{K}_2\rangle) \tag{1.7}$$

$$|\mathrm{K_S}\rangle = \frac{1}{\sqrt{1+|\epsilon|^2}}(|\mathrm{K}_2\rangle + \epsilon\,|\mathrm{K}_1\rangle), \tag{1.8}$$

where ϵ is a parameter which quantifies the CP violation. In case of a difference between the gravitational interaction on antimatter $\bar{g}$ and the

gravitational acceleration on matter g, it is expected that this would alter the gravitational mass m_g of $\bar{\mathrm{K}}^0$ in respect to K^0, effectively leading to a violation of the WEP. More specifically, the presence of an anomalous gravitational interaction would lead to an effective mass difference δm_{eff}. In the hypothesis of a spin-2 mediator (tensor interaction) for gravitational force, for kaons with speed v this difference would assume the form [Hug92]

$$\delta m_{\mathrm{eff}} = m_{\mathrm{K}^0}(g - \bar{g})\frac{U}{c^2}\frac{1+\beta^2}{1-\beta^2}e^{-r/r_g}, \tag{1.9}$$

with U being the gravitational potential, r_g the range of the gravitational interaction, and $\beta = v/c$. This expression changes in case we consider a spin-1 mediator (vector interaction) or a spin-0 mediator (scalar interaction) [Hug92]. For a vector interaction [Apo+99; Hug92]

$$\delta m_{\mathrm{eff}} = m_{\mathrm{K}^0}(g - \bar{g})\frac{U}{c^2}\frac{1}{\sqrt{1-v^2/c^2}}e^{-r/r_g}, \tag{1.10}$$

while for a scalar interaction

$$\delta m_{\mathrm{eff}} = m_{\mathrm{K}^0}(g - \bar{g})\frac{U}{c^2}e^{-r/r_g}. \tag{1.11}$$

The difference in gravitational interaction should therefore cause a modifications in the lifetimes of both $\mathrm{K_L}$ and $\mathrm{K_S}$. The CPLEAR collaboration analyzed a sample of 70 million $\mathrm{K}^0(\bar{\mathrm{K}}^0) \to \pi^+\pi^-$ events, whose rate is dependent on δm, collected over three years of activity. The events were studied as a function of the variations of the gravitational potential of the Earth, the Moon, and the Sun. Taking into account the fluctuations in the potentials and the measured decay rates, limits were put on the additional mass difference δm_{eff} and therefore on $|g - \bar{g}|$. These limits are summarized in Tab. 1.1. The experiment found no evidence of a difference between g and $\bar{g}$, setting an upper limit of the order of 1×10^{-9} on the asymmetry between gravity and antigravity. Similar conclusions were also drawn for variations of the gravitational potential due to the Milky Way and the Shapley supercluster. However, the use of these two sources require the additional hypotheses of setting an absolute gravitational potential.

1.4.2 Cyclotron frequency of trapped (anti)protons

Another indirect limit on the asymmetry between gravitational interactions on matter and antimatter can be obtained by measuring the charge-to-mass ratio q/m of protons and antiprotons. Under the assumption that CPT symmetry is conserved, this measurement can be used to indirectly test the WEP [HH91]. The argument from Hughes and Holzscheiter develops as follows: charged (anti)particles trapped into a

Source	S = 0	S = 1	S = 2
Earth	6.4×10^{-5}	4.1×10^{-5}	1.7×10^{-5}
Moon	1.8×10^{-4}	7.4×10^{-5}	4.8×10^{-5}
Sun	6.5×10^{-9}	4.3×10^{-9}	1.8×10^{-9}

Table 1.1: Upper limits on $|\bar{g} - g|$ for difference sources of gravitational potential and for different spins of the graviton mediator. The numbers shown in the Table are cited from [Apo+99].

Penning trap experience an oscillatory motion defined by the cyclotron frequency $\omega_C = qB/m$, where B is the intensity of the confining magnetic field. This frequency is identical for protons and antiprotons in absence of a gravitational interaction. When immersed in a gravitational field, these frequency should incur into gravitational redshift. If the weak equivalence principle holds, ω_C for protons presents no difference in respect to $\bar{\omega}_C$ for antiprotons. On the contrary, if an asymmetry persists, we expect $\bar{g} = \alpha g$, with $\alpha \neq 1$. This requirement translates into the condition [HH91]

$$\frac{\bar{\omega}_C - \omega_C}{\omega_C} = 3(\alpha - 1)\frac{U}{c^2}, \tag{1.12}$$

with U being the gravitational potential. The choice of an absolute gravitational potential is required by the fact that, if the WEP is violated, an offset in the gravitational potential would lead to different observed behavior depending on the reference system chosen. Therefore we have to fix a gauge in order to keep theory consistent with observations. A reasonable choice is to set U such that it goes to zero at infinity, which would be consistent with no variations in absence of gravitational fields. Hughes and Holzscheiter quantified this asymmetry factor α based on the highest precision measurements available in 1991 [Gab+90], obtaining $|\alpha - 1| < 5 \times 10^{-4}$. As of the date of this work, the best result has been obtained in 2015 by the BASE collaboration at CERN, which reduced this boundary to $|\alpha - 1| < 8.7 \times 10^{-7}$ [Ulm+15]. As the previous example, this boundary is quite strict and seems to rule out the possibility that the gravitational interaction would influence matter and antimatter differently. The nature of this measurement is anyway indirect and a direct experimental verification of the gravitational fall of antimatter is desirable to give a definite answer to this question.

1.5 The Antiproton Decelerator at CERN

The main facility which contributed to the development of experiments on cold antimatter is the Antiproton Decelerator (AD) at CERN [Mau97; HW13]. The antiprotons are produced by accelerating a beam of protons up to 26 GeV in the Proton Synchrotron (PS) and making it collide with

an iridium target [HW13]. A schematic of the accelerator/decelerator complex is shown in Fig. 1.3. The reaction reads

$$\mathrm{p}_{\mathrm{beam}} + \mathrm{p}_{\mathrm{target}} \longrightarrow \mathrm{p} + \mathrm{p} + \mathrm{p} + \bar{\mathrm{p}}, \tag{1.13}$$

which satisfies conservation of mass, momentum, and total number of nucleons. The antiprotons are then ejected with an energy of 3.6 GeV, which is subsequently cooled down to 5.3 MeV. From a beam consisting of 1.5×10^{13} protons, the conversion and cooling yield a bunch of 3×10^{7} antiprotons, which are delivered to the experiments connected to the AD. The cooling cycle has an average length of 100 s and only one experiment can be served at any given time. This results in the residing experiments taking turns and having a shift schedule of 8 h of beamtime per day, resulting in about 280 $\bar{\mathrm{p}}$ shots per shift. The AD is usually active for around seven months per year, from end of April to the first week of December. Outside of this activity period, the experiments located on the ring are usually performing hardware upgrades, measurements on positrons, or - in one specific case - keeping on measuring the properties of the antiprotons caught during the AD activity (the BASE collaboration holds the record as the only experiment on the AD which can run 365 days per year by virtue of their reservoir trap [Smo+15]). Notice that the energy of the antiproton is still fairly high compared to that required for trapping and cooling particles: the experiments at the AD usually employ thin sheets of plastic or metallic material to further reduce the energy of the antiprotons down to the keV regime [Amo+14; Amo+04b].

A further development of the antiproton decelerator facility is scheduled for 2019-2020 [PJ16], with the complete installation of the ELENA ring (Extremely Low ENergy Antiprotons) [Bar+14], which is set to deliver four bunches of 4.5×10^{6} antiprotons with an energy of 100 keV simultaneously to four experiments with a repetition rate of around 100 s. Though the total rate of antiprotons is lower in respect to the AD, the lower initial energy and the increased density of the antiproton beam should result in catching rates improved by among 10 and 100 times [PJ16; Pan17]. This claim is consistent with the results obtained by the ASACUSA experiment at CERN [Kur+15]: by making use of a radio frequency quadrupole decelerator on the so called MUSASHI line [LPB01; Ima+09], the experiment managed to decelerate antiprotons from the AD down to 100 keV and observed and increased catching rate on the same order as the one expected for ELENA.

1.6 The antihydrogen atom

The antihydrogen atom is the antimatter counterpart of the hydrogen atom, and it is composed by an antiproton and a positron in a bound

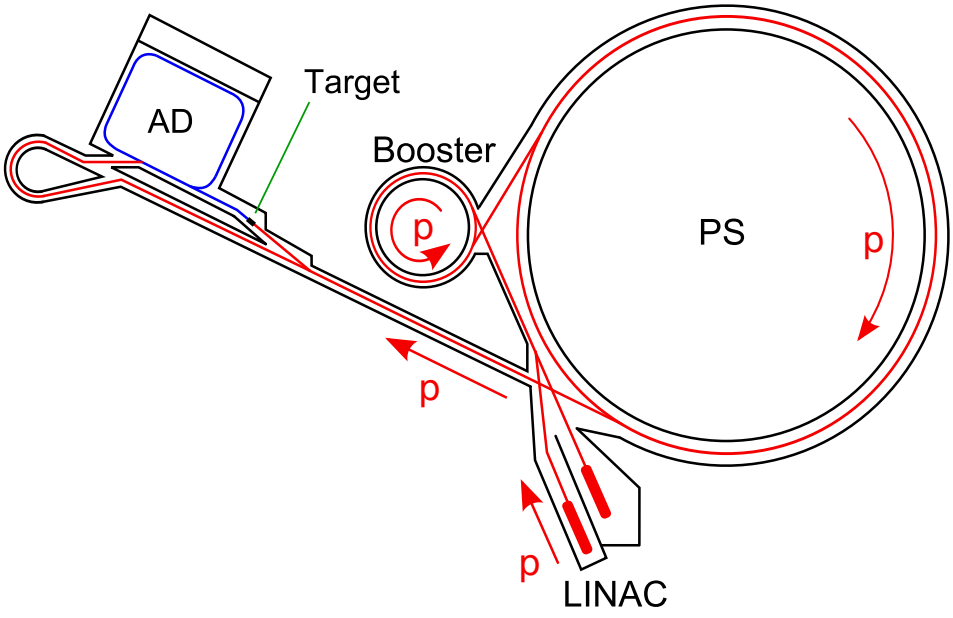

Figure 1.3: Schematic of the Antiproton Decelerator (AD) at CERN. Protons are accelerated by the Proton Synchrotron (PS) to an energy of 26 GeV and then sent colliding with an iridium target, generating 3.6 GeV antiprotons. The so-produced antiprotons are cooled down and decelerated by the AD in a 100 s cycle, and supplied to the experiments at the lower energy of 5.3 MeV [HW13]. Image created by user Tou-X at Wikimedia Commons, released under a CC-BY-SA 3.0 Unported license (`https://creativecommons.org/licenses/by-sa/3.0/deed.en`).

state. The recent experiments performed on antiprotons by the BASE collaboration found that its magnetic moment is compatible with the one of the proton with a relative uncertainty of 2×10^{-11} [Smo+17], while its inertial mass has been found compatible with the one of the proton with a relative uncertainty of 4×10^{-8} [Gab+90]. Also, its charge-to-mass ratio has been measured by the BASE collaboration in 2015 [Ulm+15] and found compatible with that of the proton on a relative precision of 10^{-12}. The physical characteristics of the positron are known with a comparable level of precision: the inertial mass of the positron is the same as the one of the electron down to a relative precision of 8×10^{-9} [Fee+93], while the charge is the same to the level of 4×10^{-8} [Par16]. It is therefore reasonable to assume that when considering antihydrogen atoms in electric and magnetic field gradients, the same parameters as hydrogen can be used to make reasonable predictions.

1.7 The AEgIS experiment

The AEgIS experiment (**A**ntimatter **E**xperiment: **g**ravity, **I**nterferometry, **S**pectroscopy) started in 2007 with the proposal by Drobychev et al. [Dro+07]. One of the leading goals of the collaboration is to perform a gravity measurement on antihydrogen to verify the weak equivalence principle (WEP) on antimatter. The experiment is currently located at the CERN Antiproton Decelerator facility and it has entered its operation phase in 2013. The envisioned experimental cycle is schematized with the help of a block diagram in Fig. 1.4: The production of antihydrogen goes through different phases:

- positrons (e^+) are produced by a β^+ radioactive ^{22}Na source and stored inside a Surko-type accumulator [MS92];
- slow antiprotons ($\bar{p}$) provided by the CERN Antiproton Decelerator are further decelerated with the use of a thin aluminum membrane and trapped into an electromagnetic ion trap called Penning-Malmberg trap [MGW06];
- the trapped antiprotons are transferred to a second Penning-Malmberg trap and cooled down by means of sympathetic cooling through interactions with electrons [RG89];
- when the positron accumulator reaches its maximum capacitance, positrons are injected into the experimental apparatus. Antiprotons are released and sent to the antihydrogen production trap by manipulating the potentials of the traps;
- positrons interact with electrons inside the channels of a film of porous silica and form positronium [MBB10; Lis+12];

- positronium is laser excited to a relatively high state in order to maximize the production efficiency [Kra+16];
- positronium atoms interact with antiprotons and form antihydrogen in a high excited state. This production process is called charge exchange reaction. A detailed treatment on the physics behind antihydrogen production is presented in Chapter 5;
- the so-produced antihydrogen is employed for a variety of measurements, including measurements on antimatter gravity.

As of the completion date of this work, the AEgIS experiment has not yet produced antihydrogen using this schematic, which shares similarities with the proof of concept developed by the ATRAP experiment in 2004 [Sto+04]. This work uses therefore the latest available estimations from the collaboration [Car17] to explore the feasibility of this approach. The theoretical background behind this process and the expected antihydrogen yield are discussed in Sec. 5.3.

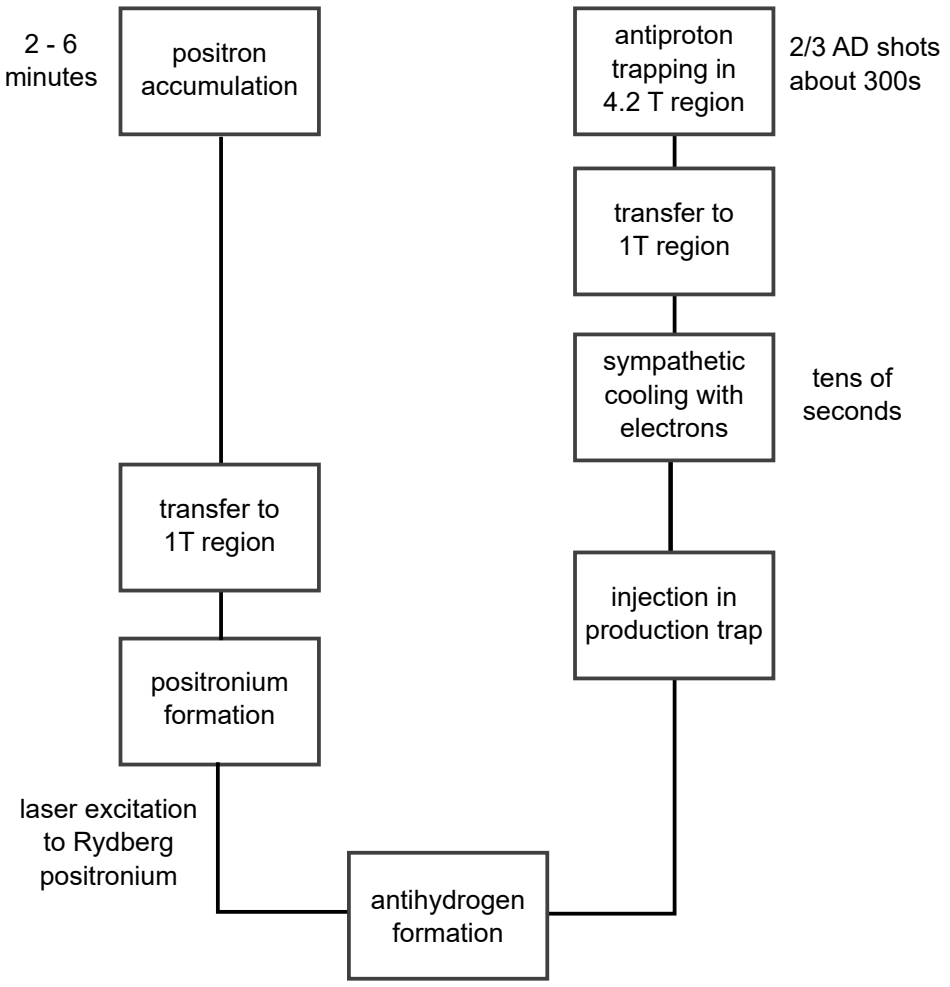

Figure 1.4: This block diagram summarizes a typical experimental cycle of the AEgIS main apparatus: around 3×10^4 antiprotons are trapped in a Penning trap with a magnetic field of 4.46 T over the course of two or three production cycles from the Antiproton Decelerator. At the same time, positrons are accumulated up to a nominal number between 1×10^7 and 1×10^8. This process usually requires several minutes. The antiprotons are transferred to a second Penning trap, this time immersed in a magnetic field of 1 T, where they are cooled through interactions with electrons. After the cooling, the antiprotons are injected into a smaller Penning trap, where they can be stored for tens of seconds without major losses. At this point, positrons are also ballistically transferred to the 1 T region and sent colliding with a target made of a porous material, which causes positronium to be formed. The positronium is then laser excited to increase the production rate and sent into the production trap to interact with the antiprotons.

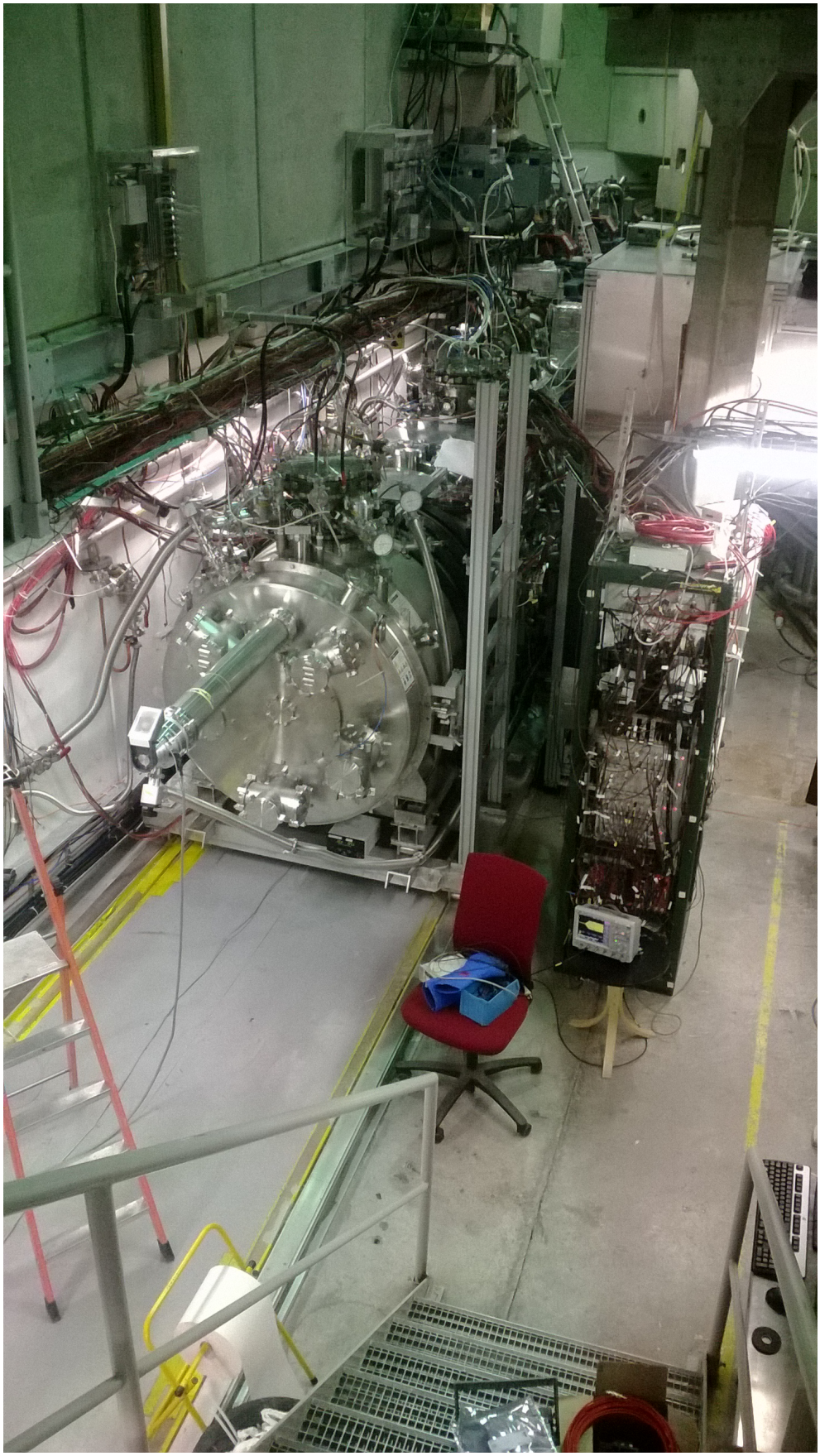

Figure 1.5: AEgIS experimental apparatus as of July 2014. Photo from [Dem14b].

Chapter 2

The Talbot-Lau interferometer

Our tool of choice to perform inertial measurements on antimatter is a device called Talbot-Lau interferometer, from the names of English scientist William Henry Fox Talbot and German physicist Ernst Lau. The former found out in the early years of 1800 that, by letting light through a periodic grating, a series of rephasings would show up right after the grating, generating a shadow image of the grating itself at multiple integers of a fixed distance [Tal36], which was later named Talbot length in his honor. This so called Talbot carpet, however, vanishes completely if the illumination on the grating is incoherent, leaving nothing but a uniform beam of light. Ernst Lau found out that, by placing a second grating identical to the first one at certain distances, the carpet could be partially recovered, as well as the periodic shadow images of the gratings [Lau48]. The combination of these two effects led to the creation of the Talbot-Lau interferometer, an optics tool that has garnered prominent use not only in classical optics but also in the field of matterwave optics: if the device is rescaled considering the de Broglie wavelength of particles λ_{dB}, the behavior is exactly the same as for light. Since its inception, this interferometer has been successfully employed to reveal interference patterns from electrons [BGB13], atoms [CL94], up to heavier molecules like C_{60} [Bre+02]. The classical version of this device has been successfully used to measure gravity on argon atoms [Obe+96], electric and magnetic fields on antiprotons [Agh+14] and on various hydrogen ions [Lan+17], giving strong arguments in favor of the feasibility of the measurement we are planning to perform. It is interesting to notice that the de Broglie wavelength of the C_{60} molecules used in the experiment from Brezger et al. [Bre+02], of the order of picometers, is of the same order of magnitude as the one expected for keV (anti)hydrogen. Therefore, a device with similar geometrical characteristics as the one employed in those condition would also prove suitable for use with this kind of par-

ticles. In the following, we introduce the working principle of this tool and we go through an explanation on how this can be applied to inertial sensing, also taking a closer look to the behavior of this device in the classical limit. A closed formula to calculate the pattern generated by the interferometer is also introduced, in order to provide a robust mathematical tool to predict the outcome of a measurement.

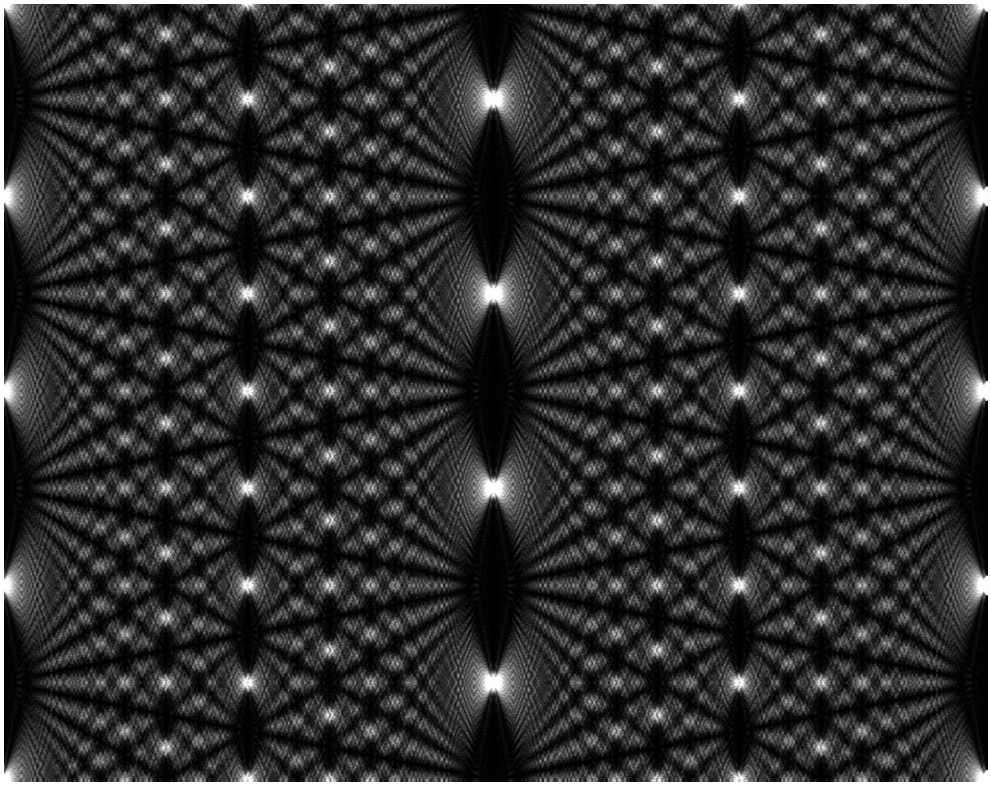

Figure 2.1: When illuminating a single grating with a coherent beam of light, multiple rephasings can be observed. The distance between the rephasings is proportional to a typical length called Talbot length.

2.1 Operating principles

2.1.1 Description and physics

The traditional Talbot-Lau interferometer is composed by two identical gratings and a position sensitive detector. The gratings have a periodicity d and an open fraction η (i.e. the ratio between the open part and the full period). The distance between the first and the second grating $L_1 = L$ is equal to the distance between the second grating and the detector L_2. A schematic of the device, together with a reference coordinate system is shown in Fig. 2.2. The pattern on the detector appears as a density

modulation with the same periodicity d as the gratings. The typical length scale of this type of interferometer is designed as Talbot length L_{T}, defined as

$$L_{\mathrm{T}} = \frac{d^2}{\lambda}, \tag{2.1}$$

where λ is the wavelength of the impinging light. When using this device with particles, λ can be replaced by the de Broglie wavelength λ_{dB}, leading to

$$L_{\mathrm{T}} = \frac{d^2}{\lambda_{\mathrm{dB}}} = \frac{d^2}{h}\sqrt{2mU}, \tag{2.2}$$

where h is the Planck constant, m the mass of the particle, and U is the kinetic energy of the particles. Notice that the device described so far can operate both in the classical, near-field and far-field regime: the relation between L and L_{T} determines the regime in which the device is being used. When $L \gg L_{\mathrm{T}}$, the device operates in the far-field regime as a Mach-Zehnder interferometer [GBB06]. In this specific configuration, the contrast C of the pattern, defined as

$$C = \frac{I_{\max} - I_{\min}}{I_{\max} + I_{\min}}, \tag{2.3}$$

$I_{\max}$ and $I_{\min}$ being the maximum and minimum intensity of the revealed signal respectively, depends only on the geometrical characteristics of the device and has no dependency on U [CSP09]. This is what is referred in literature as an achromatic setup. If $L \simeq L_{\mathrm{T}}$, the device behaves like a near-field interferometer, as the diffracted beams from the gratings overlap. This configuration constitutes a proper Talbot-Lau interferometer and is the one we elected to study in the context of this work. In the Talbot-Lau configuration, the contrast of the pattern is strongly dependent on the energy of the particles, since only particles with a specific energy have a L_{T} which matches the length of the device. This case will be discussed in detail in the next section. When $L \ll L_{\mathrm{T}}$, the signal recorded by the detector is no different than the one which would be revealed if we considered geometrical trajectories instead of a wave propagating through the device (classical regime). In this specific case, the contrast of the pattern is again independent on U and completely determined by the periodicity d and the open fraction η of the gratings. A device operating in this configuration is called moiré deflectometer [Obe+96]. Notice that when $L = nL_{\mathrm{T}}$, $n \in \mathbb{Z}^+$, the pattern generated by the Talbot-Lau interferometer is indistinguishable from its classical counterpart, yielding the same contrast as a result. This is however only true if the beam is monoenergetic, as particles with different energies match a different Talbot length. Choosing the length of the device appropriately thus becomes an important factor in the design of the experiment and has to be thought in a way to get the maximum efficiency out of the available energy range.

A twist on this perspective is considering a device with fixed distance L between the gratings and then tune the energy of the particles such that L is equal to an integer multiple of the Talbot length. From Eq. (2.2), this translates into a requirement for the kinetic energy U of the particles which reads

$$U = \frac{U_{\mathrm{T}}}{n^2} = \frac{1}{n^2}\frac{h^2 L^2}{2md^4}. \tag{2.4}$$

In this framework, we can then set the geometrical parameters of the device and see how the contrast of the pattern evolves as a function of the energy of the particles. An example of this behavior is shown in Fig. 2.3 for different open fractions.

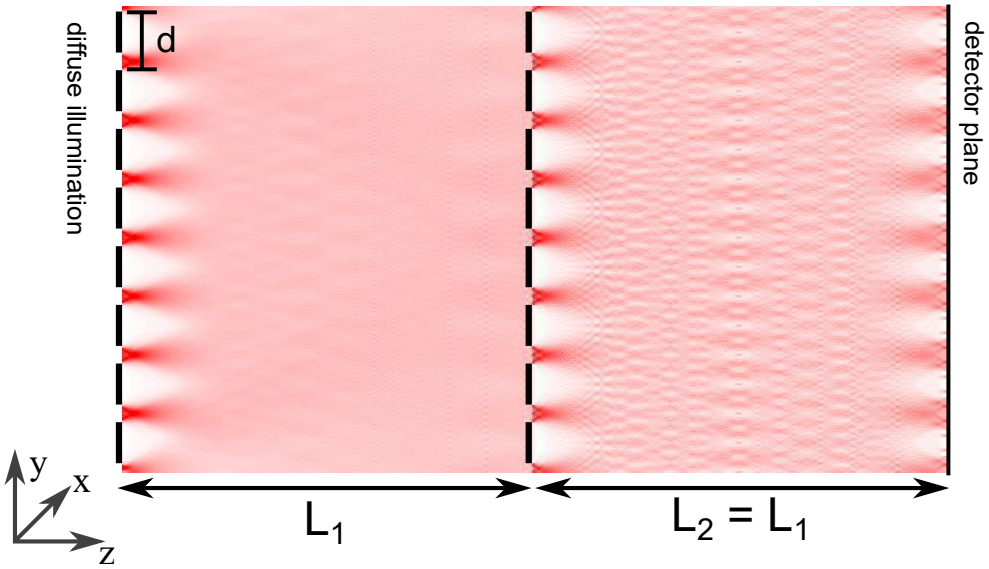

Figure 2.2: A schematic of a traditional Talbot-Lau interferometer. Two identical gratings with periodicity d and open fraction η are illuminated by a divergent source of particles (or light). The distance L_1 between the first and the second grating is equal to the distance L_2 between the second grating and a position sensitive detector. The first grating illuminates the second grating with a coherent illumination, allowing for a revival of the Talbot carpet. Figure adapted from Demetrio et al. [Dem+17].

2.1.2 Origin of the rephasings: the Talbot carpet

There are several ways to mathematically obtain the periodic rephasing due to a plane wave traveling through a grating. The following derivation is based on the work of Bergermann [Ber12] and its inclusion in the work of Bräunig [Brä14] and employs the so-called plane wave decomposition. For the sake of simplicity, we restrict our analysis in two dimensions (y and z), while ignoring the dispersion in the x direction (reference system

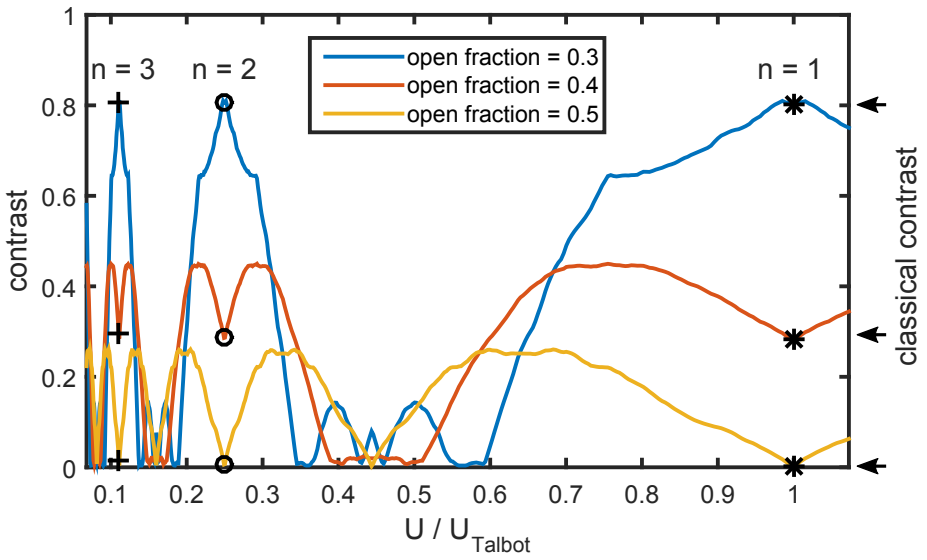

Figure 2.3: One of the characterizing properties of the periodic pattern generated by a Tabot-Lau interferometer is its contrast as a function of the energy. Here, the contrast is defined as $(I_{\max} - I_{\min})/(I_{\max} + I_{\min})$, with $I(y)$ being the intensity of the signal at the position y on the detector plane. When the energy of the incoming waves U satisfies the relation $U = U_{\mathrm{T}}/n^2$, $n \in \mathbb{Z}^+$, with U_{T} being the characteristic energy of the interferometer (Eq. (2.4)), the signal is indistinguishable from that which would be generated by the geometric trajectories of the particles through the grating. In all other configurations, the signal shape changes, modifying the contrast accordingly. The plots have been calculated using the Wigner representation [Wig32] as described in [HSA04] and [Brä14] and discussed in detail in Sec. 2.4. Figure adapted from Demetrio et al. [Dem+17].

from Fig. 2.2. A scalar field $u(y,z)$, as the one impinging on the first grating, can be decomposed in a superimposition of different waves by expressing it as the inverse Fourier transform of its spectrum. By defining the one-dimensional Fourier transform as

$$\mathcal{F}\{u(y,z=0)\} = \tilde{u}(k_y) = \int_{-\infty}^{\infty} \mathrm{d}y \; u(y,z=0)e^{-ik_y y} \tag{2.5}$$

we can rewrite $u(y,z=0)$ as

$$u(y,z=0) = \mathcal{F}_{k_y}^{-1}\{\tilde{u}(k_y)\} = \frac{1}{2\pi}\int_{-\infty}^{\infty} \mathrm{d}k_y \; \tilde{u}(k_y)e^{ik_y y}. \tag{2.6}$$

If we consider monochromatic plane waves with a fixed wavelength λ_{dB}, we get that the total wave vector $\mathbf{k}$ satisfies $|\mathbf{k}|^2 = k^2 = (2\pi/\lambda_{\mathrm{dB}})^2$. This restriction implies that the axial wave vector k_z is bound to have a value which is fixed once k_y is set

$$k_z = \pm\sqrt{\left(\frac{2\pi}{\lambda_{\mathrm{dB}}}\right)^2 - k_y^2}, \tag{2.7}$$

where the sign matches the propagation direction (plus for propagation in the positive z direction, minus for the negative z axis). In the following, we consider waves traveling in the positive z direction, therefore keeping only the positive solution. By propagating the wave in space, up to a generic position $z = \bar{z}$, it accumulates an additional phase $e^{ik_z\bar{z}}$. With this in mind, we modify Eq. (2.6) to make it valid for every z

$$\begin{aligned} u(y,z) &= \frac{1}{2\pi}\int_{-\infty}^{\infty} \mathrm{d}k_y \; \tilde{u}(k_y)e^{ik_z z}e^{ik_y y} \\ &= \frac{1}{2\pi}\int_{-\infty}^{\infty} \mathrm{d}k_y \; \tilde{u}(k_y)e^{iz\sqrt{\left(\frac{2\pi}{\lambda_{\mathrm{dB}}}\right)^2 - k_y^2}}e^{ik_y y}. \end{aligned} \tag{2.8}$$

If we define the propagator $\mathcal{P}_{k_y}(z)$ as

$$\mathcal{P}_{k_y}(z) = e^{iz\sqrt{\left(\frac{2\pi}{\lambda_{\mathrm{dB}}}\right)^2 - k_y^2}}, \tag{2.9}$$

we can rewrite Eq. (2.8) in a way which gives us a hint on how to compute the expression with the help of a computer program:

$$u(y,z) = \mathcal{F}_{k_y}^{-1}\{\mathcal{F}_y\{u(y,0)\mathcal{P}_{k_y}(z)\}\}. \tag{2.10}$$

The process is pretty straight-forward: once the intensity field at $z = 0$ is known, the wave front is discretized in vector of finite size. The vector is transformed using an FFT algorithm and multiplied by the propagator, sampled with the same finesse. The result is then anti-transformed,

in order to get the intensity field in direct space coordinates. In fact, the Talbot carpet shown in Fig. 2.2 has been calculated by evaluating Eq. (2.10) numerically at different positions $z = \bar{z}$, by considering the intensity

$$I(y,z) = \sum_{\theta} I_\theta(y,z) = \sum_{\theta} u_\theta(y,z) u_\theta^*(y,z), \tag{2.11}$$

with θ being the angle of incidence of the waves, summed up on a discrete set in order to simulate a diffuse illumination. The action of the wavefront passing through a grating can be expressed by multiplying the wave front function $u(y, z = z_{\text{grating}})$ by the grating transparency function $t(y;\eta)$, where η is the open fraction of said grating. Our ideal model of a grating consists in an infinitely thin sheet of material which is either completely transparent ($t = 1$) or completely opaque to the particles ($t = 0$), depending on the considered coordinate y. We can explicitly express $t(y;\eta)$ as [Dem+17]

$$t(y;d,\eta) = \begin{cases} 1 \text{ for } \operatorname{mod}(y,d) < \eta d \\ 0 \text{ otherwise.} \end{cases} \tag{2.12}$$

If we consider an infinite grating, $t(y;d,\eta)$ can be expressed as its Fourier series as a function of the grating vector $k_d = 2\pi/d$. The resulting expression takes the general form [Ber12; Brä14]

$$t(y;d,\eta) = \sum_{n=-\infty}^{\infty} c_n e^{ink_d y} = \sum_{n=-\infty}^{\infty} c_n e^{ik_n y}, \tag{2.13}$$

where we replaced $k_n = nk_d$ and c_n is the n-th Fourier coefficient of the series, which, for an infinite grating as the one in Eq. (2.12) is given by [Brä14]

$$\begin{aligned} c_n &= \frac{1}{d} \int_{-\frac{d}{2}}^{\frac{d}{2}} t(y;d,\eta) e^{-ink_d y} \\ &= \eta \operatorname{sinc}(\eta n) e^{-ink_d y_g} \\ &= {c'}_n e^{-ink_d y_g}, \end{aligned} \tag{2.14}$$

with the initial grating phase $2\pi y_g/d$ and the cardinal sine defined as $\operatorname{sinc}(x) = \sin(\pi x)/(\pi x)$. The dependence on the open fraction η is absorbed in the c_n coefficients and it becomes again explicit when we calculate a closed form for them. Now, consider a plane wave $u(y,z) = e^{ik_y y} e^{ik_z z}$ which impinges on a grating placed at $z = 0$. If we consider the light field $u(y, 0^-)$ just before the grating, we can write $u(y, 0^+)$ as

$$\begin{aligned} u(y,0^+) = u(y,0^-) \cdot t(y;d,\eta) &= \sum_{n=-\infty}^{\infty} c_n e^{i(k_y + k_n)y} \\ &= \sum_{n=-\infty}^{\infty} c_n e^{i(k'_n)y} \end{aligned} \tag{2.15}$$

which describes a superimposition of plane waves with wave vectors $k'_n = k_y + k_n$. This formula should not strike as excessively odd to the eye of the reader: the additional transverse wave vector is just a mathematical formulation of the interference phenomenon from an extended grating. Once again, if the field behind the grating is known, it can be retrieved at any position $z = \bar{z}$ by applying the process described in this section: Fourier transform, propagation, Fourier anti-transform. Performing the operations in order, we first get $\tilde{u}(k_y)$

$$\begin{aligned}\tilde{u}(k_y) = \mathcal{F}\{u(y,0^+)\} &= \int_{-\infty}^{\infty} \mathrm{d}y\ u(y,0^+)e^{-ik_y y} \\ &= \sum_{n=-\infty}^{\infty} c_n \int_{-\infty}^{\infty} \mathrm{d}y\ e^{i(k'_n - k_y)y} \\ &= \sum_{n=-\infty}^{\infty} c_n \delta(k'_n - k_y).\end{aligned} \tag{2.16}$$

Then, we multiply the result by the propagator $\mathcal{P}_{k_y}(z)$:

$$\tilde{u}(k_y)\cdot\mathcal{P}_{k_y}(z) = \sum_{n=-\infty}^{\infty} c_n \delta(k'_n - k_y) e^{iz\sqrt{\left(\frac{2\pi}{\lambda_{\mathrm{dB}}}\right)^2 - k_y^2}}. \tag{2.17}$$

At last, we anti-transform the result, in order to get the desired light field:

$$\begin{aligned}u(y,z) &= \frac{1}{2\pi}\sum_{n=-\infty}^{\infty} c_n \int_{-\infty}^{\infty} \mathrm{d}k_y \delta(k'_n - k_y) e^{iz\sqrt{\left(\frac{2\pi}{\lambda_{\mathrm{dB}}}\right)^2 - k_y^2}} e^{ik_y y} \\ &= \sum_{n=-\infty}^{\infty} c_n e^{iz\sqrt{\left(\frac{2\pi}{\lambda_{\mathrm{dB}}}\right)^2 - {k'_n}^2}} e^{ik'_n y}.\end{aligned} \tag{2.18}$$

Now, we expand the square root to the first order in Taylor (paraxial approximation) as

$$\sqrt{\left(\frac{2\pi}{\lambda_{\mathrm{dB}}}\right)^2 - {k'_n}^2} = \frac{2\pi}{\lambda_{\mathrm{dB}}} - \frac{{k'_n}^2 \lambda_{\mathrm{dB}}}{4\pi} + O({k'_n}^4). \tag{2.19}$$

If we consider a single plane wave impinging on the grating with an angle $\theta = 0$, we have $k_y = 0$ and, therefore $k'_n = k_n = nk_d = 2n\pi/d$. This leads to

$$\frac{{k'_n}^2 \lambda_{\mathrm{dB}}}{4\pi} = \frac{\pi n^2 \lambda_{\mathrm{dB}}}{d^2} = \frac{\pi n^2}{L_{\mathrm{T}}} \tag{2.20}$$

where L_{T} is the Talbot length as expressed by Eq. (2.2). When we substitute this expression in Eq. (2.18), we finally obtain

$$u(y,z) = e^{iz\sqrt{\left(\frac{2\pi}{\lambda_{\mathrm{dB}}}\right)^2}} \sum_{n=-\infty}^{\infty} c_n e^{ik_n y} e^{-i\pi n^2 \frac{z}{L_{\mathrm{T}}}}. \tag{2.21}$$

This final equation underlines a fact we already mentioned while introducing the Talbot carpet: when $z = 2mL_{\mathrm{T}}$, $m \in \mathbb{Z}$, the light field $u(y,z)$ is equal to $u(y,0)$, except for a global phase factor $\exp\left(iz\sqrt{\left(\frac{2\pi}{\lambda_{\mathrm{dB}}}\right)^2}\right)$. This is the so called Talbot rephasing and the reason why in literature one can find an alternative definition of the Talbot length which is $L'_{\mathrm{T}} = 2L_{\mathrm{T}}$. We analyze now Eq. (2.21) for odd integer multiples of our definition of L_{T}. Let $m \in \mathbb{Z}, z = (2m+1)L_{\mathrm{T}}$. Then, we find that

$$e^{-i\pi n^2 \frac{z}{L_{\mathrm{T}}}} = e^{-i2\pi n^2 m} \cdot e^{-i\pi n^2} = e^{-i2\pi} \cdot e^{-in^2\pi} = e^{-in\pi}. \tag{2.22}$$

We notice that, whatever the combination of n and m, $2mn^2$ is always even, while n^2 conserves the parity of n. This leads to

$$\begin{aligned} u(y, z = (2m+1)L_{\mathrm{T}}) &= e^{iz\sqrt{\left(\frac{2\pi}{\lambda_{\mathrm{dB}}}\right)^2}} \sum_{n=-\infty}^{\infty} c_n e^{ik_n y} e^{-in\pi} \\ &= e^{iz\sqrt{\left(\frac{2\pi}{\lambda_{\mathrm{dB}}}\right)^2}} \sum_{n=-\infty}^{\infty} c_n e^{in\frac{2\pi}{d}y} e^{-in\pi} \\ &= e^{iz\sqrt{\left(\frac{2\pi}{\lambda_{\mathrm{dB}}}\right)^2}} \sum_{n=-\infty}^{\infty} c_n e^{in\frac{2\pi}{d}(y-d/2)} \\ &= u(y - d/2, z = 0). \end{aligned} \tag{2.23}$$

This last equation shows that for odd multiples of L_{T} the light field constitutes a shadow image of the grating, albeit with a π phase shift (or half a period shift).

2.2 Detecting the pattern: on the use of a third grating

The shadow images generated by the rephasings described in the previous section share a non-negligible detail: the periodicity of the density modulations is the same as that of the gratings. In order to highlight how this can be critical, we remind the reader that a device geared toward keV (anti)hydrogen with a length of 10 cm requires a periodicity as small as 250 nm to match the Talbot length. Commercially available position sensitive detectors rarely go below 1 µm resolution on large surfaces, effectively limiting our ability to retrieve the structures we are looking for. There are effective workarounds to get rid of these limitations, based on using a third grating, identical to the previous two, on the detector plane. There are two possible configurations which yield the desired result of producing a readable pattern. In this section we analyze both of them separately.

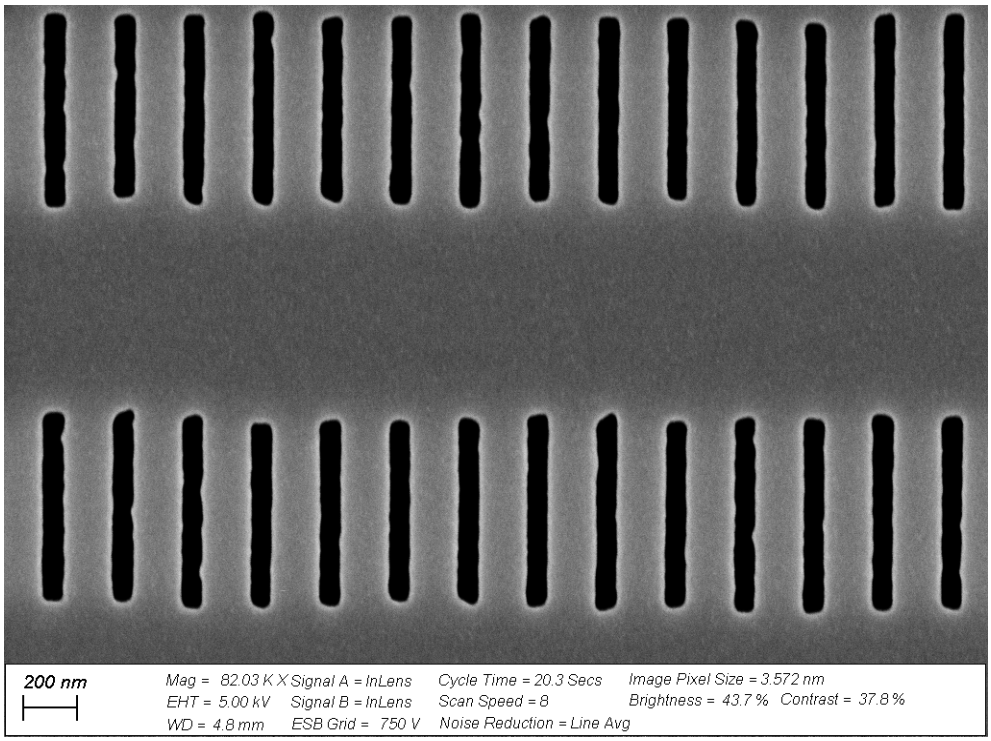

Figure 2.4: SEM picture of a nanometric grating made out of a $3\,\mathrm{mm}^2 \times 3\,\mathrm{mm}^2$ silicon nitride (Si_3N_4) via deep reacting ion-etching [Sav+95]. The periodicity d of the grating is 257 nm, with an open fraction $\eta = 0.46$. The main bars are supported by an additional transverse structure with a periodicity of 1.5 µm and an open fraction of around 60-70 %. Grating courtesy of M. Arndt, SEM picture courtesy of A. Kast.

2.2.1 The third grating as a "scanner"

The first configuration we describe, used by Oberthaler et al.[Obe+96], consists in using the third grating as a "scanning" tool, in conjunction with a particle counter. The outcome of this measurement schematic is represented in Fig. 2.5: in order to reveal the pattern we translate the third grating in the y direction, according to the previously established reference system and we simultaneously record the flux of particles going through the additional grating. Intuitively, the maximum flux is expected to be detected when the grating openings are matched to the maxima of the pattern, while, on the contrary, we expect to find a minimum when the grating has a shift of half a period in respect to the pattern. This approach has the clear advantage that it resolves the issue with the resolution of the detector by requiring no resolution at all. There is also a possible disadvantage: in order to reconstruct the pattern with a sufficient resolution, it is necessary to record several datapoints. Depending on the intensity of the source, this could require a non-negligible amount of time and the measurement could be hindered by slow drifts in intensity.

2.2.2 The third grating as a "magnifier"

The second method exploits a classical phenomenon called moiré beating or moiré effect - the same name used for the classical limit of the Talbot-Lau interferometer. The envisioned setup uses a third grating, identical to the other two, tilted by a small angle α in respect to the fringe pattern generated by the device. As shown in Fig. 2.6, the interaction between the two patterns creates beatings whose periodicity is given by [Mül16]

$$d_{\text{beat}} = \frac{d}{2\sin(\frac{\alpha}{2})}, \tag{2.24}$$

where d is the original periodicity of the grating. Notice that for $\alpha = 0$, d_{beat} diverges, which means that no beatings are observed, since their periodicity would be infinite. For $\alpha \ll 1$, we can approximate the above formula as [Lan+17]

$$d_{\text{beat}} \simeq \frac{d}{\alpha}. \tag{2.25}$$

If we consider a circular grating of radius r, the number of beatings N_{beat} is then given by

$$N_{\text{beat}} = \alpha\frac{r}{d}. \tag{2.26}$$

We see immediately that even when considering $d = 250\,\text{nm}$, and α as small as $100\,\mu\text{rad}$, we get $d_{\text{beat}} = 2.5\,\text{mm}$, which means that the structures can be easily detected by a commercial position sensitive detector.

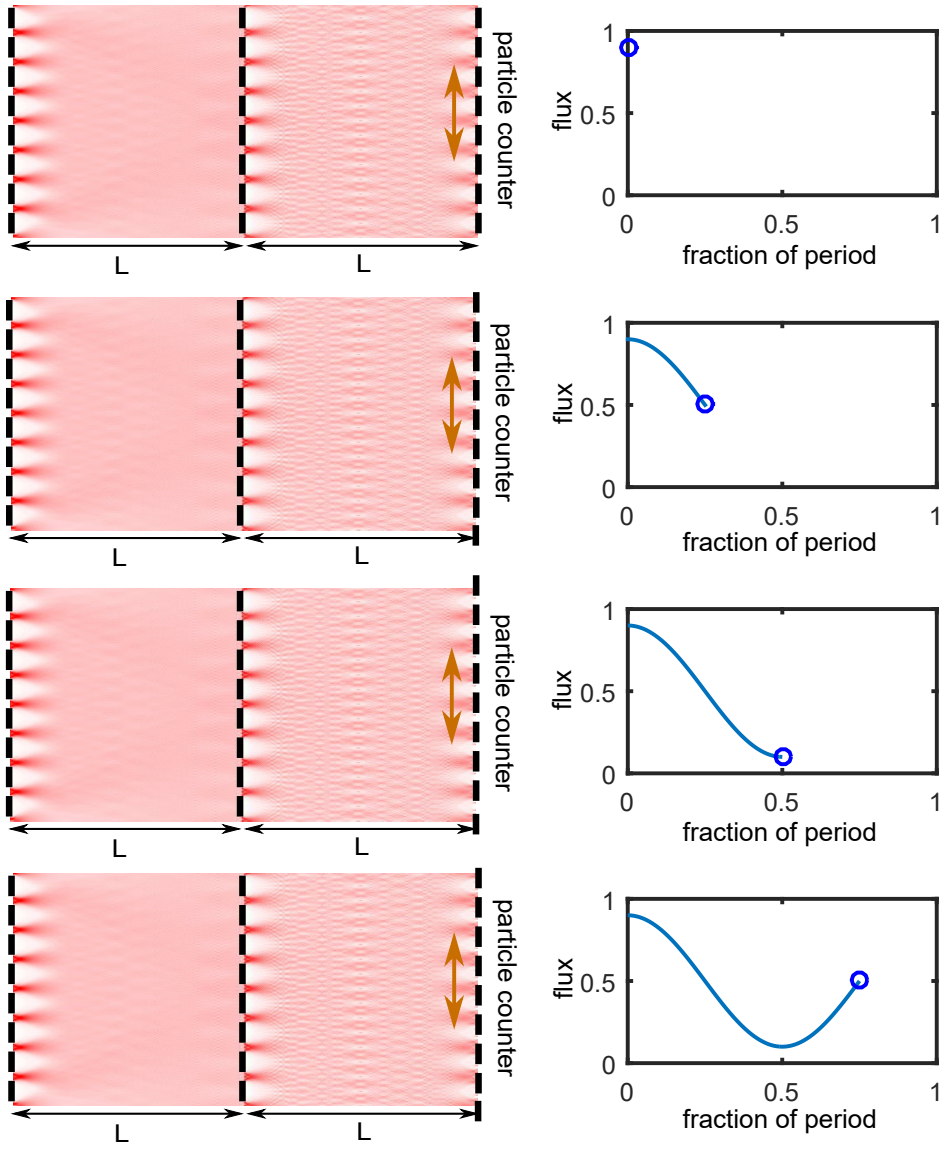

Figure 2.5: By placing a third grating on the detector plane, followed by a particle counter, we can reconstruct the pattern by translating the grating in the transverse direction (orange arrow) and recording the number of events which go through the additional grating [Obe+96; Dem+17].

This method has the advantage that it allows direct detection of the interference pattern in one shot, without need for repeated measurements in different configurations. It works as if every vertical line of the grating is a position in the scan process highlighted in Sec. 2.2.1. This has been used in the work of Lansonneur et al. [Lan+17] in order to enlarge the fringes of a moiré deflectometer with $d = 40\,\mu m$ to be detected by a MCP with $100\,\mu m$ resolution.

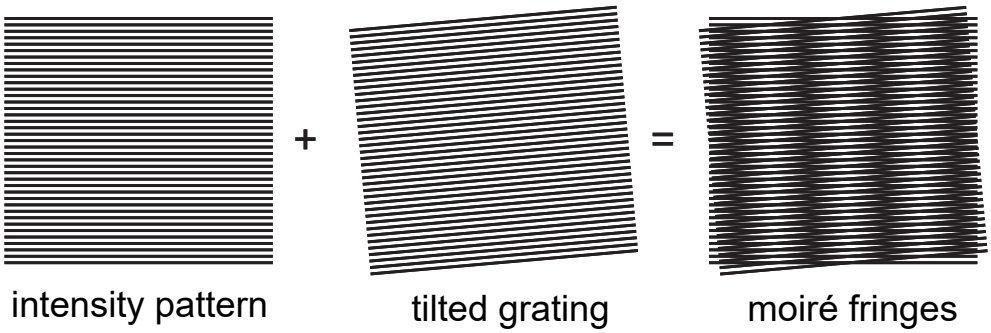

Figure 2.6: A third grating, tilted by a small angle α, create macroscopic beatings when illuminated by the periodic pattern from the first two gratings [Brä14; Mül16; Lan+17]. Those beatings can then be revealed by a position sensitive particle detector. The smaller the angle, the bigger the fringes. Bigger angles translate into an increased number of fringes. Figure from [Lan+17].

Now that we have introduced our tool of choice, it is important to understand how it can be used effectively to measure forces acting on the particles traveling between the gratings. The next section describes the general idea behind the use of a Talbot-Lau interferometer for inertial sensing and introduces a formula for the sensitivity of this device, which will be central in the following discussion.

2.3 Inertial sensing with a two-gratings device

The goal of this work is to provide an estimation on the feasibility of a gravity measurement on antihydrogen in the framework of the AEgIS experiment. Therefore, it is of utmost importance to have access to an estimator for the sensitivity of our device of choice. The title of this section is willingly generic, in that we start from the classical case (the so-called moiré deflectometer) but the result we obtain can be applied to any configuration, including the Talbot-Lau and Mach-Zehnder regime. From Sec. 2.2 we have learnt that the the use of a third grating can

help to reveal the underlining pattern. We consider the third grating to be part of the detection system and focus instead on the physical process which makes inertial sensing possible with the use of the first two gratings. The classical case gives us indeed a rather intuitive way to understand the principle and to extrapolate it later to the quantum case.

2.3.1 The force as a phase shift

If we consider geometrical trajectories, whatever is the distance between the gratings and the energy of the particle, we will always obtain a shadow pattern on the detector plane. When an external force acts on the particle beam in the direction transverse to the grating pitch, this shadow image of the grating gains a phase shift in respect to the unperturbed pattern. Fig. 2.7 provides an example of the aforementioned process and sets the axis reference system we use for the considerations expressed in this section. To derive the phase shift due the force, we build up on the formulation found in [Mül16]. Consider a beam of particles with axial velocity v_z, two identical gratings with periodicity d and open fraction η, and a detector plane. The gratings and the detector plane are distanced by L from each other, as in Fig. 2.7. Consider a uniform, constant acceleration $\mathbf{a} = a\hat{y}$. We set our reference system such that the first grating is located in the position $z = 0$, placing the second grating at $z = L$ and the detector at $z = 2L$. The time of flight τ between the gratings is therefore equal to L/v_z. This sets the times of crossing to $t = 0$, $t = \tau$, and $t = 2\tau$, for the first grating, second grating, and detector respectively. The trajectories of the particles are described by the standard uniformly accelerated motion

$$y(t) = \frac{1}{2}at^2 + v_y^0 t + y_0, \tag{2.27}$$

where v_y^0 and y_0 are the initial transverse velocity and the initial y position respectively. Since the gratings restrict the available trajectories, this places a limitation on $y(t)$. More precisely, y_0 is limited to the interval $[nd, (n+\eta)d]$, $n \in \mathbb{Z}$, while $y(\tau)$, which describes the crossing point through the second grating, has to satisfy the requirement $y(\tau) \in [md, (m+\eta)d]$, $m \in \mathbb{Z}$. We choose two random elements from these sets and we call them $\bar{y}_0$ and $\bar{y}_1$ respectively. This choice sets an additional restriction on v_y^0, since the particle is now bound to cross the second grating at $y(\tau) = \bar{y}_1$. The boundary is given by the equation

$$y(\tau) = \bar{y}_1 = \frac{1}{2}a\tau^2 + v_y^0\tau + \bar{y}_0, \tag{2.28}$$

which leads to

$$v_y^0 = \frac{\bar{y}_1 - \bar{y}_0}{\tau} - \frac{1}{2}a\tau = \bar{v}_y^0 - \frac{1}{2}a\tau. \tag{2.29}$$

With this treatment, we rewrite Eq. (2.27) as

$$y(t) = \frac{1}{2}at^2 + (\bar{v}_y^0 - \frac{1}{2}a\tau)t + \bar{y}_0, \tag{2.30}$$

from which we can obtain the arrival position of the particle on the detector at $t = 2\tau$

$$y(2\tau) = 2a\tau^2 - a\tau^2 + 2\bar{v}_y^0\tau + \bar{y}_0 = c + a\tau^2. \tag{2.31}$$

We find a clear dependence on the acceleration intensity a and we can now calculate the expected shift from the force-free case ($a = 0$) as

$$\Delta y = a\tau^2. \tag{2.32}$$

In order to translate Δy into a phase shift, we take into account the periodicity of the grating, thus obtaining $\Delta\phi$ as

$$\Delta\phi = \frac{2\pi}{d}a\tau^2. \tag{2.33}$$

The classical result still holds in the wave regime, and the phase shift expected in the wave regime is exactly the same as the one shown in Eq. (2.33) [Obe+96]. By measuring $\Delta\phi$ the magnitude of the acceleration can be therefore retrieved. Notice that both detection techniques discussed in Sec. 2.2 yield the same relative phase shift $\Delta\phi$. When using a tilted third grating, the absolute shift is also magnified by a factor d_{beat}/d, which results in the same phase shift $\Delta\phi$ described in the previous equation, without any need for adjusting the formulas [Mül16].

2.3.2 Sensitivity of the device

Now that we have a measurable quantity for determining the acceleration, it is important to also determine the sensitivity of the measurement device as a function of the number of detected events. Following [Obe+96], we consider the resolution of the device as the partial derivative of the phase shift as a function of the acceleration:

$$R_\phi = \left|\frac{\partial\Delta\phi}{\partial a}\right| = \frac{2\pi}{d}\tau^2 = \frac{2\pi}{d}\frac{L^2}{v_z^2}. \tag{2.34}$$

This is an intrinsic property of the measurement apparatus and does not take into account the statistical nature of a measurement. By modeling the detection as a poissonian event and considering, as a first approximation, a periodic sinusoidal signal, the signal-to-noise ratio is given by $C\sqrt{N_{\text{det}}}$, where C is again the contrast of the pattern as defined by Eq. (2.3) and N_{det} is the number of detected particles [Obe+96]. Combining these together, we can now define the sensitivity of our measurement

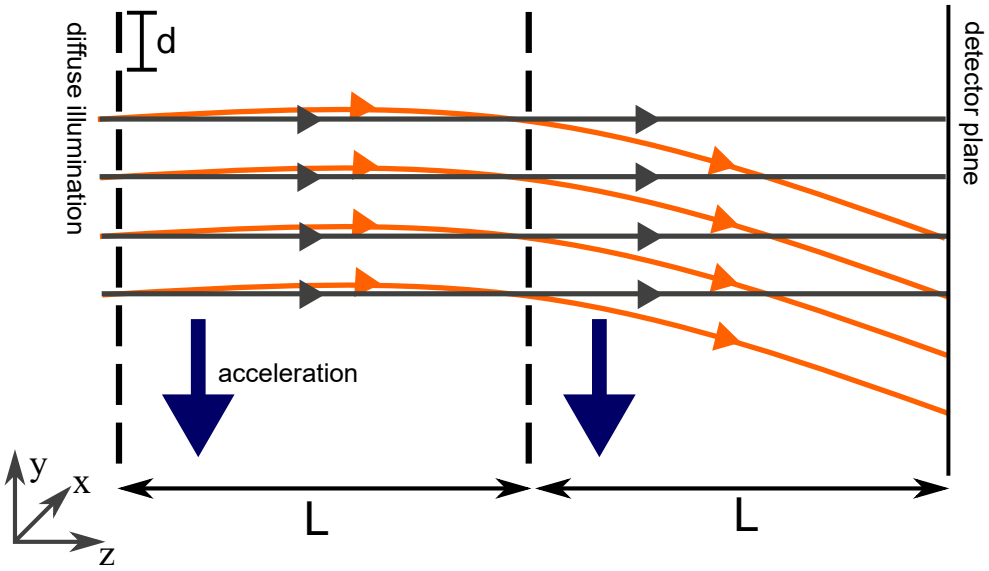

Figure 2.7: In the classical scenario, when a transverse force is applied on the particle beam traveling through the measurement device, the bending of the trajectories causes a phase shift in the recorded pattern. This phase shift is proportional to the time of flight between the gratings and to the intensity of the force.

device, named from this point on as minimum detectable acceleration (a_{min}), as

$$a_{\mathrm{min}} = \frac{d\ v_z^2}{2\pi L^2 C\sqrt{N_{\mathrm{det}}}}. \tag{2.35}$$

This equation outlines the main parameters we have to take care of in order to perform the measurement. We see that the smaller d, the better the sensitivity. Also, smaller v_z and longer L make for a better device, since the intrinsic resolution scales with the second power of both quantities. This expression for the sensitivity of the device is central to our discussion, since it constitutes the figure of merit when considering different designs for a gravity measurement on antimatter. In particular, the contrast C is tightly bound to all the other parameters: as shown in Fig. 2.3, by varying d, L, and v_z what we get is a significant modulation in contrast. This has to be taken into account when designing the device.

The next section focuses on the mathematical treatment needed to extract the shape and the intensity of the signal independently on the setup. This will give us the resources to further investigate the usage of this atom optic tool for inertial sensing.

2.4 Signal calculation in Wigner representation

In order to design a proper measurement device, we need to have access to a reliable mathematical treatment of the expected pattern. While the formulation introduced in Sec. 2.1.2 is useful for visualizing the rephasing and building the pattern, its expansion to incoherent illumination requires a lot of computation power in order to accomodate for the large number of waves needed to simulate a divergent source. Moreover, the smaller the wavelength of the incoming waves, the bigger the sampling needed not to cause artifacts and aliasing, when implemented into a computer program, as every period of the grating could contain several hundreds of wave periods. In this section, we derive instead an expression for the pattern by using the approach outlined in [Brä14], which builds up closely on the work of Hornberger et al. [HSA04]. This approach exploits the Wigner formalism [Wig32] to extract a closed formula for both the signal intensity and contrast. At the end of this section, the signal of a Talbot-Lau interferometer will be expressed as a sum of terms which can be easily implemented in a computer program, requiring less computation power than the method proposed in Sec. 2.1.2. The respective formula for the classical case is also retrieved and found structurally similar to the quantum case, further strengthening the connection between the two regimes.

If we consider a beam of particles with axial velocity v_z much bigger than its transverse velocity $v_r = \sqrt{v_x^2 + v_y^2}$, we can decouple the axial and the transverse motion and, therefore, the axial and transverse wave function. As such, we define the transverse wave function $\psi(\mathbf{r})$, $\mathbf{r} = (x, y)$ in the plane of the grating. The so-called Wigner function can be seen as a quasi-probability distribution $w(\mathbf{r}, \mathbf{p})$ in the phase space, as it does not fulfill all the normal properties of a proper probability density function, due to its abiding by Heisenberg's uncertainty principle [Hei27] for momentum $\mathbf{p}$ and position $\mathbf{r}$. The Wigner function $w(\mathbf{r}, \mathbf{p})$ is defined as [Wig32]

$$w(\mathbf{r}, \mathbf{p}) = \frac{1}{2\pi\hbar} \int_{-\infty}^{\infty} \mathrm{d}\Delta e^{-i\frac{\mathbf{p}\Delta}{\hbar}} \rho\left(\mathbf{r} - \frac{\Delta}{2}, \mathbf{r} + \frac{\Delta}{2}\right), \tag{2.36}$$

where $\rho(\mathbf{r}, \mathbf{r'})$ is the density matrix which describes our system, written as

$$\rho(\mathbf{r}, \mathbf{r'}) = \int \mathrm{d}\mu g(\mu) \psi_\mu(\mathbf{r}) \psi_\mu^*(\mathbf{r'}), \tag{2.37}$$

and $\Delta = \mathbf{r} - \mathbf{r'}$ is usually named as two-point separation. The Wigner function is the Fourier transform of the density matrix and can be used to reconstruct the pattern at the end of the interferometer, by following a strategy similar to the one outlined in Sec. 2.1.2: interaction with

the grating, transformation in the Wigner space, free propagation, anti-transformation, repeated as many times as there are gratings on the path. The next sections will focus on the free evolution of the Wigner function and its interaction with the gratings respectively, in order to be able to build a mathematical expression for the signal on the detector plane.

2.4.1 Free evolution of the Wigner function

In the paraxial approximation (Eq. (2.19)), the free evolution of the wave function $\psi(\mathbf{r})$ up until a position $z = L$ can be written as [HSA04]

$$\psi(\mathbf{r}) = \frac{p_z}{2\pi i\hbar L} e^{\frac{ip_z L}{\hbar}} \int_{-\infty}^{\infty} \mathrm{d}\mathbf{r}_0 \exp\left(i\frac{p_z}{\hbar}\frac{|\mathbf{r}-\mathbf{r}_0|^2}{2L}\right)\psi_0(\mathbf{r}_0) + O\left(\frac{\mathbf{r}}{L}\right), \quad (2.38)$$

with $\psi_0(\mathbf{r}_0)$ being the initial state. From this, we can also evolve $\rho(\mathbf{r}, \mathbf{r'})$ as [Brä14]

$$\begin{aligned}\rho(\mathbf{r},\mathbf{r}') &= \left(\frac{p_z}{2\pi\hbar L}\right)^2 \int \mathrm{d}\mathbf{r}_0\ \mathrm{d}\mathbf{r}'_0\ \exp\left(i\frac{p_z}{\hbar}\frac{|\mathbf{r}-\mathbf{r}_0|^2 - |\mathbf{r}'-\mathbf{r}'_0|^2}{2L}\right)\\ &\cdot \int \mathrm{d}\mu\ g(\mu)\psi_0^{\mu}(\mathbf{r}_0)\psi_0^{\mu *}(\mathbf{r}'_0)\\ &= \left(\frac{p_z}{2\pi\hbar L}\right)^2 \int \mathrm{d}\mathbf{r}_0\ \mathrm{d}\mathbf{r}'_0\ \exp\left(i\frac{p_z}{\hbar}\frac{|\mathbf{r}-\mathbf{r}_0|^2 - |\mathbf{r}'-\mathbf{r}'_0|^2}{2L}\right)\\ &\cdot \rho(\mathbf{r}_0,\mathbf{r'}_0).\end{aligned} \quad (2.39)$$

We thus use this formulation to describe the free evolution of the Wigner function up to a distance L as [HSA04]

$$\begin{aligned}w_L(\mathbf{r},\mathbf{p}) &= \left(\frac{1}{2\pi\hbar}\right)^2 \left(\frac{p_z}{2\pi\hbar L}\right)^2 \int \mathrm{d}\Delta\ e^{-i\frac{\mathbf{p}\Delta}{\hbar}} \int \mathrm{d}\mathbf{r}_0\ \mathrm{d}\mathbf{r}'_0\\ &\cdot \exp\left(i\frac{p_z}{\hbar}\frac{\left|\mathbf{r}-\frac{\Delta}{2}-\mathbf{r}_0\right|^2 - \left|\mathbf{r}+\frac{\Delta}{2}-\mathbf{r}'_0\right|^2}{2L}\right)\rho(\mathbf{r}_0,\mathbf{r'}_0)\\ &= \left(\frac{1}{2\pi\hbar}\right)^2 \int \mathrm{d}\Delta\ e^{-i\frac{\mathbf{p}\Delta}{\hbar}}\\ &\cdot \rho\left(\mathbf{r}-\frac{L}{p_z}\mathbf{p}-\frac{\Delta}{2}, \mathbf{r}-\frac{L}{p_z}\mathbf{p}+\frac{\Delta}{2}\right)\\ &= w_0(\mathbf{r}-\frac{L}{p_z}\mathbf{p},\mathbf{p}),\end{aligned} \quad (2.40)$$

with $\frac{L}{p_z}\mathbf{p}$ being the transverse motion which corresponds to an axial momentum p_z travelling for a length L. This expression underlines an interesting fact: the Wigner function at any position $z = L$ is just a translation of the initial Wigner function to the transverse position $\mathbf{r} - \frac{L}{p_z}\mathbf{p}$.

2.4.2 Passage through a grating

As we discussed in Sec. 2.1.2, the effect of a grating on the wave function is letting only part of the profile to be propagated through. The grating transparency function expressed by Eq. (2.12) can by straightforwardly expanded in two dimensions as

$$t(\mathbf{r}; d, \eta) = \begin{cases} 1 \text{ for } \mathrm{mod}(y, d) < \eta d \\ 0 \text{ otherwise.} \end{cases} \tag{2.41}$$

Notice that $t(\mathbf{r}; d, \eta)$ is normalized such that the total transmittance $|t(\mathbf{r}; d, \eta)|^2$ of this grating function integrated over $\mathbf{r}$ is equal to its open fraction $\eta < 1$. If we consider a wave function $\psi_i(\mathbf{r})$ impinging on such a grating, the wave function right after the grating is given by $\psi_{i+1}(\mathbf{r}) = t(\mathbf{r})\psi_i(\mathbf{r})$. Using this, in combination with Eq. (2.36) and the definition of density matrix given by Eq. (2.37), we obtain an expression for the Wigner function right after the grating:

$$\begin{aligned} w_{i+1}(\mathbf{r}, \mathbf{p}) = \int_{-\infty}^{\infty} \mathrm{d}\Delta \; e^{\frac{i\mathbf{p}\Delta}{\hbar}} t\left(\mathbf{r} - \frac{\Delta}{2}\right) t^*\left(\mathbf{r} + \frac{\Delta}{2}\right) \\ \cdot \rho_i\left(\mathbf{r} - \frac{\Delta}{2}, \mathbf{r} + \frac{\Delta}{2}\right). \end{aligned} \tag{2.42}$$

This formulation can be rewritten as a convolution with the kernel $T(\mathbf{r}, \mathbf{p})$ given by

$$T(\mathbf{r}, \mathbf{p}) = A \int_{-\infty}^{\infty} \mathrm{d}\Delta \; e^{\frac{i\mathbf{p}\Delta}{\hbar}} t\left(\mathbf{r} - \frac{\Delta}{2}\right) t^*\left(\mathbf{r} + \frac{\Delta}{2}\right), \tag{2.43}$$

with a proper normalization factor A. This leads to the expression

$$w_{i+1}(\mathbf{r}, \mathbf{p}) = \int_{-\infty}^{\infty} \mathrm{d}\mathbf{q} \; T(\mathbf{r}, \mathbf{q}) w_i(\mathbf{r}, \mathbf{p} - \mathbf{q}). \tag{2.44}$$

The convolution kernel represents the grating and is the key element to reconstruct the signal of the device.

2.4.3 Propagation through the interferometer

Now that we have all the expressions we need, we can finally obtain a formula for the detected signal. We start with an initial Wigner function $w(\mathbf{r}, \mathbf{p}) = 1$, which just means that our wave function is uniformly spread over the grating plane. Using equation Eq. (2.43), the passage through the first grating yields

$$w_1(\mathbf{r}, \mathbf{p}) = |t_1(\mathbf{r}; d, \eta)|^2. \tag{2.45}$$

Then, we use the free evolution from Eq. (2.40) to obtain the Wigner function just before the second grating as

$$w_2(\mathbf{r},\mathbf{p}) = w_1(\mathbf{r} - \frac{L}{p_z}\mathbf{p},\mathbf{p}) = \left| t_1\left(\mathbf{r} - \frac{L}{p_z}\mathbf{p}; d, \eta\right)\right|^2 . \tag{2.46}$$

The effect of the second grating, described by the convolution kernel $T_2(\mathbf{r},\mathbf{p})$, is then calculated following Eq. (2.44) and yields

$$\begin{aligned} w_3(\mathbf{r},\mathbf{p}) &= \int_{-\infty}^{\infty} \mathrm{d}\mathbf{q}\; T_2(\mathbf{r},\mathbf{q}) w_2(\mathbf{r},\mathbf{p}-\mathbf{q}) \\ &= \int_{-\infty}^{\infty} \mathrm{d}\mathbf{q}\; T_2(\mathbf{r},\mathbf{q}) \left| t_1\left(\mathbf{r} - \frac{L}{p_z}(\mathbf{p}-\mathbf{q}); d, \eta\right)\right|^2 . \end{aligned} \tag{2.47}$$

We still need to propagate $w_3(\mathbf{r},\mathbf{p})$ once more, up to the detection plane. This leads to an expression for $w_4(\mathbf{r},\mathbf{p})$:

$$\begin{aligned} w_4(\mathbf{r},\mathbf{p}) &= w_3(\mathbf{r} - \frac{L}{p_z}\mathbf{p},\mathbf{p}) \\ &= \int_{-\infty}^{\infty} \mathrm{d}\mathbf{q}\; T_2(\mathbf{r} - \frac{\mathbf{p}}{p_z}L, \mathbf{q}) \left| t_1\left(\mathbf{r} - \frac{L}{p_z}\mathbf{p} - \frac{L}{p_z}(\mathbf{p}-\mathbf{q}); d, \eta\right)\right|^2 \\ &= \int_{-\infty}^{\infty} \mathrm{d}\mathbf{q}\; T_2(\mathbf{r} - \frac{\mathbf{p}}{p_z}L, \mathbf{q}) \left| t_1\left(\mathbf{r} - 2\frac{\mathbf{p}}{p_z}L + \frac{\mathbf{q}}{p_z}L; d, \eta\right)\right|^2 . \end{aligned} \tag{2.48}$$

The Wigner function $w_4(\mathbf{r},\mathbf{p})$ represents the signal on the detector plane. In order to get an explicit expression for it, we need to write $t_1(\mathbf{r}; d, \eta)$ as a function of its Fourier coefficients.

2.4.4 Explicit mathematical formula for the signal

Now, we use the mathematics we developed in Sec. 2.1.2 in order to give a close expression for the signal formula. We restrict ourselves to the y direction in order to simplify the calculations, effectively reducing our transmission function to $t\,(y; d, \eta)$ as in Eq. (2.12). Using the coefficients from Eq. (2.14), we can calculate $|t_1\,(y; d, \eta)|^2$

$$\begin{aligned} |t_1\,(y; d, \eta)|^2 &= t_1\,(y; d, \eta) \cdot t_1^*\,(y; d, \eta) \\ &= \left(\sum_{j\in\mathbb{Z}} c_j e^{ijk_d y}\right) \cdot \left(\sum_{h\in\mathbb{Z}} c_h^* e^{-ihk_d y}\right) \\ &= \sum_{j,h\in\mathbb{Z}} c_j c_h^* e^{i(j-h)k_d y} \\ &= \sum_{j,l\in\mathbb{Z}} c_j c_{l-j}^* e^{ilk_d y} \\ &= \sum_{l\in\mathbb{Z}} C_l e^{ilk_d y}, \end{aligned} \tag{2.49}$$

where we defined the coefficient C_l as

$$C_l = \sum_{j\in\mathbb{Z}} c_j c^*_{l-j}. \tag{2.50}$$

If we make the dependence of the coefficients C_l on the initial phase of the first grating y_1 explicit, we get instead

$$|t_1(y;d,\eta)|^2 = \sum_{l\in\mathbb{Z}} C'_l e^{ilk_d(y+y_1)}, \tag{2.51}$$

where we are considering the modified coefficients

$$C'_l = \sum_{j\in\mathbb{Z}} c'_j c'^*_{l-j}. \tag{2.52}$$

With similar arguments and using the same notation, we get for the second grating

$$\begin{aligned} T_2(y,p_y) &= \sum_{j,l\in\mathbb{Z}} b_j b^*_{l-j} e^{ilk_d y}\delta\left(p_y - \hbar\pi\frac{2j-l}{d}\right) \\ &= \sum_{j,l\in\mathbb{Z}} b'_j b'^*_{l-j} e^{ilk_d(y+y_2)}\delta\left(p_y - \hbar\pi\frac{2j-l}{d}\right), \end{aligned} \tag{2.53}$$

where y_2 is the phase of the second grating and we restricted ourselves to the y direction both for the position and the momentum. Notice that $b_m = \eta\mathrm{sinc}(\eta n)e^{-ink_d y_2}$, with y_2 being the phase of the second grating, which is a perfectly analogous result to the expression found previously for c_m. By using Eq. (2.50) and Eq. (2.53), we can now further process Eq. (2.48), from which we obtain the following expression:

$$\begin{aligned} w_4(y,p_y) = \sum_{m,j,l\in\mathbb{Z}} & C_l b_j b^*_{l-j} \exp\left(i(l+j)k_d y - ik_d(2l-j)\frac{p_y}{p_z}L\right) \\ & \cdot \exp\left(i\pi l(2m-j)\frac{L}{L_\mathrm{T}}\right). \end{aligned} \tag{2.54}$$

By integrating over the transverse momentum p_y, we can then get the detectable signal on the observation plane [Brä14]:

$$\begin{aligned} w(y) &= \int_{-\infty}^{\infty} \mathrm{d}p_y w_4(y,p_y) \\ &\propto \sum_{m,l\in\mathbb{Z}} C_l b_m b^*_{m+2l} \exp\left(ilk_d y\right) \exp\left(i\pi l(2m+2l)\frac{L}{L_\mathrm{T}}\right) \\ &= \sum_{m,l\in\mathbb{Z}} C_l B^\mathrm{T}_{-2l} \exp\left(ilk_d y\right), \end{aligned} \tag{2.55}$$

where L_{T} is again the Talbot length and the grating coefficient B_j^{T} is defined as

$$B_j^{\mathrm{T}} = \sum_{m\in\mathbb{Z}} b_m b_{m-j}^* \exp\left(i\pi \frac{j^2-2mj}{2}\frac{L}{L_{\mathrm{T}}}\right). \tag{2.56}$$

We see from Eq. (2.55) that while the effect of the first grating is limited to a multiplicative factor (the C_l coefficients), the second grating actually performs a phase modulation which is dependent on the Talbot length. This dependence is what distinguish the classical, geometrical trajectories from the quantum wave propagation. We can prove that in case of no quantum influence, or when $L \ll L_{\mathrm{T}}$, the B_j^{T} coefficients reduce to their classical counterpart B_j^{C}, whose definition is the same as the C_l described by Eq. (2.50). We can in any case write B_j^{T} in a way which makes the dependence on the phase of the second grating y_2 explicit, as in Eq. (2.51):

$$B'^{\mathrm{T}}_{-2l} = B^{\mathrm{T}}_{-2l} e^{i(-2l)k_d y_2}. \tag{2.57}$$

Since only the terms with $j = -2l$ are contributing to the sum of the series in Eq. (2.55), we see that a phase shift on the level of the second grating contributes twice as much as a phase shift on the level of the first grating.

2.4.5 Signal of a three-gratings device

We argued in Sec. 2.2 that we can use a third grating to improve the detection schematic while losing a fraction of the incoming particles. We can readily expand the result from Eq. (2.55) to a three grating device by considering the convolution with a third grating $T_3(y, p_y)$, such that we can write the signal $S(y)$ as

$$\begin{aligned} S(y) &= \int_{-\infty}^{\infty}\int_{-\infty}^{\infty} \mathrm{d}p\ \mathrm{d}q\ w_4(y,q)T(y,q-p) \\ &= w(y)\left|t_3(y)\right|^2 \end{aligned} \tag{2.58}$$

which can be integrated over y to get the total flux of particles going through the three gratings

$$S = \int_{-\infty}^{\infty} \mathrm{d}y\ \mathrm{d}q\ w(y)\left|t_3(y)\right|^2. \tag{2.59}$$

The signal still depends on the position of the three gratings, i.e. on their initial phases, marked as y_1, y_2 and y_3 respectively. By making the integration explicit and considering a third grating identical to the first one, we get

$$\begin{aligned} S(y_1,y_2,y_3) &\propto \sum_{l\in\mathbb{Z}} C'_l B'^{\mathrm{T}}_{-2l} C'_l \exp\left(ik_d l(y_1+y_3-2y_2)\right) \\ &= \sum_{l\in\mathbb{Z}} (C'_l)^2 B'^{\mathrm{T}}_{-2l} \exp\left(ik_d l(y_1+y_3-2y_2)\right). \end{aligned} \tag{2.60}$$

We can thus extract the contrast C of the pattern in a similar fashion as in Eq. (2.3) by considering the maximum signal $S_{\max}$, obtained when $y_1 + y_3 - 2y_2 = 2m\pi, m \in \mathbb{Z}$, and the minimum signal $S_{\min}$, obtained when $y_1 + y_3 - 2y_2 = (2m+1)\pi, m \in \mathbb{Z}$. The contrast yields

$$\begin{aligned} C &= \frac{S_{\max} - S_{\min}}{S_{\max} - S_{\min}} \\ &= \frac{\sum_{l\in\mathbb{Z}} (C'_l)^2 B'^{\mathrm{T}}_{-2l} - (C'_l)^2 B'^{\mathrm{T}}_{-2l} e^{il\pi}}{\sum_{l\in\mathbb{Z}} (C'_l)^2 B'^{\mathrm{T}}_{-2l} + (C'_l)^2 B'^{\mathrm{T}}_{-2l} e^{il\pi}} \\ &= \frac{\sum_{l\in\mathbb{Z}} (C'_l)^2 B'^{\mathrm{T}}_{-2l} (1 - e^{il\pi})}{\sum_{l\in\mathbb{Z}} (C'_l)^2 B'^{\mathrm{T}}_{-2l} (1 + e^{il\pi})} \\ &= \frac{\sum_{n=1}^{\infty} (C'_{2n-1})^2 B'^{\mathrm{T}}_{2-4n}}{\frac{1}{2}(C'_0)^2 B'^{\mathrm{T}}_0 + \sum_{n=1}^{\infty} (C'_{2n})^2 B'^{\mathrm{T}}_{-4n}}. \end{aligned} \tag{2.61}$$

The contrast plots shown in this thesis have been produced by using Eq. (2.59) and limiting the infinite sum to a small interval of indexes (usually, $n \leq 30$) for both the coefficients in Eq. (2.52), Eq. (2.57), and Eq. (2.55). This limitation was required in order to keep the computation time in the order of minutes (or tens of minutes) when implemented in a computer program.

2.4.6 Shape of the pattern

We have now access to a set of formulas that can be used to describe the expected signal shape after two or three gratings. By considering the result from Eq. (2.60), we can write an analogous formula for a two grating device:

$$S(y_1, y_2) \propto \sum_{l\in\mathbb{Z}} C'_l B'^{\mathrm{T}}_{-2l} \exp\left(ik_d l(y_1 - 2y_2)\right). \tag{2.62}$$

Using these two equations let us visualize the pattern and predict its shape. Examples of these calculations are shown in Fig. 2.8b and 2.8d for two and three gratings respectively. For these figures, we set $L = L_{\mathrm{T}}$ and we evaluate the series using the first 50 terms. This approximation yields an error of about 1.5 % on the expected contrast of the fringes, but requires a computation time a hundred times smaller than the one required to get to a 0.1 % error with an implementation of the equations in MATLAB [MAT14] (see Fig. 2.9). We deem this trade-off acceptable in our case, and we decide to stick to this convention in order to have access to a faster way to produce test datasets at the expense of a small reduction in precision. Compare them with Fig. 2.8a and 2.8c for two and three gratings respectively, which show the signal for $L = L_{\mathrm{T}}/2$. The comparison between these plots shows that the periodicity of the signal is doubled when we choose a half-integer multiple of the Talbot length

as our target distance and that for higher open fractions (e.g. $\eta = 0.6$) the signal shows a higher contrast than in the classical case.

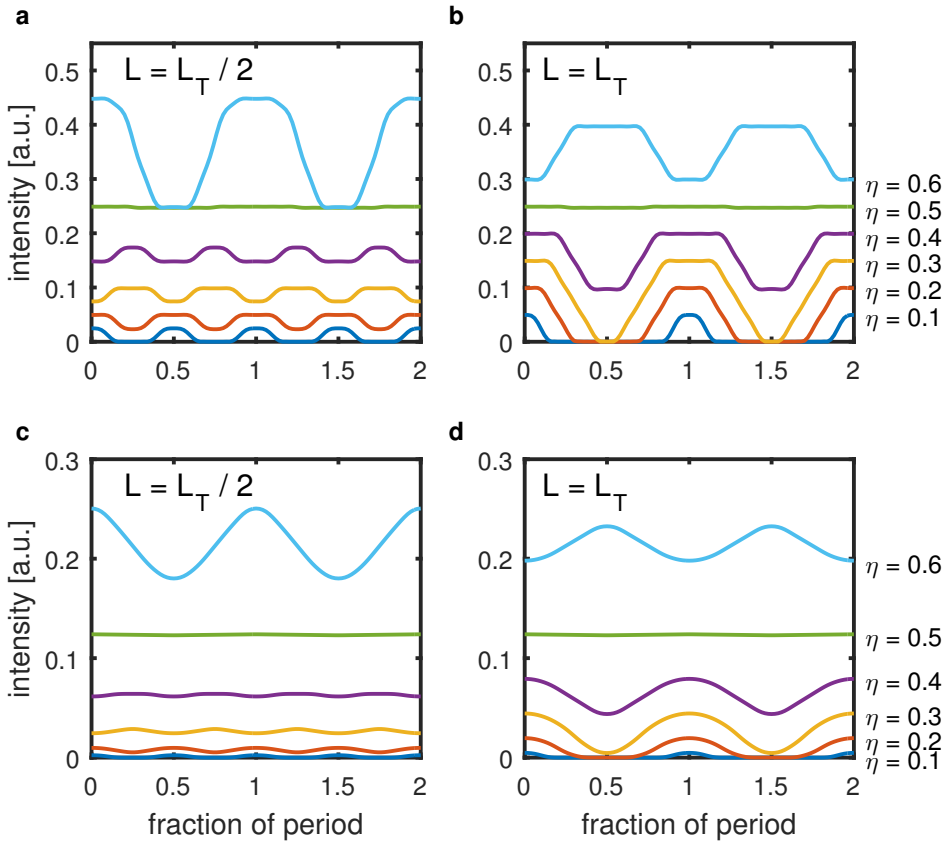

Figure 2.8: Intensity profiles for a two or three grating device, obtained by evaluating Eq. (2.60) numerically, using 50 terms for every series. The open fraction η goes fro $\eta = 0.6$ (top) down to $\eta = 0.1$ (bottom). The plot presents four different configurations: **a.** Two gratings, $L = L_T/2$; **b.** Two gratings, $L = L_T$; **c.** Three gratings, $L = L_T/2$; **d.** Three gratings, $L = L_T$, where L_T is the Talbot length as in Eq. (2.1).

2.5 Summary

In this section, we discussed the physics behind a two-grating device and its use for inertial sensing. We have first introduced the mathematics behind the Talbot carpet, then we discussed how to detect the signal of this kind of interferometer. We applied classical physics to extract an expression for the phase shift due to a constant force acting on the particles during their travel through the device and found out the corresponding phase shift which can be used to retrieve the magnitude of the acceleration. A mathematical model for the free evolution has been developed

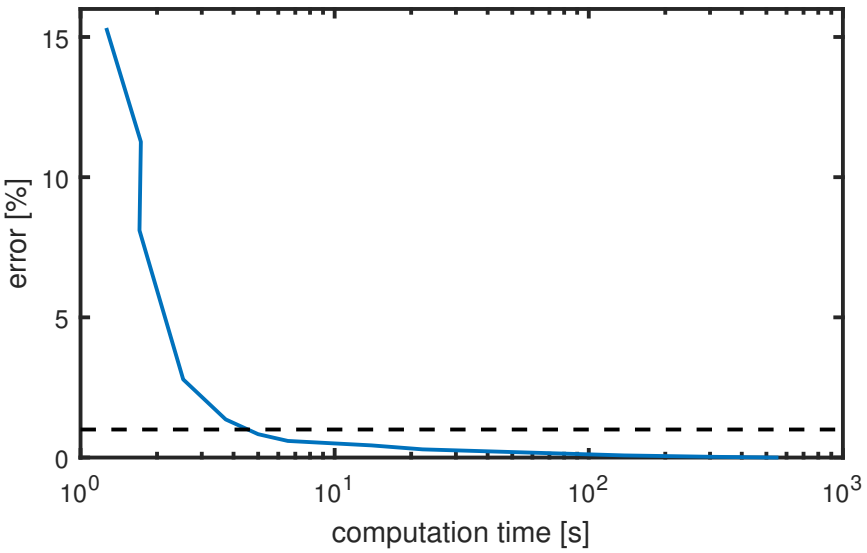

Figure 2.9: Precision of the truncated series calculation vs. computation time needed for one specific configuration. The precision is calculated against the exact contrast for a known configuration (open fraction $\eta = 0.3$, $L = L_\mathrm{T}$). The dashed line marks the 1 % precision.

and solved in order to retrieve a value for the contrast of the expected pattern depending on the geometrical characteristics of the setup. This procedure will be employed in the following sections when discussing the shortcomings and challenges related to building this device and operating it in reasonable experimental conditions.

Chapter 3

Alignment requirements for a Talbot-Lau interferometer

The results and formulas obtained in the previous chapter are all related to a device in ideal conditions, with a perfect placement of every geometrical component and infinite precision in the alignment of the gratings. However, in a realistic experiment, there are intrinsic limitations on how well an interferometer can be set up. The divergence α of the particle source also plays a significant role in determining what is the maximum allowed departure from the ideal setup before the signal vanishes.

In this chapter, we see how the various parameters of the experimental device affect the quality of the signal and its contrast, ultimately finding an empirical formula which can be used to estimate the required alignment precision. We begin by analyzing the effect of an asymmetry ΔL of the interferometer, then we proceed to independently discuss the effect of rotations β around the beam axis. The schematic in Fig. 3.1 provides a visual guide to these parameters and is later used as a basis to develop an analytic model for quantifying these effects. Notice that the formulas have been obtained by considering the classical limit of the Talbot-Lau interferometer, however their validity has been verified by performing numerical simulations in the wave regime.

3.1 Longitudinal asymmetry

The ideal setup for a Talbot-Lau like interferometer that we considered in Chapter 2 is composed by two or three identical gratings spaced by equal distances L. The presence of a first gratings creates the spatial coherence needed for illuminating the second grating with a coherent wavefront, which can then produce the distinctive Talbot carpet. However, if the distance between the second grating and the detector L_{23} and the distance L_{12} between the first two gratings are different, as in Fig. 3.1, the position of the rephasing does not coincide with the position of the

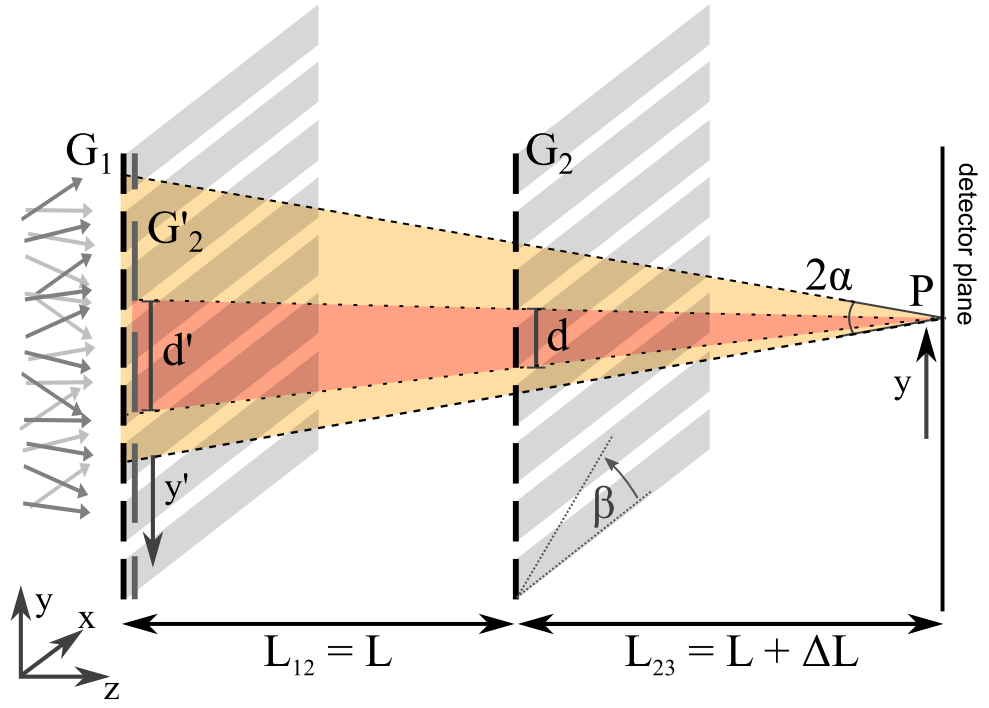

Figure 3.1: This figure schematically shows how the classical pattern is calculated to estimate the effects of an asymmetry ΔL and an angular misalignment β: for every point P on the detector, the region from which particles can reach the point is calculated by projecting the second grating (G_2) on the first one (G_1), thus identifying the effective fraction of particle which contributes to the intensity. The projected grating G_2' has a magnified periodicity d', as in Eq. (3.3). When considering a source with divergence α, the region from which a particle can reach the detector is limited by a cone with opening angle α equal to the divergence of the source (bright region). The tilt angle β is considered when extending the approach to three dimensions. The analytic treatment is explained in detail in text. Figure reproduced from [Dem+17].

detector, meaning that we obtain a signal with lower contrast than the original. Furthermore, the bigger the initial divergence α of the beam, the bigger the influence of this effect, as the size of the rephasing shrinks the more the initial beam is divergent. Since the analytic formula retrieved in Chapter 2 using the Wigner representation is valid only in case of an ideal setup (that is, no difference between L_{23} and L_{12}), and the method based on the Fourier transform shown in Sec. 2.1.2 is computationaly expensive, we follow a different approach developed by Bergermann [Ber12] and later adapted for [Dem+17]. This approach, schematized in Fig. 3.1, works by considering classical trajectories through the interferometers, as in the moiré regime, but its results have been verified performing numerical simulations in the wave regime and proved valid also when applied to a Talbot-Lau interferometer.

3.1.1 Idea behind the analytic approach

The problem of an asymmetry in the Talbot-Lau interferometer is not completely new, as it has been previously discussed by [NH08; Hor+09]. The analysis presented in these papers has been performed in the wave regime for a Talbot-Lau interferometer and, in the limit of a small divergence angle ($\alpha \ll 1$), yields a maximum acceptable displacement $\Delta L = L_{23} - L_{12}$ given by

$$\Delta L_{\text{crit}} = \frac{d}{2\alpha}. \tag{3.1}$$

If $\Delta L = \Delta L_{\text{crit}}$, the contrast of the pattern is equal to zero, causing it to vanish completely. In the following, we apply an alternative method based on the classical description of the moiré deflectometer. We will see that our method yields a result compatible with Eq. (3.1). The calculation is performed in a way which can be non-intuitive without a schematic: before delving into the detail we discuss the general idea so that it is easier to follow the process, using Fig. 3.1 to underline the key points. Instead of propagating a beam from the source (left side of the reference figure) to the detector (right side of the reference figure), we instead pick a point P on the detector plane and calculate the relative intensity which can be recorded at that point, given a source with divergence α. This is equivalent to integrating over the portion of phase space which contains all the trajectories which can reach P by starting from the source. This integral is what we want to retrieve, in order to be able to build the pattern and calculate its contrast. With the basics set, we begin with the calculation.

3.1.2 Analytic formulation

Completely divergent source

Consider a completely divergent particle source ($\alpha = \pi/2$ in two dimensions), and an device composed by two gratings, such that $L_{12} = L$, $L_{23} = L + \Delta L$. Consider a point P on the detector plane. All the particles which reach P have to pass through both gratings, indicated as $G1$ and $G2$ respectively in the schematic figure, which limits their original position to a specific region of space, given by the convolution of the first grating $G1$ and the projection $G2'$ of the second grating at the position of the first grating, using P as the projection vertex. The grating function G as a function of the position y is defined exactly as the transparency function $t(y; d, \eta)$ we introduced in Eq. (2.12), with d being the periodicity of the grating and η being the open fraction. We rewrite the definition here for the sake of clarity:

$$G(y; d, \eta) = \begin{cases} 1 \text{ if } \mathrm{mod}(y, d) < \eta d, \\ 0 \text{ elsewhere.} \end{cases} \tag{3.2}$$

As shown in Fig. 3.1, the projected image $G2'$ can be described as a grating with the same open fraction η and a magnified periodicity d', given by

$$d' = d\ \frac{L_{12} + L_{23}}{L_{23}} = d\ \frac{2L + \Delta L}{L + \Delta L}. \tag{3.3}$$

We now use the projection $G2'$ together with the first grating $G1$ to retrieve the intensity of the signal at P. As per the schematic, while moving the projection point by a distance y on the screen, the projection $G2'$ moves in the opposite direction by a position y' given by

$$y' = \frac{L}{L + \Delta L} y, \tag{3.4}$$

with the effect of translating the projection on the first grating, performing something similar to a convolution between $G1$ and $G2'$. In the following, we express $G1$ and $G2'$ as a function of Eq. (3.2) as $G1 = G(y; d, \eta)$, $G2' = G(y'; d', \eta)$. In the hypothesis of completely divergent source, the intensity I_{det} at any position y on the detector plane is therefore given by

$$I_{\mathrm{det}}(y) \propto \int_{-\infty}^{+\infty} G(\xi; d, \eta) G(\xi + y'; d', \eta) d\xi. \tag{3.5}$$

In this scenario, $\Delta L \neq 0$ causes the contrast of the fringes generated by the first two gratings to vanish completely, as the rephasing is only seen at integer multiples of L_{12}. An example of this behavior is pictured in Fig. 3.2 for increasing divergence angles: the farther we move towards

a perfectly divergent source, the smaller the maximum ΔL which still yields a signal.

As it was shown in Chapter 2, a third grating placed on the detector plane can be used to reveal the periodic pattern. If we consider a grating in scanning mode as in Sec. 2.2.1, the intensity modulation I after the additional grating $G3 = G(y; d, \eta)$ can be calculated as

$$I(y_g) \propto \int_{-\infty}^{+\infty} I_{\text{det}}(\xi) G(\xi - y_g; d, \eta) d\xi, \tag{3.6}$$

where y_g is the position offset of the third grating, as discussed in Chapter 2.

Source with limited divergence

Consider now a source with a fixed divergence $\alpha < \pi/2$. Most of the arguments we used in the previous case still hold. However, the limits of the integrals are not ranging anymore from $-\infty$ to $+\infty$, but are instead constrained to a region defined by $\xi \in [y - y_{\text{lim}}, y + y_{\text{lim}}]$. This region represents the portion of space from which particles can reach the detector, given the geometrical characteristics of the device. In this formulation, $y_{\text{lim}} = (2L + \Delta L)\ \tan(\alpha)$ is the geometrical limit imposed by the divergence angle α and y is the coordinate of the detector point at which the pattern is calculated, as shown in Fig. 3.1. We notice that, in the limit $\alpha \to \pi/2$, y_{lim} tends to ∞, reproducing the equations from Sec. 3.1.2. By proceeding further in the calculations, we get a new equation for Eq. (3.5) which takes into account the finite divergence of the beam:

$$I^{\alpha}_{\text{det}}(y) \propto \int_{y-y_{\text{lim}}}^{y+y_{\text{lim}}} G(\xi; d, \eta) G(\xi + y'; d', \eta) d\xi. \tag{3.7}$$

The interaction with the third grating is calculated exactly as in Eq. (3.6), thus obtaining for the total intensity on the detector $I^{\alpha}(y_g)$:

$$I^{\alpha}(y_g) \propto \int_{-\infty}^{+\infty} I^{\alpha}_{\text{det}}(\xi) G(\xi - y_g; d, \eta) d\xi. \tag{3.8}$$

The contrast of the pattern as a function of ΔL shows a main peak at $\Delta L = 0$, together with smaller secondary peaks of decreasing intensity. An example of this behavior is shown in Fig. 3.3, where the contrast is plotted as a function of ΔL for different divergence angles α. We see again that for a completely divergent source ($\alpha \to \pi/2$), Eq. (3.8) converges to Eq. (3.6), thus producing the same result.

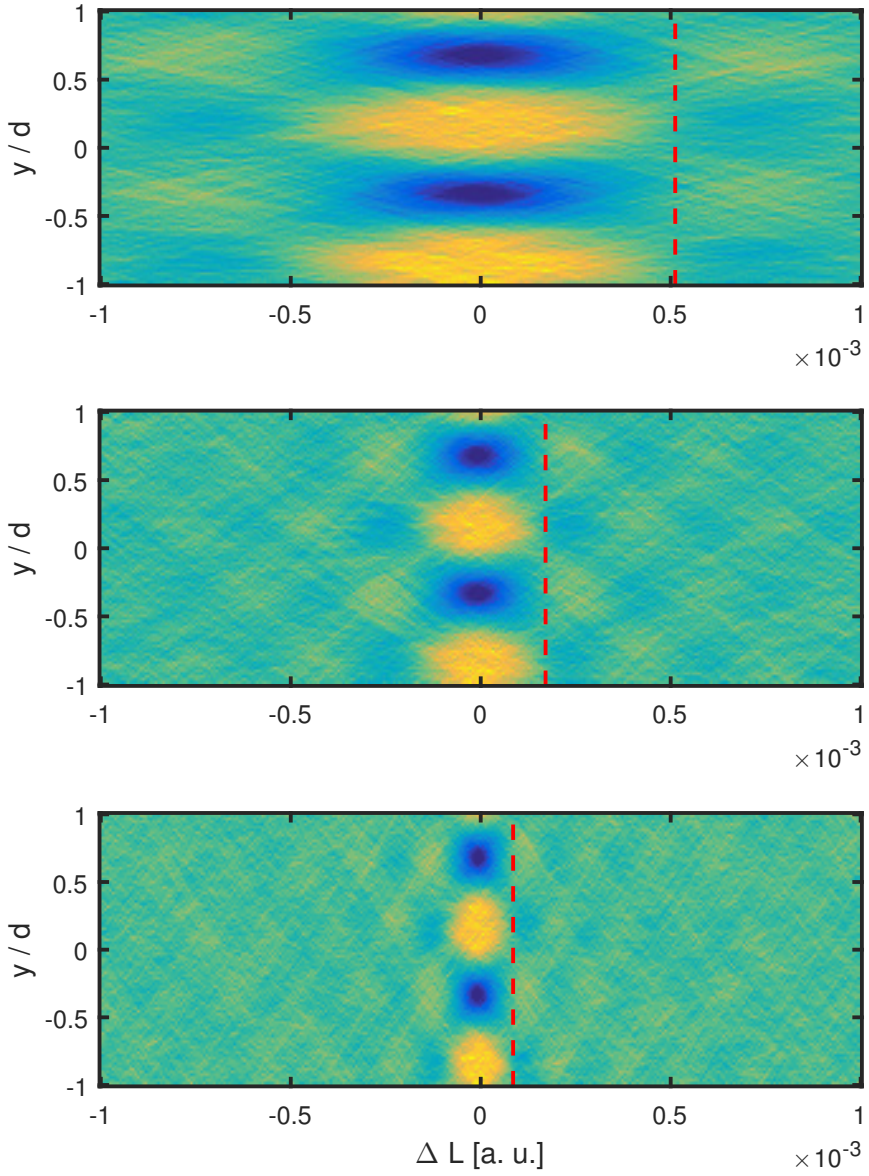

Figure 3.2: The maximum allowed asymmetry ΔL which causes the pattern on the detector plane to vanish is strongly dependent on the divergence angle α in relation to the periodicity of the grating d. From top to bottom: pattern as a function of ΔL for increasing values of divergence α. The dashed vertical line marks the position of the first zero of the contrast, after which smaller periodic rephasings can be observed. Theoretically, for a completely divergent beam, any $\Delta L \neq 0$ causes the pattern to vanish completely. For small divergence angles, the position of the first minimum is given by Eq. (3.1), while a more general formula is given by Eq. (3.9).

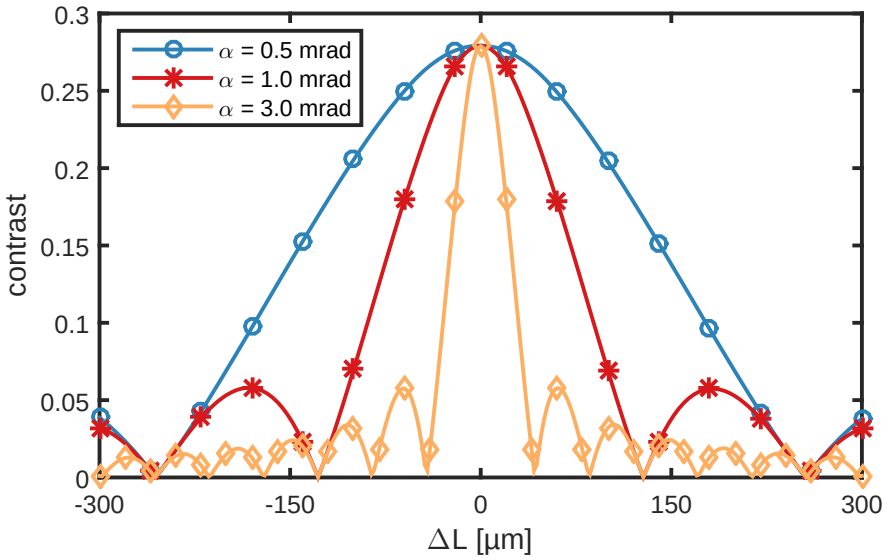

Figure 3.3: This figure shows the contrast of the classical moiré pattern as a function of $\Delta L = L_{23} - L_{12}$. When the distance $\Delta L \neq 0$, the contrast of the periodic pattern decays as a function of ΔL and the divergence angle α. For $\Delta L = d/2 \ \tan(\pi/2 - \alpha)$, the contrast is equal to zero. The position of the zeros is completely determined by those two parameters and is not affected by the magnitude of L_{12}. Figure reproduced from [Dem+17].

3.1.3 Geometrical argument for the visibility minimum

By numerically solving Eq. (3.7), we find that the position of the minima of the contrast is a function of ΔL and the divergence angle α. In this section, we offer a geometrical argument on what is our expectation for the position of the first contrast zero ΔL_{crit} and we overlap the result on the patterns produced by using the analytic process outlined above. A schematic of this intuitive approach is provided in Fig. 3.4. Consider a periodic intensity pattern with point-like intensity maxima spaced by an equal distance d, and a beam divergence α. Due to the divergence, each maximum expands into a cone with angular opening α, enlarging from a point to a uniform spot of size $d' = \Delta L \tan(\alpha)$ after a distance ΔL. If $d' = \frac{d}{2}$, the intensity profile is a uniform, flat distribution without any distinguishable features. By imposing $\Delta L_{\text{crit}} \tan(\alpha) = \frac{d}{2}$, we get [Mül17]:

$$\Delta L_{\text{min}} = \frac{d}{2\tan(\alpha)} = \frac{d}{2}\ \tan\left(\frac{\pi}{2} - \alpha\right). \tag{3.9}$$

This result is shown in Fig. 3.2 as the dashed vertical lines overlapped to the contrast plots. Notice that, despite the huge simplification of considering point-like structures, we derived a result which is completely compatible with the one from Eq. (3.1) in the limit of small divergence angles $\alpha \ll 1$, by using the Taylor expansion $\tan(\alpha) = \alpha + \mathrm{O}(\alpha^3)$. This argument can be extended to patterns with a spatial extension and it is verified by means of numerical calculations in the following section.

3.1.4 Implications of the critical distance

The geometrical formula obtained by simple considerations in Sec. 3.1.3 holds very well when tested by integrating the equations. An example of this behavior is shown in Fig. 3.2, where the position of the dashed red line has been calculated by using Eq. (3.9) while the intensity plot is a result of numerically integrating Eq. (3.8). In this subsection, we discuss the implications of this formula. As Eq. (3.9) shows, ΔL_{min} is independent on L: once the diffusion angle and the periodicity of the gratings are fixed, the other geometrical parameters are not playing any role in determining how the contrast is decaying. A consequence of this systematic effect is that depending on the divergence of the source, there is a maximum acceptable displacement after which the contrast drops sharply, which can be defined as the position of the first minimum expressed by Eq. (3.9).

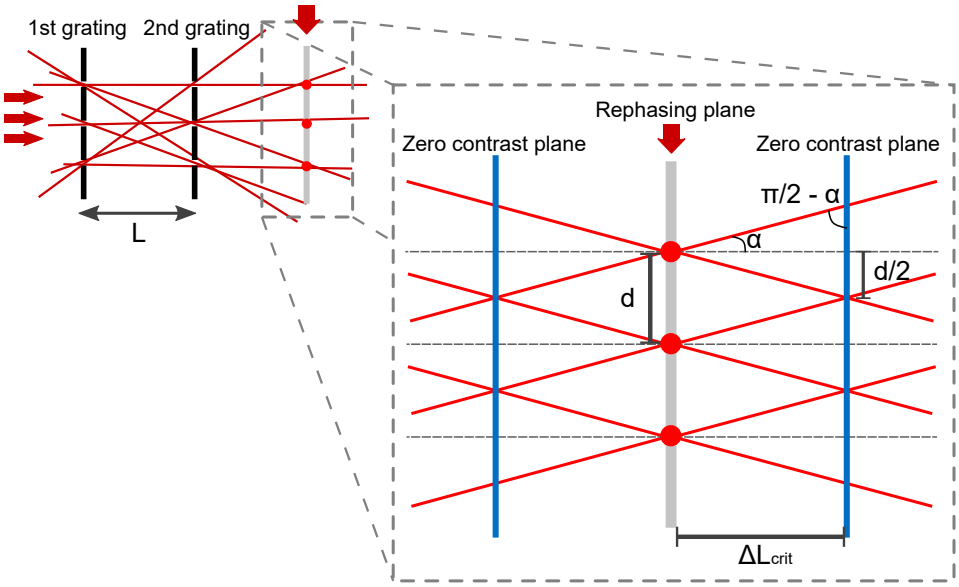

Figure 3.4: If we consider a beam with divergence α and a periodic intensity modulation, as the one generated by the two gratings of a moiré deflectometer, the pattern vanishes if it is not revealed at the correct position. Here, a displacement ΔL_{crit} in respect to the position of the pattern results in the detection of a uniform intensity profile which carries no information. From this geometrical representation, we obtain $\Delta L_{\text{crit}} = d/(2\tan(\alpha))$, as shown in Eq. (3.9).

3.1.5 Simulations in the wave regime

We derived this simple geometrical formula by considering a purely classical system and particle trajectories through the gratings. However, we have already seen how Eq. (3.9) converges to Eq. (3.1), which was calculated in the wave regime [NH08; Hor+09], for small divergence angles In order to verify the validity of our formula also for the Talbot-Lau interferometer, we expand on the formulation introduced in Sec. 2.1.2 for simulating the Talbot carpet: take a wavefront, multiply it by the grating function $G(y; d, \eta)$, Fourier transform the result, propagate it to the next grating using Eq. (2.9), antitransform as in Eq. (2.10), rinse and repeat. With the intent of simulating a divergent source, we follow the approach proposed in [Brä14] and we sum up incoherently plane waves coming from different angles, by decomposing the wave vector $\mathbf{k}$ in the two components k_y and k_z. This calculation process has been used for example to produce Fig. 2.2 and can easily be adapted to be employed with asymmetric distances between the gratings. Using this method, we find that for a range of lengths around $L = L_\mathrm{T}$, the position of the first contrast minimum is consistent with the classical scenario. However, around $L = 0.5L_\mathrm{T}$, the quantum pattern shows a half periodicity, which requires d in formula Eq. (3.9) to be replaced by $d/2$, as it can be seen in Fig. 2.1 and 2.2. This is shown in Fig. 3.5, where we see that around $L = 0.5L_\mathrm{T}$ the position of the critical minimum moves to half the classical value. However, for a large range of distances around the Talbot length, the classical prediction still holds. Examples of these behaviors are shown in Fig. 3.6. The classical result can be therefore still considered as the maximum displacement allowed while working in this region.

3.2 Rotational misalignment

The situation and setup we have considered so far could be easily reduced to two dimensions (y and z), as there was a translational symmetry on the x axis. If we tilt the second grating by an angle β around the beam axis, as shown in Fig. 3.1, however, we must also consider the x component of the position when determining if the particles passed through the gratings or not. The angle of the grating makes a difference in the resulting contrast plot: the bigger the divergence, the more the signal get degraded, even if $\Delta L = L_2 - L_1 = 0$. In order to estimate this effect, we extend the results obtained in Sec. 3.1 to two dimensions, following an approach similar to the one presented in [Dem+17]. Our goal is to find an expression for the critical angle β_crit which causes the contrast of the pattern to vanish, in a similar fashion to Eq. (3.9).

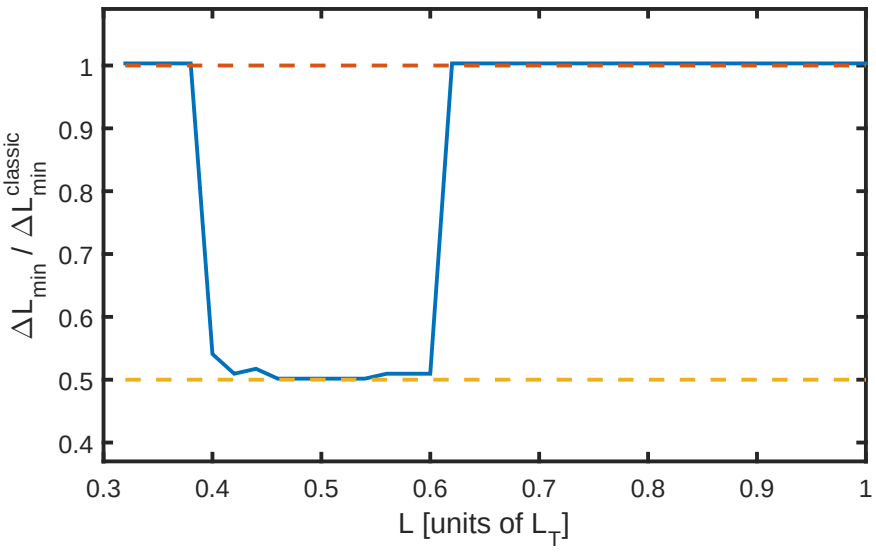

Figure 3.5: The critical asymmetry factor ΔL_{crit} in the quantum regime is the same as in the classical regime for $L \simeq L_{\text{T}}$. Around $L = 0.5L_{\text{T}}$, however, the periodicity d of the pattern is halved, moving as well the minimum to half the classical value. This behavior is consistent with what is observed in Fig. 2.1 and 2.2.

3.2.1 The problem behind a rotation

As an intuitive explanation, consider once again the schematic presented in Fig. 3.1: the first one placed in the xy-plane with slits parallel to the y-axis and the second rotated by an angle β around the z-axis. Consider also a divergence angle α in the yz-plane, while no diffusion is present on the x direction. If we take a set of planes parallel to the yz-plane and we use it to slice through the pattern for different values of x, we get a collection of one-dimensional representations equivalent to the one discussed in Sec. 3.1, with the difference that in every plane the pattern of the second grating will gain an offset $\Delta_y = x\tan(\beta)$ in respect to the original and a modified periodicity $d_\beta = d/\cos(\beta)$. An explanatory schematic is provided in Fig. 3.7. When a divergence in the x direction is considered, all the slices which are between a cone with angular opening α from the point on the screen the pattern is calculated onto have to be summed up. The combination of these two factors is what smears out the contrast of the generated pattern on the detection plane. In the following, we build an analytical treatment for the two-dimensional problem, by extending the formulas obtained in Sec. 3.1.

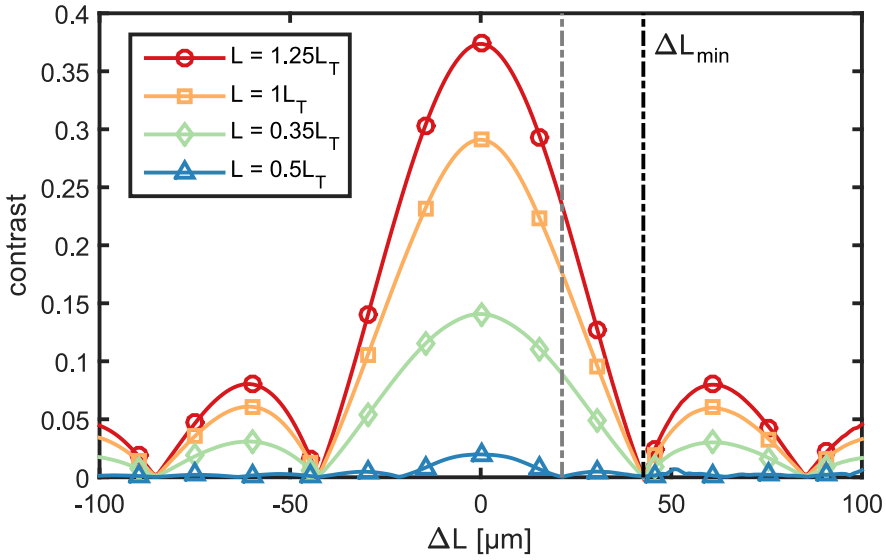

Figure 3.6: As in the classical case, the functional dependence of the contrast on the diffusion angle in the Talbot-Lau regime shows periodic minima, the first of which described by Eq. (3.9) (black vertical line). Notice that the peak contrast changes with the length. Around $L = n + \frac{1}{2}L_\mathrm{T}$, the periodicity of the pattern doubles, moving the first minimum at half its classical position (grey vertical line). The profiles shown are calculated for a divergence angle $\alpha = 3\,\mathrm{mrad}$. Figure reproduced from [Dem+17].

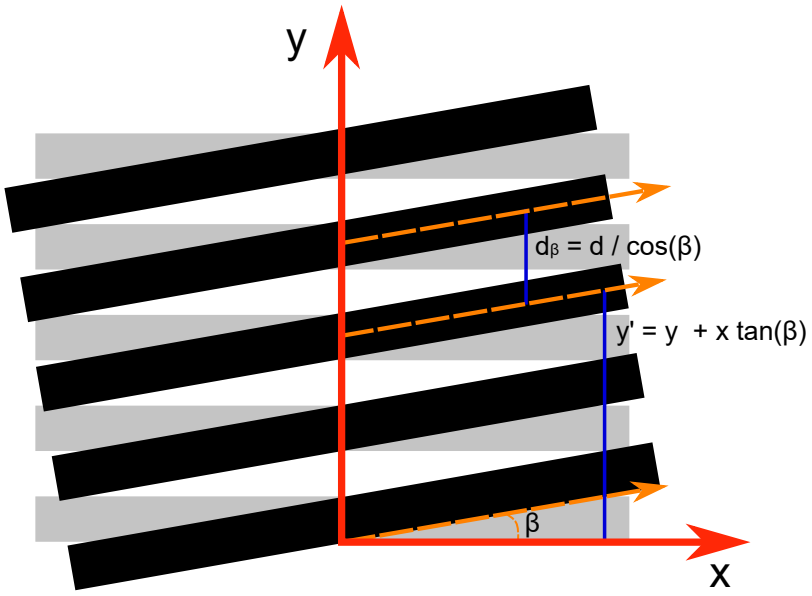

Figure 3.7: A two-dimensional grating tilted by an angle β can be seen as a series of one-dimensional gratings with periodicity $d_\beta = d/\cos(\beta)$ and an offset $\Delta y = x\tan(\beta)$.

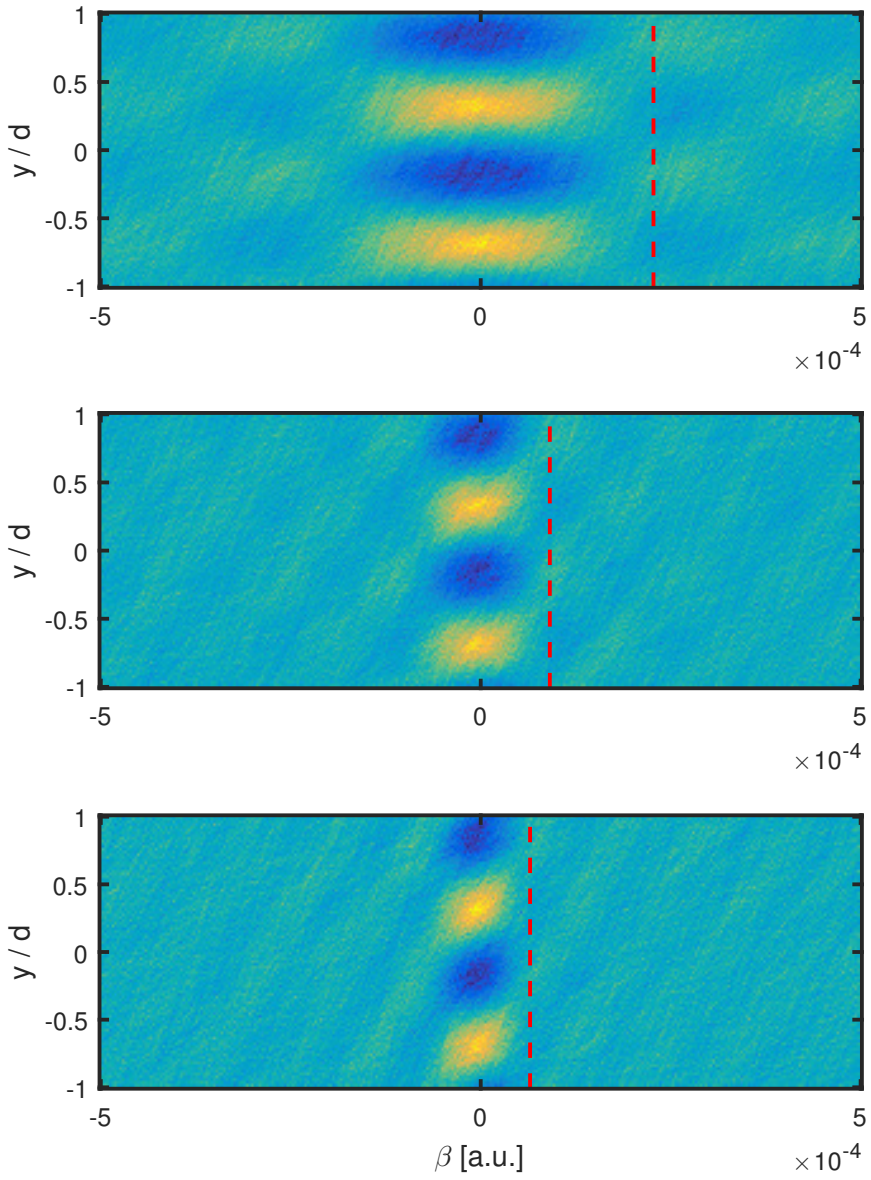

Figure 3.8: The maximum allowed angular tilt β of the second grating which causes the pattern on the detector plane to vanish is strongly dependent on the divergence angle α in relation to the periodicity of the grating d and the distance between the gratings L. From top to bottom: pattern as a function of β for increasing values of divergence α. The dashed vertical line marks the position of the first zero of the contrast, after which smaller periodic rephasings can be observed.

3.2.2 Analytical treatment

By using Fig. 3.7 as a reference, we introduce the two-dimensional grating function $G_{2D}(x, y; \beta, d, \eta)$, defined as

$$G_{2D}(x, y; \beta, d, \eta) = \begin{cases} 1 \text{ if } \mathrm{mod}(y + x\tan(\beta), d/\cos(\beta)) < \eta d/\cos(\beta) \\ 0 \text{ otherwise,} \end{cases} \tag{3.10}$$

This allows us to extend Eq. (3.7) as

$$I^{2D}_{\mathrm{det}}(x, y) \propto \int_{y-r_{\mathrm{lim}}}^{y+r_{\mathrm{lim}}} \int_{x-\sqrt{r^2_{\mathrm{lim}}-(\xi-y)^2}}^{x+\sqrt{r^2_{\mathrm{lim}}-(\xi-y)^2}} G_{2D}(u, \xi; 0, d, \eta) \cdot G_{2D}(u + x', \xi + y'; \beta, d', \eta)\, du\, d\xi. \tag{3.11}$$

The limits on this integral are given by a cone centered on $P = (x, y)$ with angular opening 2α, which projects a circular overlapping area of radius $r_{\mathrm{lim}} = (2L + \Delta L)\tan(\alpha)$ on the plane of the first grating. Here, d' is expressed by Eq. (3.3), while x' and y' are both defined by using Eq. (3.4) on x and y respectively. Notice that, as an effect of the angular difference, the resulting fringe pattern is tilted by an angle $\beta_{\mathrm{pattern}} = 2\beta$. In order to retrieve the periodic pattern by using a third grating, Eq. (3.8) is also expanded in two dimensions in a similar fashion.

We evaluate these equations numerically, in order to obtain an estimation for the contrast. The calculations show that even when the asymmetry factor is taken out ($\Delta L = 0$), the contrast of the recorded pattern decreases as the angle between the two gratings increases. An example of this behavior is shown in Fig. 3.8, where a slice of the pattern is shown as a function of β and α. Notice that this phenomenon is independent on the presence of a third grating, since the pattern becomes uniform for a geometrical overlap of the trajectories due to the angular difference between the two gratings. By performing the calculations for several combinations of divergence α, length L, and periodicity d, we find a formula which shows more than one similarity with Eq. (3.9) [Dem+17]:

$$\tan\beta_{\mathrm{crit}} = k\,\frac{d}{2L}\,\tan\left(\frac{\pi}{2} - \alpha\right), \tag{3.12}$$

where k is a constant factor, to be determined via a fit on the obtained visibility profiles, some of which are shown in Fig. 3.9. The formula shows the same functional dependence from the periodicity and the divergence angle as the one found in the one-dimensional case.

If we consider the geometrical parameters used in [Dem+17], for a divergence $\alpha = 1\,\mathrm{mrad}$, we see the first visibility minimum appearing for a rotational misalignment $\beta = 0.46 \pm 0.01\,\mathrm{mrad}$. Repeating the simulations for different geometrical configurations we obtain $k = 0.61 \pm 0.01$ as the value for the constant.

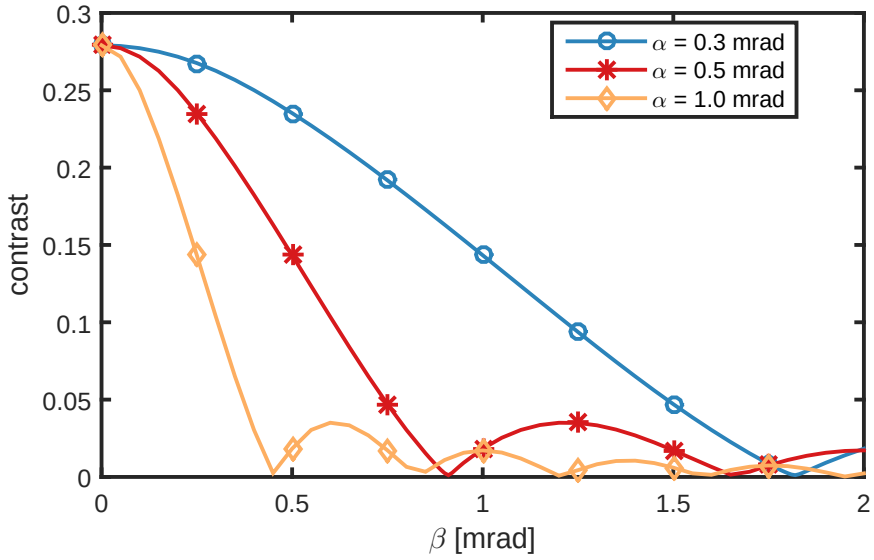

Figure 3.9: Depending on the divergence angle α, an angular difference β between the second and the first grating causes the signal to vanish. The position of the contrast minimum is linearly dependent on d and inversely proportional to L. The function which describes this position is similar to the one found for the one-dimensional case (compare Eq. (3.9) and (3.12)). Figure reproduced from [Dem+17].

It is worth mentioning that, when using a third grating to scan the pattern as in Sec. 2.2.1, the retrieved flux modulation is affected by a rotation of the third grating, due to the same moiré effect that we exploited in Sec. 2.2.2 to obtain macroscopic fringes out of a microscopic pattern. If we consider a circular area πA, with radius $\sqrt{A}$, a new macroscopic fringe appear when the tilting angle β_3 of the third grating in respect to the pattern is such that

$$\sin\left(\frac{\beta_3}{2}\right) = \frac{d}{2\sqrt{A}}, \tag{3.13}$$

Therefore, in order to get rid of macroscopic structures which would influence the flux measurement, the rotation angle β_3 has to fulfill the condition

$$\sin\left(\frac{\beta_3}{2}\right) \ll \frac{d}{2\sqrt{A}}. \tag{3.14}$$

3.3 Summary

We have analyzed the effects of both a linear asymmetry and an angular misalignment in a device composed by two or three gratings. We found out that if the device is not perfectly aligned, a divergent particle beam

can strongly reduce the quality of the periodic pattern generated by the interferometer. The effect of a longitudinal asymmetry ΔL is independent on the distance between the gratings and is proportional to the periodicity: smaller periodicities d cause the device to be more sensitive to the asymmetries (Eq. (3.9)). On the contrary, the effect of a tilt of the second grating β in respect to the first one, is proportional also to the length, to the point that longer devices suffer from bigger divergence angles the most (Eq. (3.12)). The expressions for the critical angle β_{crit} and the critical asymmetry ΔL_{crit} share the same functional dependence on periodicity and beam divergence α. Moreover, the expression for ΔL has been found compatible with a previously published result for small angles [NH08; Hor+09]. The next chapter focuses on the effects of the energy spread of the beam and how this affects the quality of the signal in combination with external forces. The combination of misalignments and forces constitutes the core of the systematic effects which have to be taken into account when designing the experiment. Knowing these limitations is an important step into approaching the construction of an optimized interferometer.

Chapter 4

Effects of energy spread and external forces

The physical and mathematical descriptions of a Talbot-Lau interferometer presented until now are valid in the condition that the experiment is carried out in a controlled environment without any unwanted force acting on the particle beam. Once these are taken into account, however, the expected pattern out of the interferometer undergoes severe alterations which degrade the quality of the signal, especially if the source has a non-null energy spread. This chapter focuses on the effects of energy spread and external fields on the signal of a Talbot-Lau interferometer. We obtain a set of formulas we can use to determine when these forces become an issue for the measurement and identify specific expressions for magnetic and electric fields when considering charged particles. The same argument is then used for neutral particles to describe the effect of forces such as gravity on the characteristics of the signal. The discussion on charged particles is accessory to the goal of studying the feasibility of a gravity measurement on antimatter. However, it provides us with some general tools and concepts that could be applied in any scenario related to ion interferometry, which is device-wise strictly correlated to the work of this thesis.

4.1 Signal averaging due to energy spread

A quick analysis of Fig. 2.3 presents us an easy to recognize feature of the Talbot-Lau interferometer: the contrast and the shape of the periodic pattern described by Eq. (2.60) depend on the energy of the particles flying through the device. If we consider particles with two different de Broglie wavelengths λ_{dB} in the same quantity, we thus expect the resulting signal to be a sum of the two patterns. This is schematized in Fig. 4.1, when the pattern for particles with λ_{dB} which corresponds to L_{T} is mixed with the pattern from particles with λ_{dB} which corresponds

to $L_T/2$. A real particle source is rarely perfectly monochromatic: most of the times, it has instead an energy distribution with a well-defined spread. For simplicity reasons, we fix the particle species and consider a single-species source, so that the changes in λ_{dB} are fully given by its energy spread. If we mark the periodic pattern generated by particles with kinetic energy U with $S(U)$, we can express the total signal S as

$$S = \int_{-\infty}^{\infty} \mathrm{d}U f(U) S(U) \tag{4.1}$$

where $f(U)$ is the energy distribution of the source. We treat this function as a probability density, such that

$$\int_{-\infty}^{\infty} \mathrm{d}U f(U) = 1 \tag{4.2}$$

The nature of $f(U)$ is strongly dependent on the geometry and the physical characteristics of the source. In order to produce quantitative estimations, we have to restrict our analysis to specific parameters. While in a real experimental scenario it is indeed required to know the full spectrum of the source in order to predict the outcome of the experiment, for some preliminary evaluations we can choose a Gaussian energy distribution peaked on the central energy of the beam [Dem+17]. The energy spread of the source is fixed to be the full width half maximum (FWHM) of the distribution, which corresponds to $\Delta U = 2\sqrt{2\ln 2}\ \sigma \simeq 2.355\sigma$. In the following, we consider therefore

$$f(U) = \frac{1}{\sigma\sqrt{2\pi}} e^{-\frac{(U-\bar{U})}{2\sigma^2}}, \tag{4.3}$$

with $\bar{U}$ being the average kinetic energy of the particles emitted by the source. We can now extend our test case to a continuous distribution of energies with different spreads, as in Fig. 4.2. An example on how the pattern changes is pictured in Fig. 4.3. As it can be seen from the figure, the energy spread alone is not a critical disturbance to the measurement, however, since its main effect is to average different patterns and generate a sort of summed up intensity profile which could also present a higher contrast than the pattern associated to the mean energy of the distribution. If we apply the same calculation to the full contrast profile shown in Fig. 2.3, we get an idea of the extent of this effect as a function of the energy. This is shown in Fig. 4.4. The picture becomes more complicate when, together with an energy spread, forces acting on the particles are taken into account. In the following section we see how this can be a game changing issue, if not handled properly.

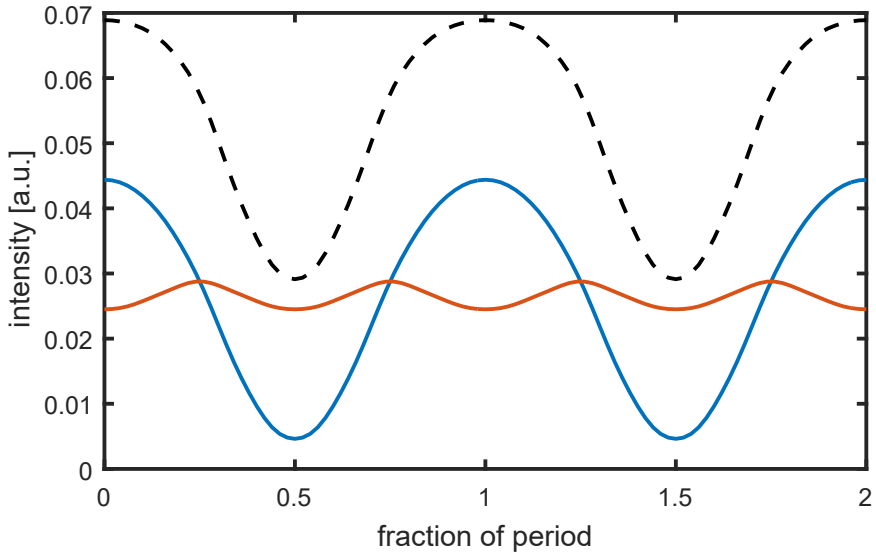

Figure 4.1: If we consider a source composed by particles with two different λ_{dB}, we send both of them through the interferometer and we detect them without performing a selection, we expect to observe a pattern (black dashed line) which is a linear combination of the patterns associated with the two species (blue line and red line respectively).

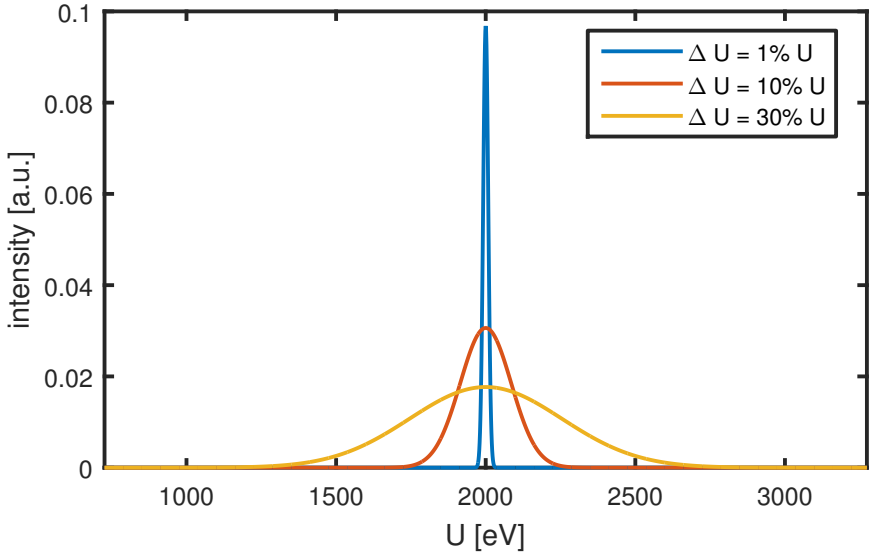

Figure 4.2: Using a Gaussian distribution for modeling the source spectrum, we are able to produce some quantitative predictions. This figure shows a sample energy distribution centered on $\bar{U} = 2\,\mathrm{keV}$ for different energy spreads.

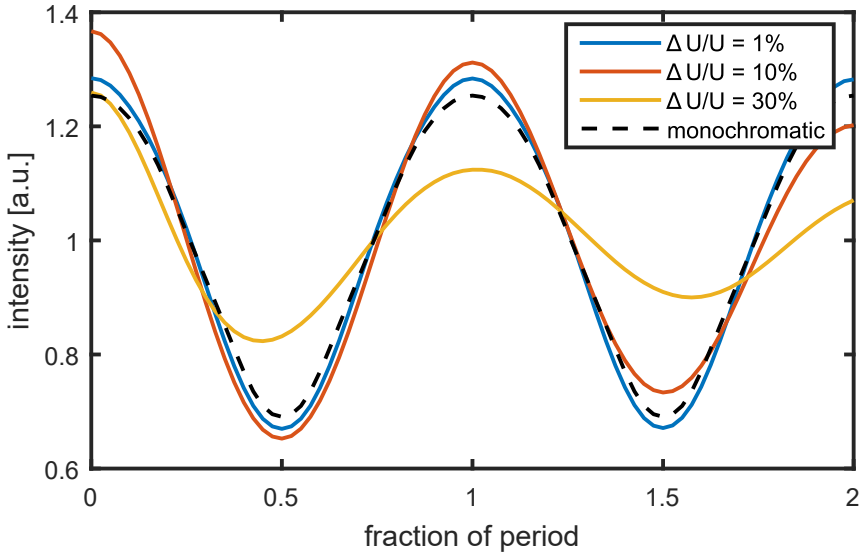

Figure 4.3: Signal shape for $\eta = 0.4$, mean energy $\bar{U} = U_{\mathrm{T}}$, and different energy spreads of a Gaussian distribution (see Fig. 4.2). Since $\bar{U} = U_{\mathrm{T}}$ represents a relative minimum for the contrast (Fig. 4.4) the pattern gets an increased contrast as a result of the averaging with neighboring energies.

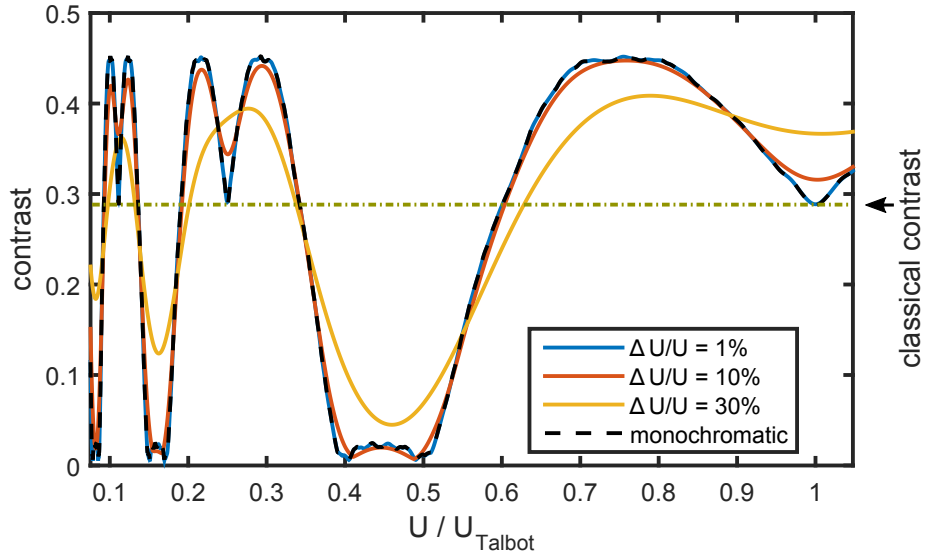

Figure 4.4: This figure shows the same contrast plot from Fig. 2.3 for a grating open fraction $\eta = 0.4$, for the energy spreads considered in Fig. 4.3. In some regions, the contrast is higher than in the monochromatic counterpart, since it gets averaged by summing up different patterns.

4.2 The effect of external forces

A Talbot-Lau interferometer can be used for inertial sensing of constant, uniform force fields, due to the fact that the phase shift exerted by the forces acting on the beam is proportional to the acceleration to which the particles are subjected. However, we remember from Eq. (2.32) that the shift is also proportional to the square time of flight τ between the gratings, given by L/v_z. This means that particles with different axial velocities v_z will experience different shifts. While this is not an issue for monoenergetic beams, when considering instead an energy distribution things get more complicated. Consider for example a simple distribution of particles with mass m and two possible energies, U_1 and U_2, which correspond to two different time of flight τ_1 and τ_2, equally distributed. Out of simplicity, we choose U_1 and U_2, with $U_1 > U_2$, such that the pattern generated on the detector screen presents no appreciable difference (e.g. $U_1 = U_\mathrm{T}$ and $U_2 = U_\mathrm{T}/9$). If we now choose a force $\mathbf{F} = ma\,\hat{\mathbf{y}}$ such that the phase difference between the two components of the distribution is equal to half a period $d/2$, the maxima of the first pattern will overlap with the minima of the second pattern, causing a noticeable reduction in contrast as we combine the two of them to retrieve the complete signal. This specific situation is illustrated in Fig. 4.5. We can derive a formula for expressing this phenomenon concretely. The value for the difference $\Delta y_1 - \Delta y_2$ which causes the summed up pattern to have the smallest visibility is exactly half of the grating period d, which is equivalent to a π shift. In order to draw further conclusions, we now express $\Delta y_1 - \Delta y_2$ as a function of the energy difference between the two classes of particles. The result of this elaboration will be used in the following as a base for treating a more generic case and drawing some conclusions useful to our goal. The first step is making the dependence on the axial velocity explicit:

$$\begin{aligned} \Delta y_1 - \Delta y_2 &= a(\tau_1^2 - \tau_2^2) \\ &= aL^2 \left(\frac{1}{v_{z1}^2} - \frac{1}{v_{z2}^2} \right). \end{aligned} \tag{4.4}$$

If we now consider the axial velocity v_z to be much bigger than the transverse velocity v_r for both particles, we can write $v = \sqrt{v_z^2 + v_r^2} \simeq v_z$. In this approximation, the kinetic energy U can be expressed as $U \simeq mv_z^2/2$. We can thus write $v_z^2 = 2U/m$, leading to

$$\begin{aligned} \Delta y_1 - \Delta y_2 &= a\frac{mL^2}{2} \left(\frac{1}{U_1} - \frac{1}{U_2} \right) \\ &= a\frac{mL^2}{2} \frac{U_2^2 - U_1^2}{U_2^2 U_1^2}. \end{aligned} \tag{4.5}$$

We now express both U_1 and U_2 as a function of the mean energy $\bar{U} = (U_1 + U_2)/2$ and the energy spread $\Delta U = U_1 - U_2$. With these

conventions, we get

$$\begin{aligned} U_1 &= \bar{U} + \frac{\Delta U}{2} \\ U_2 &= \bar{U} - \frac{\Delta U}{2}. \end{aligned} \tag{4.6}$$

We can now further elaborate on Eq. (4.5):

$$\Delta y_1 - \Delta y_2 = a\frac{mL^2}{2}\frac{4\Delta U}{4\bar{U}^2 - \Delta U^2}. \tag{4.7}$$

We apply once more a simplification and we assume that $\Delta U^2/\bar{U}^2 \ll 1$, which is fairly reasonable up to $\Delta U \simeq 0.3\bar{U}$. This way, we can neglect the ΔU term at the denominator, obtaining the expression

$$\begin{aligned} \Delta y_1 - \Delta y_2 &\simeq a\frac{mL^2}{2}\frac{\Delta U}{\bar{U}^2} \\ &= a\frac{mL^2}{2}\frac{k}{\bar{U}} \end{aligned} \tag{4.8}$$

where, in the last step, we expressed the energy spread as $\Delta U = k\bar{U}$, $k \in \mathbb{R}$. If we now consider a π shift (half a period, $d/2$), we can define a critical acceleration a_{crit} or, in an equivalent way, a critical force F_{crit} by using

$$\frac{d}{2} \stackrel{!}{=} |\Delta y_1 - \Delta y_2| = |a_{\text{crit}}|\,\frac{mL^2}{2}\frac{k}{\bar{U}}, \tag{4.9}$$

which leads to

$$\begin{aligned} |a_{\text{crit}}| &= \frac{d}{mL^2}\frac{\bar{U}}{k} \\ |F_{\text{crit}}| &= m\,|a_{\text{crit}}| = \frac{d}{L^2}\frac{\bar{U}}{k}. \end{aligned} \tag{4.10}$$

The critical acceleration which causes a π phase shift between the two particle families is directly proportional to the average energy, which means that the faster the particles (on average), the bigger the acceleration needed to split them by half a period. Understandably, it is also proportional to the period, since a bigger period means that a higher acceleration is needed to separate the species by half of it. It is inversely proportional to the energy spread constant k, which means that the bigger the separation among the two energies, the smaller the acceleration needed to get a π phase shift. Lastly, we see that it is inversely proportional to L^2, which means that the longer the path, the smaller the needed acceleration to cause the critical shift. The quantities expressed by Eq. (4.10) are restricted to this toy model with just two different energies, but we can make use of them in a more realistic scenario. If we consider a continuous distribution of energies as the ones shown in Fig. 4.2, we can give a measure to the critical acceleration by considering

the relative shift between the "fastest" particles with energy U_{fast} and the "slowest" particles with energy U_{slow}. By equating the energy spread ΔU to the FWHM of the Gaussian distribution, we can map U_{fast} and U_{slow} to U_1 and U_2 from Eq. (4.6) respectively. This leads to an identical expression for a_{crit} and F_{crit}. We decide to use this expression as our figure of merit in the following discussion, where we apply it to different experimental scenario in order to get order-of-magnitude figures in order to provide limits to the design of our device. This argument was used in the work of Lansonneur et al. [Lan+17] and Demetrio et al. [Dem+17] in order to quantify the maximum field allowed to act on the particles. In the next section, we apply this formulation to different kind of forces in order to derive expressions for the critical fields in different physical conditions.

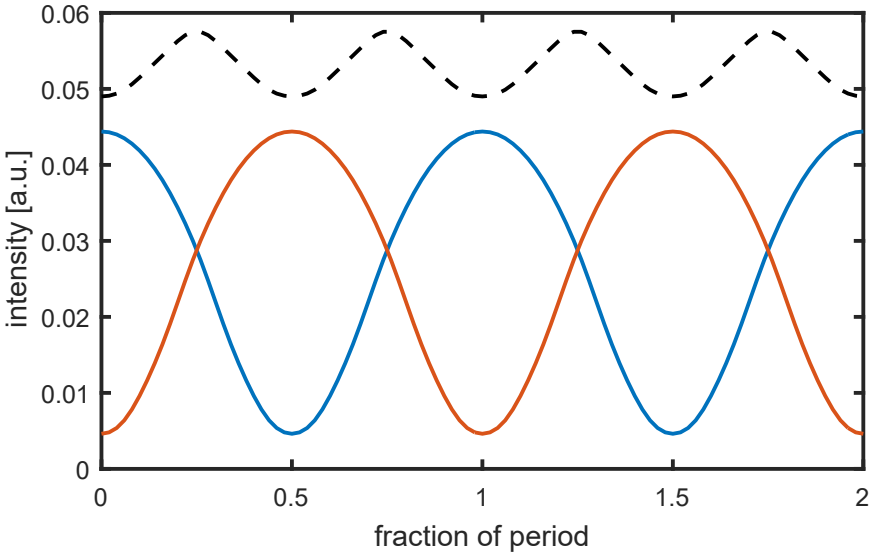

Figure 4.5: Particles with different energies U_1 (blue line) and U_2 (red line) subjected to the same acceleration $\mathbf{a}$ will experience different phase shifts due to their longer or shorter time of flight τ inside the interferometer. In the most pathological case, the two patterns can be in opposition of phase on the detector, leading to a hugely reduced contrast when summing up the signals (dashed black line).

4.2.1 Charged particles

Charged particles such as electrons and ions are subjected to the effects of magnetic and electric fields, in addition to weaker forces such as gravity. In this section, we derive expressions for the critical electric and magnetic fields which satisfy Eq. (4.10). We consider two specific interactions: a

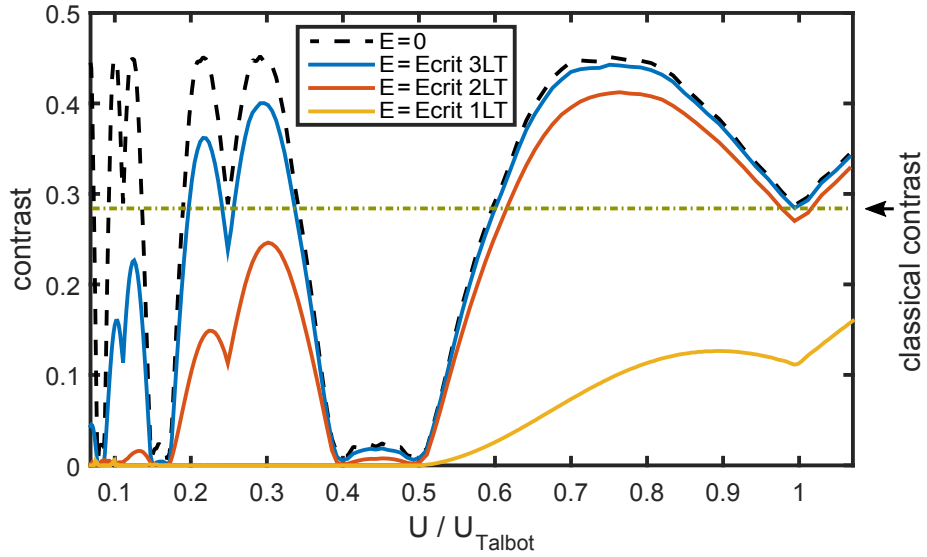

Figure 4.6: This figure shows the same contrast plot from Fig. 4.4 with an additional force acting on the particles, in particular the critical electric field calculated in Sec. 4.2.1. Such field is inversely proportional to the energy spread, so this plot proves valid for any value of ΔU. A mathematical expression for $E_{\text{crit } n\ L_T}$ is given in Eq. (4.19).

Lorentz force acting on a beam of charged particles and a simple model for inner beam interactions due to Coulomb self-repulsion.

Lorentz force

If we consider a static electric field $\mathbf{E}$ and a static magnetic field $\mathbf{B}$, the Lorentz force acting on a particle with charge q can be written as

$$\mathbf{F}_{\text{Lnz}} = q(\mathbf{v} \times \mathbf{B} + \mathbf{E}), \tag{4.11}$$

where $\mathbf{v}$ is the velocity of the particle. Since our device is sensitive only to the transverse component of the acceleration, we take into account only F_y, which is therefore expressed by

$$F_y = q(v_z B_x - v_x B_z + E_y). \tag{4.12}$$

There is a caveat: the Lorentz force is someway different from the general case we considered in Sec. 4.2, as it effectively deflects the particles in a circular trajectory, rather than in a parabolic one. However, in reasonable experimental conditions ($|\mathbf{B}| \simeq 1\,\text{G}$, $v_z \gg v_x, v_z \gg v_y$), we can consider it as a parabolic motion [Mül16]. Out of simplicity, we thus work with the assumption that the axial velocity v_z remains the same during the flight ($\Delta v_z / v_z \ll 1$) and with a condition for the transverse force which reads

$v_x B_z \ll v_z B_x$, so that the acceleration in the y direction is independent on B_z. In this framework, by elaborating on Eq. (4.12), we get an expression for the acceleration a_y

$$a_y = \frac{q}{m}(v_z B_x + E_y). \tag{4.13}$$

By using $v_z = \sqrt{2\bar{U}/m}$, we get

$$a_y = \frac{q}{m}\left(\sqrt{\frac{2\bar{U}}{m}} B_x + E_y\right). \tag{4.14}$$

If we compare this expression with the critical acceleration from Eq. (4.10), we can separately obtain a formulation for the critical electric field E_{crit} and the critical magnetic field B_{crit}, by setting the other field to zero respectively. Thus we obtain [Dem+17; Lan+17]

$$E_{\text{crit}} = \frac{d}{qL^2}\frac{\bar{U}}{k}, \text{ for } |\mathbf{B}| = 0 \tag{4.15}$$

$$B_{\text{crit}} = \frac{d}{qkL^2}\sqrt{\frac{m\bar{U}}{2}}, \text{ for } |\mathbf{E}| = 0, \tag{4.16}$$

To produce a concrete example, we consider the setup described in [Dem+17], with $L = 171.7\,\text{mm}$, $d = 256\,\text{nm}$, using ions with $m = m_{\text{p}} = 1.67 \times 10^{-27}\,\text{kg}$, we get the experimental fields

$$\tilde{E}_{\text{crit}} = 8.7 \times 10^{-6}\frac{\bar{U}}{k} \tag{4.17}$$

$$\tilde{B}_{\text{crit}} = 6.3 \times 10^{-10}\frac{\sqrt{\bar{U}}}{k}, \tag{4.18}$$

with $\tilde{E}_{\text{crit}}$ expressed in units of V m^{-1}, $\tilde{B}_{\text{crit}}$ in tesla and $\bar{U}$ in eV. For an energy of $\bar{U} = 2\,\text{keV}$ and $k = 1\,\%$, we get that $\tilde{E}_{\text{crit}} = 1.74\,\text{V m}^{-1}$ and $\tilde{B}_{\text{crit}} = 28.2\,\text{mG}$, going as low as $\tilde{E}_{\text{crit}} = 0.17\,\text{V m}^{-1}$ and $\tilde{B}_{\text{crit}} = 8.9\,\text{mG}$ for an energy ten times lower. Compare this with the average Earth magnetic field being around $0.5\,\text{G}$ and average electric field at the Earth surface level of $100\,\text{V m}^{-1}$ [FLS15; Cha57] to see that active or passive shielding is needed in order to perform any kind of measurement which satisfy these limits.

If we fix the length of the device to an integer multiple n of the Talbot length L_{T} (Eq. (2.2)), we can get an additional expression for the critical fields which is valid when the energy of the particles matches the n-th Talbot energy. This formula can be of interest in some application of the interferometer. By using Eq. (2.2) together with Eq. (4.15) and

Eq. (4.16), we get [Dem+17]

$$E_{\text{crit } n\ L_T} = \frac{h^2}{2md^3q}\frac{1}{k}\frac{1}{n^2}, \text{ for } |\mathbf{B}| = 0 \tag{4.19}$$

$$B_{\text{crit } n\ L_T} = \frac{h^2}{2\sqrt{2m}d^3q}\frac{1}{k\bar{U}}\frac{1}{n^2}, \text{ for } |\mathbf{E}| = 0. \tag{4.20}$$

The last two equations underline an interesting fact: the critical field associated with a multiple integer of L_T is independent on the average energy and it's completely determined by the energy spread ratio k. Conversely, the critical magnetic field does depend on the square root of the average energy, due to the fact that the magnetic force is proportional to the velocity of the particles. The fields used to create the plot in Fig. 4.6 are calculated by using Eq. (4.19).

Inner beam interactions

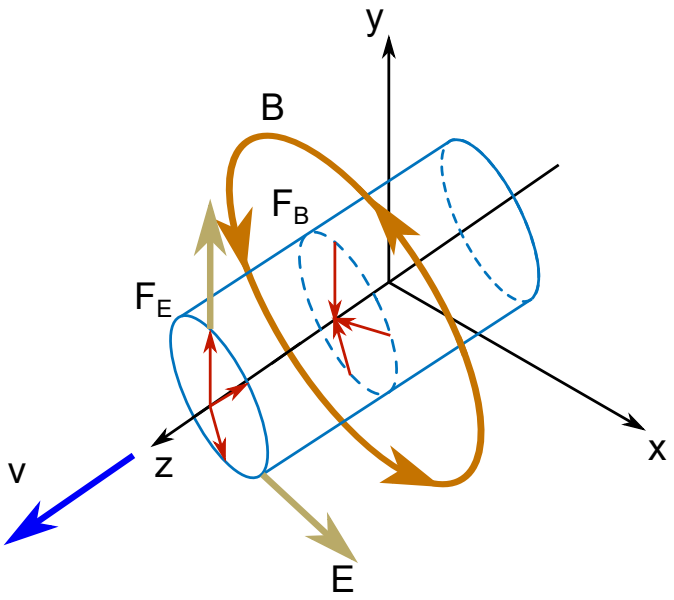

Figure 4.7: The electric and magnetic field generated by a moving distribution of charge create a net radial force in opposite directions: the electric fields tend to blow up the beam, while the magnetic field tends to squeeze it. When considering non relativistic velocities, the effects of magnetic fields are negligible compared to the electric force.

When we use charged beams, the mutual interaction between the particles can lead to an effective phase shift and to the overlap of several different patterns. The Coulomb repulsion becomes more important as the intensity of the source increases, up to a point where the shift between the two extremes of the beam is one full period d of the grating. In this

section, we closely follow the approach highlighted in [Dem+17], based on [Kal13; BSO14; Brä+15], in order to analyze this effect by means of a simplified model and to extract an evaluation for this critical beam intensity. Consider a particle species with mass m and charge q. The beam is modeled as an infinite cylinder of radius r_0, with uniform charge density ρ, and fixed axial velocity v_z. A moving distribution of charge generates both an own electric field E and a magnetic field B due to the motion of the particles. The transverse acceleration is produced by two concurring effects: a radial electric force $\mathbf{F}_E(r) = qE(r)\hat{\mathbf{r}}$ and a magnetic force $\mathbf{F}_B(\mathbf{r}) = q\mathbf{v} \times \mathbf{B}(\mathbf{r})$, where $\mathbf{r} = (x, y)$ is the radial coordinate and $r = \sqrt{x^2 + y^2}$ is the length of the vector. Notice that the magnetic field generated by a moving charge distribution shows circular field lines on a plane whose directional vector is the axis of the cylinder. This fact orients the force exerted by the magnetic field on the particles in the radial direction, contributing to the total transverse acceleration. A schematic on how the fields act on the traveling particles is shown in Fig. 4.7. The electric field inside a charge cylinder with $r \leq r_0$ can be obtained using Gauss's law and reads [Kal13; Brä+15]

$$E(r) = \frac{\rho r}{2\epsilon_0} \tag{4.21}$$

Using Ampere's law, the intensity of the tangent magnetic field which leads to a radial acceleration can be calculated as [Brä+15]

$$|B(r)| = \frac{\mu_0 j r}{2} = \frac{\mu_0 \rho v_z}{2}, \tag{4.22}$$

where the current density vector $\mathbf{j}$ is given by $\mathbf{j} = \rho\mathbf{v} = \rho v_z \hat{\mathbf{z}}$ and is parallel to the axial velocity. Notice that the direction of the force produced by the magnetic field is opposite to the one of the electric field: the expansion due to the Coulomb repulsion is opposed by a concurrent compression effect due to the magnetic force. The combined radial force is therefore given by

$$\mathbf{F}(r) = q(E(r) - v_z B(r)) = q\left(\frac{\rho r}{2\epsilon_0} - \frac{\mu_0 \rho v_z^2}{2}\right)\hat{\mathbf{r}}. \tag{4.23}$$

In order to simplify this expression, we rewrite the magnetic portion of the formula as

$$v_z B(r) = \frac{\mu_0 \epsilon_0 \rho v_z^2}{2\epsilon_0} = \frac{v_z^2}{c^2}\frac{\rho}{2\epsilon_0} = \frac{v_z^2}{c^2}E(r), \tag{4.24}$$

where we used the identity $\mu_0\epsilon_0 = c^{-2}$, c being the speed of light in

vacuum. This leads to

$$\begin{aligned}\mathbf{F}(r) &= q\left(1-\frac{v_z^2}{c^2}\right)E(r)\hat{\mathbf{r}} \\ &= q\frac{1}{\gamma^2}E(r)\hat{\mathbf{r}} \\ &= \frac{1}{\gamma^2}\frac{q\rho r}{2\epsilon_0}\hat{\mathbf{r}}\end{aligned} \tag{4.25}$$

where γ is the Lorentz factor. From this moment on, we can let the γ factor inside the equations as a modifier for the electric field. Notice, however, that for non-relativistic cases ($v_z \ll c$) $\gamma \simeq 1$, and therefore the effect of the magnetic field is negligible. In the following, we consider the non-relativistic scenario out of simplicity and we set $\gamma = 1$. Eq. (4.21) quantifies the field inside the charge distribution. In order to retrieve a number for quantifying the shift, we consider the field just outside the surface of the charge cylinder, given by [Kal13]

$$E^{\text{out}}(r) = \frac{\rho r_0^2}{2\epsilon_0 r}. \tag{4.26}$$

The field shows a maximum at $r = r_0$ and then decreases monotonically. During the travel through the measurement device, r is a function of time t, since the beam keeps on expanding due to the self-repulsion. The radial acceleration a_r acting on a particle right at the border of the cloud is then given by

$$\ddot{r} = a_r = \frac{qE^{\text{out}}(r)}{m}. \tag{4.27}$$

In order to find the trajectories as a function of the axial position, we can perform a transformation and express a_r as [Kal13]

$$a_r = \frac{\mathrm{d}^2 r}{\mathrm{d}t^2} = v_z^2\frac{\mathrm{d}^2 r}{\mathrm{d}z^2}, \tag{4.28}$$

which, by reversing the equation, let us deduce the implicit formula

$$\frac{\mathrm{d}^2 r}{\mathrm{d}z^2} = \frac{a_r}{v_z^2} = \frac{q\rho r_0^2}{2m\epsilon_0 v_z^2 r} = \frac{K}{r} \tag{4.29}$$

where K is a constant. The real trajectories can be then numerically calculated by reversing the integral function

$$z = \frac{r_0}{\sqrt{2K}}G\left(\frac{r}{r_0}\right)\int_1^{r/r_0}\frac{\mathrm{d}u}{\sqrt{\ln(u)}}. \tag{4.30}$$

By setting a specific value for r, we can therefore get the associated value for the axial component z which is needed to have that specific

beam expansion. It is interesting to notice that for $r/r_0 \simeq 1$, $G\left(\frac{r}{r_0}\right)$ can be approximated by a simpler formulation. If we consider small beam expansions, such that $r - r_0 \ll r_0$, we can express the integrand through a Taylor series around $r/r_0 = 1$. Since we are looking for expansions of the order of the grating period d, this assumption is reasonable until $d/r_0 \ll 1$. By expanding the denominator around $u = 1$, we obtain

$$\frac{1}{\sqrt{\ln(u)}} \simeq \frac{1}{\sqrt{u-1}}. \tag{4.31}$$

Replacing the integrand with its approximation, we finally obtain

$$G\left(\frac{r}{r_0}\right) \simeq \int_1^{r/r_0} \frac{\mathrm{d}u}{\sqrt{u-1}} = 2\sqrt{\frac{r-r_0}{r_0}}, \tag{4.32}$$

thus leading to

$$z = \frac{\sqrt{2}r_0}{K}\sqrt{\frac{r-r_0}{r_0}}, \tag{4.33}$$

which is exactly the trajectory described by a particle subjected to a uniform, constant radial acceleration $a_r(r) = a_r(r_0)$. As shown in Fig. 4.8,

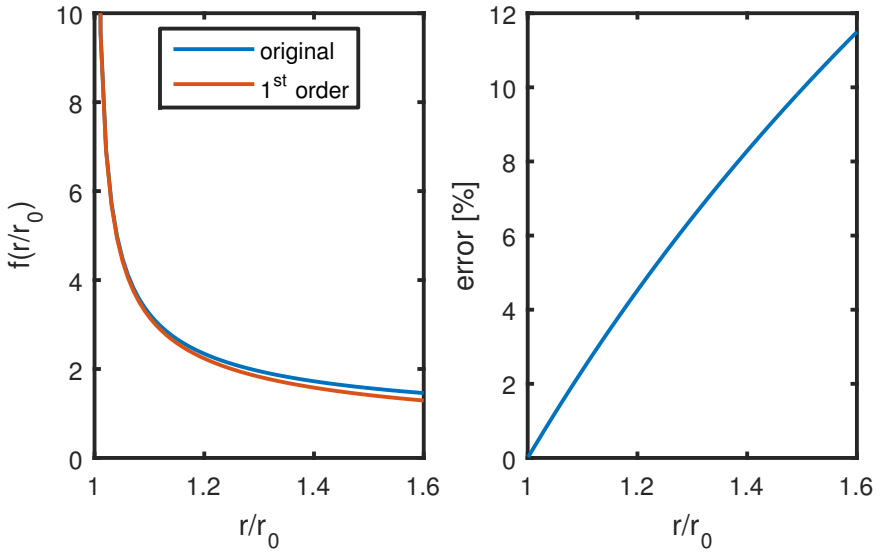

Figure 4.8: By using Eq. (4.31), we can obtain integrable trajectories for particles at the surface of a cylindrical charge distribution. The error produced by the approximation is acceptably low for small deviation from the original beam radius (i.e. $r - r_0 \ll r_0$). Since we are interested in shifts of the order of the grating period d, as long as $d \ll r_0$ the approximation proves valid.

for $r/r_0 \simeq 1$, the error caused by using the first order expansion is less

than 1 %, therefore we use the approximation in order to retrieve a figure of merit in this situation. By considering the shift $\Delta y = r - r_0$, we have that a particle at the surface will experience a phase shift equal to half the period in respect to the center of the beam if

$$\begin{aligned} \frac{d}{2} &\stackrel{!}{=} a_r(r_0)\tau^2 \\ &= \frac{q\rho r_0}{2\epsilon_0 m}\frac{L^2}{v_z^2}. \end{aligned} \tag{4.34}$$

We now express ρ as a function of the incoming flux of particles Φ^{in} as

$$\rho = q\frac{\Phi^{\text{in}}}{v_z}, \tag{4.35}$$

so that we obtain

$$\frac{d}{2} = \frac{q^2\Phi^{\text{in}} r_0}{2\epsilon_0 m}\frac{L^2}{v_z^3}. \tag{4.36}$$

We can invert Eq. 4.36 to find an expression for the critical flux $\Phi^{\text{in}}_{\text{crit}}$ which would generate this kind of shift, which becomes the figure of merit when a detailed analysis is needed:

$$\begin{aligned} \Phi^{\text{in}}_{\text{crit}} &= d\frac{\epsilon_0 m}{q^2 r_0}\frac{v_z^3}{L^2} \\ &= \frac{2\sqrt{2}\epsilon_0}{q^2\sqrt{m}r_0}\frac{d}{L^2}\bar{U}^{-\frac{3}{2}}. \end{aligned} \tag{4.37}$$

In the last passage we replaced the average axial velocity v_z using the classical kinetic energy $\bar{U} = mv_z^2/2$, in the hypothesis that $v_z \gg v_r$. For the test setup considered in [Dem+17], using $m = m_{\text{p}}$ and $\bar{U} = 2\,\text{keV}$, this translates into $\Phi^{\text{in}}_{\text{crit}} = 1.2 \times 10^{15}\,\text{m}^{-2}\,\text{s}^{-1}$. With a cross section of $1\,\text{mm}^2$, which is reasonable for a well collimated beam, we get $\Phi^{\text{in}}_{\text{crit}} = 1.2 \times 10^9\,\text{Hz}$, well in the range of ion sources like the one described in [Sor+10].

This derivation for the critical flux does not however take into account the energy spread $\Delta U = k\bar{U}$ of the source. We can introduce a second expression for the critical flux nearer in meaning to the original formulation of the critical force expressed by Eq. (4.10). Therefore, we define this critical flux $\bar{\Phi}^{\text{in}}_{\text{crit}}$ as the one which causes two particles with energy U_1 and U_2, given by Eq. (4.6), to be separated by half a grating period $d/2$ If we express the incoming flux Φ^{in} as in Eq. (4.35) in terms of the mean energy $\bar{U}$ and we combine it with Eq. (4.9), we obtain

$$\begin{aligned} \frac{d}{2} &= \frac{q^2\Phi^{\text{in}} r_0}{2\epsilon_0\sqrt{2m\bar{U}}}\frac{mL^2}{2}\frac{k}{\bar{U}} \\ &= k\frac{q^2\Phi^{\text{in}} r_0}{4\sqrt{2}\epsilon_0}\frac{\sqrt{m}L^2}{\bar{U}^{\frac{3}{2}}}. \end{aligned} \tag{4.38}$$

This leads to a very similar expression for $\bar{\Phi}^{\text{in}}_{\text{crit}}$, which can be written as

$$\bar{\Phi}^{\text{in}}_{\text{crit}} = \frac{1}{k}\Phi^{\text{in}}_{\text{crit}} \tag{4.39}$$

which means that $\bar{\Phi}^{\text{in}}_{\text{crit}}$ is always higher than $\Phi^{\text{in}}_{\text{crit}}$ when $k < 1$, which is true for most of the particles sources consider in this kind of experiments. Therefore, when designing a device for charged particles, it is more reasonable to consider $\Phi^{\text{in}}_{\text{crit}}$ as the target figure of merit when performing the experiment.

4.2.2 Neutral particles

Neutral particles are affected by forces which are vastly different from the ones considered for charged particles. Some of them, such as gravity, act also on ions or electrons but usually are weak compared to e.g. electromagnetic interactions and are therefore neglected in the subsequent analysis. Others are just targeting neutral particles, like the ones connected to the Zeeman split or the Stark dipolar force. In this section we consider some examples and apply the generic formulas from Sec. 4.2.

Gravity

Gravity is as straightforward as a vertical, homogeneous force can be in limited volumes of space. As its local effect directly translates into a force $\mathbf{F} = -mg\hat{\mathbf{y}}$, Eq. (4.10) can be applied to derive the average energy $\bar{U}_g$ which, given $a_{\text{crit}} = g$ would cause a split of half a period. If we set

$$g = \frac{d}{mL^2}\frac{\bar{U}_g}{k}, \tag{4.40}$$

we obtain for an expression for $\bar{U}_g$

$$\bar{U}_g = k\frac{gmL^2}{d}. \tag{4.41}$$

By using for example the setup described in [Dem+17], with $L = 171.7\,\text{mm}$, $d = 256\,\text{nm}$, using $m = m_{\text{H}} = 1.67 \times 10^{-27}\,\text{kg}$ and $|g| = 9.81\,\text{m}\,\text{s}^{-2}$, we get

$$\bar{U}_g = k\ 1.2 \times 10^{-2}\,\text{eV}. \tag{4.42}$$

For $k = 1$, this energy is equivalent to a temperature of around 137 K if we consider the corresponding thermal energy. This means that for a temperature smaller than 137 K, gravity can cause the signal to lose contrast if the energy distribution is so broad that the FWHM is equal to the mean energy. In more controlled conditions, e.g. $k = 0.01$, the critical temperature becomes as low as 1.4 K for the same geometrical

parameters. In this particular case, increasing the period of the gratings by e.g. ten times would take away the issue, since the limit energy is directly proportional to it. We discuss this aspects of the planning process and deal with thermal distributions in detail in Sec. 5, where we analyze a possible design for a gravity measurement using a Talbot-Lau interferometer.

Magnetic field gradients

Some neutral atoms and particles have a magnetic moment of the order of the Bohr magneton $\mu_B = 9.274 \times 10^{-24}\,\mathrm{J\,T^{-1}}$ [MNT16]. This quantity can be expressed as a function of physical constants as [Cow81]

$$\mu_B = \frac{e\hbar}{2m}, \tag{4.43}$$

where $e = 1.6 \times 10^{-19}\,\mathrm{C}$ is the elementary charge. This magnetic moment couples with magnetic field gradients, causing a net acceleration towards the minimum of this magnetic potential (low field seekers) or, conversely, towards its maximum (high field seekers). The magnetic moment $\mathbf{M}$ can be in many cases approximated by

$$\mathbf{M} = g_j \frac{q}{2m} \mathbf{J}, \tag{4.44}$$

with g_j being a suitable Landé g-factor [Lan21; Cow81] connected with the angular momentum and $\mathbf{J}$ being the total angular momentum of the particle. The potential energy associated with $\mathbf{M}$ is therefore

$$U_M = -\mathbf{M} \cdot \mathbf{B} = -g_j \frac{e}{2m} JBcos(\theta), \tag{4.45}$$

where $\mathbf{B}$ is the external magnetic field and θ is the angle between the field and the direction of the angular momentum. If we consider $\mathbf{M}$ independent on the position, the force acting on the particle is therefore

$$\mathbf{F}_M = -\nabla U_M = g_j \frac{e}{2m} J\nabla |\mathbf{B}| cos(\theta). \tag{4.46}$$

Here, particles with positive magnetic moment will be attracted by magnetic field minima, while particles with negative magnetic moment will follow the field. The goal of this work is to discuss the application of a Talbot-Lau interferometer for studying the gravitational interaction with antimatter and our candidate species is antihydrogen, we perform our evaluations in this specific framework. A detailed discussion on how magnetic fields gradient affect antihydrogen atoms in various energy states can be found in [Dem14b]. As an approximation, we consider a first

order Zeeman splitting as the source of the magnetic interaction in neutral atoms. We can thus use an expression for the Landé factor g_j given by [Cow81]

$$g_j = 1 + (g_e - 1)\frac{j(j+1) + s(s+1) - l(l+1)}{2j(j+1)}, \tag{4.47}$$

with $g_e \simeq 2$ being the electron gyromagnetic factor, j, s and l being the quantum numbers associated with the total angular momentum $\mathbf{J}$, the intrinsic spin $\mathbf{S}$, and the orbital angular momentum $\mathbf{L}$. We consider $\hbar m_j$ as the projection of the spin in the direction of the magnetic field, which we consider as our quantization axis, leading to a force

$$\mathbf{F}_M = g_j \ \mu_B \ m_j \nabla |\mathbf{B}| , \tag{4.48}$$

where we used Eq. (4.43). By using Eq. (4.10), we obtain

$$g_j \ \mu_B \ m_j \, |(\nabla |\mathbf{B}|)_{\text{crit}}| = \frac{d}{L^2}\frac{\bar{U}}{k}, \tag{4.49}$$

which gives

$$|(\nabla |\mathbf{B}|)_{\text{crit}}| = \frac{1}{g_j \ \mu_B \ m_j}\frac{d}{L^2}\frac{\bar{U}}{k}. \tag{4.50}$$

Since the maximum value for m_j scales with the principal quantum number n, as $j = l + s$ and $l < n$, a hydrogenoid atom in an excited state experiences a magnetic force up to $\sim n$ times bigger than in the ground state, up to a maximum $m_j = n - s$. Furthermore we see that if we keep $s = 1/2$ as for an electron in an atomic orbital, the bigger j and l become, the more g_j approaches 1. In the following, we can thus consider $g_j = 1$ and $m_j = n - 1/2$ which goes to $m_j \simeq n$ for large principal quantum numbers $n \gg 10$, since the goal of this section is to give an order-of-magnitude estimation for the critical field gradient, leading to

$$|(\nabla |\mathbf{B}|)_{\text{crit}}| \simeq \frac{1}{\mu_B \ n}\frac{d}{L^2}\frac{\bar{U}}{k}, \tag{4.51}$$

which, as expected, shows an inverse dependence on the principal quantum number n, meaning that for excited atoms the threshold for the critical gradient is lowered in respect to ground-state atoms. For the test device described in [Dem+17], with $L = 171.7\,\text{mm}$ and $d = 256\,\text{nm}$, we get

$$|(\nabla |\mathbf{B}|)_{\text{crit}}| \simeq 0.15\frac{\bar{U}}{n \ k}, \tag{4.52}$$

with $(\nabla |\mathbf{B}|)_{\text{crit}}$ expressed in $\text{T}\,\text{m}^{-1}$ and $\bar{U}$ in eV. This result proves that in realistic experimental conditions the effect of the magnetic interaction for neutral atoms can be neglected, unless in presence of really high

field gradients, low-energies or high-order excitations for the atoms. We can now compare this force to gravity, in order to draw a parallel with Sec. 4.2.2. The magnetic field gradient $(\nabla |\mathbf{B}|)_g$ which is equivalent to the gravitational acceleration is given by

$$|(\nabla |\mathbf{B}|)_{\text{crit}}| \simeq \frac{mg}{\mu_B \, n}. \tag{4.53}$$

For $n = 1$ and $m = m_{\text{H}}$, this leads to the empirical value [Dem14a]

$$|(\nabla |\mathbf{B}|)_{\text{crit}}| \simeq 2 \times 10^{-3} \,\text{T}\,\text{m}^{-1} = 0.2 \,\text{G}\,\text{cm}^{-1}. \tag{4.54}$$

Notice that if the gradient is bigger than $(\nabla |\mathbf{B}|)_g$, the gravitational acceleration becomes shadowed by these forces, meaning that in order to perform a proper measurement the homogeneity of the surrounding field has to be properly taken under control. The most advisable experimental condition would be having $\nabla |\mathbf{B}|$ at least one order of magnitude smaller than g, in order to avoid systematic errors during the measurement.

Electric field gradients

Neutral particles can be also subjected to the effects of non-homogeneous electric fields, due to their electric dipole moment. For a hydrogen atom with principal quantum number n immersed in an electric field $\mathbf{E}$, in absence of magnetic fields, the energy levels can be schematized as [Dro+07; Gil14]

$$U_n = \frac{U_0}{n^2} + 3\frac{ea_0}{2} k \; n \, |\mathbf{E}| \,, \tag{4.55}$$

where $U_0 = -13.6\,\text{eV}$, $a_0 \simeq 0.53 \times 10^{-10}\,\text{m}$ [MNT16] is the Bohr radius, e is the elementary charge, and k is the so-called parabolic quantum number, which ranges from $-(n - |m| - 1)$ to $(n - |m| - 1)$ in steps of two, where m is the magnetic quantum number [Dro+07; Gil14]. The corresponding force is therefore given by

$$\mathbf{F}_n^E = -\frac{3}{2} e a_0 k \; n \nabla |\mathbf{E}| \,. \tag{4.56}$$

A hydrogen atom in the ground state has no electric dipole, therefore the effect of this interaction is theoretically zero in the simplest scenario. For our evaluation, we set $k = n$, in order to derive an upper limit to the estimation of the critical gradient $|(\nabla |\mathbf{E}|)_{\text{crit}}|$. By using once more Eq. (4.10) we obtain

$$\frac{3}{2} e a_0 n^2 \, |(\nabla |\mathbf{E}|)_{\text{crit}}| = \frac{d}{L^2} \frac{\bar{U}}{k_U}, \tag{4.57}$$

where we have re-labeled the energy dispersion constant k as k_U in order to avoid confusion. This leads to

$$|(\nabla |\mathbf{E}|)_{\text{crit}}| = \frac{d}{L^2} \frac{2}{3 e a_0 n^2} \frac{\bar{U}}{k_U}. \tag{4.58}$$

For the test device described in [Dem+17], with $n = 1$, $L = 171.7\,\mathrm{mm}$ and $d = 256\,\mathrm{nm}$, we get the empirical formula

$$|(\nabla |\mathbf{E}|)_{\mathrm{crit}}| = 1.09 \times 10^5 \frac{\bar{U}}{k_U}, \tag{4.59}$$

with $|(\nabla |\mathbf{E}|)_{\mathrm{crit}}|$ in $\mathrm{V\,m^{-2}}$ and $\bar{U}$ in eV. We notice that this value is huge, and therefore even with an energy dispersion $k_U = 100\,\%$ should not be of any concern, unless in specific experimental conditions. In a similar fashion as in Sec. 4.2.2, we retrieve now the value of the electric field gradient which can mimic the effects of gravity:

$$|(\nabla |\mathbf{E}|)_{\mathrm{crit}}| \simeq \frac{2mg}{3ea_0n^2}. \tag{4.60}$$

For $n = 1$ and $m = m_{\mathrm{H}}$, this leads to the empirical value

$$|(\nabla |\mathbf{E}|)_{\mathrm{crit}}| \simeq 1.3 \times 10^3\,\mathrm{V\,m^{-2}} = 13\,\mathrm{V\,m^{-1}\,cm^{-1}}. \tag{4.61}$$

This value indicates a field which changes by $13\,\mathrm{V\,m^{-1}}$ every cm, which is not usually found in nature. We can ignore the effects of the electric field if the experimental conditions do not cause a field which varies with this order of magnitude. Notice however that, since the critical field goes with n^{-2}, a Rydberg state with $n = 30$ would decrease this value by around three orders of magnitude, lowering it to the range of variations we can witness in non-controlled environments.

4.3 Summary

In this chapter, we have studied the effects of the energy spread of the particle source, in combination with external forces acting on the particles, and the consequent degradation of the pattern of the interferometer. We discussed the influence of these two phenomena for both charged and neutral particles, which identify two different application regimes for a Talbot-Lau interferometer. We found a general formula which establishes the critical force F_{crit} which causes a Gaussian energy distribution to produce a pattern with severely reduced contrast. We applied this formula first to interactions affecting charged particles, like electric fields and magnetic fields. Then, we used it to retrieve critical values related to gravity, electric field gradients, and magnetic field gradients. Since the goal of this work is to discuss the feasibility of a gravity measurement on antimatter, we performed as well calculations to see what is the magnitude of magnetic and electric field gradients which could mimic gravity. The result is that, on ground state antihydrogen, a magnetic gradient of $0.2\,\mathrm{G\,cm^{-1}}$ creates an interaction as strong as the gravitational acceleration, while electric field gradients constitute a minor problem, starting to emulate gravity at $13\,\mathrm{V\,m^{-1}\,cm^{-1}}$.

Chapter 5

Simulation of a gravity measurement with antihydrogen

Until now, we have mainly discussed systematic effects and perturbations which have to be taken care of in order to perform any sort of inertial measurement using a Talbot-Lau interferometer. Chapter 3 dealt with the requirements for the alignment of the gratings in order to get a non-zero signal, while Chapter 4 focused on the disturbances caused by forces acting on the particles. This chapter is meant to wrap things up and offer numerical estimations on the feasibility of a gravity measurement on antihydrogen, taking into account realistic parameters for the antimatter source.

The use of a two or three-grating device to measure forces is not a novelty in the field of atomic and particle physics: the interested reader can read details about past implementations of this technique in [Obe+96], [Agh+14], and [Lan+17], where a similar device has been employed to perform a variety of inertial measurements.

In 2007, this technique has been referenced in the proposal of the AEGIS experiment [Dro+07], with the purpose of measuring the gravitational acceleration which antihydrogen is subject to, though the characteristics of the particle source were mostly evaluated from theoretical calculations and had no experimental support at the time. As of today, it is clear that to reach the envisioned 1 % precision, a lot of not-yet-available technological improvements are required. We focus therefore on a so-called "sign measurement" of the gravitational acceleration, which accounts for a 30 % precision: since the gravitational acceleration g is equal to around $9.81\,\mathrm{m\,s^{-2}}$, having $\sigma \simeq 3\,\mathrm{m\,s^{-2}}$ would allow us to confirm or reject antigravity with a confidence interval of 3σ. While this is still a coarse measurement, it would be more accurate than the only experimental data available as of the date of this work [Amo+13]: currently, direct

measurement on antimatter gravity constrain the (anti)gravitational acceleration $\bar{g}$ to the interval $-65g < \bar{g} < 110g$.

In the following, we consider two target levels of precision: the aforementioned "sign measurement" and a 10 % measurement ($1\,\mathrm{m\,s^{-2}}$), which can be seen as the next step toward a higher accuracy.

This chapter represents the main result of this work and is divided into several subsections.

We start by analyzing various procedures with which antihydrogen has been experimentally produced, obtaining quantitative numbers for the parameters of the source, such as intensity and temperature. Since the first cold antihydrogen production in 2002 [Amo+02], two methods have been successfully used for creating antihydrogen: *direct mixing* of positrons and antiprotons [Amo+02; Amo+14] and *charge exchange* between antiprotons and positronium [Sto+04]. Both methods result in the capture of a positron by an antiproton, forming a neutral antiatom. These two mechanisms exploit different reactions and produce antihydrogen in vastly different quantities with unique physical properties. We study them in detail at the beginning of the chapter

Afterwards, we build a numerical model to estimate the accuracy of a gravity measurement, with emphasis on how to take into account the geometry of the experiment. Since this work has been produced in the framework of the AEgIS collaboration, we consider the currently available measurement volume contained in the main vacuum chamber of the experiment.

Finally, we consider two different scenarios, namely a "short configuration" (interferometer placed at the exit of the antihydrogen production trap, inside the vacuum chamber of the main experiment), and a "long configuration" (interferometer placed outside the main AEgIS apparatus, in its own vacuum chamber as a sub-unit of the experiment), which were originally analyzed in an internal collaboration report by the author in conjunction with the rest of the Heidelberg group [Brä+15][1]. We use part of this report as a basis for our evaluation, while developing some additional techniques to take into account a wider range of effects.

5.1 Parameters of the antiproton source

As we have seen in Sec. 1.5, the only source of cold hadronic antimatter currently available is the CERN Antiproton Decelerator (AD). This deceleration ring provides bunches of 3×10^7 antiprotons at 5.3 MeV, with a repetition rate of around 100 s. Since the AD can not supply more than one experiment at once, the experiments installed on the ring observe eight hour shifts with a rotating schedule, resulting in a total of around

[1] a copy of this report is included in Appendix Sec. B

288 antiproton shots per measurement day. We previously pointed out in Sec. 1.5 that the improved ELENA ring will be activated in early 2020, boosting the catching rate of antiprotons by a factor between 10 and 100. However, since no direct measurement on the trapping efficiency on the newly installed decelerator is already available, we use the current AD data in the following evaluations.

The antiproton bunch from the AD is still too fast to be caught in electromagnetic traps: as a rule of thumb, an electric potential of 1 V is required to stop the motion of a particle with a kinetic energy of 1 eV, meaning that a 5.3 MV potential would be needed to stop the antiprotons in their current status[2]. In order to trap a part of the bunch, thin aluminum foils of different thickness are placed just after the extraction point of the Antiproton Decelerator [Kra+13]. About half of the antiprotons annihilate inside the foil, while the surviving part collide with the atoms of the material and lose energy, emerging with a broad energy distribution which presents a consistent tail of particles with kinetic energy smaller than 10 keV [Kra+13; Car17]. These are the particles which get caught and subsequently cooled by the antimatter experiments placed on the AD. Out of the 3×10^7 antiprotons, a standard catching procedure results in around 1×10^4 antiprotons trapped per AD shot. These particles can be then used for a variety of experiments, including but not limited to, antihydrogen formation.

5.2 Direct mixing

Direct mixing is a broad category which encompasses all the antihydrogen production procedures based on the direct interaction between positrons and antiprotons inside the same electromagnetic trap. The geometry of the trap and the actual process vary between the experiments [Amo+04b; And+11], leading to different results in terms of temperature and velocity distribution of the produced particles. In this section, we follow the summary given by Holzscheiter et al. [HCN04] to introduce the principal formation mechanisms and their impact on the number of produced antihydrogen atoms.

5.2.1 Theoretical background

The simplest reaction which leads to antihydrogen formation is in principle the so-called spontaneous radiative recombination (SRR) with the emission of a photon:

$$\bar{\mathrm{p}} \; + \; e^+ \longrightarrow \bar{\mathrm{H}} \; + \; h\nu. \tag{5.1}$$

[2]Delving into the physics of electromagnetic traps is outside the scope of this work. A good introduction to the topic can be found in the work of Blaum et al. [BNW10].

In this reaction, the photon is required to ensure that both momentum and energy are conserved. However, for sufficiently low temperatures and high density ρ_e of the positron plasma, the main reaction which leads to antihydrogen formation is a three-body recombination process [GHA94]:

$$\bar{\mathrm{p}} \ + \ e^+ \ + \ e^+ \longrightarrow \bar{\mathrm{H}} \ + \ e^+. \tag{5.2}$$

According to Müller and Wolf [MW97], the antihydrogen formation reaction can be seen as a complex process which includes three different contributions: the aforementioned spontaneous radiative recombination, a three-body reaction, and a a complex interplay between collisional and radiative recombination. [SBD75]. With these considerations, the total antihydrogen production rate $\alpha_{\bar{\mathrm{H}}}$ (cm^3/s) is given by:

$$\alpha_{\bar{\mathrm{H}}} = \alpha^{\mathrm{SRR}} + \alpha^{\mathrm{TBR}} + \alpha^{\mathrm{rad}}. \tag{5.3}$$

Here, α^{SRR} is the recombination rate for SSR, α^{TBR} is the production rate for a three-body reaction, and α^{rad} is the production rate due to collision-radiative recombination. The expected density of produced antihydrogen atoms $\rho_{\bar{\mathrm{H}}}$ per second is therefore [MK69]

$$\frac{\mathrm{d}\rho_{\bar{\mathrm{H}}}}{\mathrm{d}t} = \alpha \rho_e \rho_{\bar{\mathrm{p}}}, \tag{5.4}$$

if we ignore the antihydrogen atoms in excited states which ionize right after their production. This leads to a total number of expected antihydrogen atoms $N_{\bar{\mathrm{H}}}$ per second given by

$$\frac{\mathrm{d}N_{\bar{\mathrm{H}}}}{\mathrm{d}t} = \alpha \rho_e N_{\bar{\mathrm{p}}}, \tag{5.5}$$

with $N_{\bar{\mathrm{p}}}$ being the number of antiprotons injected in the trap. The three components of the production rate show different dependencies on the temperature T_e of the positron plasma. For the spontaneous radiative recombination process [SBD75; MW97]:

$$\alpha^{\mathrm{SRR}} = 4.3 \times 10^{-13} \left(\frac{1\,\mathrm{eV}}{k_{\mathrm{B}} T_e} \right)^{0.63} \mathrm{cm}^3/\mathrm{s}, \tag{5.6}$$

where k_{B} is Boltzmann constant. For the three-body recombination process, we consider the recombination rate obtained by Pohl et al. [PVS08], which builds up on the work of Mansbach and Keck [MK69]:

$$\alpha^{\mathrm{TBR}} = k_{\mathrm{TBR}} \rho_e \left(\frac{1\,\mathrm{eV}}{k_{\mathrm{B}} T_e} \right)^{\frac{9}{2}}, \tag{5.7}$$

where $k_{\mathrm{TBR}} = 1.42 \times 10^{-27}\,\mathrm{cm}^6/\mathrm{s}$. This equation gives a valid approximation of the production rate if we assume that all Rydberg states with

binding energy $E_n < k_B T$ are destroyed again by collisions inside the plasma and if no magnetic field is considered [MW97]. In case of production of antihydrogen in strong magnetic fields, the actual recombination rate is reduced by at least one order of magnitude [GO91; Rad+14]. For the collisional-radiative recombination [SBD75]:

$$\alpha^{\mathrm{rad}} = [8.3 \times 10^{-18}\,\mathrm{cm}^3/\mathrm{s}] \left(\frac{\rho_e}{1\,\mathrm{cm}^3}\right)^{0.37} \left(\frac{1\,\mathrm{eV}}{k_B T_e}\right)^{2.18}. \tag{5.8}$$

In Fig. 5.1 we can see the evolution of the different production rates as a function of T_e for a typical positron density $\rho_e = 10^7\,\mathrm{cm}^{-3}$. The figure shows that for temperatures below 100 K, the three body recombination process is the leading reaction for antihydrogen production, with collisional-radiative recombination becoming more prominent as the temperature increases. Notice that the three body recombination process strongly favors high-excited Rydberg states: the work of Pajek and Schuch [PS97] shows that, if we consider a uniform velocity distribution, the partial production rate α_n^{TBR} for (anti)hydrogen with principal quantum number n is proportional to n^6, up to the limit where $E_n \simeq k_B T$. Thus, an imbalance towards high-excited Rydberg states is expected.

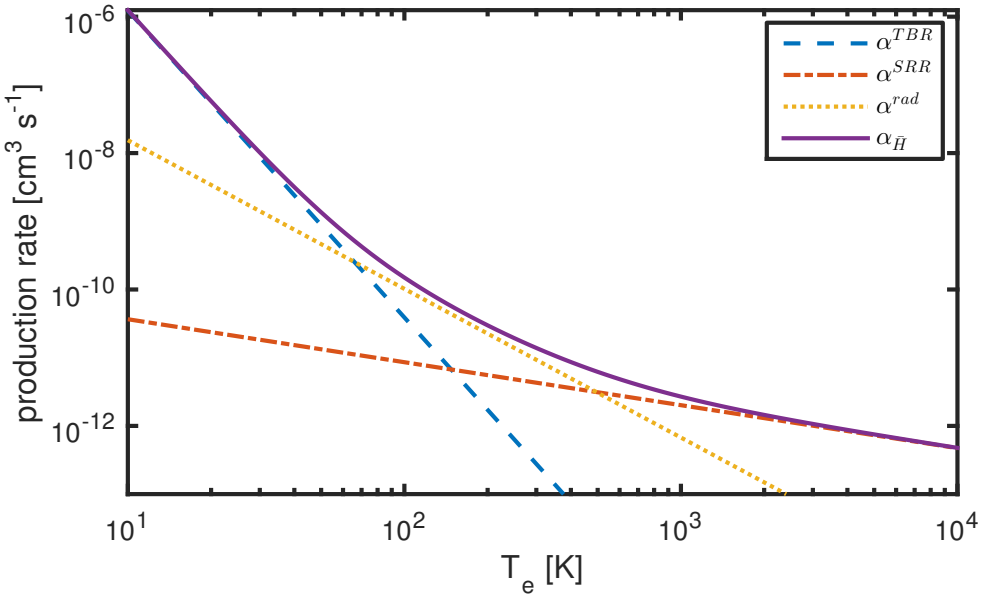

Figure 5.1: Antihydrogen production rate for the different production channels described in Eqs. (5.6), (5.7), and (5.8) as a function of the positron cloud temperature T_e, with positron density $\rho_e = 10^7\,\mathrm{cm}^{-3}$. Notice that for temperatures below 100 K, the three body recombination process becomes the dominant one, while the spontaneous recombination becomes negligible by several orders of magnitude.

5.2.2 Experimental results

The ATHENA collaboration [Amo+04a] and, subsequently, the ALPHA collaboration [Amo+14] realized a series of experiments with antihydrogen produced via direct mixing, providing experimental numbers for the production rate and its dependency on the temperature. The ATHENA collaboration used a nested Penning trap design with electrodes cooled at 15 K in thermal equilibirum with a plasma of around 7×10^7 positrons ($\rho_e = 1.7 \times 10^8\,\mathrm{cm}^{-3}$) [Amo+04b]. A cloud of about 10^4 antiprotons with an average energy of 30 eV was then injected into the trap, allowing for three minutes of continuous interaction. As shown in Fig. 5.1, the dominant process in this configuration is the three body recombination, even considering the reduction due to the presence of a magnetic field of several tesla. The collaboration reported a production rate of around 2500 antiatoms per production cycle (around 450 s) [Amo+04a]. The velocity distribution was however found to be non-uniform, with an equivalent axial temperature $T_\parallel$ one order of magnitude bigger than the transversal temperature $T_\perp$ ($T_\parallel = 150\,\mathrm{K}$, $T_\perp = 15\,\mathrm{K}$) [Mad+05]. With these parameters, the intrinsic divergence of the particle source $\alpha = \sqrt{T_\perp / T_\parallel}$ was of the order of $300\,\mathrm{mm\,m}^{-1}$, which means that after a path of one meter the beam would expand to a diameter of around 60 cm. The subsequent analysis performed by Fujiwara et al. [Fuj+08] showed that the dependency of the production rate on the temperature of the positron cloud was not compatible with Eq. (5.7): the production rate was found proportional to $T_e^{1.1\pm0.5}$ instead of the expected $T_e^{4.5}$. This difference is to be imputed to the fact that antiprotons and positrons are not in thermal equilibrium during the production process [Mad+05], resulting in a non-isotropic temperature distribution, and the fact that Eq. (5.7) has been derived in the hypothesis of infinite positron plasma [Fuj+08], which is not compatible with the experimental data. Further simulations by Radics et al. [Rad+14] seem to underline the fact that the shape and initial conditions of the positron plasma are strongly affecting the scaling of the production rate. These calculations predict a weaker dependence on the temperature than the one from Eq. (5.7), which is at least qualitatively consistent with the measurements from ATHENA.

The ALPHA collaboration reported instead that the temperature of their positron cloud reached 71 ± 10 K despite the electrodes being cooled down to about 7.5 K, which increased to 194 ± 23 K when the antiprotons were injected inside the trap [And+11]. Antiprotons and positrons were then in thermal equilibrium, resulting in an isotropic production of antihydrogen during a 1 s mixing process. With around 7×10^6 positrons ($\rho_e = 7 \times 10^7\,\mathrm{cm}^{-3}$) and 4.5×10^4 trapped antiprotons, the experiment yielded on average around 2000 antihydrogen antiatoms per production cycle, with a cycle lasting more than two AD shots [Amo+14].

Notice that in both experiments, the production of antiatoms is a

continuous process which lasts as long as the two particle species interact with each other, making it difficult to assign a precise time-of-flight to every particle detected. This aspect plays an important role when designing a measurement device for measuring forces acting on the system.

5.2.3 Assumptions for the subsequent evaluation

Combining the theoretical background from Sec. 5.2.1 with the experimental numbers of Sec. 5.2.2, we can setup a realistic scenario for a gravity measurement on antihydrogen by using direct mixing. In the following, we consider an average length of four full AD cycles (400 s), allowing for the stacking of two antiproton bunches and leaving three minutes for cooling and mixing operations. Since the ALPHA production schematic, which yields 2000 $\bar{\mathrm{H}}$/cycle with $T_{\parallel} = T_{\perp} = 200\,\mathrm{K}$, produces antihydrogen at both higher temperature, in smaller numbers and in a uniform distribution, we can consider it worse than the ATHENA production schematic in every aspect for our discussion. For the subsequent evaluation, we therefore consider only the ATHENA experiment, which yields 2500 $\bar{\mathrm{H}}$/cycle with $T_{\parallel} = 150\,\mathrm{K}$ and $T_{\perp} = 15\,\mathrm{K}$.

5.3 Charge exchange

Another strategy to produce antihydrogen is the so-called *charge exchange* mechanism between antiprotons and positronium (Ps), a bound state between an electron and a positron. This method has been successfully employed by the ATRAP collaboration in 2004 to produce antihydrogen [Sto+04] and it is planned to be used by the AE$\bar{\mathrm{g}}$IS collaboration as its primary mean to get cold antiatoms [Dro+07]. This section details some properties of the positronium atom before presenting an introduction to the charge exchange production mechanism.

5.3.1 Positronium

Positronium is a bound state between a positron (e^+) and an electron (e^-). Its existence was predicted in 1934 [Moh34], where it was labeled as "electrum", and was experimentally verified for the first time in 1951 [Deu51]. For all intents and purposes, positronium can be described using the Hamiltonian of a hydrogen atom, by considering a reduced mass $\mu = m_e/2$, with $m_e = 9.11 \times 10^{-31}\,\mathrm{kg}$. As hydrogen, positronium can assume two different spin configurations S in its ground state: the triplet state $S = 1$, also known as ortho-positronium (o-Ps) and the singlet state $S = 0$, also known as para-positronium (p-Ps). Due to the fact that this exotic atom is composed by a particle and its antiparticle, it is inherently unstable and incurs into annihilation in a short period of

time. Ortho-positronium decays into an odd number of photons, with annihilation in three photons being the leading channel, with an average lifetime [Kar04]

$$t_{\text{o-Ps}} = \frac{1}{\Gamma_{3\gamma}} = \frac{9\pi}{2(\pi^2 - 9)} \frac{\hbar}{m_e c^2} \alpha^6 = 142\,\text{ns}, \tag{5.9}$$

where $\alpha = 1/137$ is the fine structure constant and $\Gamma_{3\gamma}$ is the decay rate. Para-positronium decays in an even number of photons, with two photons being the main channel, with an average lifetime [Kar04]

$$t_{\text{p-Ps}} = \frac{1}{\Gamma_{2\gamma}} = \frac{2\hbar}{m_e c^2} \alpha^5 = 125\,\text{ps}, \tag{5.10}$$

where $\Gamma_{2\gamma}$ is the decay rate. It is interesting to point out that the $2s$ state of the positronium is metastable with a lifetime of 1.1 µs, a factor eight longer than the o-Ps lifetime [Coo+15].

5.3.2 Theoretical background

Charge exchange is a production process for antihydrogen which originates from the interaction between an antiproton $\bar{\text{p}}$ and a positronium atom Ps. Introduced for the first time by Deutch et al. in 1986 [Deu+86], the reaction which leads to the formation of antihydrogen is the following:

$$\bar{\text{p}} \; + \; \text{Ps} \longrightarrow \bar{\text{H}} \; + \; e^- . \tag{5.11}$$

Quantum mechanics calculations by Kadyrov et al. [Kad+15] and Rawlins et al. [Raw+16] based on the two-center convergent close-coupling method [KB02] have shown that for a positronium principal quantum number $n_{\text{Ps}} \leq 3$, the cross section of this reaction scales with a n_{Ps}^4 power law. A simulation by Krasnický et al. [Kra+16], using a classical trajectory Monte Carlo (CTMC) method, has expanded this result for higher principal quantum numbers ($3 < n_{\text{Ps}} \leq 50$), finding the same behavior as the previous works. The simulation shows that the n_{Ps}^4 power law is valid only in absence of magnetic fields. Moreover, the cross section of the reaction is a function of the ratio k_v between the velocity of the center of mass v_{cm} of the positronium and the classical orbital velocity of the positron in the Ps atom. In a field-free environment, for $k_v < 0.3$, the cross section is proportional to a $1/E_{\text{cm}}^{\text{Ps}}$, with $E_{\text{cm}}^{\text{Ps}}$ being the center-of-mass energy of the positronium. From these considerations, one could argue that in order to increase the production rate of antihydrogen, it is desirable to obtain highly excited Rydberg positronium ($n_{\text{Ps}} \gg 1$) with a low average velocity (low temperature). Thus the reaction to consider is

$$\bar{\text{p}} \; + \; \text{Ps}^* \longrightarrow \bar{\text{H}}^* \; + \; e^- , \tag{5.12}$$

with both the original positronium and the antihydrogen atom in an excited state with principal quantum numbers n_{Ps} and $n_{\bar{\mathrm{H}}}$ respectively. Notice that together with the aforementioned charge exchange interaction, there are other reaction channels which result in simple scattering between the positronium and the antiprotons, with no antihydrogen formation. Among these, we find the following reactions:

$$\begin{aligned} \bar{\mathrm{p}} \ + \ \mathrm{Ps}^*(n,l,m) &\longrightarrow \bar{\mathrm{p}} \ + \ \mathrm{Ps}^*(n,l,m) \\ \bar{\mathrm{p}} \ + \ \mathrm{Ps}^*(n,l,m) &\longrightarrow \bar{\mathrm{p}} \ + \ \mathrm{Ps}^*(n',l',m') \\ \bar{\mathrm{p}} \ + \ \mathrm{Ps}^*(n,l,m) &\longrightarrow \bar{\mathrm{p}} \ + \ e^+ \ + \ e^-, \end{aligned} \tag{5.13}$$

where n, l, and m are the quantum numbers of the positronium atom [Kra+16]. These reactions have to be separately considered in order to determine the proper reaction rate and any realistic simulation has to include these effects. Provided that no channel is neglected, in the region in which the cross section scales as $1/E_{\mathrm{cm}}^{\mathrm{Ps}}$, the distribution of $n_{\bar{\mathrm{H}}}$ is strictly dependent on n_{Ps}: the simulations performed by Krasnický et al. [Kra+16] show that $n_{\bar{\mathrm{H}}}$ has an asymmetric distribution peaked on $n_0 = \sqrt{2}n_{\mathrm{Ps}}$, with a tail for $n_{\bar{\mathrm{H}}} < n_0$ and a small spread (Fig. 5.2). The presence of magnetic fields reduces the cross section of the production process for every k_v below a specific threshold value k_v^x, which depends on the magnetic field. For a magnetic field $B < 1\,\mathrm{T}$ and $n_{\mathrm{Ps}} < 18$, the effect of the fields on the cross section are deemed tolerable [Kra+16]. Notice that due to the lack of experimental data, there is no consensus on the actual dependence of the cross section on the quantum numbers of the positronium: a subsequent quantum calculation by Kadyrov et al. [Kad+17] argued that for $n_{\mathrm{Ps}} > 3$ the formation of antihydrogen via charge exchange is suppressed and evolves instead with a power law n_{Ps}^2. The n_{Ps} power law relation should still hold if the kinetic energy of the positronium is such that its de Broglie wavelength is smaller than its size ($T_{\mathrm{Ps}} > 20\,\mathrm{K}$), such that the quantum effects are shadowed by the classical interactions [Com17]. This poses however a limit on the cooling of positronium atoms, requiring a balance between temperature and effective cross section. However, it must be noted that this process is expected to yield antihydrogen with the same velocity distribution as the underlying antiprotons, meaning that the temperature of the antiproton cloud would determine the temperature of the produced antiatoms without barely any influence from the positronium [Kra+16; Sto+04].

5.3.3 Experimental results

As of the publication date of this thesis, the charge exchange process has been successfully applied to protons to form hydrogen by Merrison et al. in 1997 [Mer+97] and to antiprotons in a two-step approach by the ATRAP collaboration in 2004 [Sto+04]. We analyze the latter, as

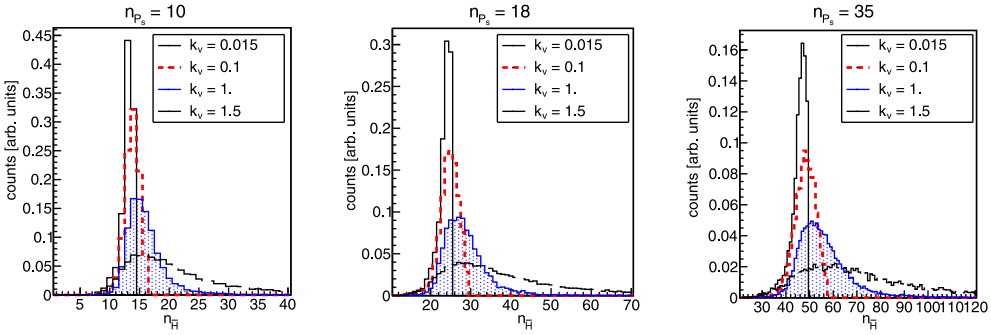

Figure 5.2: Normalized distribution of the principal quantum number $n_{\bar{\mathrm{H}}}$ of the antihydrogen produced via charge exchange as a function of the principal quantum number n_{Ps} of the positronium, for different values of the ratio k_v between the velocity of the center of mass v_{cm} and the classical orbital velocity of the positron in the Ps atom. Reprinted figure with permission from [Kra+16]. Copyright 2018 by the American Physical Society.

it was carried out in physical conditions which can be compared to the ones with which ALPHA and ATHENA achieved direct mixing, as seen in Sec. 5.2.2. In order to get excited positronium to increase the charge exchange cross section, the ATRAP collaboration took advantage of two consecutive interactions, as envisioned by Hessels et al. in 1998 [HHC98]:

$$\mathrm{Cs}^* \ + \ e^+ \longrightarrow \mathrm{Ps}^* \ + \ \mathrm{Cs}^+ \tag{5.14}$$

$$\bar{\mathrm{p}} \ + \ \mathrm{Ps}^* \longrightarrow \bar{\mathrm{H}}^* \ + \ e^-. \tag{5.15}$$

The cesium atoms were laser excited up to $n = 37$ and were subsequently injected into the positron trap, interacting with a positron plasma and made interacting for around 100 s. Typically, around 8×10^5 excited cesium atoms were sent through 1.4×10^6 positrons cooled at 4.2 K, with a conversion efficiency of around 25 % of the trapped positrons [Spe+04]. The production peak was reached after 35 s of interaction, after an exponential growth [Sto+04; Spe+04]. The produced positronium was then made interact with 2.4×10^5 antiprotons accumulated in the span of around 1800 s [Gab+02], yielding between 100 and 200 produced antihydrogen atoms at around 4 K, assuming an isotropic distribution. For a quick estimation, this can be schematized as a source with $T_{\parallel} = T_{\perp}$, which would yield a divergence of around 1000 mm m^{-1}, even bigger than for the ATHENA production schematic. This number is expected to increase with the number of antiprotons and positrons [Sto+04]. In 2016, McConnell et al. published an improved positronium production scheme which provides a 100 % positron-to-positronium conversion and would increase the antihydrogen production rate by up to a factor 500 [McC+16]. In an optimistic scenario, this would result in up to 10^5 antihydrogen

atoms for production cycle at a temperature of 1.2 K, which constitutes a huge improvement on the state-of-the-art numbers.

5.3.4 Assumptions for the subsequent evaluation

In the following, we consider three separate charge exchange scenarios: the experimental result from ATRAP, the theoretical improvement pointed out by [McC+16], and an estimated scenario for the AEgIS experiment. For the ATRAP scenario, we used the numbers from the original paper of 2004, as they were experimentally achieved. The improvement in the quantity of available positronium is considered as a simple multiplicative factor on its original statistics. For both configurations (experiment and theoretical boost), we fix the antihydrogen temperature to 4 K, which has been experimentally reached by the collaboration.

Since this work has been developed in the framework of the AEgIS collaboration, despite the lack of experimental data, we use a theoretical scenario based on the thesis of Caravita [Car17], which depicts the current status and achievements of the experiment. The AEgIS experiment managed to trap and cool 1.8×10^5 antiprotons by stacking three AD shots in a cloud of about 200 mm^3. Considering 3×10^7 positronium atoms and the cross section from [Kra+16], an optimistic expectation for numbers of produced antihydrogen is around 40 antihydrogen atoms per 500 s production cycle for the lowest achieved positronium temperature [Car17; Car18]. The measured antiproton temperature is of the order of some tens of kelvin. In the following, we assume a test temperature of 20 K. Results can be scaled accordingly with relative ease.

5.4 Comparison of the considered parameters

In the following we apply the calculations for a gravity measurement on the test conditions underlined in Sec. 5.2.3 and 5.3.4, analyzing them separately. Table 5.1 acts as a summary of the scenarios outlined in the previous sections and is used as a reference throughout the calculations.

5.5 Measurement principle

As we discussed in Chapter 2, the outcome of a force field measurement using a Talbot-Lau interferometer has an intrinsic lower bound to its sensitivity, in the form of a minimum detectable acceleration a_{min} expressed by Eq. (2.35), which we rewrite here for the sake of clarity:

$$a_{\mathrm{min}} = \frac{d}{2\pi C \tau^2 \sqrt{N_{\mathrm{det}}}} \tag{5.16}$$

Production type	$\bar{\text{H}}$/ cycle	cycle [s]	$T_{\parallel}$ [K]	$T_{\perp}$ [K]
Direct mixing A (ATHENA)	2500	400	150	15
Direct mixing B (ALPHA)	2000	400	200	200
Charge exchange A (ATRAP)	200	1800	4	4
Charge exchange B (ATRAP)	100000	1800	4	4
Charge exchange C (AE$\bar{\text{g}}$IS)	40	500	20	20

Production type	cycles/day	$\bar{\text{H}}$/day
Direct mixing A (ATHENA)	72	1.8×10^4
Direct mixing B (ALPHA)	72	1.44×10^4
Charge exchange A (ATRAP)	16	3.2×10^3
Charge exchange B (ATRAP)	16	1.6×10^6
Charge exchange C (AE$\bar{\text{g}}$IS)	58	2.32×10^3

Table 5.1: A summary of the five production scenarios analyzed. The last two entries in the tables (Charge Exchange B and C) are theoretical scenarios based on simulations and experimental numbers for positronium atoms and antiprotons. A "day" is defined here as a 8-hour shift, in compliance with the Antiproton Decelerator schedule.

where d is the periodicity of the gratings, C is the contrast of the pattern - which depends on the energy of the particles, N_{det} is the number of particles which reach the detector and τ is the time of flight between the gratings when considering a force which doesn't affect the axial velocity of the particle. In order to put a lower boundary on the precision of the measurement, we need to provide numbers for all these quantities. From Chapter 4, we know that if the source is not monoenergetic, the resulting contrast is heavily dependent on the shape of the distribution, which is in turn dependent on the parameters of the source. This is also true for the number of detected particles N_{det}, which is dependent on both the source and the geometry of the interferometer. A more precise formula which would take into account all these parameters reads

$$a_{\min} = \frac{d}{2\pi C L^2 \sqrt{\eta^3 N_{\text{prod}}}} \int_{v_{\parallel}=0}^{\infty} f(u) u^2 du, \tag{5.17}$$

where L is the distance between the gratings, $v_{\parallel}$ is the axial velocity of the particles, $f(v_{\parallel})$ is the axial velocity distribution, η is the open fraction of the gratings and N_{prod} is the number of produced particles. Notice that $f(v_{\parallel})$ depends on the geometrical acceptance of the device and must be used needed to obtain N_{det} from N_{prod}, while C is not constant and depends in a non trivial way on the geometry of the interferometer and on the shape of velocity distribution of the particles. In the following, we develop a numerical model to fill the blanks in Eq. (5.17). The first part deals with the parameters of the source, while the second considers the

geometry of the interferometer. The results of both parts are combined in order to produce a realistic estimation of the measurement time required as a function of the desired measurement precision.

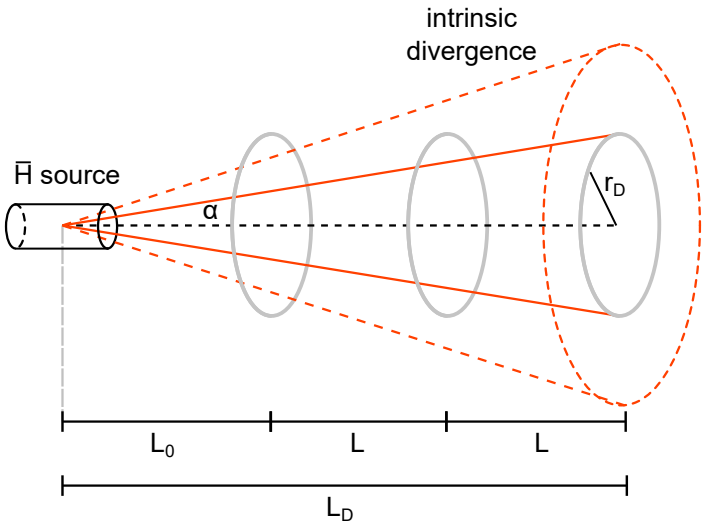

Figure 5.3: Schematic of the experimental procedure: antihydrogen $\bar{\mathrm{H}}$ is produced inside a Penning trap and then sent through the interferometer. The distance between the source point and the first grating is marked as L_0, while the distance between the elements of the interferometer is equal to L. The detector radius r_D determines the angular acceptance and thus the maximum accepted divergence $\alpha = r_D/L_D$ which still lets particles reach the detector.

5.6 Details of the numerical model

Given a circular particle detector with radius r_D and detection efficiency η_D placed at a distance L_D from the particle source, as schematized in Fig. 5.3, the fraction of particles which get detected is dependent on the solid angle $\Omega_D = \pi r_D^2/L_D^2$. If we consider a divergent, monochromatic particle source, this geometrical efficiency is quickly calculated as

$$N_{\mathrm{det}} = \frac{\Omega_D}{4\pi} N_{\mathrm{prod}}. \tag{5.18}$$

This is not generally true, as when it comes down to a more complex velocity distribution an integration is required to retrieve the fraction of particles effectively reaching the detector as a function of the axial velocity $v_\parallel$. Given a velocity distribution $f_\perp(v_\perp)$ such that $\int_{-\infty}^{\infty} f_\perp(u)du = 1$,

$v_\perp$ being the transverse velocity, the probability $P(v_\parallel)$ that a particle with axial velocity $v_\parallel$ reaches the detector is given by

$$P(v_\parallel) = \int_{-v_\perp^{\max}}^{v_\perp^{\max}} f_\perp(u)du \leq 1, \tag{5.19}$$

where $v_\perp^{\max}$ is the maximum transverse velocity which allows a particle with axial velocity $v_\parallel$ to reach the detector:

$$v_\perp^{\max} = v_\parallel \frac{r_D}{L_D}. \tag{5.20}$$

Given a distribution of axial velocities $g_\parallel(v_\parallel)$, such that $\int_{-\infty}^{\infty} g_\parallel(u)du = 1$, the total fraction of particles reaching the detector is then given by:

$$\left(\frac{N_{\text{det}}}{N_{\text{prod}}}\right)_{\text{geom}} = \int_0^\infty g_\parallel(u)P(u)du, \tag{5.21}$$

where the integration is performed for $v_\parallel \geq 0$ in order to exclude particles which travel in the direction opposite to the detector. In order to get the real number of detected particles, this number has to be multiplied by the efficiency of the detector η_D and the transmission coefficient of the interferometer, which is the product of the open fraction η of the single gratings, yielding an additional factor η^3. Taking this into account, we proceed to write the fraction of detected particles as

$$\frac{N_{\text{det}}}{N_{\text{prod}}} = \eta_D\ \eta^3 \left(\frac{N_{\text{det}}}{N_{\text{prod}}}\right)_{\text{geom}} \tag{5.22}$$

Equation (5.19) and (5.22) are central to the following discussion. In Chapter 2 we discussed how the signal of a Talbot-Lau interferometer depends on the kinetic energy of the incoming particles, such that particles with different velocities generate different patterns. The de Broglie wavelength λ_{dB} depends on the kinetic energy of the particles, and therefore on $v_{\text{tot}} = \sqrt{v_\parallel^2 + v_\perp^2}$. The resulting signal $S_{v\parallel}(y)$ associated with the axial velocity $v_\parallel$ has thus to be integrated over the distribution of transverse velocities, by modifying Eq. (5.19):

$$S_{v\parallel}(y) = \int_{-v_\perp^{\max}}^{v_\perp^{\max}} f_\perp(u)S(y; \sqrt{v_\parallel^2 + u^2})du, \tag{5.23}$$

where $S(y; v)$ is the pattern generated by particles with total velocity v. This leads to a resulting signal $S(y)$ which is obtained by integrating $S_{v\parallel}(y)$ over $g_\parallel(u)$, in a similar fashion to Eq. (5.21), thus obtaining [Brä+15]

$$S(y) = \int_0^\infty g_\parallel(u)S_u(y)du. \tag{5.24}$$

The contrast C of the signal is therefore calculated as

$$C = \frac{\max(S(y)) - \min(S(y))}{\max(S(y)) - \min(S(y))}. \tag{5.25}$$

This expression, albeit being correct for the situation considered, is computationally expensive: the signal of the interferometer has to be numerically calculated for every possible total velocity, leading to long computation times when implemented in a computer program. It is therefore reasonable to look for a valid simplification in order to speed up the calculations. In the approximation $v_\perp^{\max} \ll v_\parallel$, we have that

$$v_{\text{tot}} \simeq v_\parallel + \frac{v_\perp^{\max 2}}{2v_\parallel} = v_\parallel \left(1 + \frac{r_D^2}{2L_D^2}\right), \tag{5.26}$$

which is obtained by using Eq. (5.20). If we consider relatively small angular acceptances, such that $r_D^2 \ll L_D^2$ (paraxial approximation), we can assume that $S(y; \sqrt{v_\parallel^2 + u^2})$ in Eq. (5.23) is independent on the transverse velocity and take it out of the integral as a constant. Therefore, we can write an approximated equation for $S(y)$ that is easier to compute numerically. This approximation reads:

$$S(y) \simeq \int_0^\infty g_\parallel(u) P(u) S(y; u) du, \tag{5.27}$$

where u is now the axial velocity of the particles.

Due to the numeric approach used in Chapter 2 for determining the signal of the Talbot-Lau interferometer, we elect to perform again a numerical calculation of the expected interferometric signal, discretizing Eq. (5.24) by sampling both $g_\parallel(u)$ and $f_\perp(u)$ with a finite number of points. The resulting discretized sum reads

$$S(y) \simeq \sum_{i=0}^{n} g_\parallel(u_i) P(u_i) S(y; u_i) \Delta u, \tag{5.28}$$

with Δu being the velocity interval used for the sampling and n the number of points considered. An analogous operation is performed to calculate $P(u_i)$. Considering cylindrical symmetry, we can consider $f_\perp(u)$ and $g_\parallel(u)$ to be thermal distribution, in accordance to the physical properties of the produced antihydrogen. Thus, we use a Maxwell-Boltzmann 1-dimensional distribution for $g_\parallel(u)$ and a 2-dimensional Maxwell-Boltzmann distribution for $f_\perp(u)$, to take into account the possibility of having different radial and axial temperatures (as it was for example found in the ATHENA experiment - see Sec. 5.2.2). Now we have all the tools to determine the expected signal and efficiency of a measurement, given the geometrical parameters of the detector and the gratings.

5.7 Velocity distributions

In the previous section, we discussed how to calculate the interferometric signal given arbitrary distributions for the axial and the transverse component of the velocity. From Sec. 5.1, we conclude that a thermal distribution is a reasonable candidate for both the transverse and axial velocity profile. In particular, for the axial distribution $g_{\parallel}(v)$ we assume a one-dimensional Maxwell-Boltzmann distribution, given by

$$g_{\parallel}(v) = \sqrt{\frac{m}{2\pi k_{\mathrm{B}} T}} e^{-\frac{mv^2}{2k_{\mathrm{B}}T}}, \tag{5.29}$$

with m being the mass of antihydrogen, k_{B} being the Boltzmann constant and T the temperature of the antihydrogen cloud in kelvin. For the transverse distribution $f_{\perp}(v)$, we consider instead a two dimensional Maxwell-Boltzmann speed distribution, given by

$$f_{\perp}(v) = \frac{mv}{2\pi k_{\mathrm{B}} T} e^{-\frac{mv^2}{2k_{\mathrm{B}}T}}. \tag{5.30}$$

We use the data from Tab. 5.1 to assign values to both average temperatures, according to the configuration which is simulated. These distributions are depicted in Fig. 5.4 for the parameters of the ATHENA experiment, summarized in the aforementioned table. Once $g_{\parallel}(v)$ and $f_{\perp}(v)$ are fixed, the signal $S(y)$ from Eq. (5.28) is completely determined, as it is its contrast C. Notice that the mean velocity of the particle reaching the detector can in principle only be estimated once we know the geometrical parameters of the detector, since these will cut out a significant part of the produced particles, skewing the distribution in favor of faster antiatoms. This effect is shown in Fig. 5.5. We also see in Fig. 5.7 that, when considering a ratio $0.01 \leq r_D/L_D \leq 1$, the mean velocity undergoes a relative variation of only around 4 %, despite being sensibly higher than in the unconstrained case. This means that while the paraxial approximation $r_D/L_D \ll 1$ holds, the velocity variation is not so prominent, and also the shape of the contrast plots does not change significantly, as it is shown in Fig. 5.6. Nevertheless, we perform this calculation for each separate configuration.

As a side note, if we consider different open fractions η and perform calculations for an array of possible choices, we find substantially different results. An example of this effect is shown in Fig. 5.8, where we produce a plot similar to Fig. 5.6 for $\eta = 0.25$, 0.3, 0.35, and 0.4 respectively. For the following discussion, we fix $\eta = 0.3$, as it yields the best sensitivity for detecting phase shifts [Obe+96].

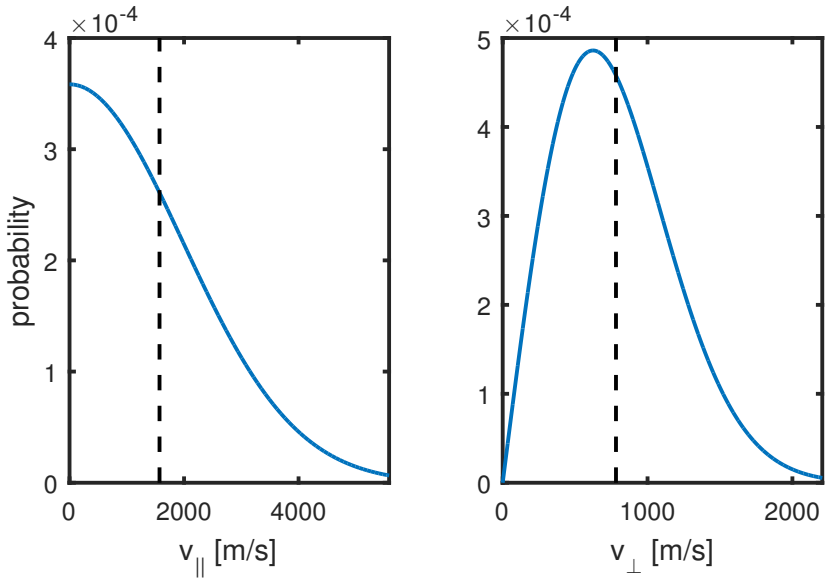

Figure 5.4: Velocity distributions for $T_{\parallel} = 150\,\mathrm{K}$ and $T_{\perp} = 15\,\mathrm{K}$, described respectively by Eqs. (5.29) and (5.30). This is the configuration which corresponds to the ATHENA mixing process, as summarized in Tab. 5.1. The vertical dashed lines mark the mean velocity of the particles for each distribution. Notice that for the axial distribution, only positive values of the velocity are considered, since all particles generated in the negative direction can not hit the detector

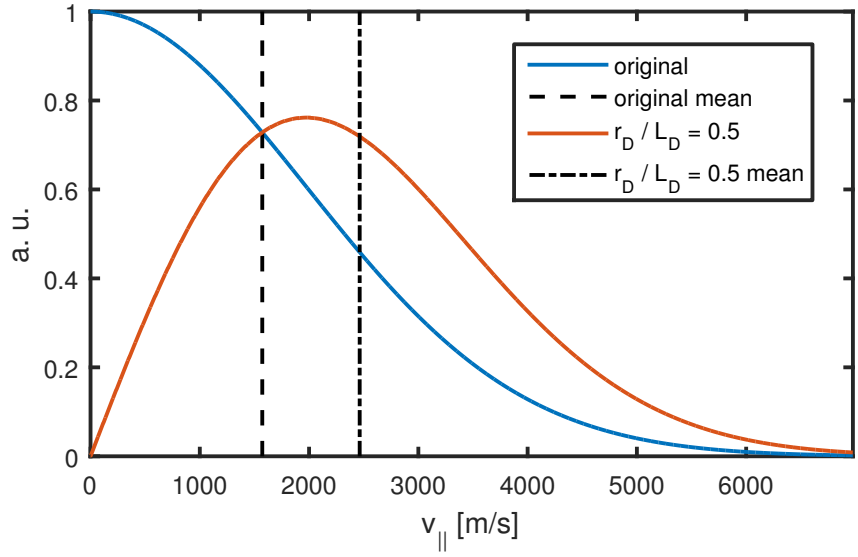

Figure 5.5: Axial velocity distribution with and without geometrical restrictions (arbitrary units). When considering the angular acceptance of the detector, the resulting axial velocity distribution is skewed towards higher velocities, resulting in an increased average (dot-dashed line).

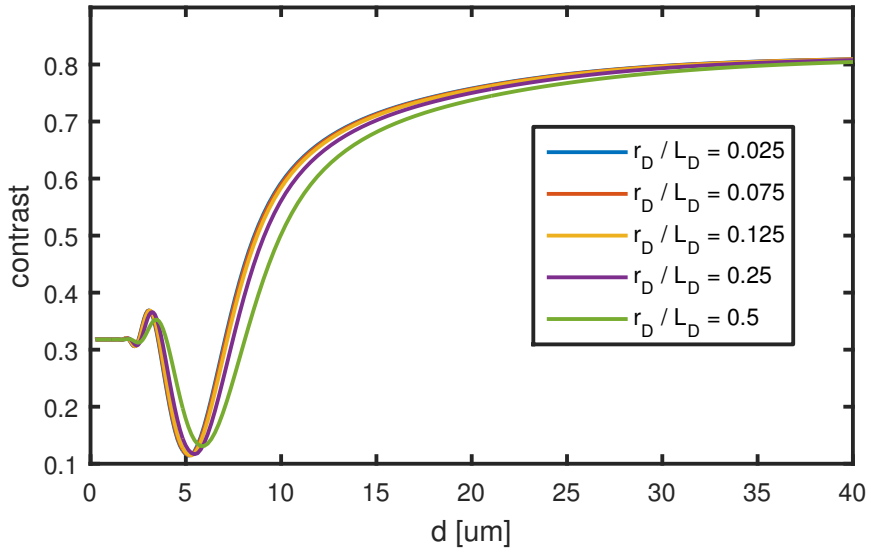

Figure 5.6: Contrast C of the interference pattern obtained using the velocity distribution shown in Fig. 5.5, for $L = 5\,\mathrm{cm}$ and different geometric ratios r_D/L_D. Notice that the profile shifts towards higher grating periods as the geometric ratio becomes bigger. This plot has been obtained by considering an open fraction $\eta = 0.3$.

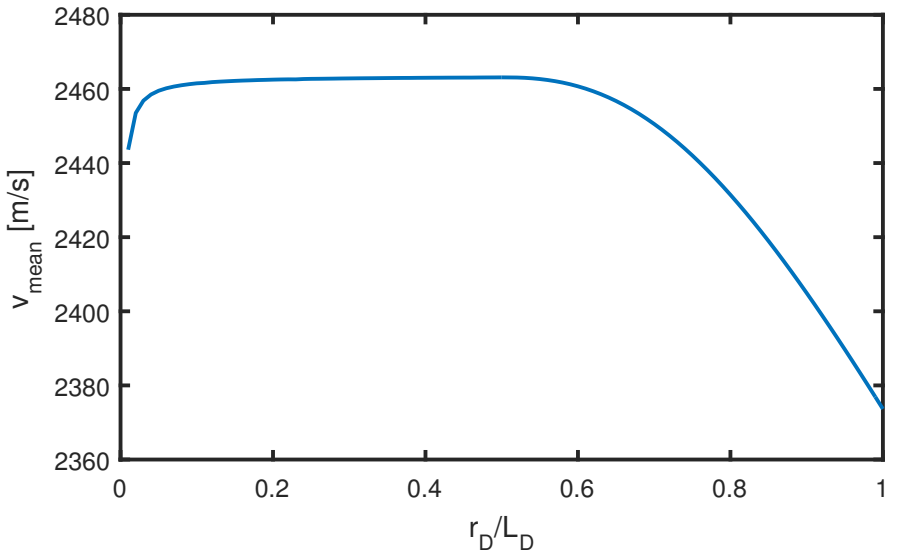

Figure 5.7: Mean axial velocity distribution as a function of the geometrical acceptance r_D/L_D, which defines the maximum transverse velocity allowed to reach the target. Notice that while the average value is higher than in the non-constrained case (see Fig. 5.5), the actual variation is around 4 %. For $r_D/L_D \to \infty$, this velocity is expected to converge to the original mean from the unconstrained distribution.

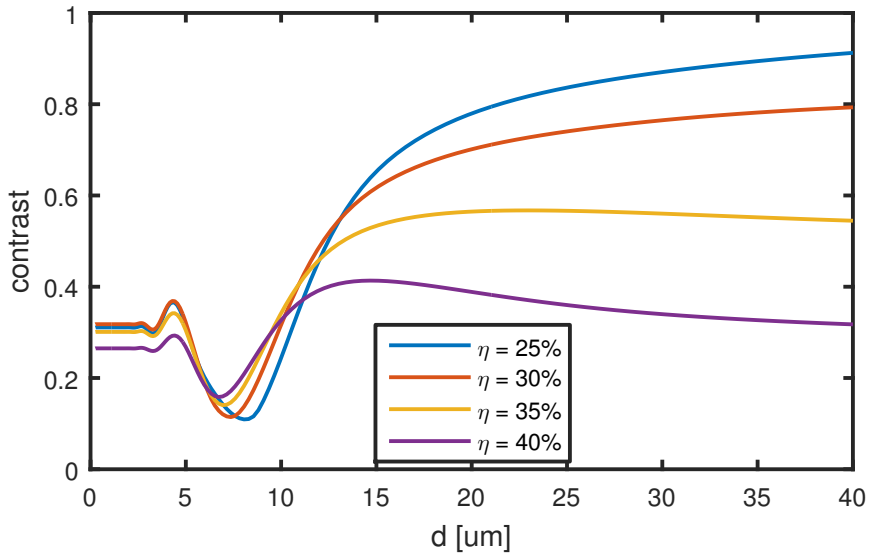

Figure 5.8: Contrast C of the interference pattern obtained using the velocity distribution shown in Fig. 5.5 for different open fractions η. In this plot, a length $L = 10\,\text{cm}$ is considered, with the detector radius r_D adjusted such that we get a fixed geometric ratio $r_D/L_D = 0.06$.

5.8 Constraints on the measurement volume

The choice of geometry for the interferometer is strictly connected to the available space in the target experiment and it is mainly dictated by both theoretical and practical limits: on the one hand, a longer distance L between the gratings induces a bigger phase shift due to the target force, while, on the other hand, makes it more difficult to perform an alignment which is compliant to the limits exposed in Chapter 3. Furthermore, a longer L also means that the particles are exposed for a longer time to spurious interactions, which could cause an additional phase shift or degrade the signal.

5.8.1 Geometrical constraints

A huge geometrical acceptance is a requisite in order to increase the ratio between detected and produced particles, while at the same time putting a stricter limit on the maximum accepted misalignment between the gratings. Moreover, the choice is also subsided to the available region of space where the force due to the gradient of external fields (magnetic and electric in the case of antihydrogen) are smaller than the gravitational interaction.

A typical detector size that one can consider ranges from around 5 to

$40\,\mathrm{cm}^2$, as seen for commercial MCPs [Ham16], which is equivalent to a radius between 1.25 and 8 cm. Another possibility is to build an array of detectors using silicon chip detectors like the $2\,\mathrm{cm}^2$ Timepix3 [Poi+14], in order to overcome detection area limitations, or to make an effective use of scintillators to track down antimatter annihilation stars.

More stringent limitations are due to both the geometry of the antiproton trapping system and the presence of field gradients which could affect the measurement. For the former, if we consider the existing AEgIS apparatus, we have a maximum detector radius $r_D^{\max} = 32.5\,\mathrm{mm}$ and a maximum detector distance $L_D^{\max} = 690\,\mathrm{mm}$ [Brä+15]. For the latter, we consider as a limit the region of space in which the effect of field gradients is sufficiently smaller than gravity. For ground-state antihydrogen, this requirement translates into having a magnetic field with a gradient smaller than $0.2\,\mathrm{G\,cm}^{-1}$ [Dem14a; Dem14b], as discussed in Chapter 4. This value scales proportionally with $1/n$, n being the principal quantum number of the antiatom. Inside the current AEgIS apparatus, the region in which this condition is true for ground-state antihydrogen is restricted to a radius $r_D^{\mathrm{safe}} = 1.5\,\mathrm{mm}$ and a maximum distance $L_D^{\mathrm{safe}} = 10\,\mathrm{cm}$ [Brä+15], which becomes even smaller when considering excited states. These parameters are summarized in Tab. 5.2. Reaching the required magnetic field homogeneity in a future improvement, however, is not out of the realm of possiblities: NMR machines already have magnets with fields above 1 T with the target homogeneity on spherical volumes of around 50 cm of radius [Kel06].

In the following, we ignore the field limitation and we consider $r_D \leq r_D^{\max}$ and the total length of the device $L_D = 2L + L_0 \leq L_D^{\max}$, where L_0 is the distance between the particle source and the first grating.

$L_D^{\max}$	690 mm
L_D^{safe}	100 mm
$r_D^{\max}$	32.5 mm
r_D^{safe}	1.5 mm

Table 5.2: Geometrical parameters of the available experimental region inside the AEgIS apparatus. The parameters labeled with *max* are referred to the maximal geometrical space available for the measurement, while the parameters labeled with *safe* are referred to the size of the region whose magnetic field gradient is such that $a_B \ll g$, where a_B is the acceleration due to the magnetic field gradient on ground-state antihydrogen. Values from the report by Bräunig et al. [Brä+15].

5.8.2 Cut-off velocity

An additional limitation is given by the length L which would cause the particles to have a shift due to the gravitational acceleration $\mathbf{g}$ bigger than the periodicity d of the grating, after which it is not possible to determine its value effectively. For a particle with axial velocity $v_\parallel$, this sets the requirement

$$|\mathbf{g}|\,\tau^2 < d \;\Rightarrow\; |\mathbf{g}|\,\frac{L^2}{v_\parallel^2} < d \tag{5.31}$$

leading to the condition

$$v_\parallel > v_{\mathrm{cut}} \stackrel{!}{=} L\sqrt{\frac{|\mathbf{g}|}{d}}. \tag{5.32}$$

This equation lets us define a cut-off velocity v_{cut} below which the phase shift of the pattern is too extensive to extract information and just contributes to the background. Fig. 5.9 shows this formula applied to a sample configuration, while Fig. 5.10 shows the dependence of v_{cut} on the periodicity d and the distance L between the gratings.

The particles for which $v_\parallel$ does not fulfill Eq. (5.31) do not contribute to the signal, creating a background which severely decreases the contrast of the overall signal (see Fig. 5.11).

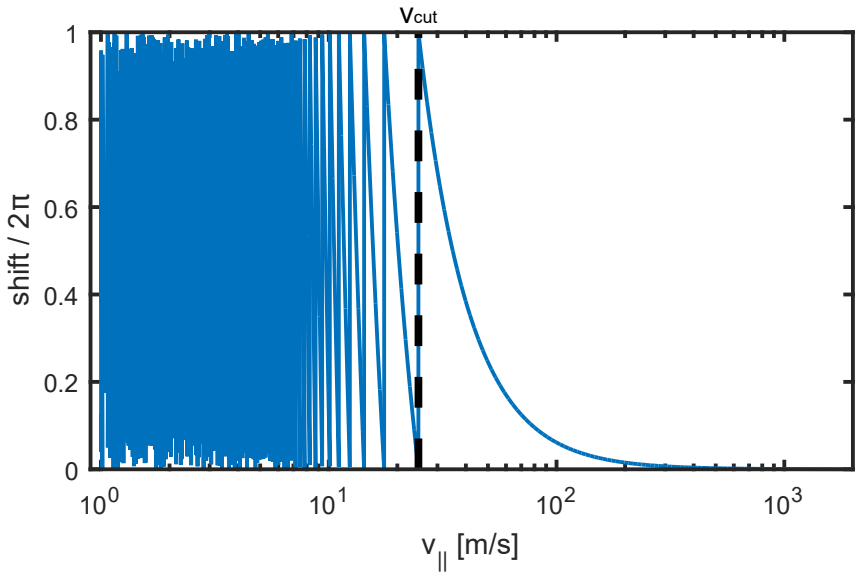

Figure 5.9: Phase shift as a function of velocity for $L = 5\,\mathrm{cm}$ and $d = 40\,\mu\mathrm{m}$, considering the gravitational acceleration $g = 9.81\,\mathrm{m\,s^{-1}}$. The vertical dashed line indicates the cut-off velocity v_{cut} below which the phase shift is bigger than the periodicity d of the gratings.

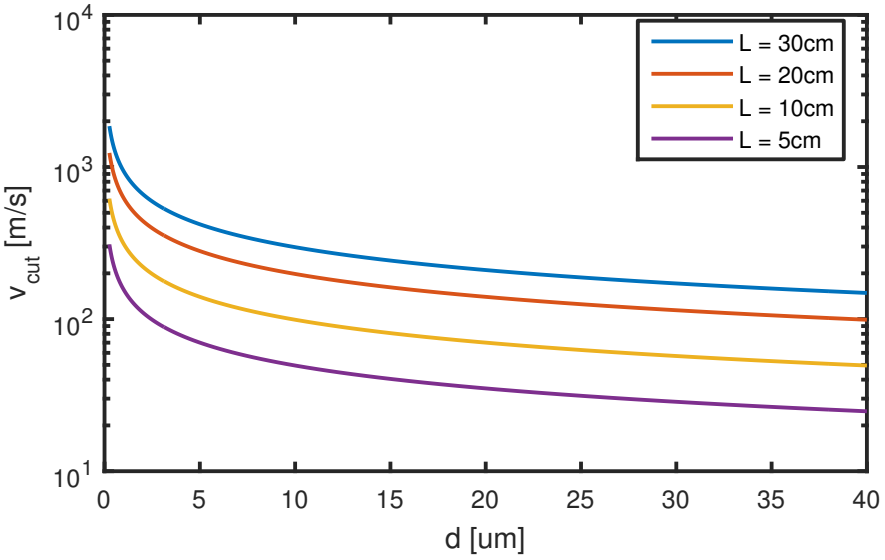

Figure 5.10: Cut-off velocity v_{cut} as a function of d and L. For $v_{\parallel} < v_{\text{cut}}$, the phase shift due to the action of gravitational acceleration is bigger than one grating period, thus generating a background for the measurement.

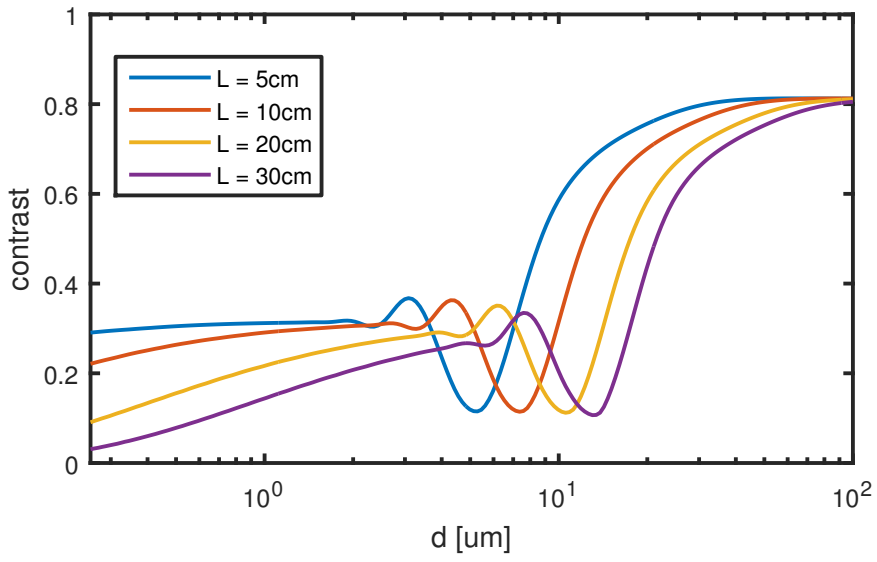

Figure 5.11: Contrast C of the interference pattern for $\eta = 0.3$ in presence of a gravitational acceleration for $T_{\parallel} = 150\,\text{K}$. Changing the length of the device causes a drop in visibility due to the patterns of the slower particles overlapping.

5.8.3 Summary of the constraints and design decisions

By considering all the above points, we decide to follow some general guidelines:

- *open fraction* - we choose an open fraction $\eta = 0.3$, which is the one which guarantees the best sensitivity as a function of the number of particles detected [Obe+96];
- *periodicity of the gratings* - if we want to have an energy-independent, robust measurement tool which has a limited dependence on the geometrical acceptance of the detector (see Fig. 5.6), we could decide to aim for having a visibility near to the classical result. This advocates in favor of choosing $d \geq 20\,\mu m$, which would be a safe assumption for a consistent part of the considered grating distances L, as shown in Fig. 5.11. In spite of this, there is also the possibility to make a case by case decision and go for the smallest possible grating periodicity which grants at least a 20 % contrast, in order to have a pattern which can be clearly reconstructed. In the following we use this second assumption, since it leads to better results in the estimation;
- *cut-off velocity* - we decide to discard all the configurations whose combination of d and L cause more than 10 % of the particles from the distributions underlined in Sec. 5.7 to have a velocity lower than the cut-off velocity. This last requirement is distribution-dependent and must be determined on a case by case basis;
- *information available on detection* - we consider to have no information on time of flight and we expect to be able to reconstruct the shift based on the knowledge of the velocity distribution of the produced particles. Therefore, we consider the particles indistinguishable on an energy basis and the combined pattern as the detected signal.

5.8.4 Available space and possible configurations

In the framework of the AEgIS experiment, we have access to two different options when designing the measurement device: placing it inside the main vacuum chamber, just outside the production trap, or placing it outside the main experimental chamber as its own sub-unit. A schematic which depicts both choices is presented in Fig. 5.12. Both approaches have different advantages and disadvantages.

As discussed in Sec. 5.8.1, inside the main vacuum chamber there is a maximum available linear space of 690 mm, with a radius of 32.5 mm.

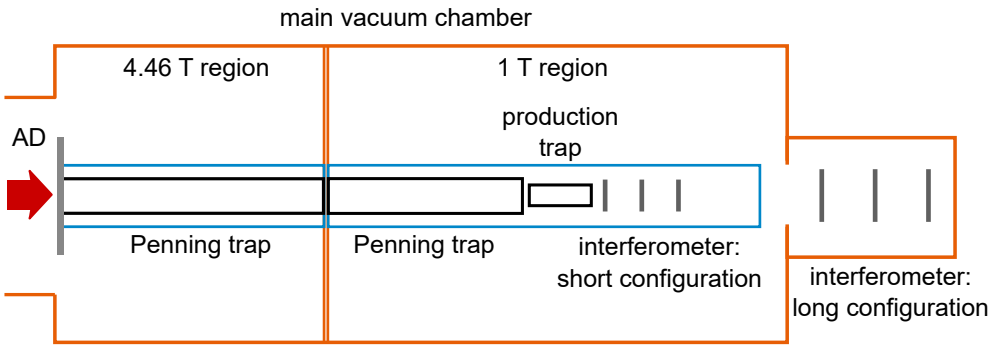

Figure 5.12: Schematic (not to scale) of the AEgIS experiment, with the two proposed configurations for the interferometer. The orange line marks the outer limit of the experimental vacuum chamber, containing the superconducting magnets used to generate the magnetic field used for the trapping system and the liquid helium vessel needed to keep them at their operating temperature. More details about the experimental apparatus can be found in [Car17]. The blue line marks the portion of the vacuum chamber which hosts the traps and can (potentially) host the interferometer in the short configuration. The three penning traps used for antiprotons are depicted in black, with the production trap being the source of antihydrogen. The *short configuration* consists in placing the interferometer inside the 1 T magnetic field, near the edge of the production trap, while the *long configuration* is achieved by placing the interferometer in its own sub-unit outside of the main vacuum chamber.

Building the device nearer to the source has an advantage in terms of statistics: since the source in the ATHENA scenario has a divergence of $300\,\mathrm{mm\,m^{-1}}$ and in both the ATRAP and AEgIS scenario an approximate divergence of $1000\,\mathrm{mm\,m^{-1}}$, placing the detector nearer would grant a higher yield of detected particles. On the converse side, cryogenic conditions require additional care in the choice of materials, in order to avoid that the thermal shrinking of the interferometer could affect its alignment. Moreover, the field gradients due to the surrounding magnetic field of 1 T have to be taken care of, as the magnetic dipole interaction could mask the effect of gravity.

Placing the interferometer outside the main vacuum chamber shows some notable advantages: the measurement device could be built in its own vacuum chamber at room temperature, far enough from the superconducting magnets of the experiment to be considered in a field-free region. Not having the geometrical limitations of the bore would also allow for bigger detectors, even if probably not big enough to compensate for the huge divergence of the source. The minimal distance from the production trap in this scenario would be 80 cm, which would account for a beam diameter of - at minimum - 50 cm before entering the interferometer.

In the following, we use the notation introduced in Fig. 5.3 and we analyze both scenarios separately:

- a *short configuration*, with the distance L_0 from the source to the first grating equal to 10 cm and a detector radius r_D of 3 cm;
- a *long configuration*, with the distance L_0 from the source to the first grating equal to 80 cm and a detector radius r_D of 10 cm, taking advantage of looser geometrical constraints.

A preliminary work on both scenarios has been presented to the collaboration in the form of an internal report by our research group in 2015 [Brä+15]. An unedited version of the report is included in Appendix B.

5.9 Open questions on the design of the experiment

Aside from the technological challenges connected with the control of field gradients and the alignment of the interferometer, there are some open questions which could affect the design of the experimental device. Most notably:

- how to obtain the "zero position" to which the gravitational phase shift is referenced to;

- how to determine that the measured shift is, indeed, due to gravity and not to any other interaction.

Concerning the referencing issue, in 2014 the AEgIS collaboration measured a phase shift induced by electric fields on antiprotons by superimposing a light interferometer using the same measurement device [Agh+14; Brä14]. This allowed for the determination of an absolute reference position to quantify the phase shift. A similar technique could be employed for a gravity measurement on antihydrogen, but this would require a precise choice for the periodicity of the gratings and the length of the device, such that the interferometer could be used both for light and particles at the same time.

Concerning the question on how to make sure that the measured interaction is indeed gravity, we could apply an interesting idea from the so-called COW experiment, a neutron interferometric gravimeter who took its name from Colella, Overhauser and Werner, who performed it in 1975 [COW75]: if the particles are subjected to an acceleration g, perpendicular to the grating slits, and the whole interferometer is rotated by an angle θ around the axis, the resulting phase shift $\Delta\phi_\theta$ would be given by

$$\Delta\phi_\theta = \frac{2\pi}{d} g \cos(\theta)\, \tau^2 = \Delta\phi_0 \cos(\theta), \tag{5.33}$$

where $\Delta\phi_0$ is the phase shift for the non-rotated device, d is the periodicity of the gratings, and τ is the time of flight. Therefore, by performing a series of measurements for different $\theta \neq 0$, the force can be identified as purely vertical by measuring the evolution of the phase shift as a function of θ. In the most optimistic projection, this means that at least one additional measurement would be required to conclude that gravity is the force being measured.

The evaluations from the following sections are based on a scenario in which one measurement is all that is required to obtain the gravitational acceleration with a known precision. These results can be easily scaled to other, more stringent, scenarios by multiplying the time needed for one measurement to the number of measurements required to perform the experiment in the desired configuration.

5.10 Sensitivity for different configurations

By putting together all the considerations from the previous sections, we can now produce an estimation on the required measurement time for performing a measurement with the required precision. The estimator for this analysis is the minimum detectable acceleration times square root of particles produced, $a_{\min}\sqrt{N_{\text{prod}}}$. This estimator expresses the sensitivity

of the measurement device as a function of the number of produced particles and it can easily be scaled by knowing the total number of produced antihydrogen atoms.

We begin by considering the *short configuration* highlighted in the previous section. Afterwards, we analyze the *long configuration*, out of the geometrical limits of the AEgIS vacuum chamber. For both configurations, we consider four different values of the distance L between the gratings, 5, 10, 20, and 30 cm, and a periodicity d of the grating between 250 nm and 100 µm.

Concerning the systematic effects described in Chapter 3 and 4, we assume a perfectly aligned interferometer ($\Delta L = 0$, $\beta = 0$) in absence of external forces other than gravity to limit our analysis to the most ideal case.

The analysis is split into two steps: first, we use consider the production schematics which makes use of direct mixing (*direct mixing A*), then the schematics which implement charge exchange (*charge exchange A/B/C*), as of Tab. 5.1.

5.10.1 Short configuration, direct mixing

The first configuration we analyze is the one related to the ATHENA experiment (*direct mixing A* in Tab. 5.1). This amounts to using an axial temperature of $T_\parallel = 150\,\mathrm{K}$ and a transverse temperature of $T_\perp = 15\,\mathrm{K}$. These temperature translate into an intrinsic beam divergence which is given by the ratio between the average transverse and axial velocities $v_\perp/v_\parallel = \sqrt{T_\perp/T_\parallel} \simeq 300\,\mathrm{mm\,m^{-1}}$. The result of the numerical evaluations from Sec. 5.6 is shown in Fig. 5.13. Removing the particles below the cut-off velocity, defined by Eq. (5.32), in this specific configuration does not play a big role, as the contrast plot is just improved for $L = 30\,\mathrm{cm}$.

According to the plot, the configuration which offers the best sensitivity is the one with $d = 250\,\mathrm{nm}$ and $L = 10\,\mathrm{cm}$, which grants a pattern with a contrast higher than 20 % while keeping the same sensitivity as $L = 20\,\mathrm{cm}$. Notice that this is not true anymore when increasing the periodicity d, but the contrast remains higher for a broad range of configurations. The maximum allowed divergence of the beam α is therefore $r_D/(L_0 + 2L) = 100\,\mathrm{mm\,m^{-1}}$, smaller than the natural spread of the beam. This results in a shift Δy_g of around 40 nm for the average velocity, which corresponds to a relative phase $\phi_g = \Delta y_g/d \sim \pi/3$. By using the estimation from Chapter 3, an interferometer designed to work in these experimental conditions has a maximum allowed asymmetry $\Delta L_{\mathrm{crit}} = 1.3\,\mu\mathrm{m}$ due the divergence of the beam and a maximum allowed angular misalignment $\beta_{\mathrm{crit}} = 8\,\mu\mathrm{rad}$ (see Eq. (3.9) and Eq. (3.12) respectively), which can be experimentally challenging to reach.

If we consider the best configuration, the minimum detectable ac-

celeration times square root of particles produced is of the order of 10^3. This translates into a requirement of 1×10^6 particles produced in order to get a sensitivity of $1\,\mathrm{m\,s^{-2}}$ (∼10 % of gravity), while around 1.1×10^5 particles would be required for a sensitivity of $3\,\mathrm{m\,s^{-2}}$ (∼30 % of gravity, the so-called sign measurement). With an estimated production rate of $1.8 \times 10^4 \bar{\mathrm{H}}$/day, this sets a requirement of 6 days of continuous measurement to reach a precision of 30 %, while about 60 days of measurement are required for reaching a 10 % accuracy. These numbers point out that a sign measurement could be feasible in this specific configuration, provided that the magnetic field in the experimental volume can be made as homogeneous as needed and the alignment requirements can be satisfied with the due precision.

The configuration labeled as *direct mixing B* (ALPHA) shows an even smaller number of produced antihydrogen atoms at higher temperature in a uniform, non-directional distribution. It is therefore safe to assume that the prediction for this measurement is worse than for the considered ATHENA parameters.

5.10.2 Short configuration, charge exchange

We now analyze the three scenarios which make use of charge exchange, namely ATRAP (experimental and theoretical) and AE$\bar{\mathrm{g}}$IS. The advantage in respect to direct mixing is a lower temperature for the produced antihydrogen, which would lead to a higher sensitivity in a small volume. The disadvantage is due to the non-directional, uniform distribution of the produced particles, which leads to an increase in the losses due to the geometrical acceptance of the detector. The results for the configuration labeled as *charge exchange A* (ATRAP) are summarized in Fig. 5.14. In this regime, we consider a uniform source with a temperature of 4 K. We see that due to the low velocity of the particles, the visibility drop for longer L causes the sensitivity to get significantly worse for small periodicities.

According to the Fig. 5.14, one possible configuration for a gravity measurement has $d = 1.8\,\mu\mathrm{m}$ and $L = 5\,\mathrm{cm}$. With this choice, the maximum divergence α of the beam is $r_D/(L_0 + 2L) = 150\,\mathrm{mm\,m^{-1}}$, while the average fall due to gravity is of the order of $0.3\,\mu\mathrm{m}$, which corresponds to a phase shift of around $\pi/3$. By using the estimation from Chapter 3, an interferometer designed to work in these experimental conditions has a maximum allowed asymmetry $\Delta L_{\mathrm{crit}} = 7\,\mu\mathrm{m}$ and a maximum allowed angular misalignment $\beta_{\mathrm{crit}} = 80\,\mu\mathrm{rad}$. These parameters would grant a contrast of around 20 %, which is in the range we deem acceptable for a measurement. The minimum detectable acceleration is around $2 \times 10^3\,\mathrm{m\,s^{-2}}\sqrt{N_{\mathrm{prod}}}$, which corresponds to about 4×10^6 particles produced to get down to a sensitivity of $1\,\mathrm{m\,s^{-2}}$ (∼10 % of gravity) or around

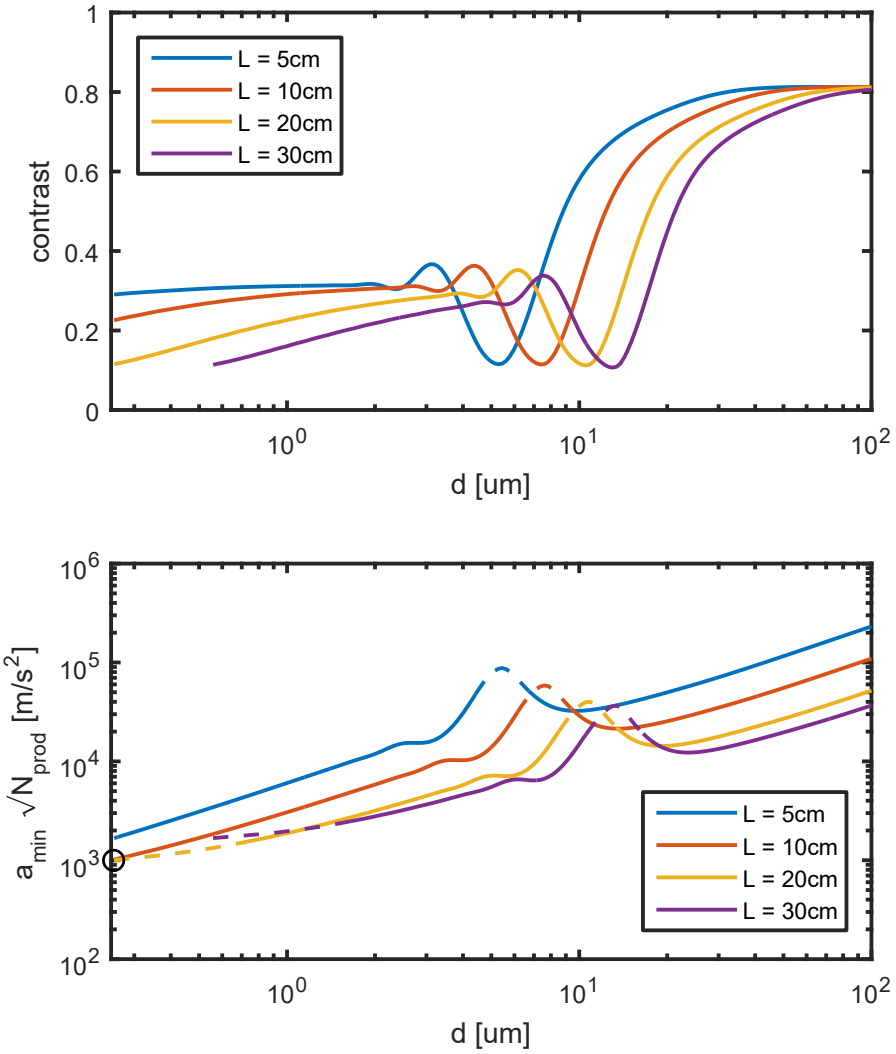

Figure 5.13: *Direct Mixing A (ATHENA)* from Tab. 5.1 ($T_{\parallel} = 150\,\mathrm{K}$, $T_{\perp} = 15\,\mathrm{K}$) in a short configuration ($r_D = 3\,\mathrm{cm}$, $L_0 = 10\,\mathrm{cm}$). *Top:* Contrast C of the interference pattern for $\eta = 0.3$ in presence of a gravitational acceleration. The plot lines start from the periodicity which allows for more than 90 % of the generated particles to be used, as described in Sec. 5.8. *Bottom*: minimum detectable acceleration times square root of particles produced $a_{\mathrm{min}}\sqrt{N_{\mathrm{prod}}}$ plotted for the same configuration. A dashed line means that the contrast for that particular configuration is smaller than 20 % and is not considered viable for a measurement according to the constraints we set. The configuration we use in the measurement time calculations is marked by a black circle.

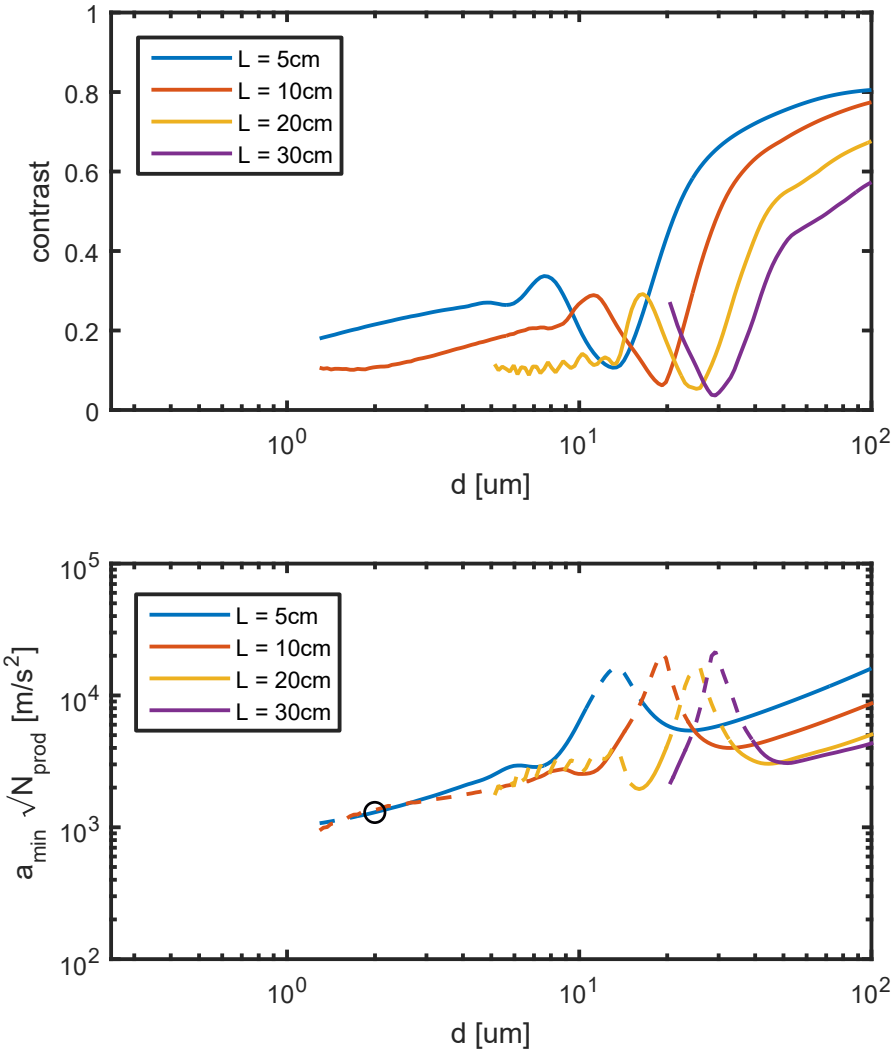

Figure 5.14: *Charge Exchange A/B (ATRAP)* from Tab. 5.1 ($T_\parallel = T_\perp = 4\,\mathrm{K}$) in a short configuration ($r_D = 3\,\mathrm{cm}$, $L_0 = 10\,\mathrm{cm}$). *Top:* Contrast C of the interference pattern for $\eta = 0.3$ in presence of a gravitational acceleration. The plot lines start from the periodicity which allows for more than 90 % of the generated particles to be used, as described in Sec. 5.8. *Bottom*: minimum detectable acceleration times square root of particles produced $a_{\mathrm{min}}\sqrt{N_{\mathrm{prod}}}$ plotted for the same configuration. A dashed line means that the contrast for that particular configuration is smaller than 20 % and is not considered viable for a measurement according to the constraints we set. The configuration we use in the measurement time calculations is marked by a black circle.

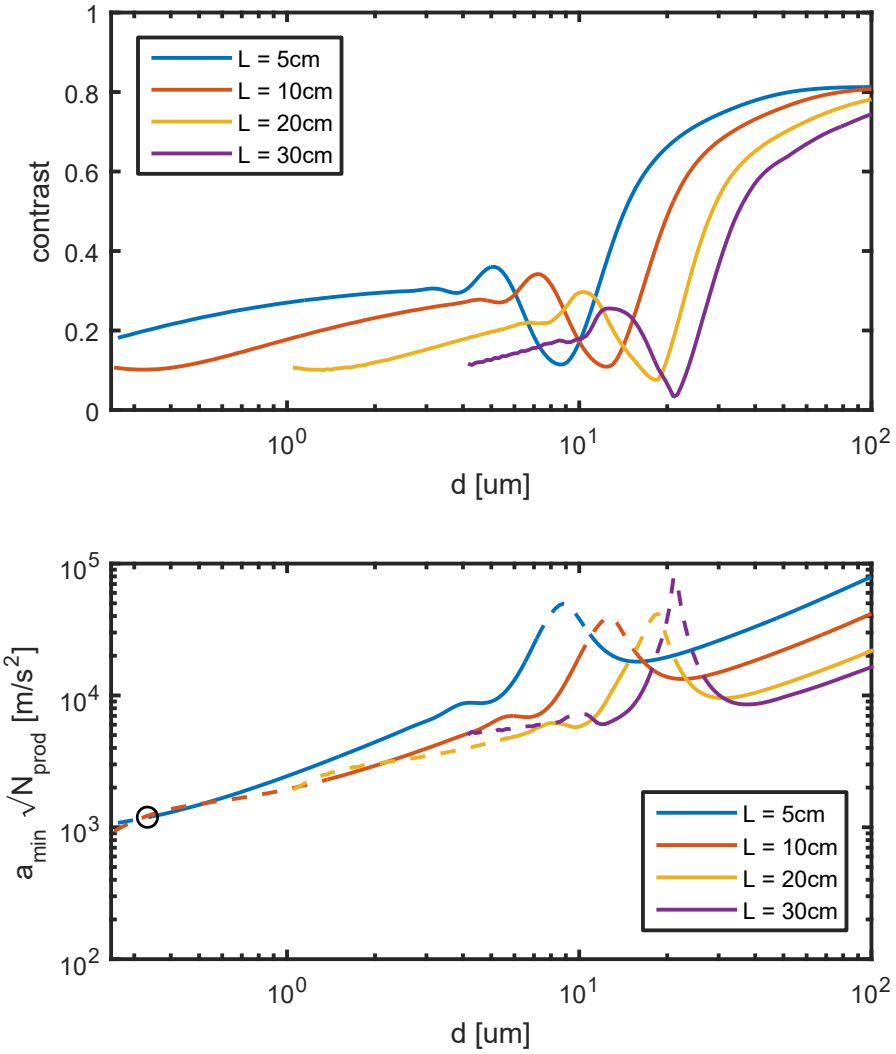

Figure 5.15: *Charge Exchange C (AEgIS)* from Tab. 5.1 ($T_{\parallel} = T_{\perp} = 20\,\mathrm{K}$) in a short configuration ($r_D = 3\,\mathrm{cm}$, $L_0 = 10\,\mathrm{cm}$). *Top:* Contrast C of the interference pattern for $\eta = 0.3$ in presence of a gravitational acceleration. The plot lines start from the periodicity which allows for more than 90 % of the generated particles to be used, as described in Sec. 5.8. *Bottom*: minimum detectable acceleration times square root of particles produced $a_{\mathrm{min}}\sqrt{N_{\mathrm{prod}}}$ plotted for the same configuration. A dashed line means that the contrast for that particular configuration is smaller than 20 % and is not considered viable for a measurement according to the constraints we set. The configuration we use in the measurement time calculations is marked by a black circle.

4.4×10^5 particles produced for a sensitivity of $3\,\mathrm{m\,s^{-2}}$ (∼30 % of gravity). If we consider the numbers from Tab. 5.1, we see that with the numbers from the 2004 experiment, this would still ask for about 140 days of continuous measurement. However, if the hypothetical production boost predicted in the work of McConnell et al. [McC+16] would prove true, the measurement would prove feasible in one day of antihydrogen production (scenario labeled *charge exchange B* in Tab. 5.1).

The AEgIS scenario (*charge exchange C*) shows even different properties and optimal conditions: by using the information from Fig. 5.15, we see that due to the increased temperature of the particles, the drop in contrast is less noticeable to the point that we can consider using gratings with a periodicity as small as 350 nm and still retain more than 20 % contrast. We decide therefore to consider the configuration $d = 350\,\mathrm{nm}$ and $L = 5\,\mathrm{cm}$. This would however reduce the maximum allowed displacements by almost one order of magnitude, down to $\Delta L_{\mathrm{crit}} = 1.1\,\mu\mathrm{m}$ and a maximum allowed angular misalignment $\beta_{\mathrm{crit}} = 15\,\mu\mathrm{rad}$. With this choice, the average fall due to gravity is of the order of 60 nm, which corresponds to a phase shift of around $\pi/3$. In this specific configuration, the minimum detectable acceleration times square root of particles is on the order of 10^3. In order to get down to a sensitivity of $1\,\mathrm{m\,s^{-2}}$ (∼10 % of gravity), 1×10^6 particles are needed, while for a sensitivity of $3\,\mathrm{m\,s^{-2}}$ (∼30 % of gravity) we talk about 1.1×10^5 particles. Compared with the production rates of Tab. 5.1, this seems not as feasible, requiring about 50 days of continuous integration for performing a sign measurement. This becomes especially concerning if more than one repetition of the measurement is needed to confirm the experimental result, as we discussed in Sec. 5.9.

5.10.3 Remarks on the magnetic gradient limitations

Before performing the calculations, we chose to use the full available measurement volume inside the experimental vacuum bore. It is interesting to check how these numbers would change when limiting ourselves to the available gradient-free region. As mentioned in Tab. 5.2, the region of space where the magnetic field gradient has an effect smaller than gravity on ground-state antihydrogen is a small cylinder with a total length $L_D^{\mathrm{safe}} = 10\,\mathrm{cm}$ and a radius $r_D^{\mathrm{safe}} = 1.5\,\mathrm{mm}$, placed at around 7 cm from the center of the production trap [Brä+15]. We use the results from Fig. 5.13, Fig. 5.14, and Fig. 5.15 to estimate what is the consequence of restricting the measurement to this "safe volume", by considering the plots for $L = 5\,\mathrm{cm}$ and scaling the minimum detectable acceleration by a factor $r_D^{\mathrm{max}}/r_D^{\mathrm{safe}} = 20$ to take into account the reduced size of the detector. It is clear that an experiment in these conditions is not go-

ing to work: by optimizing the setup for these geometrical restrictions, we see that the minimum detectable acceleration $a_{\min}\sqrt{N_{\text{prod}}}$ goes up to $4 \times 10^4\,\text{m/s}^2\sqrt{\text{Hz}}$, which translates into a required number of particles of around 2×10^9 for a 10 % measurement and 2×10^8 for a 30 % measurement, which represents a net increase of more than two orders of magnitude in time. Therefore, we deem the measurement with the current restrictions due to fields unfeasible and we keep considering the maximum available volume for the rest of the discussion.

5.10.4 Summary for the short configuration

In Tab. 5.3 we summarize the best configurations found by analyzing each one of the different production schematics for the so-called short configuration ($r_D = 3\,\text{cm}$, $L_0 = 10\,\text{cm}$).

Configuration	d^{best}	L^{best}	$a_{\min}\sqrt{N_{\text{prod}}}$
Direct mixing A (ATHENA)	250 nm	10 cm	$1 \times 10^3\,\text{m/s}^2\sqrt{\text{Hz}}$
Charge exchange A/B (ATRAP)	1.8 µm	5 cm	$2 \times 10^3\,\text{m/s}^2\sqrt{\text{Hz}}$
Charge exchange C (AEgIS)	350 nm	5 cm	$1 \times 10^3\,\text{m/s}^2\sqrt{\text{Hz}}$

Configuration	days for 30 %	days for 10 %
Direct mixing A (ATHENA)	6	56
Charge exchange A (ATRAP)	138	1250
Charge exchange B (ATRAP)	< 1	2
Charge exchange C (AEgIS)	48	435

Table 5.3: Optimal configurations for different production schematics in a short configuration and estimated measurement time for both a sign measurement (30 % precision) and a 10 % measurement

5.10.5 Long configuration, direct mixing

In this section, we perform numerical estimations for the so-called *long configuration* in the *direct mixing A* production scenario (Tab. 5.1.

The analytical treatment is performed in the same way as for the *short configuration*, with the advantage that we have now no constraints on the maximum grating radius, aside from the several technical challenges required to build them. We go as far as considering $r_D = 10\,\text{cm}$, which would result in a ten times increase in detecting efficiency and a three times smaller minimum detectable acceleration. Gratings of this size have been effectively produced for a periodicity $d = 40\,\mu\text{m}$ [Hau12].

By performing the numerical analysis once more, we obtain the results shown in Fig. 5.16. We see that, despite the increase in detecting efficiency, the overall minimum detectable acceleration is higher than in

the short configuration, mostly due to the losses over an 80 cm path. For a periodicity $d = 250\,\text{nm}$, we get that the minimum detectable acceleration times square root of particles produced is of the order of 2×10^3 for $L = 10\,\text{cm}$, if we keep our requirement of having at least 20 % contrast. This translates into a requirement of 4×10^6 particles produced in order to get a sensitivity of $1\,\text{m}\,\text{s}^{-2}$ (∼10 % of gravity), while around 4.4×10^5 particles would be required for a sensitivity of $3\,\text{m}\,\text{s}^{-2}$ (∼30 % of gravity). In this geometry, the maximum allowed divergence is on the same order as for the short configuration, asking for the same alignment precision. If we compare these numbers with the ones obtained in Sec. 5.10.1, we see that the requirements are about four times higher, causing a proportional increase on the measurement time - from five days of continuous measurement to twenty just to obtain a 30 % precision, unless the detector size is increased by an additional factor two, up to $r_D = 20\,\text{cm}$, therefore cutting down the expected integration time by a factor four.

Twenty days of continuous measurement are not completely out of the realm of the possibility, but would still require the measurement apparatus to remain stable for a prolonged period of time. As before, we ignore the ALPHA scenario (*direct mixing B*), since it fares significantly worse than the one considered in this section.

5.10.6 Long configuration, charge exchange

In this section we review the production processes labelled as *charge exchange A/B/C* in Tab. 5.1.

For the ATRAP configuration (*charge exchange A* and *charge exchange B*), the results of the evaluations are shown in Fig. 5.17. When comparing these numbers with the ones for the *short configuration*, we see an increase in the minimum detectable acceleration by a factor 1.5, which translates into three times more particles needed in order to reach the same sensitivity as in Sec. 5.10.2. However, if the production boost predicted by McConnell et al. [McC+16] is experimentally verified, the measurement would be feasible also in this configuration.

When considering the AEgIS configuration (*charge exchange C* - $T_\parallel = T_\perp = 20\,\text{K}$), we witness a factor three increase in the minimum detectable acceleration instead. This result is shown in Fig. 5.18.

We already discussed in Sec. 5.10.2 that the measurement is already barely feasible in the short configuration, so an increase in measurement time would predictably make the situation worse.

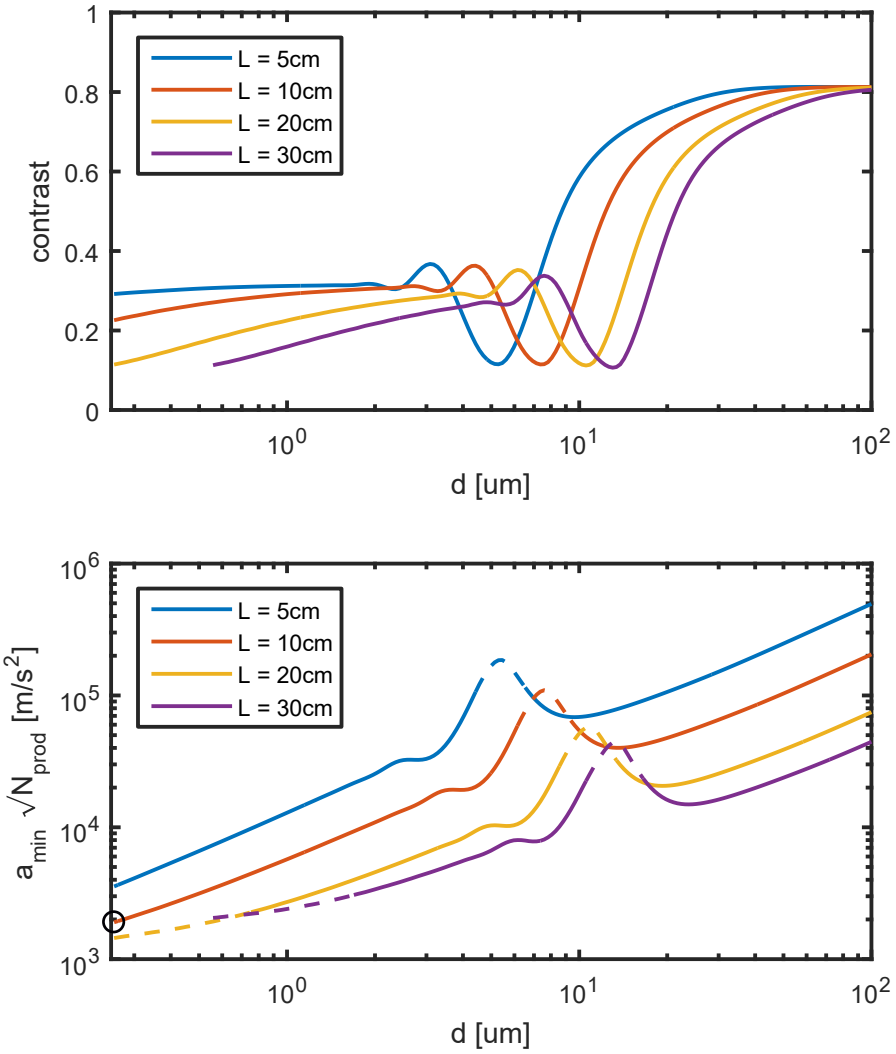

Figure 5.16: *Direct Mixing A (ATHENA)* from Tab. 5.1 ($T_{\parallel} = 150\,\mathrm{K}$, $T_{\perp} = 15\,\mathrm{K}$) in a long configuration ($r_D = 10\,\mathrm{cm}$, $L_0 = 80\,\mathrm{cm}$). *Top:* Contrast C of the interference pattern for $\eta = 0.3$ in presence of a gravitational acceleration. The plot lines start from the periodicity which allows for more than 90 % of the generated particles to be used, as described in Sec. 5.8. *Bottom*: minimum detectable acceleration times square root of particles produced $a_{\mathrm{min}}\sqrt{N_{\mathrm{prod}}}$ plotted for the same configuration. A dashed line means that the contrast for that particular configuration is smaller than 20 % and is not considered viable for a measurement according to the constraints we set. The configuration we use in the measurement time calculations is marked by a black circle.

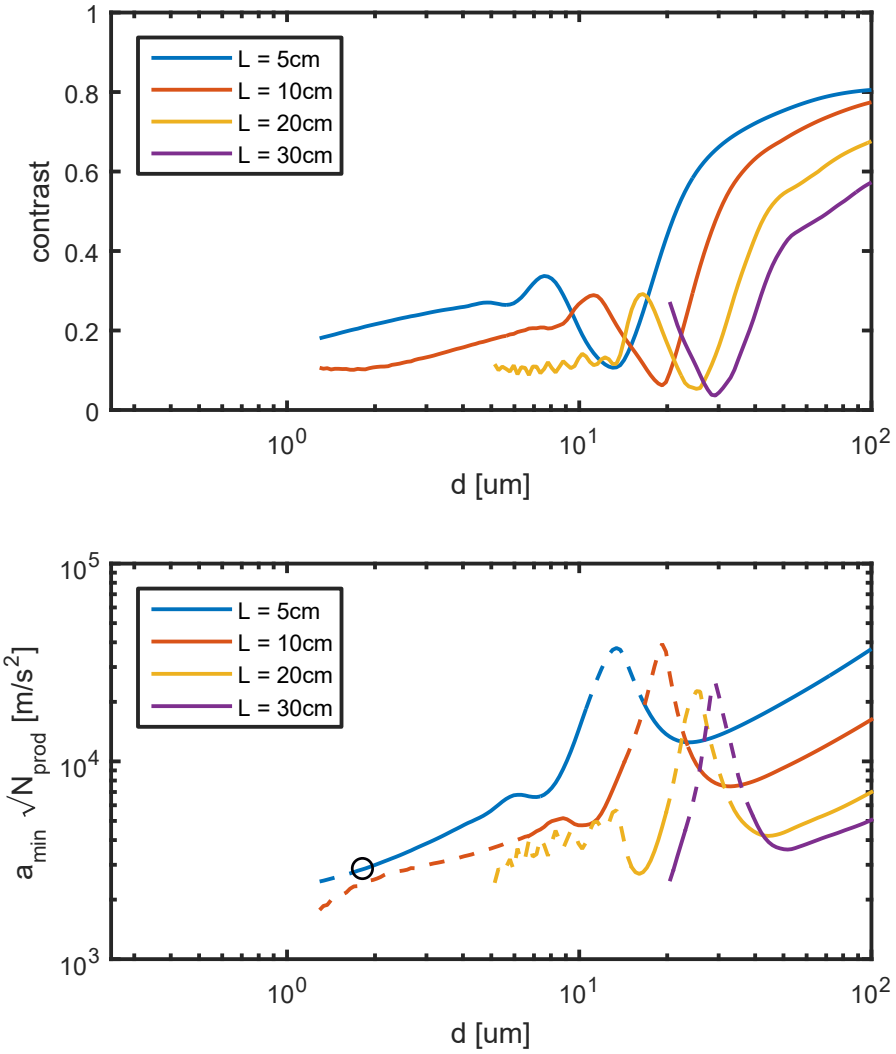

Figure 5.17: *Charge Exchange A/B (ATRAP)* from Tab. 5.1 ($T_\parallel = T_\perp = 4\,\mathrm{K}$) in a long configuration ($r_D = 10\,\mathrm{cm}$, $L_0 = 80\,\mathrm{cm}$). *Top:* Contrast C of the interference pattern for $\eta = 0.3$ in presence of a gravitational acceleration. The plot lines start from the periodicity which allows for more than 90 % of the generated particles to be used, as described in Sec. 5.8. *Bottom*: minimum detectable acceleration times square root of particles produced $a_{\mathrm{min}}\sqrt{N_{\mathrm{prod}}}$ plotted for the same configuration. A dashed line means that the contrast for that particular configuration is smaller than 20 % and is not considered viable for a measurement according to the constraints we set. The configuration we use in the measurement time calculations is marked by a black circle.

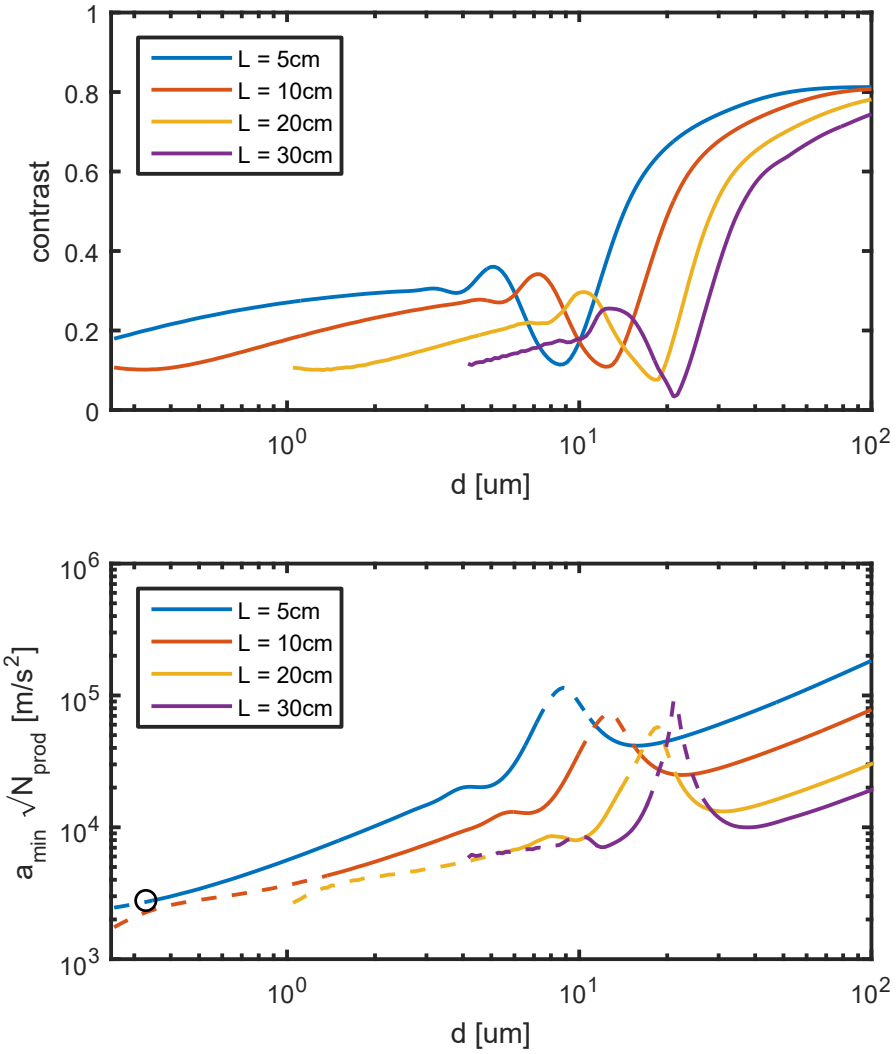

Figure 5.18: *Charge Exchange C (AEgIS)* from Tab. 5.1 ($T_{\parallel} = T_{\perp} = 20\,\mathrm{K}$) in a long configuration ($r_D = 10\,\mathrm{cm}$, $L_0 = 80\,\mathrm{cm}$). *Top:* Contrast C of the interference pattern for $\eta = 0.3$ in presence of a gravitational acceleration. The plot lines start from the periodicity which allows for more than 90 % of the generated particles to be used, as described in Sec. 5.8. *Bottom*: minimum detectable acceleration times square root of particles produced $a_{\mathrm{min}}\sqrt{N_{\mathrm{prod}}}$ plotted for the same configuration. A dashed line means that the contrast for that particular configuration is smaller than 20 % and is not considered viable for a measurement according to the constraints we set. The configuration we use in the measurement time calculations is marked by a black circle.

5.10.7 Summary for the long configuration

In Tab. 5.4 we summarize the best configurations found by analyzing each one of the different production schematics for the so-called long configuration ($r_D = 10\,\mathrm{cm}$, $L_0 = 80\,\mathrm{cm}$).

Configuration	d^{best}	L^{best}	$a_{\min}\sqrt{N_{\mathrm{prod}}}$
Direct mixing A (ATHENA)	250 nm	10 cm	$2 \times 10^3\,\mathrm{m/s^2}\sqrt{\mathrm{Hz}}$
Charge exchange A/B (ATRAP)	1.8 µm	5 cm	$3 \times 10^3\,\mathrm{m/s^2}\sqrt{\mathrm{Hz}}$
Charge exchange C (AEgIS)	350 nm	5 cm	$3 \times 10^3\,\mathrm{m/s^2}\sqrt{\mathrm{Hz}}$

Configuration	days for 30 %	days for 10 %
Direct mixing A (ATHENA)	24	224
Charge exchange A (ATRAP)	414	3750
Charge exchange B (ATRAP)	2	6
Charge exchange C (AEgIS)	432	3915

Table 5.4: Optimal configurations for different production schematics in a long configuration and estimated measurement time for both a sign measurement (30 % precision) and a 10 % measurement.

5.11 Summary

To conclude this section, we summarize the results of the simulations for the configurations we considered in two tables, one for the short configuration (Tab. 5.5) and one for the long configuration (Tab. 5.6). The short configuration consists of gratings with a radius of 3 cm with a maximum available linear extension of 69 cm, while the long configuration has no hard limitations in both length and radius of the gratings, aside from the vast technical challenges required to produce these components.

We see that, among the scenarios which use published experimental data, the short configuration offers smaller measurement times for direct mixing, as long as we can use the full extent of the AEgIS vacuum chamber: a device with a length of 20 cm and a radius of 3 cm placed at 10 cm from the source would allow for a 30 % precision in 6 days of continuous measurement.

This is true in the hypothesis that the magnetic field gradients are under control on the whole experimental volume: a gradient of $0.2\,\mathrm{G\,cm^{-1}}$ would cause the same phase shift as gravity on ground state antihydrogen, hindering the possibility to obtain a sensible result. Currently, the region of space with a homogeneity which satisfies this boundary is a small cylinder with a length of 10 cm and a radius of 1.5 mm. If we restrict the measurement to this region, the expected measurement time increases by around 400 times.

In a long configuration, the number of required days of measurement is around three to four times higher. This is mostly due to the huge intrinsic divergence of the particle source (greater than $300\,\mathrm{mm\,m^{-1}}$), which causes huge losses on a longer path. The field homogeneity required to perform the measurement is the same as in the short configuration, albeit on a bigger scale (r_D up to 10 cm).

Short configuration	days for 30 %	days for 10 %
Direct mixing A (ATHENA)	6	56
Charge exchange A (ATRAP)	138	1250
Charge exchange B (ATRAP)	< 1	2
Charge exchange C (AE$\bar{\text{g}}$IS)	48	435

Table 5.5: Days of continuous measurement needed to perform a gravity measurement on $\bar{\text{H}}$ for different production schematics in a short configuration.

Long configuration	days for 30 %	days for 10 %
Direct mixing A (ATHENA)	24	224
Charge exchange A (ATRAP)	414	3750
Charge exchange B (ATRAP)	2	6
Charge exchange C (AE$\bar{\text{g}}$IS)	432	3915

Table 5.6: Days of continuous measurement needed to perform a gravity measurement on $\bar{\text{H}}$ for different production schematics in a long configuration.

In the ideal conditions, with the production rates achieved as of the end of 2017, it seems not feasible to perform a gravity measurement on antihydrogen using charge exchange production without extensive measurement time (50 or more days in the most optimistic setup), especially when considering the fact that a repetition of the measurement might be needed to measure the gravitational interaction.

However, the improvement in positronium production achieved by the ATRAP collaboration in 2016 [McC+16], which would lead to an exponential increase in antihydrogen yield, together with the ten to one hundredfold antiproton catching efficiency improvement due to the installation of the ELENA antiproton decelerator between 2019 and 2020 [Bar+14; PJ16; Pan17], could make this measurement feasible in a reasonable amount of time. Once the problems with the source efficiency are quenched, the technological challenge connected to performing the experiment reside in stabilizing the interferometer, such that the alignment requirements highlighted in Chapter 3 are satisfied for the whole duration of the measurement, and in producing a sufficiently field-free volume for an unperturbed flight through the gratings, compliant with the limits described in Chapter 4.

Chapter 6

Conclusions and outlook

The goal of this work was to present a feasibility study for a gravity measurement on antihydrogen to be performed with the current, state-of-the-art production rates for neutral antimatter.

We started by describing and analyzing our tool of choice, the Talbot-Lau interferometer, an atom optic tool successfully used to verify the wave nature of several kind of particles and, in its classical limit, to perform inertial measurements on a variety of species. We obtained analytical formulas and numerical procedures to calculate the expected signal for this kind of device, considering both a two and a three-grating setup. We then estimated the sensitivity of the device to external forces and its possible application to measure gravity.

A special care has been reserved to the study of the systematic effects which degrade the quality of the generated patterns: in particular, we studied the consequences of a misalignment and asymmetry of the interferometer, obtaining quantitative formulas which can be used in the design of an actual device. Those expression depend on the geometrical parameters of the interferoemter, such as the periodicity of the gratings and the distance between them, and on the divergence of the particle source.

The effects of external forces, such as those due to magnetic and electric field gradients, have also been discussed. We derived expressions that can be employed to estimate the effects of unwanted interactions as a function of the energy spread of the source.

We combined all of the previous into a theoretical framework to evaluate the feasibility of the aforementioned gravitational measurement, considering different production mechanisms and geometries. Specifically, two different antihydrogen production processes have been analyzed in detail: direct mixing of positrons and antiprotons and charge exchange between positronium and antiprotons.

The results of the evaluation, summarized in Tab. 6.1, show that, with the state-of-the-art production rates for antihydrogen, direct mixing

would provide a feasible strategy to perform a gravity measurement on antimatter in the framework of the AEḡIS experiment: a compact setup of around 20 cm of length and 6 cm diameter, placed at 10 cm from the particle source would allow for a gravity measurement with an accuracy of 30 % in about six continuous days of measurement. This comes however at the cost of strict requirements on the robustness of the interferometric setup (asymmetry tolerance smaller of the order 1 µm, alignment tolerance smaller than 10 µrad) and on the control of the external fields (magnetic field gradient smaller than $0.2\,\mathrm{G\,cm^{-1}}$, if the antihydrogen is in the ground state). This last requirement sets a serious experimental challenge, since the current homogeneity of the magnetic field in the experimental region is compliant with this limit only on a cylinder with total length 10 cm and a diameter of 3 mm. If these additional limitations are not overcome, the measurement time increases by around a factor four hundred.

The other antihydrogen production schematic, charge exchange, does not currently seem to be a suitable candidate for a measurement, requiring at its best around fifty days of continuous measurement in the short configuration setup. However, with a projected five hundredfold increase in production rate, as advocated by the ATRAP collaboration, and the commissioning of the ELENA antiproton decelerator, this process could be seen as a more alluring alternative, providing a smaller antimatter temperature and an increased control over the source parameters.

Short configuration ($r_D = 3\,\mathrm{cm}$, $L_0 = 10\,\mathrm{cm}$)

Based on available data

Configuration	days for 30 %	days for 10 %
Direct mixing A (ATHENA)	6	56
Charge exchange A (ATRAP)	138	1250

Based on estimations

Configuration	days for 30 %	days for 10 %
Charge exchange B (ATRAP)	< 1	2
Charge exchange C (AEḡIS)	48	435

Table 6.1: Days of continuous measurement needed to perform a gravity measurement on $\bar{\mathrm{H}}$ for different production schematics in a short configuration. These scenarios have been discussed in detail in Chapter 5.

6.1 Outlook and developments

Since the AEḡIS collaboration our group is part of has yet to produce antihydrogen, the focus of our local research group is the development of

the measuring device. In particular, a Talbot-Lau interferometer is being developed in Heidelberg and being tested in a side project to reveal the wave nature of protons and antiprotons, which is in itself an ambitious goal in the field of particle physics, as interference from antimatter is yet to be observed. By performing research and development to reach this achievement, we have to deal with the same kind of systematic effects which can prevent the success of a gravity measurement: instead of having to do with gradients, we have to reduce the effects of stray electric and magnetic fields, as described in Chapter 4, while the alignment limits described in Chapter 3 have to be taken care on a level which is of the same order of magnitude as expected for the main experiment. In particular, the alignment procedures developed to reach this goal will be an important cornerstone in the development of the device for the gravity measurement. A picture of the interferometer is shown in Fig. 6.1: it is currently composed of three gratings with periodicity $d = 257\,\mathrm{nm}$ of the type shown in Fig. 2.4, separated by $L \simeq 1\,\mathrm{cm}$ and mounted on top of mirror holders which can be used to improve the alignment of the device. The mirror mounts are in turn fixed on piezo actuators for fine tuning alignment. The interferometer is aligned using the Littrow reflection of a blue laser on its grating structure, in order to reach a precision better than $100\,\mu\mathrm{rad}$. There has been preliminary work to design a system of three independent Mach-Zehnder interferometers to monitor the alignment of the gratings in real time [Fri17], which could be implemented as a future improvement.

The development of the prototype interferometer and the experimentation on both the field and the alignment limits will prove crucial to design the device for the gravity measurement, as most of the technical challenges underlined in this work have to be properly solved to achieve this intermediate result.

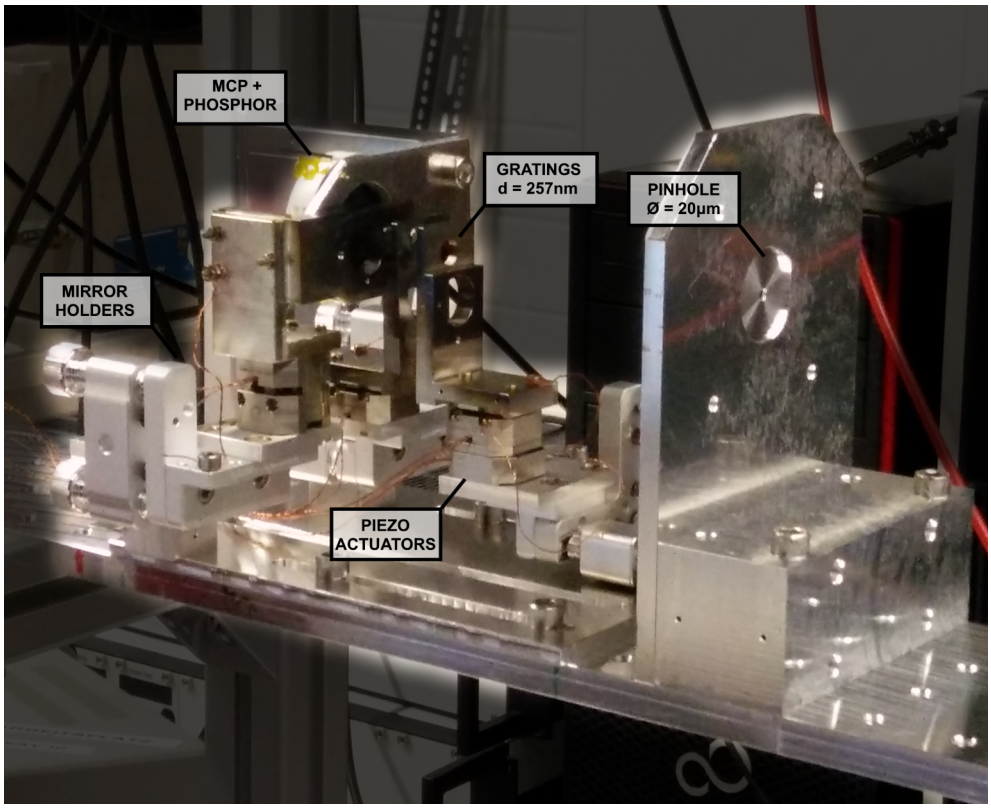

Figure 6.1: Picture and schematic of the proton interferometer being built in Heidelberg. Gratings with a period $d = 257\,\mathrm{nm}$ are mounted on piezo-actuators and mirror holders to take care of the alignment in the limits discussed in Sec. 3. The distance between the gratings is around $1\,\mathrm{cm}$, but it is planned to be increased up to around $10\,\mathrm{cm}$ in order to observe the contrast modulation depicted in Fig. 2.3. The readout is managed via a micro channel plate (MCP) followed by a phosphor screen, whose signal is read via a CCD camera. A pinhole with diameter $20\,\mu\mathrm{m}$ is placed in front of the device to reduce the divergence of the beam, relaxing the alignment limits.

Publications

As a member of a big experimental collaboration, my doctoral work has to be divided into personal contributions, which are directly related to my work in Heidelberg, and indirect contributions, which are instead related to the work performed at CERN. These two types of contribution are listed in separate sections.

Heidelberg group papers

Here you find the list of the papers published by the Oberthaler group from the AEḡIS collaboration to which I have significantly contributed during my doctoral studies. Both papers have been used for producing the results of this thesis.

P. Lansonneur, P. Bräunig, A. Demetrio, S. R. Müller, P. Nedelec, and M. K. Oberthaler
"*Probing electric and magnetic fields with a moiré deflectometer*".
Nucl. Instr. Meth. Phys. Res. A 862 (2017), pp. 49-53.
DOI: 10.1016/j.nima.2017.04.041

A. Demetrio, S. R. Müller, P. Lansonneur, and M. K. Oberthaler.
"*Progress toward a large-scale ion Talbot-Lau interferometer*".
Phys. Rev. A 96 (2017), p. 063604.
DOI: 10.1103/PhysRevA.96.063604.
(*corresponding author* - this paper is included in the Appendix).

AEḡIS collaboration papers

Here you find a list of the papers published by the AEḡIS collaboration during my doctoral studies with myself as an author. By virtue of the rules of the collaboration, all active members are part of the collaboration for more than one year are included in the author list. My personal contributions to most of these papers have been indirect, in the form of the development of software tools to control the experimental process (discussed in Appendix A) or taking part to experimental shifts during the data taking runs.

Papers

Aghion, S., et al. (AEḡIS collaboration)
"Positron bunching and electrostatic transport system for the production and emission of dense positronium clouds into vacuum".
Nucl. Instr. Meth. Phys. Res. B, 362 (2015): 86-92.

Caravita, R., et al. (AEḡIS collaboration).
"Towards a gravity measurement on cold antimatter atoms".
Nuovo Cimento C, 39 (2016): 237.

Aghion, S., et al. (AEḡIS collaboration).
"Laser excitation of the n = 3 level of positronium for antihydrogen production".
Phys. Rev. A, 94.1 (2016): 012507.

Pacifico, N., et al. (AEḡIS collaboration together with the Timepix collaboration).
"Direct detection of antiprotons with the Timepix3 in a new electrostatic selection beamline".
Nucl. Instr. Meth. Phys. Res. A, 831 (2017), 12-17.
***** Concerning this paper, our local group worked on the construction and characterization of the electrostatic line used to select antiproton at different energies. Our group made substantial contributions on testing and improving the hardware.

Consolati, G., et al. (AEḡIS collaboration).
"Positronium for Antihydrogen Production in the AEGIS Experiment".
Acta Phys. Pol. A, 132.5 (2017).

Aghion, S., et al. (AEḡIS collaboration).
"Measurement of antiproton annihilation on Cu, Ag and Au with emulsion films".
J. Inst., 12.04 (2017): P04021.

Aghion, S., et al. (AEḡIS collaboration).
"Characterization of a transmission positron/positronium converter for antihydrogen production."
Nucl. Instr. Meth. Phys. Res., B 407 (2017): 55-66.

Doser, M., et al. (AEḡIS collaboration).
"AEgIS at ELENA: outlook for physics with a pulsed cold antihydrogen beam."
Phil. Trans. R. Soc. A, 376.2116 (2018): 20170274.

Conference proceedings

Kimura, M., et al. (AEgIS collaboration).
"Testing the Weak Equivalence Principle with an antimatter beam at CERN".
J. Phys.: Conference Series, 631, 1 (2015).

Pistillo, C., et al. (AEgIS collaboration).
"Emulsion detectors for the antihydrogen detection in AEgIS".
Hyperfine Interact., 233.1-3 (2015): 29-34.

Testera, G., et al. (AEgIS collaboration).
"The AEgIS experiment".
Hyperfine Interact., 233.1-3 (2015): 13-20.

Consolati, G., et al. (AEgIS collaboration).
"Experiments with low-energy antimatter".
EPJ web of conferences, 96 (2015).

Kellerbauer, A., et al. (AEgIS collaboration).
"Probing antimatter gravity–The AEGIS experiment at CERN".
EPJ Web of Conferences, 126, 02016 (2016).

Consolati, G., et al. (AEgIS collaboration).
"Positronium for Antihydrogen Production in the AEGIS Experiment".
Acta Phys. Pol. A, 132.5 (2017).

Aghion, S., et al. (AEgIS collaboration).
"Measurement of antiproton annihilation on Cu, Ag and Au with emulsion films".
J. Inst., 12.04 (2017): P04021.

Brusa, R. S., et al. (AEgIS collaboration).
"The AEgIS experiment at CERN: measuring antihydrogen free-fall in earth's gravitational field to test WEP with antimatter".
J. Phys.: Conference Series, 791, 1 (2017).

Prelz, F., et al. (AEgIS collaboration).
"The DAQ system for the AEgIS experiment".
J. Phys.: Conference Series, 898, 3 (2017).

Appendix A

Armadillo: a software for the AEgIS experiment

During my time as a member of the AEgIS collaboration, I have developed a software utility to improve the efficiency of the measurement process. Until end of 2014, the normal measurement pipeline in the AEgIS experiment went as follows:

- an excel (.xlsx) file is prepared by one of the members of the trap group. Each row of the file represent an action over the electrodes of the trap system or on the experiment hardware (positron accumulator, electron gun, MCP...);
- the file is manually fed to a LabView program which parses it and sends it row by row to a NI PXI Embedded Real-Time controller (RT) using the time information from a column of the file;
- the data sent to the PXI are periodically downloaded by a Field-Programmable-Gate-Array (FPGA), which in turn transmits the information to the hardware, starting the experimental chain.

This process had an obvious flaw: the first step, writing the configuration files, was not accessible to the average shifter since its complexity. An error on a single setting could cause damage to the hardware severe enough to require opening the vacuum chamber to fix. At the time of this writing, only three people in the collaboration have the necessary knowledge to write down those configuration files[1]. Moreover, this limited the number of measurements during a shift and did not allow for quick modifications of the parameters, effectively losing a lot of beamtime in the process.

At the end of 2014, I developed an original idea of Daniel Krasnický to design a software interface which could make it easier for the average

[1] and for *no reason* they should be allowed to board the same plane at the same time

shifter to start a measurement without having to modify the underlying excel files. The result of this work is a Visual C# application originally named *Run Manager for AEgIS*. Between 2014 and 2018, I have mantained and updated the application, leading to its current version, which is used by the collaboration to run all measurements during a shift. The original name of the application has been changed to *Armadillo - **A**EgIS **R**un **MA**nager: **D**irect **I**nterface for **L**ow-**L**evel **O**perations*. The program could be originally used to perform single measurements or scan on multiple parameters in an automated way.

Figure A.1: The logo of Armadillo - **A**EgIS **R**un **MA**nager: **D**irect **I**nterface for **L**ow-**L**evel **O**perations. Copyright ©: Andrea Demetrio, 2017

The measurement pipeline changed as follows:

- an expert writes a sample excel file for a measurement procedure and an additional file with a list of parameters which can be modified. These parameters contain also hard limits for the values, such that no hardware damage can be caused by an incorrect input;
- the people on shift open the procedure through Armadillo and modify the required parameters to run the measurement;
- Armadillo writes a new excel file using the original as a basis, with the parameters modified by the shifter, then it updates a text file with the run number and the current status;
- the original AEgIS LabView interface reads the Armadillo output and, when a new measurement is issued, it parses the excel files and sends it to the PXI;

- the FPGA downloads the information from the PXI and sends it to the hardware, starting the experimental chain.

These changes allowed for non-expert personnel to run measurements and modify the input files without having access to the underlying code and increased the number of measurements per shift exponentially, especially for positron and electron experimental procedures [Car+15; Tes+15].

In 2016, the program was updated by Giovanni Cerchiari from the AEḡIS collaboration to include a pipeline of measurements to act as an automatic feed to the LabView program. In 2017, I modified this version to implement some additional features, like expected measurement time and parameters defined by mathematical formulas. This improvements were possible due to some interactions with Davide Pagano, also from the AEḡIS collaboration, who suggested to use multi-threaded operations for making the measurement time calculations non-blocking when using the interface.

In its current incarnation, Armadillo is consistently used to perform experimental runs and it is part of the tools that new shifters have to learn to run the experiment.

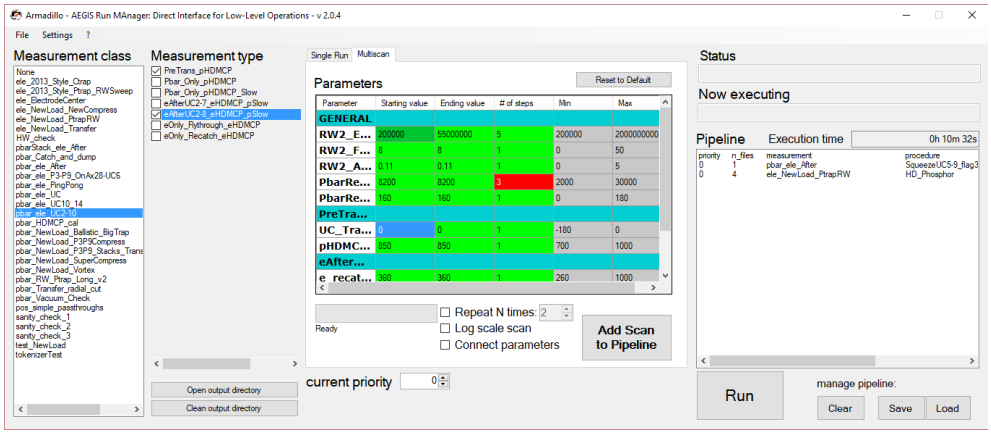

Figure A.2: The GUI of Armadillo, version 2.0.4. *Left:* the **Measurement Class** column lists all the available measurement prototypes, each of which can have several measurement types, listed in the **Measurement Type** column. *Center:* the spreadsheet is used to edit parameters, with color-coded cells to indicate whether the input was valid or not and whether the default parameter was changed or not. *Right:* the measurement pipeline, with additional information such as the number of repetitions and expected measurement time.

Appendix B

Limits on a gravity measurement with a non-collimated antihydrogen source

This appendix contains the original report (July, 2015) about the feasibility of a gravity measurement on antihydrogen in an unedited form. The assumptions from this report present substantial differences compared to the ones considered in this work. Refer to Chapter 5 for an in-depth comparison between the approach developed for this disseration and the one shown in this document. The main discrepancies are listed in the following:

- in the report, the source parameters were largely overestimated, both in terms of effective production rate (a factor 10 on direct mixing) and of the length of the production cycle (100 s instead of ≥ 400 s);

- in the report, no third grating was considered, removing a multiplication factor η from the effective flux and increasing the amount of particles reaching the detector by three times. In this work, we decide to use three gratings, therefore requiring the additional η factor;

- while working in the short configuration, we considered only the so-called "safe volume" (see Tab. 5.2) instead of exploring the possibility of having a better control over the magnetic field;

- the shape of the velocity distributions was supposed to be a three-dimensional Maxwell-Boltzmann for the axial direction. In this work, we separated the three distributions in the three dimensions

and analyzed them separately as a function of the geometry of the interferometer;

- we assumed to have time-of-flight measurements for charge exchange. In this work, we considered the most general case of a detector with no time resolution;
- in the original report, we did not consider any cut-off velocity.

The core concept of this report was presented during a collaboration meeting in June 2015 [Dem+15] and subsequently summarized in the following document.

Limits on a gravity measurement with a non-collimated antihydrogen source

P. Bräunig, A. Demetrio, S. Müller and M. Oberthaler

Kirchoff-Institute for Physics, Heidelberg

This report examines the limits of a gravity measurement within the AEḡIS framework. Special emphasis is put onto the fringe pattern's visibility to be expected if one reaches the wave regime and on the scaling of the sensitivity with the available volume. The goal of this report is to provide an overview on what is the minimum volume in relation to the number of produced particles which would grant a gravity sign measurement with the currently available technology. All the calculations in this report have been carried out assuming $\|\vec{g}\| \simeq 9.81\,\mathrm{m\,s^{-2}}$ for both matter and antimatter.

1. Introduction

The performance of the gravity measuring device is expressed in terms of the minimal detectable acceleration[1, 2], i.e. the shot-noise limit for a given configuration and number of detected antihydrogen atoms ($\bar{H}$)

$$a_{\min} = \frac{d}{2\pi\ \mathcal{V}\ \tau^2\sqrt{N_{\mathrm{det}}}}\ . \tag{1}$$

In case of isotropic antihydrogen production, equation 1 can be written as a function of the number of produced particles, leading to

$$a_{\min} = \underbrace{\frac{d}{2\pi\,\mathcal{V}\,\eta\,r}}_{\text{gratings}} \cdot \underbrace{\frac{2(L_{1\mathrm{st}}+2L)}{L^2}}_{\text{geometry}} \cdot \underbrace{\frac{2\,kT}{m}\frac{1}{\sqrt{N_{\mathrm{prod}}}}}_{\bar{H}\text{ source}}\ , \tag{2}$$

where the following parameters are used:

- d grating periodicity
- $\mathcal{V}$ visibility of the fringe pattern
- $L_{1\mathrm{st}}$ distance between the source and the first grating
- L grating separation
- $\tau = L/v$ time of flight
- η open fraction of the gratings
- r radius of the gratings
- N_{det} number of detected atoms
- N_{prod} number of produced atoms

It is important to note that equation 1 is only valid for a sufficient number of particles detected, since it represents the central limit. Here, we consider a minimum number of 1000 particles detected. Additionally, the visibility $\mathcal{V}$ is not a constant. In the simple case of a (classic) moiré deflectometer it depends solely on the grating's open fraction η. A three grating deflectometer using gratings with an open fraction of 30 % results[1, 2] in a visibility ν of approximately 80 %. For a Talbot-Lau interferometer, the visibility is also a function of the Talbot length $L_{\mathrm{T}} = d^2/\lambda_{\mathrm{dB}}$ and the grating separation L

$$\mathcal{V} = \mathcal{V}(\eta, L_{\mathrm{T}}, L)\ . \tag{3}$$

The de Broglie wavelength

$$\lambda_{\mathrm{dB}} = \frac{h}{p} = \frac{h}{m\,v} \tag{4}$$

leads to the Talbot length [3, 4]

$$L_{\mathrm{T}} = \frac{d^2}{\lambda_{\mathrm{dB}}} = \frac{m\,v\,d^2}{h}\ . \tag{5}$$

The visibility of a Talbot-Lau interferometer's fringe pattern is high if the grating separation equals a multiple integer of the Talbot length $L = n\ L_{\mathrm{T}}$ and is low if this is not fulfilled. For a given configuration, the exact shape of the fringe pattern, and thus its visibility, can elegantly be determined using the free evolution of the Wigner function

$$w(\mathbf{r},\mathbf{p}) = \frac{1}{2\pi\hbar}\int \mathrm{d}\boldsymbol{\Delta}\, e^{\frac{i\mathbf{p}\boldsymbol{\Delta}}{\hbar}}\,\rho\left(\mathbf{r}-\frac{\boldsymbol{\Delta}}{2},\mathbf{r}+\frac{\boldsymbol{\Delta}}{2}\right)\ . \tag{6}$$

A detailed discussion can be found in [5, 2]. The important result of this derivation is the shape of the fringe pattern. This is given by

$$S\,(y_3, v) \propto \sum_{l\,\in\,\mathbb{Z}} (A'_l)^2 B'^{(\mathrm{T})}_{2l}(v)\ \exp\left(k_d il\ (y_3+\Delta y)\right), \tag{7}$$

where $k_d = 2\pi/d$ is the grating vector, y_3 is the position of the (movable) third grating and $\Delta y = g\tau^2 = gL^2/v^2$ is the phase shifted induced by gravity. The coefficient A correspond to the first and the third grating (for this reason this coefficient is squared) and B is a coefficient that describes the influence of the second grating. A is given by

$$A'_l = \sum_{j\,\in\,\mathbb{Z}} a'_j\ a'^{*}_{j-l}\ , \tag{8}$$

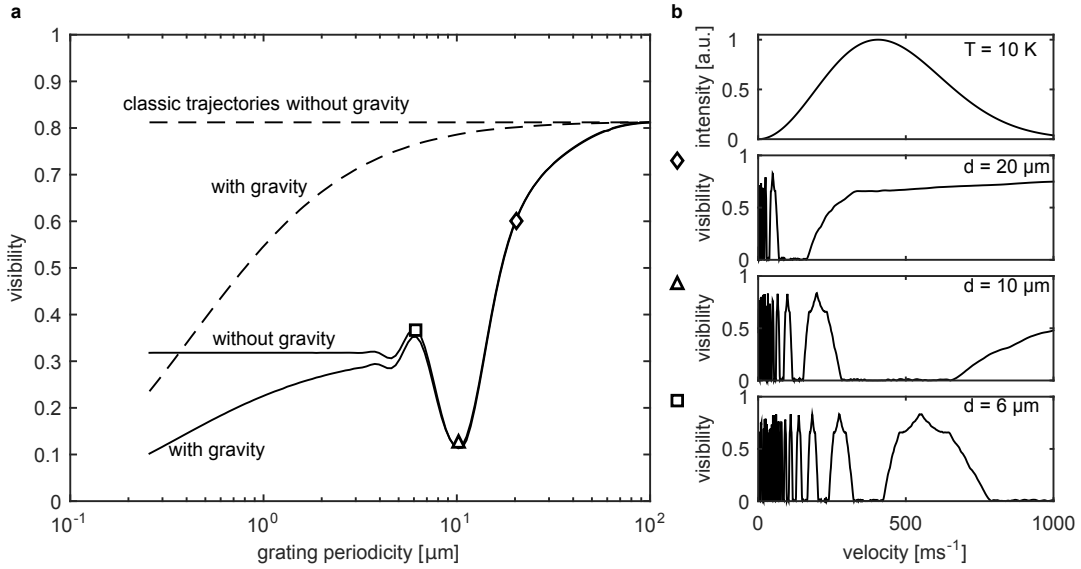

Figure 1: Visibility of a Talbot-Lau interferometer as a function of the grating periodicity (5 cm grating separation, 10 K antihydrogen temperature and $\eta = 0.3$ open fraction). For a large grating period, the system approaches the classic regime. Two effects cause the visibility to decrease: (a) Different velocity classes are shifted due to gravity by a different amount following $\Delta y = g\tau^2 = gL^2/v^2$. This smears out the fringe pattern. It is important to note that this also occurs in a classic moiré deflectometer. (b) Visibility decrease due to Talbot length mismatch for three exemplary grating periods. The figure on the top depicts the Maxwell-Boltzmann-like velocity distribution. The three figures below show the visibility of each velocity for the grating periods 20 μm, 10 μm and 4 μm. One can see that that not all velocities contribute to the fringe signal. In the classic regime, the visibility is nearly flat. For smaller grating periods, the distinct peaks of high visibility correspond to the rephasing of the Talbot pattern which scales with d^2.

where a are simply Fourier coefficients

$$a_n = \eta\,\mathrm{sinc}(n\,\eta)\cdot e^{-ink_d y_\mathrm{i}} = a'_n \cdot e^{-ink_d y_\mathrm{i}} \tag{9}$$

of the Fourier series of an amplitude grating with open fraction η described by

$$t_i(y) = \sum_{n\,\in\,\mathbb{Z}} a_n \exp\left(ink_d y\right)\ . \tag{10}$$

Thus, the coefficients of the first and third grating describe simple masking or shadowing of the beam. In a Talbot-Lau interferometer, the influence of the second grating is considerably different as it includes particle diffraction at this grating's passage. This is expressed in the second coefficient

$$B_j^{(\mathrm{T})}(v) = \sum_{m\,\in\,\mathbb{Z}} b_m b^*_{m-j} \exp\left(i\pi\frac{j^2-2mj}{2}\frac{L}{L_T}\right) \tag{11}$$

$$= \sum_{m\,\in\,\mathbb{Z}} b_m b^*_{m-j} \exp\left(i\pi\frac{j^2-2mj}{2}\frac{L\ h}{m\ v\ d^2}\right)\ , \tag{12}$$

which includes an additional phase factor that depends on the Talbot length L_T. With equation 7, one can extract the visibility using a monochromatic beam with velocity v via

$$\mathcal{V} = \frac{\max(S)-\min(S)}{\max(S)+\min(S)}\ . \tag{13}$$

For a given velocity distribution $p(v)$, the visibility is not the same for each velocity class as the condition $L = n\ L_\mathrm{T}$ can not simultaneously be fulfilled. Additionally, the fringe patterns of the different velocity classes are shifted by a different amount. This smearing of the pattern results in a further reduction of the visibility. Thus, if no time-of-flight is available, the resulting fringe pattern is given by the integral

$$S(y_3) \propto \int S(y_3, v)\ p(v)\ \mathrm{d}v\ . \tag{14}$$

In the following, we assume the velocities to be Maxwell-Boltzmann distributed:

$$p(v) \propto v^2\ \exp\left(-\frac{mv^2}{2k_B T}\right)\ . \tag{15}$$

Figure 1 shows the result of an exemplary configuration ($L = 50$ mm, $T = 10$ K and $\eta = 0.3$) where one can grasp the different effects that come into play considering the visibility of the fringe pattern.

2. Scenarios

Two different experimental scenarios seem accessible in the near future. The first one is the antihydrogen production via charge exchange of antiprotons and positronium. The second one is the direct mixing of antiprotons

and positrons. As flux, temperature and solid angle of emission are quite different, these are treated separately. Before describing the differences between the two scenarios more closely, one can summarize the assumptions that both have in common:

- The antihydrogen atoms are produced in a high Rydberg state but decay to the ground state with the hyperfine splitting quantum number F = 0, 1 before entering the measurement volume.
- The magnetic field gradient in the measurement volume is considerably smaller than $0.2\,\mathrm{G\,cm^{-1}}$. For ground-state antihydrogen, this corresponds to an acceleration of approximately $10\,\mathrm{m\,s^{-2}}$ [6, 7].
- The detector has a quantum efficiency of 100 %.
- A shift of 8 hours with one antiproton shot every 100 s leads to 288 shots per shift.
- A sign measurement of the gravitational acceleration corresponds to a precision of 30 %, so that a null result is excluded with 3σ.

One should note that the first two assumptions are critical but the discussion how this could be realized goes beyond the scope of this manuscript.

2.1. Available Volume

Two geometric configuration are considered here. The first one is to place the measurement apparatus inside the 1 T magnet, the second one is to place it on the outside.

2.1.1. Inside the 1 T magnet

The available volume inside the chamber is approximately a cylinder with a length of 690 mm from the end of the antihydrogen production trap and a maximum radius of 32.5 mm in the narrowest point. The position of the first grating has been set at the end of the production trap, 70 mm far from the estimated antihydrogen production point.

Another limitation which has to be overcome in order to perform the measurement in this region is the effect of the magnetic field on the trajectories of the particles. For ground-state antihydrogen, the region in which the magnetic field gradient is significantly smaller than the limit described in section 2 is approximately a cylinder 10 cm long from the end of the trap and 3 mm wide in the radial direction [6, 7].

Here, we decided to analyse different geometric setups, the longest of which would require an expansion of the cryogenic chamber: the distance between the gratings varies from 5 cm to 40 cm, while the radius of the gratings varies from 1.5 mm to 25 mm, in order to fit these restrictions. Notice that only the smallest measurement device ($L = 5\,\mathrm{cm}$, $r = 1.5\,\mathrm{mm}$) would fit the region in which the magnetic field effect is negligible.

2.1.2. Outside the 1 T magnet

Outside the apparatus the volume constraints are less restrictive than inside. As a result, the maximum radius for the gratings has been considered equal to 50 mm, which is the current dimension of the 40 µm period gratings. The distance between the antihydrogen production point and the first grating has been considered equal to 800 mm. The distance between the gratings varies from 50 mm to 400 mm.

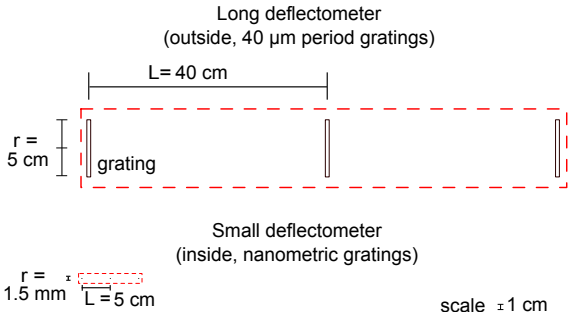

Figure 2: Scale drawing which compares the devices considered in this report: the smallest one is designed such as it would fit the current magnetic field constraints inside the bore, while the largest one has been designed to be used with the biggest gratings available at the moment.

2.2. Charge Exchange

For this process, we assume that a temperature of 10 K is reached in the first experimental realisation. The temperature of the produced antihydrogen has been considered equal to 10 K[8]. The emission is not isotropic, due to the rotation of the $\bar{\mathrm{p}}$ plasma, but the efficiency at T = 10 K is smaller only by a factor of the order of 10 % compared to the isotropic emission (see figure 3). Thus, one can apply formula 1, assuming a 4π isotropic formation. According to reference [8], the production rate has been considered equal to 3 antihydrogen atoms every 3 antiproton shots (300 s). Assuming 288 antiproton shots per shift, this leads to a total production rate of $\sim 10^2$ antihydrogen atoms/shift. As shown in figure 8a, for small periodicities the measurement of the time-of-flight would grant a higher visibility than in direct mixing case, mostly due to the fact that each velocity class can be grouped separately. This production scheme has been considered only for a measurement inside the existing apparatus (figure 9).

By knowing the production rate, one can estimate the time needed to see at least 10^3 particles on the detector, since - as mentioned in section 1 - this is a necessary condition to run any statistical analysis. Assuming a sample configuration, the number of detected particle is given by:

$$N_{\mathrm{det}} = \eta^2 \frac{\Delta\Omega}{4\pi} N_{\mathrm{prod}} \,, \tag{16}$$

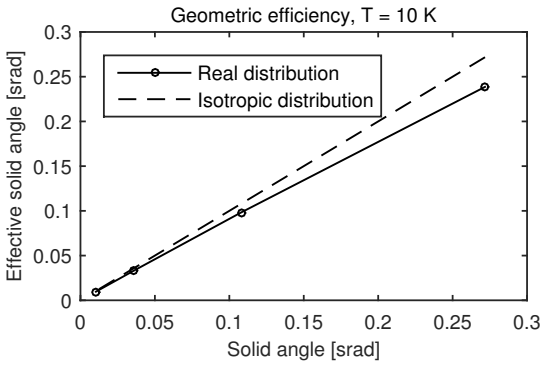

Figure 3: Geometric efficiency of charge exchange production as a function of the solid angle. The plot has been obtained by means of a Monte Carlo simulation on 10^9 particles per point. The parameters of the simulation have been set according to the calculations performed in reference [8]. The asymptotic limit in the figure presented is the isotropic 4π emission. Notice that for T = 10 K, the loss in efficiency due the rotation of the antiproton plasma is approximately 10% while compared with an isotropic production.

where

$$\Delta\Omega \;=\; \frac{\pi r^2}{(L_{1\mathrm{st}}+2L)^2}\;. \tag{17}$$

With $L_{1\mathrm{st}} = 7\,\mathrm{cm}$, $L = 5\,\mathrm{cm}$, $r = 25\,\mathrm{mm}$, and $\eta \;= 0.3$, this yields:

$$N_{\mathrm{det}} \;\simeq\; 4.9\;10^{-5} N_{\mathrm{prod}}\;, \tag{18}$$

leading to $N_{\mathrm{prod}} \simeq 1.8\;10^6$ for $N_{\mathrm{det}} \;= 1000$. Assuming the production rate stated above and 288 antiproton shots per day, this leads to $1.8\;10^3$ days of integration ($\simeq$5 years of continuous measurement). An insight on this estimation for different values of L and r is provided in figure 5. This graph should be carefully considered when reviewing the results shown in figure 9. Figure 13 summarizes the situation in detail for the shortest inside configuration.

2.3. Direct Mixing

In the process of direct mixing, the emission of antihydrogen atoms is not isotropic. Following N. Madsen et al. (Athena[9]), the radial temperature is factor 10 smaller than the longitudinal temperature. Consequently, the radial velocity is reduced by a factor $\sqrt{10}$, causing the atoms to leave the production volume in two cone-shaped beams as depicted in figure 4. This also requires a small modification in the minimal detectable acceleration which is given in this case by equation 19.

$$a_{min} = \underbrace{\frac{d}{2\pi\,\mathcal{V}\,\eta\,r}}_{\text{gratings}} \cdot \underbrace{\frac{(L_{1\mathrm{st}}+2L)}{L^2}}_{\text{geometry}} \cdot \underbrace{v_{\parallel}\;\cdot v_{\perp}}_{\text{velocities}} \cdot \underbrace{\frac{\sqrt{2}}{\sqrt{N_{\mathrm{prod}}}}}_{\bar{H}\text{ source}}\;. \tag{19}$$

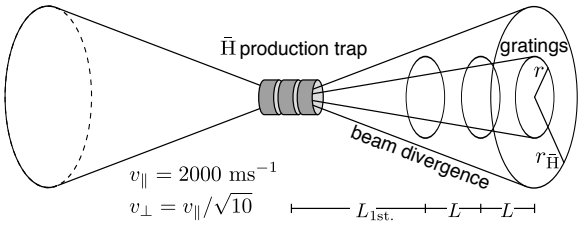

Figure 4: In the direct mixing production, the radial temperature is a factor 10 smaller than the axial temperature[9]. The antihydrogen emission is therefore not isotropic, instead, it can be described by two cones defined by the radial and the longitudinal velocity.

No time-of-flight information is retrieved. As a result, the shift due to gravity has to be smaller than half the period of the grating. This condition is included in formula 1 and accounts for loss in sensitivity for small periodicities: since the patterns due to different velocity classes cannot be distinguished, the resulting fringe visibility will drop for small periods (see figure 8b). However, it should be noted that in this case there would be no problem due to huge magnetic filed gradients before the measurement volume as far as the gradient inside the deflectometer is significantly smaller than $0.2\,\mathrm{G\,cm^{-1}}$. In this configuration, the expected production rate would be $1.5\;10^4$ particles each antiproton shot ($\sim$100 s). Assuming 288 antiproton shots per shift, this leads to a total production rate of $\sim 4.3\;10^6$ antihydrogen atoms/shift.

This production scheme has been considered both for a measurement inside (figure 10) and outside the cryogenic chamber (figure 11).

Following the same motivations expressed in section 2, one can estimate the time needed to detect 10^3 particles in a similar fashion. Assuming the anisotropic distribution expressed by equation 19, the number of detected particle is given by:

$$N_{\mathrm{det}} \;=\; \eta^2 \frac{r^2}{2\;r_{\mathrm{beam}}^2} N_{\mathrm{prod}}\;, \tag{20}$$

where

$$r_{\mathrm{beam}} \;=\; v_{\perp}\;\frac{L_{1\mathrm{st}}+2L}{v_{\parallel}} \;=\; \frac{L_{1\mathrm{st}}+2L}{\sqrt{10}}\;. \tag{21}$$

Equation 20 can be then rewritten as

$$N_{\mathrm{det}} \;=\; \eta^2 \frac{5\;r^2}{(L_{1\mathrm{st}}+2L)^2} N_{\mathrm{prod}}\;, \tag{22}$$

With $L_{1\mathrm{st}} = 7\,\mathrm{cm}$, $L = 5\,\mathrm{cm}$, $r = 25\,\mathrm{mm}$, and $\eta \;= 0.3$, this yields:

$$N_{\mathrm{det}} \;\simeq\; 9.72\;10^{-3} N_{\mathrm{prod}}\;, \tag{23}$$

leading to $N_{\mathrm{prod}} \simeq 10^5$ for $N_{\mathrm{det}} \;= 1000$. Assuming the production rate stated above and 288 antiproton shots per day, this leads to less than one day of integration. An

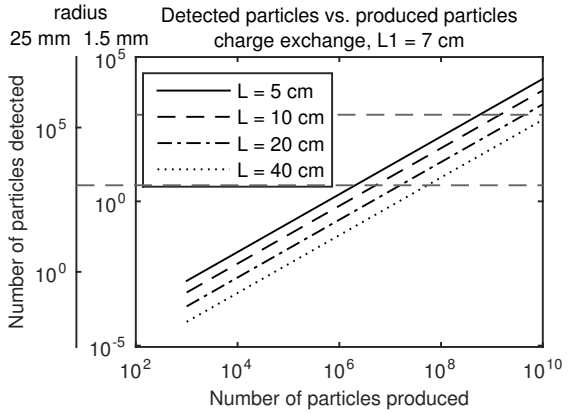

Figure 5: Number of particles detected as a function of the number of particles produced, following equation 16 for charge exchange production. Here $L_{1\mathrm{st}} = 7\,\mathrm{cm}$, $T = 10\,\mathrm{K}$. The dashed horizontal lines highlight the number of particles produced which results in 10^3 particle detected.

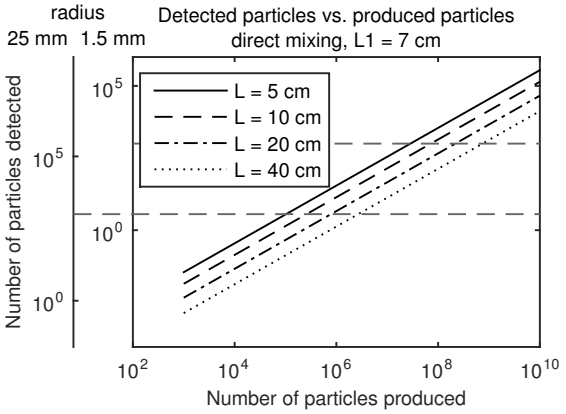

Figure 6: Number of particles detected as a function of the number of particles produced, following equation 16 for direct mixing production. Here $L_{1\mathrm{st}} = 7\,\mathrm{cm}$, $L_{1\mathrm{st}} = 80\,\mathrm{cm}$, $T_{\parallel} = 200\,\mathrm{K}$, $T_{\perp} = 20\,\mathrm{K}$. The dashed horizontal lines highlight the number of particles produced which results in 10^3 particle detected.

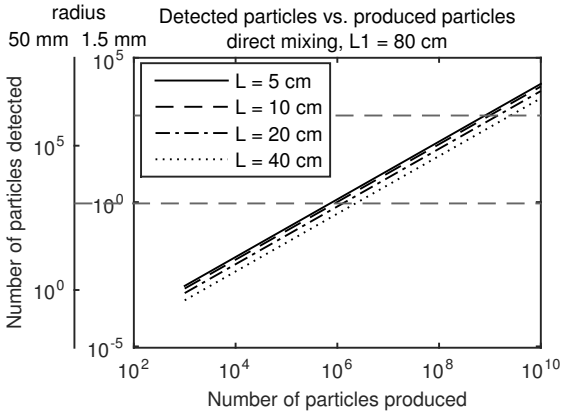

Figure 7: Number of particles detected as a function of the number of particles produced, following equation 16 for direct mixing exchange production. Here $L_{1\mathrm{st}} = 80\,\mathrm{cm}$, $T_{\parallel} = 200\,\mathrm{K}$, $T_{\perp} = 20\,\mathrm{K}$. The dashed horizontal lines highlight the number of particles produced which results in 10^3 particle detected.

insight on this estimation for different values of L and r is provided in figures 6 and 7. These two graphs should be carefully considered when reviewing the results shown in figures 10 and 11 respectively. Figure 14 summarizes the situation in detail for the longest configuration.

Conclusions

Both production methods have been reviewed according to the most recent data provided by the groups in the collaboration. According to the calculations shown, it seems not feasible to perform a gravity measurement by means of charge exchange production, mainly due to statistics: at least 10^6 particles have to be produced in order to detect 10^3 particles on the detector, leading to $\sim$ 3.5 10^3 shifts (10 years of continuous measurement), as shown in figures 9 and 5. Concerning direct mixing approach, in the region in which magnetic field gradients are negligible (setup with $L_{1st} = 7\,\mathrm{cm}$, $L = 5\,\mathrm{cm}$, $r = 1.5\,\mathrm{mm}$, and $d = 265\,\mathrm{nm}$), about 1.5 10^8 particles have to be produced, as shown in figure 10, leading to approximately 35 shifts The number of detected particles would be higher than 10^3, thus satisfying the statistics required. However, it seems not feasible to make antihydrogen atoms decay to the ground state before reaching the first grating in this configuration, thus limiting its use for the gravity measurement.

If the deflectometer is instead placed outside the 1 T magnet (thus removing the radial limitation due to the internal space), the minimum distance from the production point would be approximately 80 cm. In this case, by employing direct mixing production, 50 mm radius gratings, $L = 40\,\mathrm{cm}$ and $d = 40\,\mu\mathrm{m}$, less than 10 shifts would be required to perform a sign measurement (see figures 11 and 12).

Notice that this result could get worse due to a number of factors, including but not limited to the actual production rate achievable in two years, the performance of the detector, the design of a measurement device and a data analysis procedure which could actually achieve the precision shown in this report.

Moreover, if time-of-flight information is not retrieved, more than one configuration could be necessary to perform the measurement, thus increasing the required time. Magnetic fields have also to be taken into account, since a gradient of $0.2\,\mathrm{G\,cm^{-1}}$ could fake out gravity.

References

[1] M. K. Oberthaler. Inertial sensing with classical atomic beams. *Physical Review A*, 54(4):3165–3176, 1996.

[2] Philippe H. M. Bräunig. *Atom Optical Tools for Antimatter Experiments*. PhD thesis, Heidelberg University, 2014.

[3] E. Lau. Beugungserscheinungen an Doppelrastern. *Annalen der Physik*, 437:417–423, 1948.

[4] H. F. Talbot. Facts relating to Optical Science No IV. *Philosophical Magazine Series 3*, 9(56):401–407, 1836.

[5] K. Hornberger, J. E. Sipe, and M. Arndt. Theory of decoherence in a matter wave Talbot-Lau interferometer. *Physical Review A*, 70(5), 2004.

[6] A. Demetrio. Gravity measurement in a shorter configuration, 2014.

[7] A. Demetrio. Gravity measurement on antihydrogen in AEgIS: numerical simulation of perturbative effects. Master's thesis, Università degli Studi di Genova, 2014.

[8] AEgIS Genoa group. Antihydrogen formation by charge exchange: summary of realistic numbers, 2015.

[9] N. Madsen et al. Spatial distribution of cold antihydrogen formation. *Physical Review Letters*, 2005.

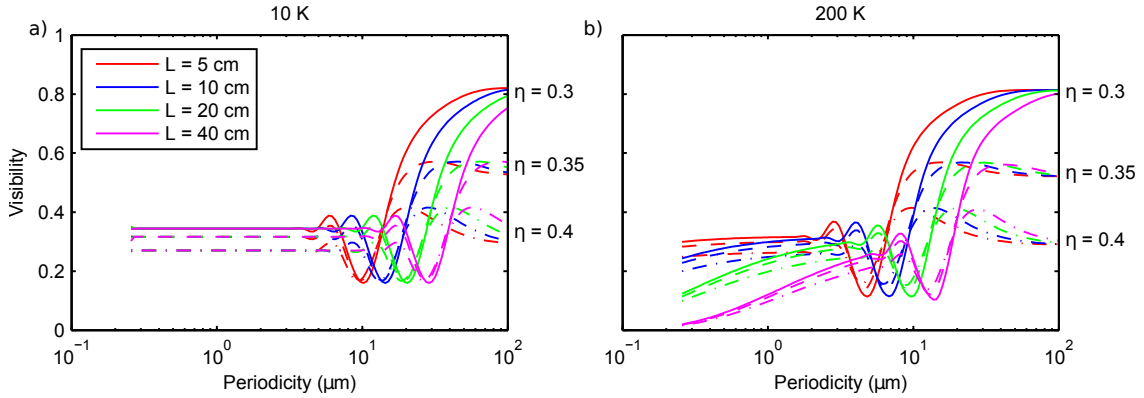

Figure 8: Visibility as a function of the grating periodicity for different grating separation L and opening fractions η. Each opening fraction is represented with a different line style. (a) Charge exchange production at 10 K. There is no visibility decrease due to gravity as one can perform a time-of-flight measurement here. (b) Direct mixing at 200 K.

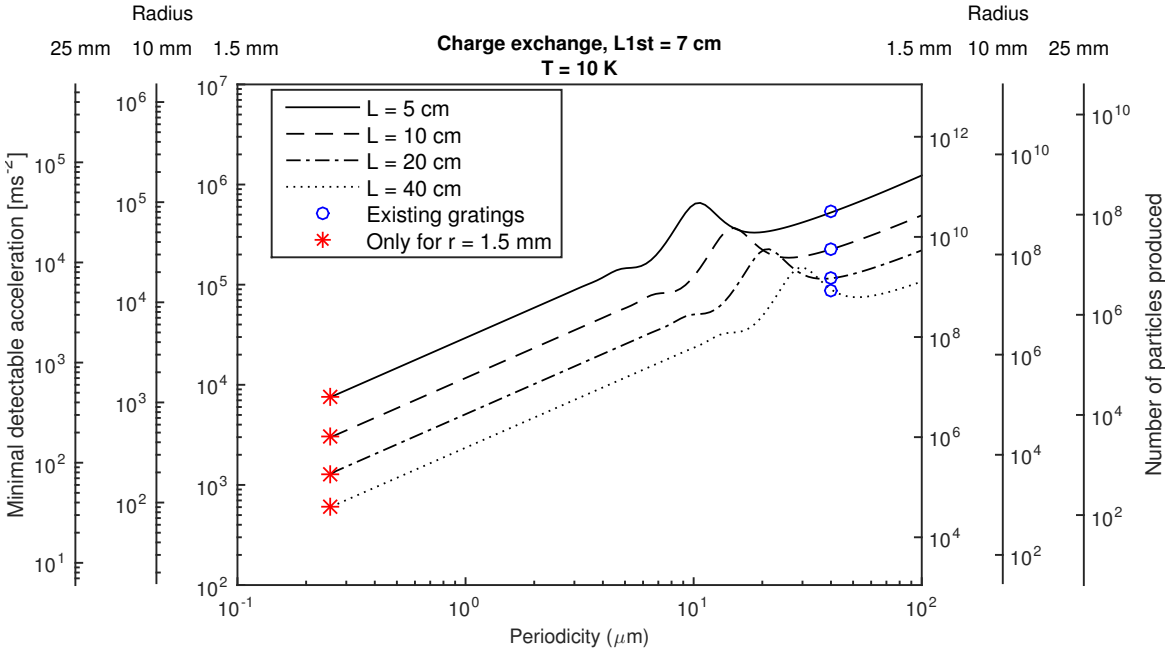

Figure 9: Left axes: minimal detectable acceleration divided by the square root of the number of produced particles. Different lengths L and grating radii r. 10 K. Right axes: number of produced antihydrogen atoms required to reach a relative precision of 30 % (a.k.a. sign measurement). Notice that the number presented on the right axes does not include the minimum detected number of 1000 particles considered in section 1: the data presented have to be compared and scaled according to figure 5.

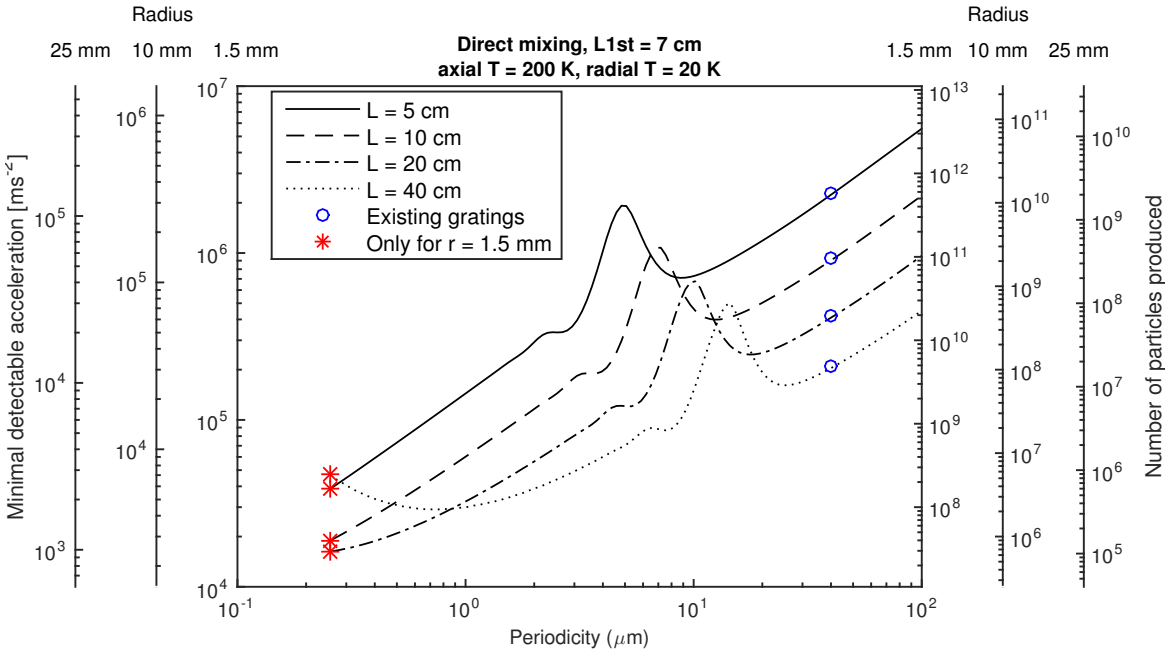

Figure 10: Left axes: minimal detectable acceleration divided by the square root of the number of produced particles. Distance from the antihydrogen production point $L_{1st} = 7\,\mathrm{cm}$. Different lengths L and grating radii r. Axial temperature equal to 200 K, radial temperature equal to 20 K. Right axes: number of produced antihydrogen atoms required to reach a relative precision of 30 % (a.k.a. sign measurement).Notice that the number presented on the right axes does not include the minimum detected number of 1000 particles considered in section 1: the data presented have to be compared and scaled according to figure 6.

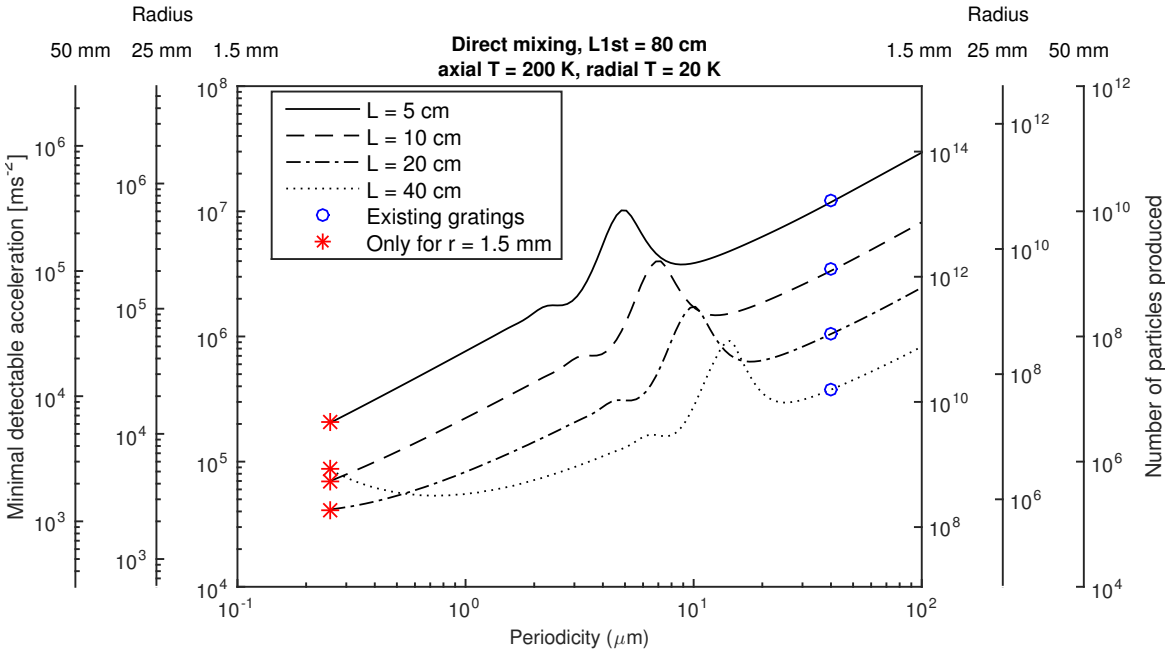

Figure 11: Left axes: minimal detectable acceleration divided by the square root of the number of produced particles. Distance from the antihydrogen production point $L_{1st} = 80\,\text{cm}$. Different lengths L and grating radii r. Axial temperature equal to 200 K, radial temperature equal to 20 K. Right axes: number of produced antihydrogen atoms required to reach a relative precision of 30 % (a.k.a. sign measurement). Notice that the number presented on the right axes does not include the minimum detected number of 1000 particles considered in section 1: the data presented have to be compared and scaled according to figure 7.

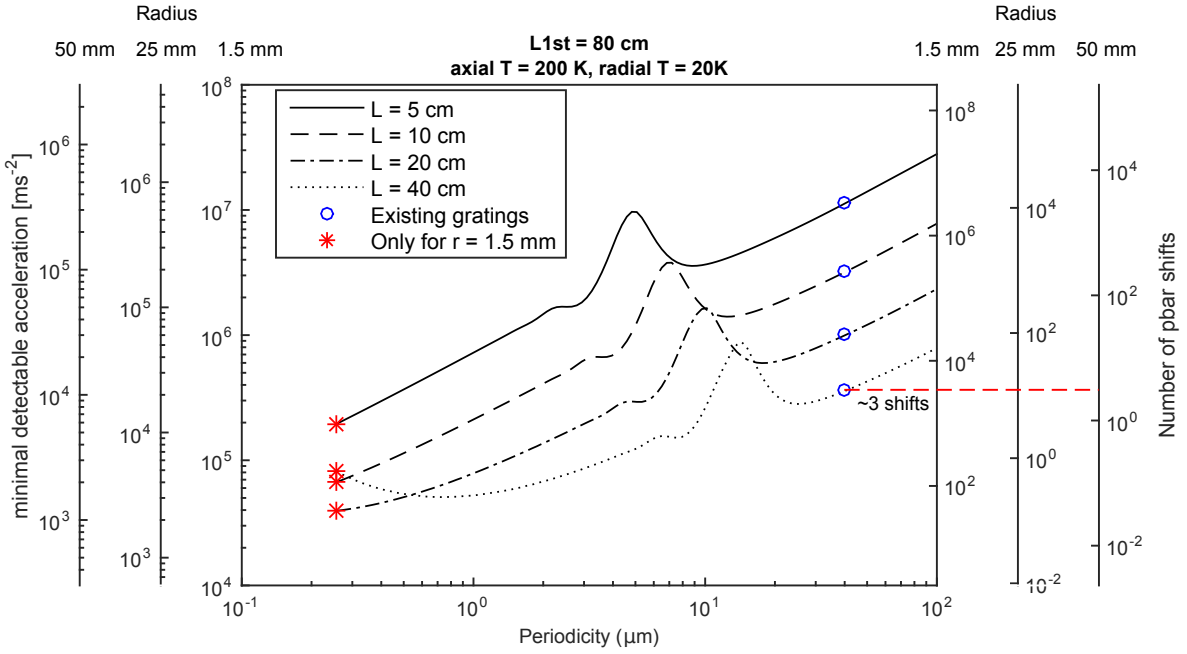

Figure 12: Left axes: minimal detectable acceleration divided by the square root of the number of produced particles. Distance from the antihydrogen production point $L_{1st} = 80\,\text{cm}$. Different lengths L and grating radii r. Axial temperature equal to 200 K, radial temperature equal to 20 K. Right axes: number of required 8 h $\bar{\text{p}}$ shifts to reach a relative precision of 30 % (a.k.a. sign measurement) assuming 15000 antihydrogen atoms produced every 100 s. By employing $d = 40\,\mu\text{m}$, $r = 5\,\text{cm}$ gratings, $L = 40\,\text{cm}$, the number of shifts needed to perform the measurement would be of the order of 3. According to figure 7, the number of particles detected in this configuration would be higher than 10^3, thus satisfying the statistics required for the validity of equation 1.

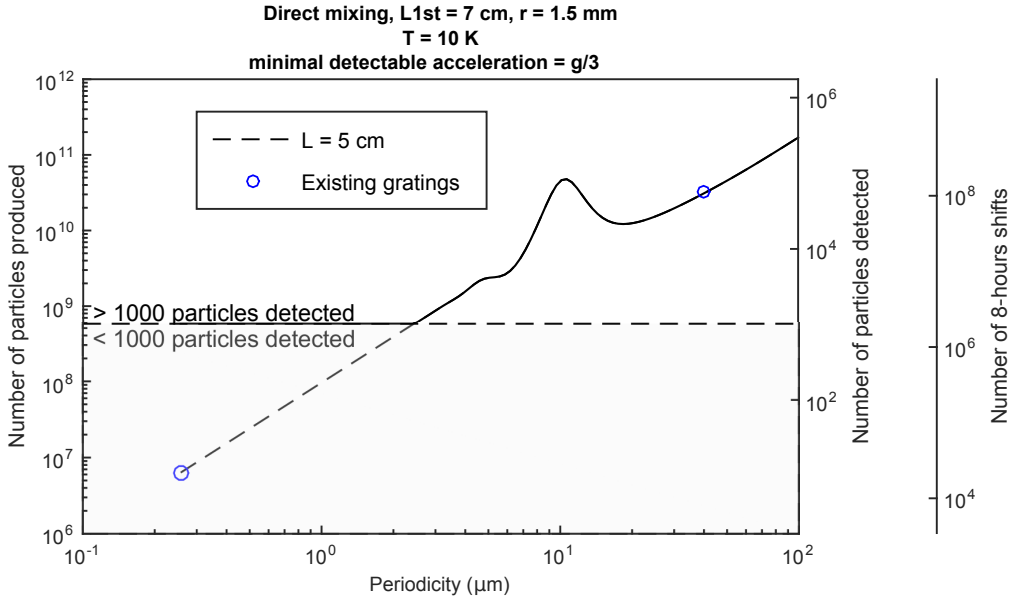

Figure 13: Left axis: number of particle produced in order to have $\|\vec{a}_{\min}\| = g/3$. Distance from the antihydrogen production point $L_{1st} = 7\,\text{cm}$. $L = 5\,\text{cm}$, $r = 1.5\,\text{mm}$. Production temperature equal to 10 K. Inner right axis: number of particles detected relative to the number of particles produced shown on the left axis. Outer right axis: number of required 8 h $\bar{\text{p}}$ shifts to reach a relative precision of 30 % (a.k.a. sign measurement) assuming 3 antihydrogen atoms produced every 300 s.

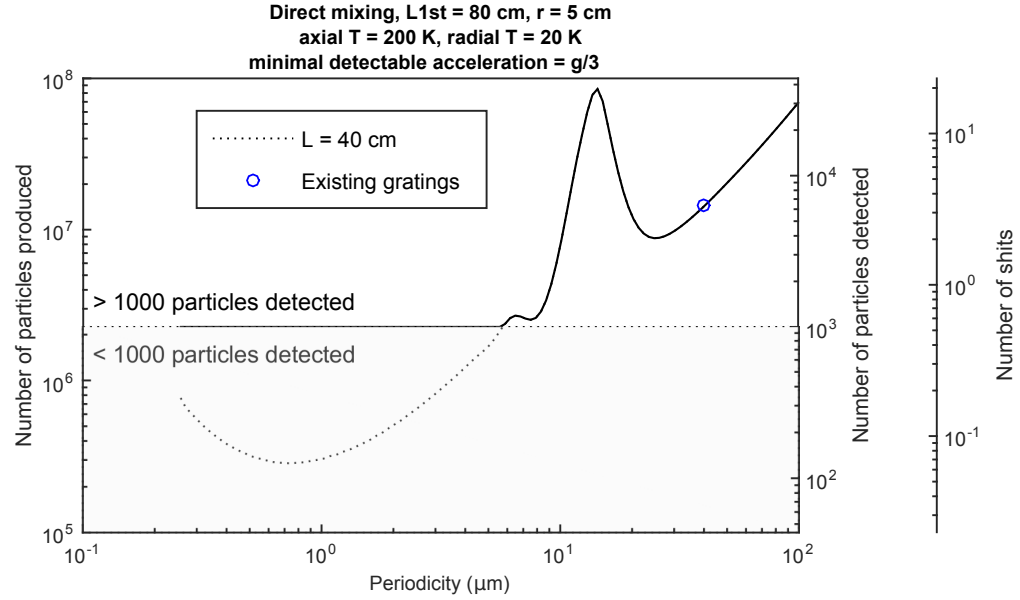

Figure 14: Left axis: number of particle produced in order to have $\|\vec{a}_{\min}\| = g/3$. Distance from the antihydrogen production point $L_{1st} = 80\,\text{cm}$. $L = 40\,\text{cm}$, $r = 50\,\text{mm}$. Axial temperature equal to 200 K, radial temperature equal to 20 K. Inner right axis: number of particles detected relative to the number of particles produced shown on the left axis. Outer right axis: number of required 8 h $\bar{\text{p}}$ shifts to reach a relative precision of 30 % (a.k.a. sign measurement) assuming 15000 antihydrogen atoms produced every 100 s.

Appendix C

Progress toward a large-scale ion Talbot-Lau interferometer

This appendix contains the paper published on the alignment and field constraints for a Talbot-Lau interferometer. The results and the formulas presented in this paper have been as a basis for the development in Chapter 3 and Chapter 4. The formulas for the critical fields were originally introduced in [Lan+17], and subsequently improved for the paper added in this appendix. The paper is reported in an unedited form, in compliance with the copyright and terms of use from APS Journals, concerning the use of an authored paper in a dissertation.

PHYSICAL REVIEW A **96**, 063604 (2017)

Progress toward a large-scale ion Talbot-Lau interferometer

Andrea Demetrio,[1,*] Simon R. Müller,[1] Pierre Lansonneur,[2] and Markus K. Oberthaler[1]
[1]*Kirchhoff-Institut für Physik, Im Neuenheimer Feld 227, 69120 Heidelberg, Germany*
[2]*Institut de Physique Nucléaire de Lyon, CNRS, IN2P3, 69622 Villeurbanne, France*
(Received 27 October 2017; published 4 December 2017)

The Talbot-Lau interferometer is a proven tool to perform measurements in the near-field regime. It has been extensively used for investigating the wave nature of electrons, atoms, and complex organic molecules. However, when designing devices with high geometrical acceptances, which would be desirable when dealing with low-intensity sources of particles, the alignment requirements become much more stringent. Furthermore, if the particles are charged, the influence of external fields becomes quickly non-negligible when increasing the length of the device. This paper focuses on both the geometric and physical constraints of an ion Talbot-Lau interferometer, with emphasis on the scaling of such constraints with the size of the device. Mathematical formulas which set limits on the critical parameters are derived and applied to a test setup for protons.

DOI: 10.1103/PhysRevA.96.063604

I. INTRODUCTION

The wave-particle duality is one of the most defining phenomena related to quantum mechanics. Since the experiment performed by Davisson and Germer [1], this constitutive property of matter has been verified several times, for different kind of particles, ranging from electrons [2–4] to organic compounds [5]. A common concept among these experiments is the design and use of a setup which allows the wave function of the particles to self-interfere or be macroscopically diffracted. Among the devices designed for this purpose, the Talbot-Lau near-field interferometer has seen prominent use in the past two decades, having been successfully applied to electrons [6], atoms [7], fullerenes [8], and, in its Kapitza-Dirac variant, even larger organic molecules [9].

A device of this type has been proposed to be used with antiprotons [10], dealing at once with charged particles heavier than the electron and a low-luminosity, highly divergent source. The latter constraint makes an interferometer with a large active area necessary.

However, when scaling up the device to get a higher geometrical acceptance, a precise alignment of all its elements becomes critical. Moreover, when increasing the length of the device, the influence of external forces acting on the particles increases quadratically with its size, setting strict limits on their maximum allowed energy spread, depending on the intensity of the force.

This paper focuses on both the geometrical and the physical constraints of such a device, with emphasis on electric and magnetic interactions which would affect the design of an ion Talbot-Lau interferometer.

II. TALBOT-LAU INTERFEROMETER

In its most common variant, the Talbot-Lau interferometer is composed of two material gratings with periodicity d and open fraction η. The two gratings are spaced by a distance L. A diffusive beam of particles with de Broglie wavelength λ_{dB} impinging on the first grating generates an interference pattern, as shown in Fig. 1. The pattern appears as a density modulation with periodicity d and corresponding position $\phi = 2\pi y/d$ when observed on a plane placed at the same distance L from the second grating.

The device described so far can act in the classical regime, in the near-field wave regime, or in the far-field wave regime, depending on its geometrical parameters. The typical length scale which is considered to distinguish the three regimes is called the Talbot length and is defined as

$$L_{\mathrm{T}} = \frac{d^2}{\lambda_{\mathrm{dB}}} = \frac{d^2}{h}\sqrt{2mU}, \tag{1}$$

with m being the mass of the particle, U the kinetic energy, and h the Planck constant. If $L \gg L_{\mathrm{T}}$, the device operates in the far-field regime as a Mach-Zehnder interferometer [11]. In this configuration, the contrast of the pattern, defined as

$$C = \frac{I_{\max} - I_{\min}}{I_{\max} + I_{\min}}, \tag{2}$$

where $I_{\max}$ and $I_{\min}$ are the maximum and the minimum intensity, respectively, reveals no dependence on the de Broglie wavelength of the particles (achromatic setup) [12]. If $L \approx L_{\mathrm{T}}$, the device operates in the near-field regime and the contrast shows a dependence on both the energy of the particles and the open fraction η of the gratings, as shown in Fig. 2. This is what is referred to as the Talbot-Lau interferometer. In the limit of $L \ll L_{\mathrm{T}}$, the pattern is generated by the classical trajectories of the particles. This is again an achromatic setup, with the contrast of this pattern depending only on the open fraction η. A device which operates in these conditions is commonly referred to as the moiré deflectometer [13–15]. For specific configurations satisfying $L = nL_{\mathrm{T}}$, with $n \in \mathbb{Z}^+$, the Talbot-Lau interference pattern is indistinguishable from the corresponding classical pattern [16,17]. The ideal configuration to reveal the wave behavior of the test particles is therefore not at this resonance condition.

In a typical experiment, the length of the device is fixed, while the energy of the particles is tuned. Thus one expects that for certain energies U_n the condition $L = nL_{\mathrm{T}}$ is fulfilled.

*Corresponding author: talbotsystematics@matterwave.de

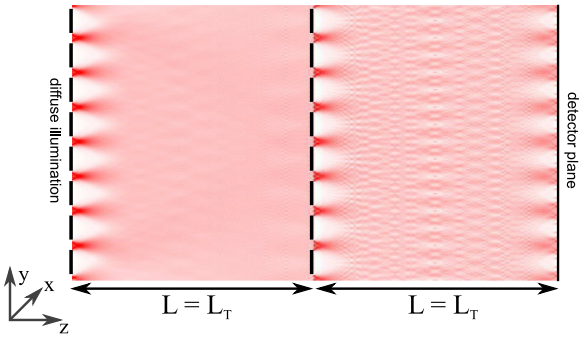

FIG. 1. Diffuse illumination (light, particles) impinging on a Talbot-Lau interferometer generates the so-called Talbot carpet. The first grating generates the spatial coherence, allowing the second grating to create the pattern. A third grating can be used to read the pattern.

These energies are directly derived from Eq. (1):

$$U_n = \frac{U_{\text{Talbot}}}{n^2} = \frac{h^2 L^2}{2md^4}\frac{1}{n^2}, \quad n \in \mathbb{Z}^+. \tag{3}$$

In order to reveal quantum interference, these specific rephasing distances (energies) are not useful, but a modulation of the contrast as a function of the energy is a clear indicator of the wave behavior of the test particles.

In an experimental realization of the device, the periodic pattern can be read out with the use of a position-sensitive detector. If the periodicity of the pattern is smaller than the resolution of the detector, the use of a third grating, identical to the first two, is required to extract the information: When the additional grating is tilted around the beam axis, beatings with periodicity inversely proportional to the rotation angle appear,

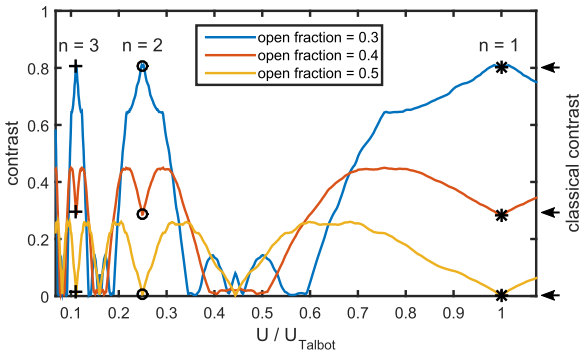

FIG. 2. Contrast of the pattern as a function of the energy of a proton beam. This plot is valid for a device composed of three gratings, the third one being scanned [13] or tilted [15] to read out the pattern. The shape of the contrast profile is strongly affected by the open fraction η of the gratings. The black markers highlight $U = U_n$ for $n = 1,2,3$ where the Talbot-Lau signal is indistinguishable from the classic moiré signal [see Eq. (3)]. The plot has been calculated following the approach by Hornberger *et al.* [16], based on calculating the intensity pattern using the Wigner representation [18]. The plots are arranged from top to bottom, according to the legend.

making the interference pattern observable on a large scale [15], thus allowing for the use of a detector with a significantly reduced constraint on the spacial resolution. As an alternative, the third grating can be used to scan the original pattern, by translating it in the direction perpendicular to the slits and recording the transmitted particle flux for every position [9,13]. The device considered in the following discussion employs a scanned third grating.

It is worth mentioning that the Kapitza-Dirac variant of the Talbot-Lau interferometer, which replaces the second grating with a standing wave [9,19], does not provide a significant advantage when working with ions. The interaction rate scales like $m^{-1/2}$, requiring a significantly higher laser power than for electrons (which is of the order of GW cm^{-2}) [20,21] to achieve similar results, and the interaction area of the phase grating cannot be scaled to larger sizes without defocusing the laser and thus losing significant intensity. Furthermore, the use of a pulsed laser with a continuous source of particles implies that the duty cycle of the laser ($\approx 10^{-7}$) directly translates into a flux reduction within the interferometer.

III. CONTRAST REDUCTION DUE TO SYSTEMATIC EFFECTS

While the ideal contrast of the interference pattern is only dependent on the energy of the particles, once the device geometry is fixed, in any experimental realization it is strongly dependent on the alignment of the device and on the influence of external forces, such as gravity or electric interactions. In this section, we discuss three families of systematic effects which concur in degrading the quality of the signal: misalignment of the gratings, energy spread of the particle source, and external forces acting on the particles. In the latter, emphasis is put on the Lorentz force interaction, which becomes prominent when dealing with charged particles.

For the following discussion, we use specific experimental parameters which are currently available. The production of nanometric gratings with thin silicon nitrate membranes, like the ones described in Ref. [22], limits the energy of the charged particles due to the limited stopping power of the material. Thus we consider a proton source with tunable energy in the keV regime, of the type covered in Ref. [23]. In this configuration, $\lambda_{\text{dB}} \approx 1$ pm. The geometrical parameters of the device are $d = 256$ nm, $L = 171.7$ mm, and $\eta = 0.4$, thus yielding $U_{\text{Talbot}} = 5.64$ keV. The classical rephasing is thus expected also for $U_2 = 1.41$ keV and $U_3 = 627$ eV.

A. Geometrical constraints

The pattern is extremely sensitive to deviations from the ideal geometry: Differences in the distance between the gratings and the detector plane or small relative tilts of the gratings can consistently affect the quality of the signal. In the following, we consider two specific scenarios: longitudinal asymmetries and rotational misalignment around the beam axis.

1. Longitudinal asymmetry

In the optimal configuration, the device can be operated with a fully divergent source of particles and still produces

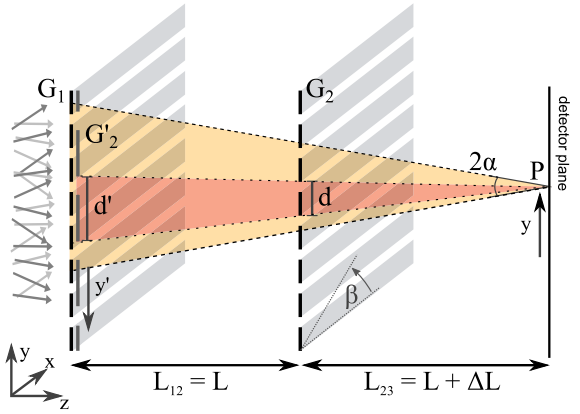

FIG. 3. Schematic showing how the classical pattern is calculated. For every point P on the detector, the region from where particles can reach the point is calculated by projecting the second grating (G_2) on the first one (G_1), thus identifying the effective fraction of the particle which contributes to the intensity. The projected grating G_2' has a magnified periodicity d', as in Eq. (5). When considering a source with divergence α, the region from which a particle can reach the detector is limited by a cone with opening angle α equal to the divergence of the source (bright region). The tilt angle β is considered when extending the approach to three dimensions. The analytic treatment is explained in detail in the text.

a pattern with the expected maximal contrast. In any experimental scenario, the divergence of the source puts constraints on its geometrical characteristics: An asymmetry ΔL between the distance from the first to the second grating L_{12} and the distance from the second to the third grating L_{23} strongly affects the contrast of the pattern. The effects of this asymmetry can be calculated analytically in the simple case of a moiré deflectometer, whose signal is equivalent to the Talbot-Lau interferometer whenever the length of the device matches a multiple of L_T.

The process is schematized in Fig. 3. Consider a point P on the detector plane. We calculate the intensity of the signal which illuminates this point by considering the allowed geometrical trajectories. All the particles which reach P have to pass through both gratings, indicated as $G1$ and $G2$, respectively, therefore limiting their original position to a specific region of space. In the case of $G2$, this region can be interpreted as its shadow image $G2'$, obtained using P as a focal point. Suppose we have a source with divergence α, $L_{12} = L$, $L_{23} = L + \Delta L$, grating periodicity d, and open fraction η. The grating function G as a function of the position y is defined as

$$G(y;d,\eta) = \begin{cases} 1 & \text{for } \mathrm{mod}(y,d) < \eta d \\ 0 & \text{otherwise.} \end{cases} \tag{4}$$

As a result, the projected image $G2'$ can be described as a grating with the same open fraction η and a magnified periodicity d', given by

$$d' = d\frac{L_{12} + L_{23}}{L_{23}} = d\frac{2L + \Delta L}{L + \Delta L}. \tag{5}$$

To calculate the intensity at P, the grating $G2$ can therefore be replaced by its projection $G2'$ on the plane of the first grating [24]. As shown in Fig. 3, while moving the projection point by a distance y on the screen, $G2'$ moves in the opposite direction by a position y' given by

$$y' = \frac{L}{L + \Delta L} y. \tag{6}$$

In the following, $G1 = G(y;d,\eta)$, $G2' = G(y';d',\eta)$. If we consider a completely divergent particle source, the intensity I_{det} at any position y on the detector plane is given by

$$I_{\mathrm{det}}(y) \propto \int_{-\infty}^{+\infty} G(\xi;d,\eta)G(\xi + y';d',\eta)d\xi. \tag{7}$$

In this scenario, $\Delta L \neq 0$ causes the contrast of the fringes generated by the first two gratings to vanish completely, as the rephasing is only seen at integer multiples of L_{12}. As mentioned in Sec. II, a third grating placed on the detector plane can be used to read out the pattern. In this case, the intensity I after the additional grating $G3 = G(y;d,\eta)$ is given by

$$I(y_g) \propto \int_{-\infty}^{+\infty} I_{\mathrm{det}}(\xi)G(\xi - y_g;d,\eta)d\xi, \tag{8}$$

where y_g is the position of the third grating. If we put constraints on the divergence of the beam, the area from where particles can hit the detector is limited to a region of space $\xi \in [y - y_{\mathrm{lim}}, y + y_{\mathrm{lim}}]$, where $y_{\mathrm{lim}} = (2L + \Delta L)\tan(\alpha)$ is the geometrical limit imposed by the divergence angle α and y is the coordinate of the detector point at which the pattern is calculated (see Fig. 3). With these assumptions, Eq. (7) becomes

$$I^{\alpha}_{\mathrm{det}}(y) \propto \int_{y-y_{\mathrm{lim}}}^{y+y_{\mathrm{lim}}} G(\xi;d,\eta)G(\xi + y';d',\eta)d\xi. \tag{9}$$

The intensity $I^{\alpha}(y_g)$ after the third grating is then calculated as in Eq. (8):

$$I^{\alpha}(y_g) \propto \int_{-\infty}^{+\infty} I^{\alpha}_{\mathrm{det}}(\xi)G(\xi - y_g;d,\eta)d\xi. \tag{10}$$

The contrast of the pattern as a function of ΔL shows a main peak at $\Delta L = 0$, together with smaller secondary peaks of decreasing intensity. An example of this behavior is shown in Fig. 4. For a completely divergent source ($\alpha \to \pi/2$), Eq. (10) converges to Eq. (8), thus yielding the same result. For a given angle $0 \leqslant \alpha < \pi/2$, the position of the first minimum can be calculated via geometric considerations [25]:

$$\Delta L_{\mathrm{min}} = \frac{d}{2}\tan\left(\frac{\pi}{2} - \alpha\right). \tag{11}$$

In the limit of a small divergence angle ($\alpha \ll 1$), this formula is consistent with the one outlined in Ref. [26,27]. As the equation shows, ΔL_{min} is independent of L: Once the diffusion angle and the periodicity of the gratings are fixed, the other geometrical parameters do not play any role in determining how the contrast decays. A consequence of this systematic effect is that, depending on the divergence of the source, there is a maximum acceptable displacement after which the contrast drops sharply, which can be defined as the position of the first minimum expressed by Eq. (11). Notice that for $\alpha \approx \pi/2$,

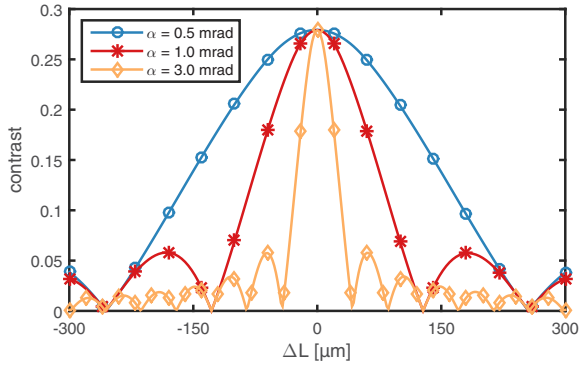

FIG. 4. Contrast of the classical moiré pattern as a function of $\Delta L = L_{23} - L_{12}$. When the distance $\Delta L \neq 0$, the contrast of the periodic pattern decays as a function of ΔL and the divergence angle α. For $\Delta L = d/2\tan(\pi/2 - \alpha)$, the contrast is equal to zero. The position of the zeros is completely determined by those two parameters and is not affected by the magnitude of L_{12}.

$\Delta L_{\min}$ tends to zero (i.e., the contrast profile tends to a δ centered in $\Delta L = 0$), while for $\alpha = 0$ (i.e., no divergence), $\Delta L_{\min}$ goes to infinity, which means that the contrast is not fading away with distance.

As previously pointed out, this mathematical formulation is valid in the classical scenario, but can be verified also in the wave regime by means of numerical simulations. The simulations performed show that for a range of lengths around $L = L_T$, the position of the first contrast minimum is consistent with the classical scenario. An example of this behavior is shown in Fig. 5. The classical result can therefore still be considered as the maximum displacement allowed while working in this region.

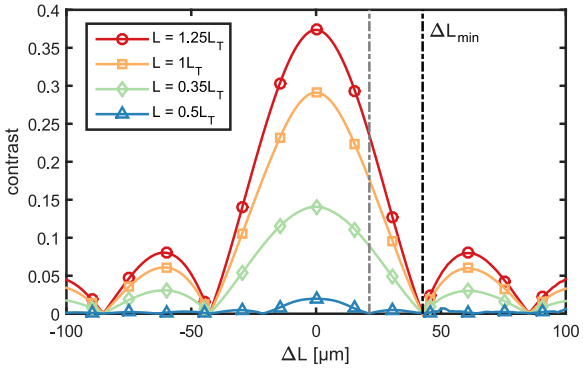

FIG. 5. As in the classical case, the functional dependence of the contrast on the diffusion angle in the Talbot-Lau regime shows periodic minima, the first of which is described by Eq. (11) (black vertical line). Notice that the peak contrast changes with the length. Around $L = n + \frac{1}{2}L_T$, the periodicity of the pattern doubles, moving the first minimum at half its classical position (gray vertical line). The profile shown is calculated for a divergence angle $\alpha = 3$ mrad.

2. *Rotational misalignment*

In the ideal case, the two gratings which generate the pattern have the same rotation angle with respect to the beam axis. When this condition is not fulfilled, the contrast of the pattern depends on the divergence of the source. In order to estimate this effect, we extend the same approach discussed in Sec. III A 1 to two dimensions, allowing for one or both gratings to be tilted around the beam axis.

As an intuitive explanation, consider two gratings: the first one placed in the xy plane with slits parallel to the y axis and the second rotated by an angle β around the z axis (shown in Fig. 3). Consider also a divergence angle α in the yz plane, while no diffusion is present in the $\hat{x}$ direction. If we take a set of planes parallel to the yz plane and we use it to slice through the pattern for different values of x, we get a collection of one-dimensional representations equivalent to the one discussed in Sec. III A 1, with the difference that in every plane the pattern of the second grating will show an offset $\phi_y = x\tan(\beta)$ and a modified periodicity $d_\beta = d/\cos(\beta)$. When a divergence in the $\hat{x}$ direction is considered, all the slices which are between a cone with angular opening α and the point on the screen at which the pattern is calculated have to be summed up. The combination of these two factors is what smears out the contrast of the generated pattern on the detection plane. By introducing the two-dimensional grating function $G_{2D}(x,y;\beta,d,\eta)$, defined as

$$G_{2D}(x,y;\beta,d,\eta) = \begin{cases} 1 & \text{for } \mathrm{mod}(y - x\tan(\beta), d/\cos(\beta)) < \eta d/\cos(\beta) \\ 0 & \text{otherwise,} \end{cases} \tag{12}$$

Eq. (9) can be extended as

$$I^{2D}_{\mathrm{det}}(x,y) \propto \int_{y-r_{\mathrm{lim}}}^{y+r_{\mathrm{lim}}} \int_{x-\sqrt{r^2_{\mathrm{lim}}-(\xi-y)^2}}^{x+\sqrt{r^2_{\mathrm{lim}}-(\xi-y)^2}} G_{2D}(u,\xi;0,d,\eta) \times G_{2D}(u+x',\xi+y';\beta,d',\eta)\,du\,d\xi. \tag{13}$$

This formula considers a conical projection from the point $P = (x,y)$ and therefore a circular overlapping area of radius $r_{\mathrm{lim}} = (2L + \Delta L)\tan(\alpha)$ on the plane of the first grating. Here d' is expressed by Eq. (5), while x' and y' are both defined by using Eq. (6) on x and y, respectively. Notice that, as an effect of the angular difference, the resulting fringe pattern is tilted by an angle $\beta_{\mathrm{pattern}} = 2\beta$. To retrieve the profile after a third grating, Eq. (10) is also expanded in two dimensions in a similar fashion.

The intensity profile can be evaluated numerically. The calculations show that even when the asymmetry factor is taken out ($\Delta L = 0$), the contrast of the recorded pattern decreases as the angle between the two gratings increases. This phenomenon is independent of the presence of a third grating, since the pattern becomes uniform for a geometrical overlap of the trajectories due to the relative rotation of the first two gratings. By geometric considerations, we derive the following formula for the angular difference β_{crit} which causes the contrast to drop to zero:

$$\tan\beta_{\mathrm{crit}} = k\frac{d}{2L}\tan\left(\frac{\pi}{2} - \alpha\right), \tag{14}$$

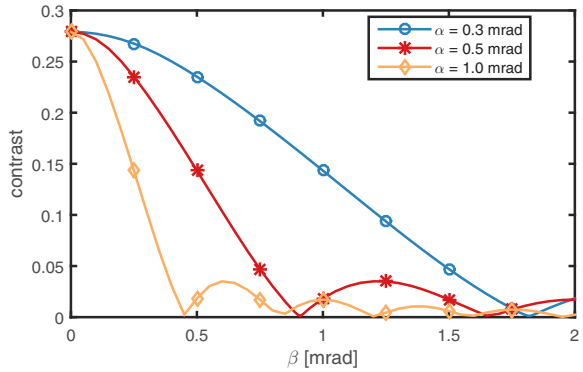

FIG. 6. Depending on the divergence angle α, an angular difference β between the second and the first grating causes the signal to vanish. The position of the contrast minimum is linearly dependent on d and inversely proportional to L. The function which describes this position is similar to the one found for the one-dimensional case [compare Eqs. (11) and (14)].

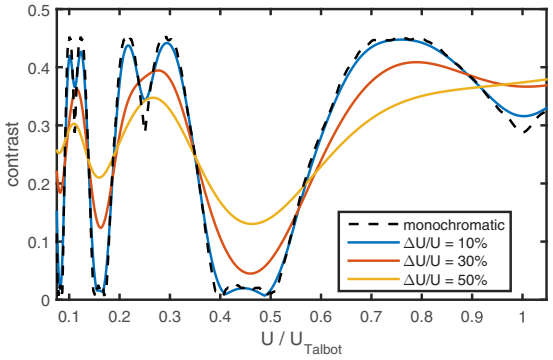

FIG. 7. Contrast of the pattern as a function of the energy of the particle beam for different values of the energy spread. The open fraction considered in this plot is $\eta = 0.4$. Each curve is obtained by considering a normal distribution centered on each energy value, with a FHWM equal to the energy spread ΔU. For every point on the plot, the ratio $\Delta U/U$ is fixed to the value shown in the legend. Notice that for an energy spread up to 10%, there is only a negligible difference from the monochromatic case.

where k is a constant factor, to be determined via numerical calculations. Profiles for a different divergence angle α are shown in Fig. 6. Notice that the formula shows the same functional dependence as in the one-dimensional case [see Eq. (11) as a comparison].

In the representative geometrical configuration, for a divergence $\alpha = 1$ mrad, the visibility minimum appears for $\beta = (0.46 \pm 0.01)$ mrad. Repeating the simulations for different geometrical configurations yields $k = 0.61 \pm 0.01$ as the value for the constant.

It is worth mentioning that, when using a third grating to scan the pattern, the retrieved flux modulation is affected by a rotation of the third grating, due to the moiré effect. Therefore, the rotation angle β_3 of the third grating with respect to the pattern has to fulfill the condition

$$\sin\left(\frac{\beta_3}{2}\right) \ll \frac{d}{2\sqrt{A}}, \tag{15}$$

where A is the area over which the flux is integrated.

B. Energy spread of the particle beam

Experimental ion sources are not perfectly monochromatic: The particle beam produced always has a nonzero energy spread. As shown in Fig. 2, particles with different energies generate patterns with different contrast: Having an energy distribution means that different patterns get summed up, leading to modifications to the recorded signal. A precise knowledge of the energy distribution is therefore required in order to calculate the expected contrast profile. If the averaging effect is such that the contrast of the pattern becomes lower than or equal to the classical value, the quantum nature of the particle cannot be convincingly proven. Figure 7 shows contrast plots for various energy spreads $\Delta U/U$. In the example, the energy distribution is modeled as a normalized Gaussian distribution centered on each energy. The energy spread is thus defined as the full width half maximum (FWHM) of each distribution. As can be seen in Fig. 7, the effect is not dramatic, since even for an energy spread of 30% the contrast modulation is still clearly visible and above the classical expected value for a consistent part of the energy spectrum. Once external forces are taken into consideration, the effect of a nonmonochromatic beam is more accentuated.

C. External forces

If the particles are affected by an external force $\vec{F}$ during their crossing of the interferometer, the pattern recorded at the detector position is subject to a phase shift which depends on both the magnitude of the force and the time-of-flight τ between the gratings. Assuming a constant acceleration a_y along the grating periodicity (see the coordinate system in Fig. 1), the phase shift for a monochromatic beam is given by [13]

$$\Delta\phi = \frac{2\pi}{d} a_y \tau^2, \tag{16}$$

with

$$\tau = \frac{L}{v_z} = L\sqrt{\frac{m}{2U}}. \tag{17}$$

Notice that, since the phase shift $\Delta\phi$ is energy dependent, a force acting on the particles lowers the contrast of the pattern in the presence of an energy spread ΔU. A critical force $\vec{F}_{\text{crit}}$ can therefore be defined as the force leading to a phase shift of π between the fastest and the slowest particles in the distribution. For a given Gaussian energy distribution (mean energy U and FWHM ΔU) we estimate the critical force assuming $U_{\text{fast}} = U + \Delta U/2$ and $U_{\text{slow}} = U - \Delta U/2$. By considering a uniform constant force, the critical force intensity F_{crit} is derived from Eq. (16) as

$$\pi \stackrel{!}{=} \phi_{\text{slow}} - \phi_{\text{fast}} = \pi F_{\text{crit}} \frac{L^2}{d}\left(\frac{\Delta U}{U_{\text{fast}} U_{\text{slow}}}\right), \tag{18}$$

which leads to

$$F_{\text{crit}} = \frac{d}{L^2}\frac{1}{4}\frac{4U^2 - (\Delta U)^2}{\Delta U}, \tag{19}$$

which, in the limit of small energy spread, i.e., $(\Delta U)^2 \ll U^2$, can be further simplified to

$$F_{\text{crit}} \approx \frac{d}{L^2}\frac{U^2}{\Delta U}. \tag{20}$$

Notice that if a generic energy distribution is considered, an integration is instead required to get a precise quantitative result. In the following, two specific examples are considered: a constant Lorentz force and the self-repulsive Coulomb interaction inside a charged particle beam.

1. *Lorentz force*

Charged particles are susceptible to electric and magnetic fields which make the observation of interference more challenging. We therefore assume a Lorentz force for constant uniform fields $\vec{E}$ and $\vec{B}$. Since the interferometer is only sensitive to force acting perpendicular to the grating slits, we are interested in the transverse component of the Lorentz force, which can be written as

$$\vec{F}_y^{\text{Lorentz}} = q[E_y + (v_z B_x - v_x B_z)]\hat{y}, \tag{21}$$

where q is the charge of the particle.

In the limit of $v_z B_x \gg v_x B_z$, which is a reasonable assumption when working with collimated particle beams and assuming the two components of the magnetic fields to have the same order of magnitude, Eq. (21) can be written as

$$\vec{F}_y^{\text{Lorentz}} = q(E_y + v_z B_x)\hat{y}. \tag{22}$$

A definition for the critical electric field E_{crit} and magnetic field B_{crit} is derived by setting $\|\vec{B}\|$ and $\|\vec{E}\|$ to zero, respectively [15]:

$$E_{\text{crit}} = \frac{d}{L^2}\frac{U^2}{q\Delta U} \quad \text{for } \|\vec{B}\| = 0, \tag{23}$$

$$B_{\text{crit}} = \frac{d}{L^2}\sqrt{\frac{m}{2}}\frac{U^{3/2}}{q\Delta U} \quad \text{for } \|\vec{E}\| = 0. \tag{24}$$

In the geometric configuration considered, these fields assume the form

$$\tilde{E}_{\text{crit}} = 8.7 \times 10^{-6}\frac{U}{\delta}, \tag{25}$$

$$\tilde{B}_{\text{crit}} = 6.3 \times 10^{-10}\frac{\sqrt{U}}{\delta}, \tag{26}$$

where $\delta = \Delta U/U$, $\tilde{E}_{\text{crit}}$ is in units of V m^{-1}, U is in eV, and $\tilde{B}_{\text{crit}}$ is in tesla. Notice that, while the critical electric field scales linearly with the energy, the magnetic field scales just with the square root. Therefore, by increasing the energy, the influence of the electric field is reduced faster than that of the magnetic field. If we consider $U = 2$ keV and $\delta = 1\%$, Eqs. (25) and (26) yield $E_{\text{crit}} = 1.74\ \text{V m}^{-1}$ and $B_{\text{crit}} = 28.2$ mG, respectively. As a comparison, consider that the fields measured in Ref. [15] in a similar experimental setup are of the order of $1\ \text{V m}^{-1}$ and 10 mG, respectively, already lower than the critical values considered, although no special care has been taken to minimize the fields. Hence, it is reasonable to assume that lower fields are achievable via a suitable electric and magnetic shielding.

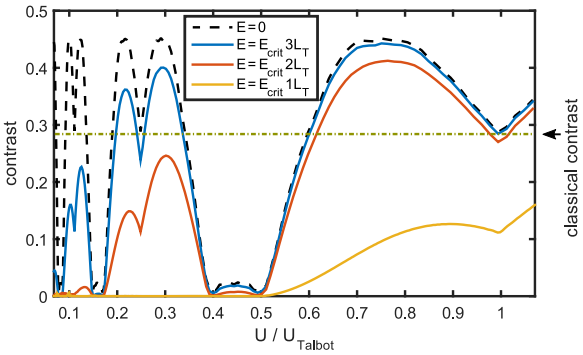

FIG. 8. Effects of external forces, combined with the energy spread of the source, lower the contrast of the pattern. Here we consider $\Delta U/U = 1\%$. Each line represents the expected contrast for a given electric field in units of the critical field $E_{\text{crit}nL_T}$, defined as in Eq. (27). No magnetic field is considered.

Another specific situation which is relevant in this context appears when the distance between the gratings is fixed to an integer multiple of the Talbot length. There the contrast of the pattern is the same as in the classical scenario: This can be a desirable feature to get a reference signal in a known configuration and compare it to the theoretical expectations. Fixing $L = nL_T$ is equivalent to changing the length of the device for every energy U used, which is the opposite approach of what was considered above (tuning the energy of the particles in a fixed-length device). With these specifications, Eqs. (23) and (24) can be written as

$$E_{\text{crit}nL_T} = \frac{h^2}{2md^3q}\frac{1}{\delta}\frac{1}{n^2}, \tag{27}$$

$$B_{\text{crit}nL_T} = \frac{h^2}{2\sqrt{2m}d^3q}\frac{1}{\delta\sqrt{U}}\frac{1}{n^2}. \tag{28}$$

The expressions underline an interesting fact: If the distance between the gratings is fixed to a multiple of the Talbot length, the critical electric field depends on the relative energy spread δ but not directly on the energy. The same does not hold for the critical magnetic field, which instead becomes smaller as the energy increases. An application of Eq. (27) is shown in Fig. 8, where different values of the electric field are applied to a contrast profile with $\delta = 1\%$, calculated as the ones shown in Fig. 7.

2. *Inner beam interactions*

When two or more charged particles are moving inside the device, an additional field is generated by their interaction. The particles mutually repel each other, effectively increasing the size of the beam as well as the distance between the center and the edges of the charge distribution. In order to give an upper limit estimation on this effect, consider a beam of particles with mass m and charge q. The beam is homogeneous and cylindrical, with initial radius r_0, axial

velocity v_z, and uniform charge density ρ. The beam is assumed to be nonrelativistic ($\gamma \approx 1$), which is a justified approximation in the energy range considered. This has the additional effect of making the contribution of the magnetic fields generated by the moving charge distribution negligible [28]. With these assumptions, the radial electric field $E_R(r)$ is given by

$$E_{\mathrm{R}}(r) = \begin{cases} \dfrac{\rho r}{2\epsilon_0} & \text{for } r \leqslant r_0 \\ \dfrac{\rho r_0^2}{2\epsilon_0 r} & \text{otherwise.} \end{cases} \tag{29}$$

The field has a maximum for $r = r_0$, after which it decreases monotonically. Using this construction, the expanded radius r_{beam} at any axial position z can be calculated by numerically inverting [28]

$$z = \frac{r_0}{\sqrt{2K}} F\left(\frac{r_{\mathrm{beam}}}{r_0}\right) = \frac{r_0}{\sqrt{2K}} \int_1^{r_{\mathrm{beam}}/r_0} \frac{dy}{\sqrt{\ln(y)}}, \tag{30}$$

where the constant K is given by

$$K = \frac{q\rho r_0^2}{2\pi\epsilon_0 m v_z^2}. \tag{31}$$

It is interesting to note that for $r_{\mathrm{beam}}/r_0 \ll 1$,

$$F\left(\frac{r_{\mathrm{beam}}}{r_0}\right) \simeq 2\sqrt{\frac{r_{\mathrm{beam}} - r_0}{r_0}}, \tag{32}$$

which is equivalent to considering a constant field $E_R(r_0)$ applied to the particles for the duration of the flight. When $r_{\mathrm{beam}}/r_0 \ll 1$, the error introduced by considering this first-order expansion is smaller than 1%. Since we are interested in a beam divergence of the order of the periodicity d of the grating, until $d/r_0 \ll 1$, we can therefore consider a constant radial acceleration $\vec{a} = qE_R(r_0)/m\hat{r}$. This has the additional benefit of allowing us to obtain a maximum acceptable value for the particle flux. With this hypothesis, using Eqs. (16) and (29), a particle on the cylinder's surface subjected to $E_R(r_0)$ experiences a total phase shift

$$\phi = \frac{2\pi y}{d} = \frac{2\pi}{d} a\tau^2 = \frac{2\pi}{d} \frac{q\rho r_0}{2m\epsilon_0} \frac{L^2}{v_z^2}. \tag{33}$$

By expressing ρ as a function of the particle flux Φ^{in}, we obtain

$$\phi = \frac{2\pi}{d} \Phi^{\mathrm{in}} r_0 \frac{q^2}{2m\epsilon_0} \frac{L^2}{v_z^3} = \frac{2\pi}{d} \Phi^{\mathrm{in}} r_0 \frac{q^2\sqrt{m}}{4\sqrt{2}\epsilon_0} L^2 U^{-3/2}. \tag{34}$$

In the case that the position shift y exceeds half the periodicity d ($\Delta\phi = \pi$), the contrast of the pattern will be consistently reduced. Considering this as the limiting condition, we estimate a critical flux $\Phi^{\mathrm{in}}_{\mathrm{crit}}$ as

$$\Phi^{\mathrm{in}}_{\mathrm{crit}} = \frac{2\sqrt{2}\epsilon_0}{q^2\sqrt{m} r_0} \frac{d}{L^2} U^{3/2}. \tag{35}$$

In the geometric configuration analyzed and choosing protons as the test species, with $U = 2$ keV, it follows that $\Phi^{\mathrm{in}}_{\mathrm{crit}} = 1.2 \times 10^{15}$ m^{-2} s^{-1}. By considering, for example, $r_0 = 1$ mm, we get $\Phi^{\mathrm{in}}_{\mathrm{crit}} \pi r_0^2 = 3.8 \times 10^9$ Hz. These intensities are well in the range of sources of the type described in Ref. [23], but still far higher than the requirements of a typical experiment (which normally requires 10^2–10^3 detected particles on the detector surface to reveal the pattern). Therefore, in the experimental conditions considered, this effect can be consistently neglected.

IV. CONCLUSION

In this paper, several systematic effects which degrade the signal of a scalable Talbot-Lau interferometer for charged particles have been analyzed. These effects can be categorized into three distinct families: effects related to the misalignment of the gratings, the energy spread of the source, effects due to the external fields.

A displacement of the detector plane in relation to the distance between the first two gratings causes a consistent reduction of the contrast. The displacement limit which makes the contrast drop to zero is calculated and is found to be independent of the distance between the gratings. Moreover, this displacement is found to be the same both in the particle and in the wave regime. A rotational misalignment between the gratings of the interferometer leads to a reduced contrast as well. Numerical simulations have been used to set limits on this effect in the classical picture. Since both these effects are proportional to the divergence of the beam, they become more restrictive when considering large-area interferometers for low-intensity, noncollimated sources, such as in antimatter experiments.

The energy spread of the source plays a role into averaging the visibility, thus reducing the effective difference in contrast for different energies. However, an energy spread as high as 30% still allows for measuring the wave behavior of the particles.

The presence of external electric or magnetic fields combined with the aforementioned energy spread causes a sharp reduction in contrast, depending on the geometrical characteristics of the device. The limiting force which causes the pattern to vanish is calculated and both the electric and magnetic field intensities are separately obtained. The effects of the inner beam interactions are evaluated and an expression for the maximum flux allowed before said interactions cause a significant drop in contrast is obtained.

ACKNOWLEDGMENTS

The authors would like to thank P. Bräunig for advice and useful discussions. The authors are very thankful for the discussions within the AEgIS Collaboration about the feasibility for the realization of a Talbot-Lau interferometer for antiprotons. This work was supported by the Deutsche Forschungsgemeinschaft (Grant No. OB164/10-1).

[1] C. Davisson and L. H. Germer, Phys. Rev. **30**, 705 (1927).
[2] C. Jönsson, Z. Phys. **161**, 454 (1961).
[3] B. McMorran, J. D. Perreault, T. Savas, and A. Cronin, Ultramicroscopy **106**, 356 (2006).

[4] R. Bach, D. Pope, S.-H. Liou, and H. Batelaan, New J. Phys. **15**, 033018 (2013).
[5] M. Arndt, O. Nairz, J. Vos-Andreae, C. Keller, G. van der Zouw, and A. Zeilinger, Nature (London) **401**, 680 (1999).
[6] R. Bach, G. Gronniger, and H. Batelaan, Appl. Phys. Lett. **103**, 254102 (2013).
[7] J. F. Clauser and S. Li, Phys. Rev. A **49**, R2213 (1994).
[8] B. Brezger, L. Hackermüller, S. Uttenthaler, J. Petschinka, M. Arndt, and A. Zeilinger, Phys. Rev. Lett. **88**, 100404 (2002).
[9] S. Gerlich, S. Eibenberger, M. Tomandl, S. Nimmrichter, K. Hornberger, P. J. Fagan, J. Tüxen, M. Mayor, and M. Arndt, Nat. Commun. **2**, 263 (2011).
[10] P. Bräunig, J. Storey, and M. K. Oberthaler, AEgIS Collaboration report, 2014 (unpublished).
[11] G. Gronniger, B. Barwick, and H. Batelaan, New J. Phys. **8**, 224 (2006).
[12] A. Cronin, J. Schmiedmayer, and D. Pritchard, Rev. Mod. Phys. **81**, 1051 (2009).
[13] M. K. Oberthaler, S. Bernet, E. M. Rasel, J. Schmiedmayer, and A. Zeilinger, Phys. Rev. A **54**, 3165 (1996).
[14] S. Aghion *et al.*, Nat. Commun. **5**, 4538 (2014).
[15] P. Lansonneur, P. Bräunig, A. Demetrio, S. R. Müller, P. Nedelec, and M. K. Oberthaler, Nucl. Instrum. Methods Phys. Res. Sect. A **862**, 49 (2017).
[16] K. Hornberger, J. E. Sipe, and M. Arndt, Phys. Rev. A **70**, 053608 (2004).
[17] S. Sala, M. Giammarchi, and S. Olivares, Phys. Rev. A **94**, 033625 (2016).
[18] E. Wigner, Phys. Rev. **40**, 749 (1932).
[19] S. Gerlich, L. Hackermüller, K. Hornberger, A. Stibor, H. Ulbricht, M. Gring, F. Goldfarb, T. Savas, M. Müri, M. Mayor, and M. Arndt, Nat. Phys. **3**, 711 (2007).
[20] D. L. Freimund, K. Aflatooni, and H. Batelaan, Nature (London) **413**, 142 (2001).
[21] D. L Freimund and H. Batelaan, Phys. Rev. Lett. **89**, 283602 (2002).
[22] T. A. Savas, S. N. Shah, M. L. Schattenburg, J. M. Carter, and H. I. Smith, J. Vac. Sci. Technol. B **13**, 2732 (1995).
[23] P. Sortais, T. Lamy, J. Médard, J. Angot, L. Latrasse, and T. Thuillier, Rev. Sci. Instrum. **81**, 02B314 (2010).
[24] F. Bergermann, Diploma thesis, University of Heidelberg, 2012 (unpublished).
[25] S. R. Müller, internal report, 2017 (unpublished).
[26] S. Nimmrichter and K. Hornberger, Phys. Rev. A **78**, 023612 (2008).
[27] K. Hornberger, S. Gerlich, H. Ulbricht, L. Hackermüller, S. Nimmrichter, I. V. Goldt, O. Boltalina, and M. Arndt, New J. Phys. **11**, 043032 (2009).
[28] T. Kalvas, in *Proceedings of the CAS-CERN Accelerator School: Ion Sources, Senec, 2012*, edited by R. Bailey (CERN, Geneva, 2013), pp. 537–564.

References

[ABB97] T. Azuma, J. S. Bakos, and H. Bluhme. *Atomic spectroscopy and collisions using slow antiprotons*. Tech. rep. CERN-SPSC-97-19. SPSC-P-307. Geneva: CERN, 1997 (cit. on p. 14).

[Agh+14] S. Aghion et al. "A moiré deflectometer for antimatter". In: *Nat. Commun.* 5 (2014), p. 4538 (cit. on pp. 12, 27, 89, 114).

[Agh+17] S. Aghion et al. "Characterization of a transmission positron / positronium converter for antihydrogen production". In: *Nucl. Instr. Meth. Phys. Res. B* 407 (2017), pp. 55–66 (cit. on p. 12).

[Ahm+16] M. Ahmadi et al. "An improved limit on the charge of antihydrogen from stochastic acceleration". In: *Nature* 529.7586 (2016), pp. 373–376 (cit. on p. 11).

[Ahm+17a] M. Ahmadi et al. "Antihydrogen accumulation for fundamental symmetry tests". In: *Nat. Commun.* 8.1 (2017) (cit. on p. 11).

[Ahm+17b] M. Ahmadi et al. "Observation of the 1S–2S transition in trapped antihydrogen". In: *Nature* 541.7638 (2017), pp. 506–510 (cit. on p. 11).

[Ahm+17c] M. Ahmadi et al. "Observation of the hyperfine spectrum of antihydrogen". In: *Nature* 548.7665 (2017), pp. 66–69 (cit. on p. 11).

[Ahm+18] M. Ahmadi et al. "Characterization of the 1S–2S transition in antihydrogen". In: *Nature* (2018) (cit. on p. 11).

[Amo+02] M. Amoretti et al. "Production and detection of cold antihydrogen atoms". In: *Nature* 419 (2002), pp. 456–459 (cit. on pp. 11, 90).

[Amo+04a] M. Amoretti et al. "The ATHENA antihydrogen apparatus". In: *Nucl. Instr. Meth. Phys. Res.* 518.3 (2004), pp. 679–711 (cit. on p. 94).

[Amo+04b] M. Amoretti et al. "Antihydrogen production temperature dependence". In: *Phys. Lett. B* 583.1 (2004), pp. 59–67 (cit. on pp. 20, 91, 94).

[Amo+13] C. Amole et al. "Description and first application of a new technique to measure the gravitational mass of antihydrogen". In: *Nat. Commun.* 4 (2013), p. 1785 (cit. on pp. 12, 89).

[Amo+14] C. Amole et al. "The ALPHA antihydrogen trapping apparatus". In: *Nucl. Instr. Meth. Phys. Res. A* 735 (2014), pp. 319–340 (cit. on pp. 20, 90, 94).

[And+11] G. Andresen et al. "Search for trapped antihydrogen". In: *Phys. Lett. B* 695.1 (2011), pp. 95–104 (cit. on pp. 91, 94).

[Apo+99] A. Apostolakis et al. "Tests of the Equivalence Principle with neutral kaons". In: *Phys. Lett. B* 452.3-4 (1999), pp. 425–433 (cit. on pp. 17–19).

[Bar+14] W. Bartmann et al. "Extra Low Energy Antiproton ring ELENA : from the conception to the implementation phase". In: CERN-ACC-2014-0144 (2014), 4 p (cit. on pp. 20, 127).

[Ber12] F. Bergermann. "Characterization of the moiré deflectometer for the AEgIS experiment". Diploma Thesis. University of Heidelberg, 2012 (cit. on pp. 30, 33, 55).

[BGB13] R. Bach, G. Gronniger, and H. Batelaan. "An electron Talbot-Lau interferometer and magnetic field sensing". In: *Appl. Phys. Lett.* 103.25 (2013), p. 254102 (cit. on pp. 12, 27).

[Bil15] C. F. H. Billert. "Three-grating moiré deflectometer for antiprotons". Bachelor's thesis. University of Heidelberg, 2015 (cit. on p. 12).

[BNW10] K. Blaum, Y. N. Novikov, and G. Werth. "Penning traps as a versatile tool for precise experiments in fundamental physics". In: *Contemp. Phys.* 51.2 (2010), pp. 149–175 (cit. on p. 91).

[Brä+15] P. Bräunig, A. Demetrio, S. R. Müller, and M. K. Oberthaler. *Limits on a gravity measurement with a non-collimated antihydrogen source.* internal collaboration note. 2015 (cit. on pp. 79, 90, 102, 108, 113, 120).

[Brä14] P. Bräunig. "Atom optical tools for antimatter experiments". PhD thesis. University of Heidelberg, 2014 (cit. on pp. 30, 31, 33, 39, 43, 44, 47, 62, 114).

[Bre+02] B. Brezger, L. Hackermüller, S. Uttenthaler, J. Petschinka, M. Arndt, and A. Zeilinger. "Matter-wave interferometer for large molecules". In: *Phys. Rev. Lett.* 88 (10 2002), p. 100404 (cit. on pp. 12, 27).

[BSO14] P. Bräunig, J. Storey, and M. K. Oberthaler. *AtliX - Antimatter Talbot-Lau Interferometry Experiment*. Internal note - AEgIS collaboration. 2014 (cit. on p. 79).

[Car+15] R. Caravita, O. Forslund, I. Larsen, L. Marx, Z. Mazzotta, B. Rienacker, and S. Mariazzi. *Advances in positron activity in the main cryostat*. AEgIS collaboration meeting. 2015 (cit. on p. 139).

[Car17] R. Caravita. "Towards measuring gravity on neutral antimatter". PhD thesis. Università degli studi di Genova, 2017 (cit. on pp. 23, 91, 99, 112).

[Car18] R. Caravita. personal communication. 2018 (cit. on p. 99).

[Cha+11] G. Chardin et al. *Proposal to measure the Gravitational Behaviour of Antihydrogen at Rest*. Tech. rep. CERN-SPSC-2011-029. SPSC-P-342. Geneva: CERN, 2011 (cit. on p. 11).

[Cha57] J. Chalmers. *Atmospheric electricity*. Pergamon Press, 1957 (cit. on p. 77).

[Cha93] G. Chardin. "CP violation and antigravity (revisited)". In: *Nucl. Phys. A* 558.0 (1993), pp. 477–495 (cit. on p. 11).

[CL94] J. F. Clauser and S. Li. "Talbot-von Lau atom interferometry with cold slow potassium". In: *Phys. Rev. A* 49 (4 1994), R2213–R2216 (cit. on pp. 12, 27).

[Com17] D. Comparat. personal communication. 2017 (cit. on p. 97).

[Coo+15] D. A. Cooke et al. "Observation of positronium annihilation in the 2S state: towards a new measurement of the 1S-2S transition frequency". In: *Hyperfine Interact.* 233.1-3 (2015), pp. 67–73 (cit. on p. 96).

[COW75] R. Colella, A. W. Overhauser, and S. A. Werner. "Observation of Gravitationally Induced Quantum Interference". In: *Phys. Rev. Lett.* 34.23 (1975), pp. 1472–1474 (cit. on p. 114).

[Cow81] R. Cowan. *The theory of atomic structure and spectra*. Los Alamos Series in Basic and Applied Sciences. University of California Press, 1981 (cit. on pp. 84, 85).

[CSP09] A. Cronin, J. Schmiedmayer, and D. Pritchard. "Optics and interferometry with atoms and molecules". In: *Rev. Mod. Phys.* 81.3 (2009), pp. 1051–1129 (cit. on p. 29).

[Dem+15] A. Demetrio, P. Bräunig, S. R. Müller, and M. K. Oberthaler. *Limits on gravity measurement with a non-collimated antihydrogen source*. AEgIS general meeting. 2015 (cit. on p. 142).

[Dem+17] A. Demetrio, S. R. Müller, P. Lansonneur, and M. K. Oberthaler. "Progress toward a large-scale ion Talbot-Lau interferometer". In: *Phys. Rev. A* 96 (6 2017), p. 063604 (cit. on pp. 30, 31, 33, 38, 54, 55, 59, 62, 64, 66, 67, 70, 75, 77–79, 82, 83, 85, 87).

[Dem14a] A. Demetrio. *Gravity measurement in a shorter congurations*. AEgIS general meeting. 2014 (cit. on pp. 86, 108).

[Dem14b] A. Demetrio. "Gravity measurement on antihydrogen in AEgIS: numerical simulation of perturbative effects". Master's thesis. Università degli studi di Genova, 2014 (cit. on pp. 25, 84, 108).

[Deu+86] B. I. Deutch, A. S. Jensen, A. Miranda, and G. C. Oades. "Anti-p capture in neutral beams". In: *eConf* C860410 (1986), p. 371 (cit. on p. 96).

[Deu51] M. Deutsch. "Evidence for the formation of positronium in gases". In: *Phys. Rev.* 82.3 (1951), pp. 455–456 (cit. on p. 95).

[Dro+07] G. Drobychev et al. "Proposal for the AEGIS experiment at the CERN Antiproton Decelerator (Antimatter Experiment: Gravity, Interferometry, Spectroscopy)". In: (2007) (cit. on pp. 11, 12, 16, 22, 86, 89, 95).

[Eöt90] R. von Eötvös. "Uber die Anziehung der Erde auf verschiedene Substanzen". In: *Mathematische und Naturwissenschaftliche Berichte aus Ungarn* 8 (1890), pp. 65–68 (cit. on p. 14).

[Fee+93] M. S. Fee, S. Chu, A. P. Mills, R. J. Chichester, D. M. Zuckerman, E. D. Shaw, and K. Danzmann. "Measurement of the positronium 1^3S_1-2^3S_1 interval by continuous-wave two-photon excitation". In: *Phys. Rev. A* 48.1 (1993), pp. 192–219 (cit. on p. 22).

[FLS15] R. Feynman, R. Leighton, and M. Sands. *The Feynman lectures on physics, Vol. II: The new millennium edition: Mainly electromagnetism and matter*. Hachette, 2015 (cit. on p. 77).

[Fri17] P. Friebel. "Grating alignment using Mach-Zehnder interferometers". Bachelor's thesis. University of Heidelberg, 2017 (cit. on p. 131).

[Fuj+08] M. C. Fujiwara et al. "Temporally controlled modulation of antihydrogen production and the temperature scaling of antiproton-positron recombination". In: *Phys. Rev. Lett.* 101 (5 2008), p. 053401 (cit. on p. 94).

[Gab+02] G. Gabrielse et al. "Stacking of cold antiprotons". In: *Phys. Lett. B* 548.3-4 (2002), pp. 140–145 (cit. on p. 98).

[Gab+90] G. Gabrielse, X. Fei, L. Orozco, R. Tjoelker, J. Haas, H. Kalinowsky, T. Trainor, and W. Kells. "Thousandfold improvement in the measured antiproton mass". In: *Phys. Rev. Lett.* 65.11 (1990), pp. 1317–1320 (cit. on pp. 19, 22).

[GBB06] G. Gronniger, B. Barwick, and H. Batelaan. "A three-grating electron interferometer". In: *New J. Phys.* 8.10 (2006), p. 224 (cit. on p. 29).

[GHA94] G. Gabrielse, L. Haarsma, and K. Abdullah. "Trapped positrons for antihydrogen". In: *Hyperfine Interact.* 89.1 (1994), pp. 371–380 (cit. on p. 92).

[Gil14] R. Gilmore. *Stark effect*. 2014 (cit. on p. 86).

[GO91] M. E. Glinsky and T. M. O'Neil. "Guiding center atoms: Three-body recombination in a strongly magnetized plasma". In: *Physics of Fluids B: Plasma Physics* 3.5 (1991), pp. 1279–1293. eprint: `https://doi.org/10.1063/1.859820` (cit. on p. 93).

[Ham16] Hamamatsu Photonics. *MCP (microchannel plate) and MCP assembly*. Catalog. 2016 (cit. on p. 108).

[Han16] J. S. Hangst. *Addendum to the ALPHA proposal: The ALPHA-g apparatus*. Tech. rep. CERN-SPSC-2016-031. SPSC-P-325-ADD-1. Geneva: CERN, 2016 (cit. on pp. 11, 12).

[Hau12] F. C. Haupert. "A moiré deflectometer as gravimeter for antihydrogen". PhD thesis. University of Heidelberg, 2012 (cit. on p. 121).

[HB05] J. S. Hangst and P. Bowe. *ALPHA proposal*. Tech. rep. CERN-SPSC-2005-006. SPSC-P-325. Geneva: CERN, 2005 (cit. on p. 14).

[HCN04] M. H. Holzscheiter, M. Charlton, and M. M. Nieto. "The route to ultra-low energy antihydrogen". In: *Phys. Rep.* 402 (2004), pp. 1–101 (cit. on p. 91).

[Hei27] W. Heisenberg. "Über den anschaulichen Inhalt der quantentheoretischen Kinematik und Mechanik". In: *Z. Phys.* 43.3-4 (1927), pp. 172–198 (cit. on p. 43).

[HH91] R. J. Hughes and M. H. Holzscheiter. "Constraints on the gravitational properties of antiprotons and positrons from cyclotron-frequency measurements". In: *Phys. Rev. Lett.* 66.7 (1991), pp. 854–857 (cit. on pp. 18, 19).

[HHC98] E. A. Hessels, D. M. Homan, and M. J. Cavagnero. "Two-stage Rydberg charge exchange: An efficient method for production of antihydrogen". In: *Phys. Rev. A* 57.3 (1998), pp. 1668–1671 (cit. on p. 98).

[Hor+09] K. Hornberger, S. Gerlich, H. Ulbricht, L. Hackermüller, S. Nimmrichter, I. V. Goldt, O. Boltalina, and M. Arndt. "Theory and experimental verification of Kapitza-Dirac-Talbot-Lau interferometry". In: *New J. Phys.* 11.4 (2009), p. 043032 (cit. on pp. 55, 62, 68).

[HSA04] K. Hornberger, J. E. Sipe, and M. Arndt. "Theory of decoherence in a matter wave Talbot-Lau interferometer". In: *Phys. Rev. A* 70 (5 2004), p. 053608 (cit. on pp. 31, 43, 44).

[Hug92] R. J. Hughes. "New test of the equivalence principle for the antiproton". In: *Phys. Rev. D* 46.6 (1992), R2283–R2286 (cit. on p. 18).

[HW13] M. Hori and J. Walz. "Physics at CERN's Antiproton Decelerator". In: *Prog. Part. Nucl. Phys.* 72 (2013), pp. 206–253 (cit. on pp. 11, 19–21).

[Ima+09] H. Imao et al. "ASACUSA MUSASHI: New progress with intense ultra slow antiproton beam". In: *Hyperfine Interact.* 194.1-3 (2009), pp. 71–76 (cit. on p. 20).

[Kad+15] A. Kadyrov, C. Rawlins, A. Stelbovics, I. Bray, and M. Charlton. "Antihydrogen Formation via Antiproton Scattering with Excited Positronium". In: *Phys. Rev. Lett.* 114.18 (2015) (cit. on p. 96).

[Kad+17] A. S. Kadyrov, I. Bray, M. Charlton, and I. I. Fabrikant. "Quantum suppression of antihydrogen formation in positronium-antiproton scattering". In: *Nat. Commun.* 8.1 (2017), p. 1544 (cit. on p. 97).

[Kal13] T. Kalvas. "Beam extraction and transport". In: *Proc. CAS - CERN Accelerator School: Ion Sources, Senec, Slovakia, 29 May - 8 June 2012*. Ed. by R. Bailey. CERN. Geneva: CERN, 2013, pp. 537–564 (cit. on pp. 79, 80).

[Kar04] S. G. Karshemboim. "Precision study of positronium: Testing bound state QED theory". In: *Int. J. Mod. Phys. A* 19.23 (2004), pp. 3879–3896 (cit. on p. 96).

[KB02] A. S. Kadyrov and I. Bray. "Two-center convergent close-coupling approach to positron-hydrogen collisions". In: *Phys. Rev. A* 66.1 (2002) (cit. on p. 96).

[Kel06] P. Keller. *Technologies for precision magnetic field mapping*. MetroLab Instruments (www.metrolab.com). 2006 (cit. on p. 108).

[Kra+13] D. Krasnický et al. "AEgIS experiment commissioning at CERN". In: AIP, 2013 (cit. on p. 91).

[Kra+16] D. Krasnický, R. Caravita, C. Canali, and G. Testera. "Cross section for Rydberg antihydrogen production via charge exchange between Rydberg positroniums and antiprotons in a magnetic field". In: *Phys. Rev. A* 94.2 (2016) (cit. on pp. 23, 96–99).

[Kur+15] N. Kuroda et al. "The ASACUSA CUSP: an antihydrogen experiment". In: *Hyperfine Interact.* 235.1-3 (2015), pp. 13–20 (cit. on p. 20).

[Lan+17] P. Lansonneur, P. Bräunig, A. Demetrio, S. R. Müller, P. Nedelec, and M. K. Oberthaler. "Probing electric and magnetic fields with a moiré deflectometer". In: *Nucl. Instr. Meth. Phys. Res. A* 862 (2017), pp. 49–53 (cit. on pp. 27, 37, 39, 75, 77, 89, 155).

[Lan21] A. Landé. "Über den anomalen Zeemaneffekt (Teil I)". In: *Z. Phys.* 5.4 (1921), pp. 231–241 (cit. on p. 84).

[Lau48] E. Lau. "Beugungserscheinungen an Doppelrastern". In: *Ann. Phys. (Berlin)* 437.7-8 (1948), pp. 417–423 (cit. on pp. 12, 27).

[Lis+12] L. Liszkay et al. "Positron annihilation in latex-templated macroporous silica films: pore size and ortho-positronium escape". In: *New J. Phys.* 14.6 (2012), p. 065009 (cit. on p. 22).

[LPB01] A. M. Lombardi, W. Pirkl, and Yu. V. Bylinsky. "First operating experience with the CERN decelerating RFQ for anti-protons". In: *Conf. Proc.* C0106181 (2001), pp. 585–587 (cit. on p. 20).

[Mad+05] N. Madsen et al. "Spatial distribution of cold antihydrogen formation". In: *Phys. Rev. Lett.* 94.3 (2005) (cit. on p. 94).

[MAT14] MATLAB. *version 8.4.0 (R2014b)*. The MathWorks Inc., Natick, Massachusetts. 2014 (cit. on p. 49).

[Mau97] S. Maury. "The Antiproton Decelerator: AD". In: *Hyperfine Interact.* 109.1/4 (1997), pp. 43–52 (cit. on pp. 11, 19).

[MBB10] S. Mariazzi, P. Bettotti, and R. S. Brusa. "Positronium cooling and emission in vacuum from nanochannels at cryogenic temperature". In: *Phys. Rev. Lett.* 104.24 (2010) (cit. on p. 22).

[McC+16] R. McConnell et al. "Large numbers of cold positronium atoms created in laser-selected Rydberg states using resonant charge exchange". In: *J. Phys. B* 49.6 (2016), p. 064002 (cit. on pp. 98, 99, 120, 122, 127).

[Mer+97] J. P. Merrison et al. "Hydrogen formation by proton impact on positronium". In: *Phys. Rev. Lett.* 78.14 (1997), pp. 2728–2731 (cit. on p. 97).

[MGW06] F. Major, V. Gheorghe, and G. Werth. *Charged particle traps: Physics and techniques of charged particle field confinement*. Springer Series on Atomic, Optical, and Plasma Physics. Springer, 2006 (cit. on p. 22).

[MK69] P. Mansbach and J. Keck. "Monte Carlo trajectory calculations of atomic excitation and ionization by thermal electrons". In: *Phys. Rev.* 181 (1 1969), pp. 275–289 (cit. on p. 92).

[MNT16] P. J. Mohr, D. B. Newell, and B. N. Taylor. "CODATA recommended values of the fundamental physical constants: 2014". In: *Rev. Mod. Phys.* 88 (3 2016), p. 035009 (cit. on pp. 84, 86).

[Moh34] S. Mohorovičić. "Möglichkeit neuer Elemente und ihre Bedeutung für die Astrophysik". In: *Astron. Nachr.* 253.4 (1934), pp. 93–108 (cit. on p. 95).

[Mor58] P. Morrison. "Approximate nature of physical symmetries". In: *Am. J. Phys.* 26.6 (1958), pp. 358–368 (cit. on p. 11).

[MS92] T. J. Murphy and C. M. Surko. "Positron trapping in an electrostatic well by inelastic collisions with nitrogen molecules". In: *Phys. Rev. A* 46.9 (1992), pp. 5696–5705 (cit. on p. 22).

[Mül16] S. R. Müller. "Moiré deflectometer for charged particles". Master's thesis. University of Heidelberg, 2016 (cit. on pp. 37, 39–41, 76).

[Mül17] S. R. Müller. internal report (unpublished). 2017 (cit. on p. 60).

[MW97] A. Müller and A. Wolf. "Production of antihydrogen by recombination of $\overline{p}$ with e+: What can we learn from electron–ion collision studies?" In: *Hyperfine Interact.* 109.1 (1997), pp. 233–267 (cit. on pp. 92, 93).

[Nag+17] H. Nagahama et al. "Sixfold improved single particle measurement of the magnetic moment of the antiproton". In: *Nat. Commun.* 8 (2017), p. 14084 (cit. on p. 11).

[NH08] S. Nimmrichter and K. Hornberger. "Theory of near-field matter-wave interference beyond the eikonal approximation". In: *Phys. Rev. A* 78 (2 2008), p. 023612 (cit. on pp. 55, 62, 68).

[Obe+96] M. K. Oberthaler, S. Bernet, E. M. Rasel, J. Schmiedmayer, and A. Zeilinger. "Inertial sensing with classical atomic beams". In: *Phys. Rev. A* 54 (4 1996), pp. 3165–3176 (cit. on pp. 12, 27, 29, 37, 38, 41, 89, 104, 111).

[Pac+16] N. Pacifico et al. "Direct detection of antiprotons with the Timepix3 in a new electrostatic selection beamline". In: *Nucl. Instr. Meth. Phys. Res. A* 831 (2016), pp. 12–17 (cit. on p. 12).

[Pan17] S. Pandolfi. "First antiprotons in ELENA". In: (2017) (cit. on pp. 20, 127).

[Par16] Particle Data Group. "Review of particle Physics". In: *Chin. Phys. C* 40.10 (2016), p. 100001 (cit. on p. 22).

[PJ16] C. Pralavorio and H. K. Jarlett. "A new ring to slow down antimatter". In: (2016) (cit. on pp. 20, 127).

[Poi+14] T. Poikela et al. "Timepix3: a 65K channel hybrid pixel readout chip with simultaneous ToA/ToT and sparse readout". In: *J. Inst.* 9.05 (2014), p. C05013 (cit. on p. 108).

[PS97] M. Pajek and R. Schuch. "Three-body recombination of ions with electrons in cooler-storage rings". In: *Hyperfine Interact.* 108.1 (1997), pp. 185–194 (cit. on p. 93).

[PVS08] T. Pohl, D. Vrinceanu, and H. R. Sadeghpour. "Rydberg atom formation in ultracold plasmas: Small energy transfer with large consequences". In: *Phys. Rev. Lett.* 100.22 (2008) (cit. on p. 92).

[Rad+14] B. Radics, D. J. Murtagh, Y. Yamazaki, and F. Robicheaux. "Scaling behavior of the ground-state antihydrogen yield as a function of positron density and temperature from classical-trajectory Monte Carlo simulations". In: *Phys. Rev. A* 90.3 (2014) (cit. on pp. 93, 94).

[Raw+16] C. M. Rawlins, A. S. Kadyrov, A. T. Stelbovics, I. Bray, and M. Charlton. "Calculation of antihydrogen formation via antiproton scattering with excited positronium". In: *Phys. Rev. A* 93.1 (2016) (cit. on p. 96).

[RG89] S. L. Rolston and G. Gabrielse. "Cooling antiprotons in an ion trap". In: *Hyperfine Interact.* 44.1 (1989), pp. 233–245 (cit. on p. 22).

[Sav+95] T. A. Savas, S. N. Shah, M. L. Schattenburg, J. M. Carter, and H. I. Smith. "Achromatic interferometric lithography for 100-nm-period gratings and grids". In: *J. Vac. Sci. Technol. B* 13.6 (1995), pp. 2732–2735 (cit. on pp. 16, 36).

[SBD75] J. Stevefelt, J. Boulmer, and J.-F. Delpech. "Collisional-radiative recombination in cold plasmas". In: *Phys. Rev. A* 12 (4 1975), pp. 1246–1251 (cit. on pp. 92, 93).

[Sch+08] S. Schlamminger, K.-Y. Choi, T. A. Wagner, J. H. Gundlach, and E. G. Adelberger. "Test of the equivalence principle using a rotating torsion balance". In: *Phys. Rev. Lett.* 100.4 (2008) (cit. on p. 16).

[Smo+15] C. Smorra et al. "A reservoir trap for antiprotons". In: *Int. J. Mass Spectrom.* 389 (2015), pp. 10–13 (cit. on p. 20).

[Smo+17] C. Smorra et al. "A parts-per-billion measurement of the antiproton magnetic moment". In: *Nature* 550.7676 (2017), pp. 371–374 (cit. on pp. 11, 22).

[Sor+10] P. Sortais, T. Lamy, J. Médard, J. Angot, L. Latrasse, and T. Thuillier. "Ultracompact/ultralow power electron cyclotron resonance ion source for multipurpose applications". In: *Rev. Sci. Instrum.* 81.2 (2010), 02B314 (cit. on p. 82).

[Spe+04] A. Speck, C. Storry, E. Hessels, and G. Gabrielse. "Laser-controlled production of Rydberg positronium via charge exchange collisions". In: *Phys. Lett. B* 597.3-4 (2004), pp. 257–262 (cit. on p. 98).

[Sto+04] C. H. Storry et al. "First Laser-Controlled Antihydrogen Production". In: *Phys. Rev. Lett.* 93 (26 2004), p. 263401 (cit. on pp. 23, 90, 95, 97, 98).

[Tal+88] C. Talmadge, J. .-.-P. Berthias, R. W. Hellings, and E. M. Standish. "Model-Independent Constraints on Possible Modifications of Newtonian Gravity". In: *Physical Review Letters* 61.10 (1988), pp. 1159–1162 (cit. on p. 15).

[Tal36] H. Talbot. "Facts relating to optical science. No. IV". In: *Phil. Mag. Series 3* 9.56 (1836), pp. 401–407. eprint: `http://dx.doi.org/10.1080/14786443608649032` (cit. on pp. 12, 27).

[Tes+15] G. Testera, D. Krasnický, F. Sorrentino, and R. Caravita. *Work with electrons (Jan.-Feb 2015)*. AEgIS collaboration meeting. 2015 (cit. on p. 139).

[THK06] S. Thraenert, E. Hassan, and R. Krause-Rehberg. "Orthopositronium lifetime measurement – positron source activity and statistics". In: *Nucl. Instr. Meth. Phys. Res. B* 248.2 (2006), pp. 336–339 (cit. on p. 12).

[Ulm+15] S. Ulmer et al. "High-precision comparison of the antiproton-to-proton charge-to-mass ratio". In: *Nature* 524.7564 (2015). Letter, pp. 196–199 (cit. on pp. 11, 19, 22).

[Wag+12] T. A. Wagner, S. Schlamminger, J. H. Gundlach, and E. G. Adelberger. "Torsion-balance tests of the weak equivalence principle". In: *Classical and Quantum Gravity* 29.18 (2012), p. 184002 (cit. on p. 15).

[Wid99] E. Widmann. "Antiprotonic atom formation and spectroscopy-ASACUSA experiment at CERN-AD". In: *Nucl. Phys. A* 655.1-2 (1999), pp. c353–c362 (cit. on p. 14).

[Wig32] E. Wigner. "On the quantum correction for thermodynamic equilibrium". In: *Phys. Rev.* 40 (5 1932), pp. 749–759 (cit. on pp. 31, 43).

[Wil14] C. M. Will. "The confrontation between general relativity and experiment". In: *Living Rev. Relativ.* 17.1 (2014), p. 4 (cit. on pp. 13, 15, 16).

Acknowledgments

These last three and half years of my life have turned it completely upside down. Moving to a new country and learning a new language is something that shakes you from the depths, and, someway, changes you. There have been times in which I have felt like a foreigner in a foreign land, lost without a beacon, but, fortunately, I have been supported by some amazing people that deserve the credit for not having let me float adrift. I am deeply grateful to

Prof. Dr. Markus K. Oberthaler, for having accepted me in his research group and having supervised my work, offering me guidance and helping me reach my goal. I want to thank him also as a person, more than a teacher, for having given me some honest advice on how to proceed from now on.

Prof. Dr. Markus Arndt, mainly for two reasons: the first is because he found the time and the patience to correct and evaluate this work; the second is that without his gift (the nanometric gratings we are using in Heidelberg), our research group would have not managed to step into the business of ion interferometry.

Prof. Dr. Bernd Jähne and Prof. Dr. Matthias Bartelmann, for having accepted to be part of my commission, despite this work being quite far from their usual research topics.

Philippe Bräunig, for having been my first contact with the Matter-wave research group, the post-doc who drove our team and the friend who helped me settling my life in Germany at the very beginning. Stating that he saved me would be a euphemism.

Mio fratello Luca, per essermi stato vicino tutto il tempo, nonostante ottocento chilometri e rotti di distanza. Senza di te, mi sarei perso più di una volta. Grazie di cuore, fratellino!

I miei genitori, Daniela e Guerino, per non aver tentato di fermarmi quando ho deciso di trasferirmi in Germania e avermi aiutato "a distanza" per questi ultimi tre anni e mezzo. Senza il loro supporto, non ce l'avrei fatta.

Simon R. Müller, for working with me all this time and being a reference point for me in the lab. He has always been a serious colleague and someone who everybody would like to have around as a problem solver. Now, guess why all the "funny" stuff happened when he was on holiday...

Pierre Lansonneur, our friend and colleague from France who worked with us and was in charge of the proton source. Yes, Pierre, NOW we are sure they are protons. And you?

Zhongyi Feng and Angelika Klein, for having made me feel at home so far from home. Your honesty and openness helped me improve myself and see over my limitations, so that I could become a better person.

Giovanni Cerchiari, per essere stato il mio più grande supporto "italoparlante" sul posto, per le innumerevoli cene prima Im Neuenheimer Feld poi in Rohrbach... e, più in generale, per avermi sempre aiutato nel momento del bisogno.

Fabian Billert, for his help, friendship and amazing WG-parties who helped me integrating myself in this bizarre country.

Gerard and Patrick, who worked with us as Bachelor students and shared with us the "trials and tribulations" of the experimental, while giving their precious contribution to keep the experiment up and running.

Dagmar und Christiane, die mir in den letzten dreieinhalb Jahren sehr geholfen haben. Am Ende, konnte ich mit beiden Deutsch sprechen. Herzlichen Dank für alles!

Gemma, Daniel, Ruggero[1] e Lea, che nonostante la mia (ehm...) defezione, mi hanno sempre aiutato nel momento del bisogno. Senza di loro, non sarei dove sono ora. Inoltre, discutere con loro mi ha aiutato molto nel mettere insieme dati e numeri per questo lavoro.

Lukas Mairhofer, der uns bei der Ausrichtung unseres Interferometer sehr geholfen hat. Die Idee, Littrow-Reflexion zu verwenden, war lebensrettend!

[1] altrimenti noto come "quell'uomo", nel gergo locale

Davide Pagano, per aver tirato il multi-threading fuori dal cilindro al momento giusto e per interessanti discussioni sull'implementazione di software per l'esperimento.

Elisa Ludwig, die mit mir eine WG für mehr als drei Jahren geteilt hat. Du warst die beste Mitbewohnerin auf die man wünschen können! Außerdem, ist Peeta besser als Gale.

Lena Isayeva, die hat mir Deutsch gelehrt. Jetzt kann ich Romane lesen! Das wäre undenkbar, nur drei Jahren vorher!

Fereydoon, Christos, Azer, Alessandro, Filip, Tomas, Virginia, Iris... and all the members of my German class, for contributing to make my stay in Germany unforgettable!

Edoardo Milano, la persona che mi ha spronato ad imparare a programmare (per batterlo, ma questo è un altra storia). La nostra rivalità mi ha permesso di arrivare dove sono ora. Grazie di tutto!

Stefano Becce, perché non c'è stata domenica in cui non abbiamo discusso dei gran premi della Ferrari (in toni non proprio pacati che non posso riportare per motivi di decenza). Grazie per essere rimasto in contatto con me nonostante la distanza!

Andrea Torchi, perché nonostante tutto ha continuato ad inondarmi di battute orribili, come ai tempi dell'università - persino dall'altro lato della Manica.

Herr Doktor Helmut Strobel, der Babo und die Seele unserer Forschunggsruppe, der Mann unzähliger Lsungen, der Mann, der mit mir so viele Pizzas und Biere in Café Botanik geteilt hat. Müss ich noch etwas hinzufügen?

Tobias Rentrop, der sicherlich es versteht, auch wenn ich auf Italienisch es schreibe: grazie di tutto, Tobi! Mi hai aiutato a integrarmi nel gruppo e non farmi sentire un estraneo[2]!

Arno Trautmann, der mir gespornt hat, Deutsch besser zu lernen... und, tja, der auch etwas anderes gemacht hat[3].

Stefanie Czischek, die so mutig war, meine Thesis zu lesen und zu

[2] a certain accident involving a plastic horse head found in my office with a threatening message in Italian may or not may be involved in this acknowledgement

[3] see previous footnote

korrigieren, (fast) ohne etwas über mein Thema zu wissen.

Max und Philipp, für unsere "Eros Ramazzotti - Wein - Nudeln"-Abends. *Se bastasse una sola canzone...*

All the former and present remaining members of the Matterwaver Seeotter, who in one way or another, made my stay in Germany better (or at least more interesting).

The AEḡIS Collaboration at large for the nice working environment at CERN and the efforts to keep the experiment running.

Zia Michela e nonno Bertino, perché nonostante la distanza non hanno mai smesso di essermi accanto. Dopo la mia tesi, devo batterti a cirulla, nonno!

L'intera famiglia Demetrio, allargata e in continuo aumento! Tutti gli zii, zie, cugini, cugine, cuginetti e cuginette che hanno animato ogni cenone di Natale con vino, tombola e zeppole.

Nick, Enri, Rob, Luca, Ale e Mauri, i "Balordi" di Varazze, sempre pronti ad una birra ogni volta che torno a casa.

Miriana, per avermi spronato ad imparare la lingua locale ed essermi stata vicina all'inizio della mia avventura tedesca.

Arianna, per la mutua condivisione dei drammi del dottorato a mille chilometri di distanza.

La C.S.K. Varazze, che non ha mai smesso di considerarmi parte del gruppo nonostante la lontananza.

Il buon professor Borgna e il gruppo di caffeinomani che negli anni si sono ritrovati a Savona (Davide, Michela e Stefano), per la compagnia e le interessanti discussioni.

Siegfried Spiegel, Morris Weißer, Werner Lamade, Jürgen Schölles und alle die andere Mitgliedere von der Mechanische und Elektronik Werkstatt vom KIP: ohne sie, unsere Laborarbeit wäre sicherlich schwerer!

Alle die Mitlgiedere vom KIP, die mir mit Burokratie, Computerfehlern, Bestellungen und andere komische Dinge in diesen drei Jahren geholfen haben.